# EXPLOITING NANOSCALE MATERIALS PROPERTIES FOR CONTROLLED DRUG DELIVERY SYSTEMS

A thesis submitted to

## UNIVERSITY OF EAST ANGLIA

In partial fulfilment of requirements for the degree of

## DOCTOR OF PHILOSOPHY

## OCTOBER 2013

By

## Laili Che Rose

School of Chemistry

University of East Anglia

# DECLARATION

I declare that the work contained in this thesis submitted by me for the degree of Doctor of Philosophy is my work, except where due reference is made to other authors, and has not been previously submitted by me for a degree at this or any other university.

Laili Che Rose

# Abstract

The main objective of this work was to develop a novel drug delivery system exploiting special opportunities afforded by synthesis of nanoscale materials to be applied inside the colon. It must be robust enough to cope with the adverse conditions in the gastrointestinal tract (GI) and be able to reach and release "on demand" at the colon area at the right time. In this work, an oral capsule formulation with iron oxide nanoparticles (IONs) containing coating was used to transport drug and release drug in the colon.

With that in mind, the synthesis of poly (alkylcyanoacrylate) nanocapsules by microemulsion polymerisation and magnetic iron oxide nanoparticles (IONs) via a co-precipitation method were conducted. The key physical properties of the materials were characterized employing standard techniques such as HPLC, FTIR, DSC, DLS, XRD, TEM and SEM. Hard capsules filled with model drug, paracetamol, were coated with IONs containing coatings (fatty acids and paraffin). The optimum composition for the formulation of the coating embedded with the nanoparticles was explored with respect to protection of the drug payload from conditions in the GI tract as well as for effective release "on demand" using radio-frequency hyperthermia. The optimum radiofrequency and the power level for heating the nanoparticles were also determined and melting the coating using magnetic nanoparticle hyperthermia.

Results showed that paraffin-based coatings had appropriate properties for this application. Finally, taking into account all the results, a design of a novel drug delivery system, together with an experimental setup for testing the "release in demand" was proposed. The approach is generic, easy to set up and could also be applied to many other situations where delivery on demand is required.

# Table of Contents

**Chapter 4 Microemulsions as Template for the Preparation of Poly (alkylcyanoacrylate) Nanocapsules for Drug Delivery System via Microemulsion Polymerisation Method**

Chapter 7 Demonstrating *in vitro* "Release on Demand" using Magnetic Hypermia

**Chapter 8 Conclusions and Future Work**

**Appendix**

# List of Figures

# List of Tables

# List of Abbreviations

| | |
|---|---|
| AC | Alternating Current |
| DC | Direct Current |
| DLS | Dynamic Light Scattering |
| DSC | Differential Scanning Calorimetry |
| FT-IR | Fourier Transform-Infrared |
| GI | Gastrointestinal |
| HLB | Hydrophilic-Lipophilic Balance |
| HPLC | High Performance Liquid Chromatography |
| IONs | Iron Oxide Nanoparticles |
| JCPDS | Joint Committee on Powder Diffraction Standards |
| MRI | Magnetic Resonance Imaging |
| PBS | Phosphate Buffered Saline |
| SEM | Scanning Electron Microscope |
| SPIONS | Superparamagnetic Iron Oxide Nanoparticles |
| SQUID | Superconducting Quantum Interference Device |
| TEM | Transmission Electron Microscope |
| TGA | Thermogravimetry Analysis |
| UV | Ultraviolet |
| XRD | X-Ray Diffraction |
| FaSSIF | Fasted State Simulated Intestinal Fluid |
| RF | Radio Frequency |

# Acknowledgements

*I would like to take this golden opportunity to express my deepest and greatest gratitude to my supervisor, Dr Andrew Mayes for all his support, patient guidance, enthusiastic encouragement, useful critiques and advice throughout this journey. Special thank also goes to my co-supervisor, Dr Sheng Qi for her valuable advice and encouragement in every step of the way. Putting the pain and agony aside, I am glad to say that it has been a wonderful and exciting journey; an educating journey into the mystical world of fine particles.*

*I am truly blessed to have made acquaintance with friendly and understanding lab partners and technicians – Mr Ben Piggeot and Dr Marcus (Institute of Food Research) , Dr Paul Southern and Mr Joseph Bear (University College of London) and Mr Bertrand Leze and Dr Kate Bowman (University of East Anglia)*

*I would like to express my very great appreciation to University Malaysia Terengganu (UMT), Malaysian Government and University of East Anglia (UEA) for making my dream come through and making my stay here in England a pleasant and rewarding experience. Life has knocked me down a few times. It showed me things I never wanted to see. I experienced sadness and failures. Thank you to my precious God for the strength given throughout this journey.*

*Not forgetting to my beloved husband, Professor Dr Hamdan Suhaimi and my two lovely children, Haiman and Halili, for their unconditional and endless love, and also for always being there in times of need. All three of you have showered me with love and have made me become a better wife and mother. Also thank you to my mother-in-law, Hajjah Chik Norriah Yan for her pray. I love all of you very much.*

*My special thanks are extended to my beloved sisters and brothers, all my family members and friends in Malaysia and round of the world for their continuous pray, love, support and encouragement throughout my study. Thank you all.*

*Last but not least, I wish to thank to my colleagues and friends for their support and encouragement. To Armylisa's, Dr Art, Dr Sam, Dr Abdi, Dr Anong, Sonia and my best friend Mercedes Escobar – Thank you very much! .*

# Dedication

*In Loving Memory of*

*My Beloved Mother and Father*

*Hajah Fatimah Bt Md Sab*

*&*

*Haji Che Rose Bin Baba*

# CHAPTER 1

## Introduction

## 1.1 Brief Overview

"Nano-", the buzz word in modern science, is becoming increasingly used in scientific literature. Many "nano-" words such as nanometer, nanoscale, nanoscience, nanotechnology, nanostructure, nanotube etc are becoming commonly used. Nano is a prefix and it is derived from the Greek word nanos meaning dwarf, Ever since it was recognized that particles on the nano-scale had different and interesting properties compared to their bulk phase, vast amounts of research have been carried out regarding how they may be applied for different purposes and in different fields of interest. The idea of nanotechnology producing nanoscale materials and carrying out nanoscale manipulations has been around for quite some time. Nobel Prize winner, Richard P. Feynman in his talk titled *There's Plenty of Room at the Bottom* (1959) is credited for coining the idea. He considered the possibility of direct manipulation of individual atoms as a more powerful form of synthetic chemistry than those used at the time. It is from that consideration that the idea of nanotechnology was born. There is currently no accepted international definition of nanomaterials but many authors limit the size of nanoparticles to 50 nm (Kittelson, 2001) or 100 nm (Borm *et. al, 2006*).

Nanomaterials consist of various nanostructured materials, such as nanoparticles, nanocapsules, nanorods or nanoplates. They are already used in consumer products, such as sunscreens, healthcare products, textiles and paints. In nanomaterials the surface properties dominate over the bulk properties (Alivisatos, 1996; Hanada *et al.*, 2005; Lia and Zhang, 2009; Puntes *et al.*, 2001). The very large surface areas of these materials result in new and improved properties such as improved catalytic activity (Hanada *et al.*, 2005), or unique optical (Lia and Zhang, 2009) and quantum behaviour (Alivisatos, 1996). These properties can be used to overcome some of the limitations found in traditional therapeutic and diagnostic agents.

Even before Feynman, there were already traditional techniques developed in the field of interface and colloid chemistry for characterizing nanomaterials. For instance, the solution-gelation (sol-gel) process, a wet-chemical technique commonly used to synthesise a wide variety of nanomaterials was used by Michael Faraday (1857) to synthesise 'gold sols' and gold colloids were characterised using ultramicroscopy by Richard A. Zsigmondy (1909).

The magnetic properties of nanocapsules and nanoparticles have attracted much interest not only in the field of magnetic recording media such as audio and videotape (Coey, 2010), but also in the areas of medical care such as drug delivery systems, medical applications including radio frequency hyperthermia, magnetic resonance imaging (MRI), medical diagnostics and cancer therapy (Jordan *et al.*, 1999; Murray *et. al*, 2000; Mazzola, 2003; Paull *et al*, 2003; Pankhurst *et. al*, 2003 Lecommandoux *et al.*, 2006; and Gannon, *et al.,* 2008). In the last decades, much research has been devoted to the synthesis of nanoparticles. Many publications have described efficient synthetic routes to shape-controlled, highly stable, and monodisperse magnetic nanoparticles, especially in the last few years. Several methods including co-precipitation (Laurent *et al.*, 2008), thermal decomposition and/or reduction (Guardia *et al.*, 2010a,b), microemulsion synthesis (Thomann *et al.*, 2005), and sol-gel synthesis (Duraes *et al.*, 2005) can all be directed at the synthesis of high-quality magnetic nanoparticles.

## 1.2 Statement of Problem

Cancer is one of the most challenging diseases to manage and, while treatments and survival rates have improved greatly over the last 30 years, it is still a major challenge in the world of medicine. Colorectal cancer (CRC) is the third most common cancer in the United Kingdom after breast and lung cancer, with approximately 40,000 new cases registered each year resulting high mortality rate (Ferlay *et al.*, 2010). This makes it the second most common cause of cancer death in the United Kingdom. Occurrence of CRC is strongly related to age, with almost three-quarters of cases occurring in people aged 65 or over. In CRC, cells in the colon or in the rectum start

to grow in an uncontrolled way, forming a lump called the primary cancer or primary tumour. Like other cancers, CRC starts in a small area but can spread to other parts of the body to form metastatic tumours. The term CRC covers cancers in both the colon (colon cancer) and the rectum (rectal cancer).

Even though many effective drug treatments have been developed to treat this condition, the problem still prevails. The main problem is to deliver the drugs to the affected part of the GI tract in adequate doses. Due to poor and ineffective drug delivery, many patients have to face the trauma of surgical procedures. At the moment, the mode of treatment for this type of cancer is by using targeted radiotherapy and surgery. Surgery is the preferred treatment for people with localized cancer. Therefore, targeted drug treatment via chemotherapy has the potential of increasing the rate of survival.

In many drug delivery systems with the exception of tablets and liquid dosage forms, drugs are either encapsulated or entrapped inside or on the surfaces of a coated carrier, usually a capsule or some lipid nanostructure entities. This may pose a problem in delivery of the drugs into the body due to the complexity of the microenvironments inside the body such as the variation of pH as it passes through the digestive tract, the microflora of colonic bacteria and various enzymatic activities used to degrade the food substrate. Thus, the drug delivery system must be robust enough to survive these adverse changes and be able to reach and release at the targeted area at the right time. The carriers, especially the lipid-based ones, are sometimes made of multilayers of polymers. This layering of polymers may face issues of biodegradability and biocompatibility and thus limit their ability to scale up for mass production. With the huge changes in the body system, it makes this type of controlled release subjected to poor delivery and release of the drugs and thus does not always give the intended result.

With that note, a new way of colonic drug delivery so that the drug is only released at the affected part of the GI tract in adequate doses should offer significant benefits. In order to achieve this, we propose a new type of solid wax based drug capsule that can be administered orally and tracked so that once it reaches the target location the

drug can be released by melting the wax using harmless radio-waves as shown in Figure 1.1. This can be done by using wax embedded with superparamagnetic iron oxide nanoparticles (IONs). What is required is a small hand-held radiofrequency, RF coil that produces harmless radio waves. With the device placed over the patient, the radio waves produced can then be used to selectively heat the IONs. By doing so, it causes the wax on the capsule to melt and so release the drug at the target location without damaging the surrounding tissue. Heating of certain organs or tissues to temperatures between $41^{o}C$ and $46^{o}C$ preferably for cancer therapy is called hyperthermia (Jordan *et al.*, 1999). In this work, magnetic nanoparticle hyperthermia (MNH) will be employed to melt the wax. MNH heats magnetic nanoparticles using harmless RF irradiation by magnetisation reversal processes of the nanoparticles (Hegrt *et al.*, 2006).
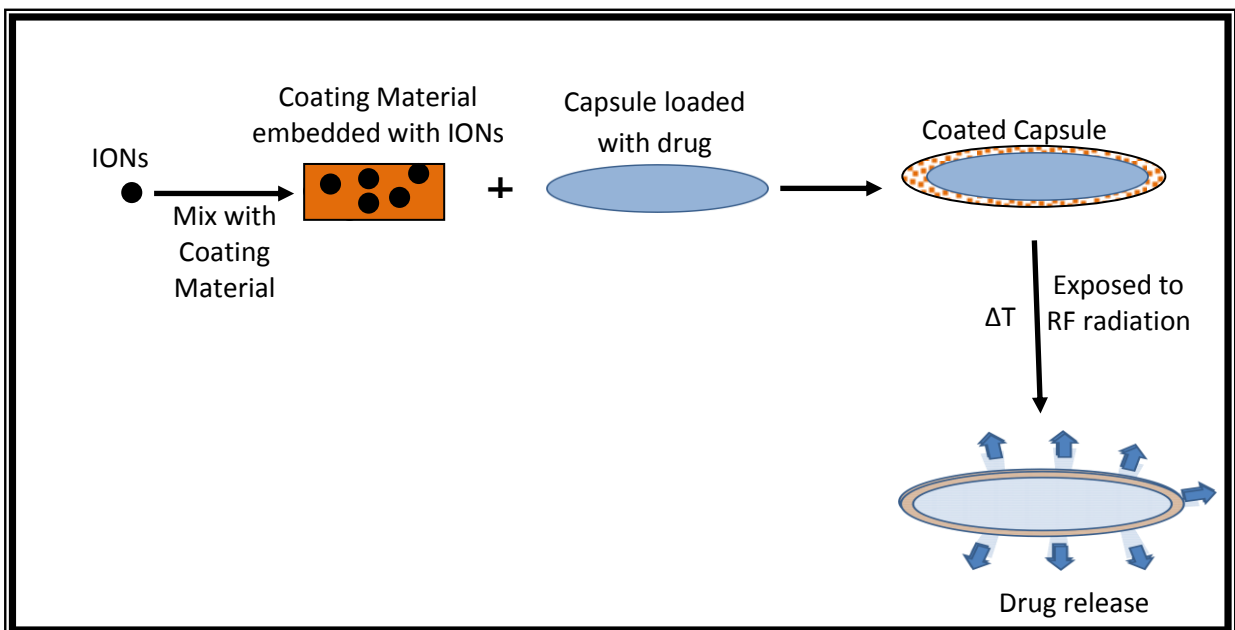


**Figure 1.1** Design of IONs embedded coated capsule loaded with drug and heated through applied field forcing the drugs to be released for a new colonic targeted drug delivery system.

## 1.3 Objectives

The main objective of this work is to develop a new, simple and robust targeted drug delivery system to be applied inside the GI tract (Figure 1.1). This new system joins IONs, magnetic hyperthermia and magnetically triggered. Solid fatty acid and paraffin based drug capsules will be embedded with IONs at optimal coating composition. The system is designed for a non-invasive physical release mechanism that works with a macroscopic, orally-delivered capsule having a universal and relatively simple encapsulating coat that can be mass produced.

In order to achieve the above objective, a number of key activities can be identified:

- Synthesise and characterise IONs
- Investigate the loading of IONs that gives the most efficient heating.
- Formulate the optimum composition for the fatty acids and paraffins and IONs to be used as coating materials to coat the capsule.
- Find the optimum radiofrequency and the power level for heating the IONs with MNH
- Study drug release under different environmental conditions which mimic the GI tract
- Propose a new and simple colonic targeted drug release system.

## 1.4 Scope of Thesis

As mentioned above, the main objective of this work is to develop a new, simple and robust targeted drug delivery system to be applied inside the GI tract. In order to achieve this, a range of key problems will be investigated. Therefore, to facilitate the understanding of the work done, this thesis will be presented and divided into 8 chapters.

Chapter 1 covers the introduction for the overall work together with the basic concepts and terminology related to nanomaterials. A brief overview, the problem

statements, gaps and how to fill the gaps plus the objective of the work will also be outlined.

Chapter 2 of the thesis provides a more detailed background to the work by presenting a literature review on the work published, mainly on nanoparticles (the major component of nanomaterials) and drug delivery. This chapter is a modest attempt to give a review of some of the past and recent advances these rapidly expanding areas, through the total literature for both of these fields is vast and it would be impossible to cover it comprehensively here.

Chapter 3 covers the materials and methodology aspects of the work. This includes the chemicals, a brief overview of scientific equipment or techniques and methodologies that are involved in undertaking the investigation.

Chapter 4 describes an initial attempt to prepare poly (alkylcyanoacrylate) nanocapsules via microemulsion polymerization. A region of water-in-oil microemulsion stabilised by non-ionic surfactant was identified and used as a template. Monomers were then added into the microemulsion template in order to obtain nanocapsules. The prepared nanocapsules were intended for use in the delivery of drugs. In addition, the use of pseudoternary phase diagrams to locate the microemulsion region and the compositions of the template will also be described in this chapter.

Chapter 5 describes the synthesis of the magnetic nanoparticles namely iron oxide nanoparticles (IONs) via a co-precipitation process. The resulting IONs were characterised using standard equipment and procedures. From these results, some of their physical properties will be elucidated and presented.

Chapter 6 discusses the formulation work on the proposed capsule to be used in the drug delivery system. Various compositions of fatty acids, paraffins and nanoparticles needed to coat the capsule were deployed in order to find the optimum composition for further tests. The optimum radiofrequency and the power level for heating employing MNH will also be described. This chapter also covers the study of dissolution of the capsules to release drug. The sensitivity and responsivity to pH and temperature of the capsules, using buffer solutions and bile salts, will be presented and discussed.

Chapter 7 will describe findings from visual observation of MNH of coated capsules. Information from visual observation should shed more light on the heating, melting and solubilising behaviour of the coated capsules. This chapter will begin by describing the work done to visually observe the behaviours of coated capsules towards heating by hyperthermia. The coated capsule in this part of the work will be subjected to different environments in order to visually observe its behaviour under applied magnetic fields. The visual observation will be done by using a thermal imaging camera, video camera and fibre-optic thermosensors. This chapter ends by proposing a simple experimental set up for drug release system and discussing the experimental results from the proposed set up.

Chapter 8 ends the thesis by summarising the main conclusions of the presented work as well as an outlook on future research directions.

## 1.5 References

Alivisatos, A. P. (1996). Semiconductor clusters, nanocrystals, and quantum dots. *Science*, **271**: 933-937.

Borm, P.J.A., Robbins, D., Haubold, S., Kuhlbusch, T., Fissan, H., Donaldson, K., Schins, R.P.F., Stone, V., Kreyling, W., Lademann, J., Krutmann, J., Warheit, D., Oberdorster, E., (2006). The potential risks of nanomaterials: a review carried out for ECETOC (review) *Part. Fibre Toxicol.*, **3**:11-46

Coey, J.M.D., (2010). Magnetism and Magnetic Materials, pg 1

Duraes, L., Costa, B., Vasques, J., Campos, J. and Portugal, A. (2005). Phase investigation of asprepared iron oxide/hydroxide produced by sol-gel synthesis. *Materials Letters* **59**, 859-863.

Faraday, M. (1857). 'The Bakerian lecture: Experimental relations og gold 9and other metals) to light, *Phil. Trans. R. Soc. Lond.*, **147**: 145-181.

Ferlay, J., Shin, H.R., Bray, F., Forman, D., Mathers, C., and Parkin, D.M. (2010). Estimates of worldwide burden of cancer in 2008: GLOBOCAN 2008, *Int. J. Cancer*, **127**: 2893-2917.

Feynman, R.P. (1959). There's plenty of room at the bottom, An Invitation to Enter a New Field of Physics, Annual meeting of the American Physical Society, California Institute of Technology, Dec. 29; or http://www.zyvex.com/nanotech/feynman.html.

Guardia, P., Perez, N., Labarta, A., and Batlle, X., (2010a). Controlled synthesis of Iron Oxide nanoparticles over a wide size range, *Langmuir*, **26**:5843-5847

Guardia, P., Perez-Juste, J., Labarta, A., Batlle, X. and Liz-Marzan, L.M. (2010b). Heating rate influence on the synthesis of iron oxide nanoparticles: the case of decanoic acid. *Chem. Commun.* **46**: 6108-6110.

Ganno, C.J., Patra, C.R., Bhattacharya, R., Mukerjee, P. And Curley, S.A. (2008). Intracellular gold nanoparticles enhance non-invasive radifrequency thermal destruction of human gastrointestinal cancer cells, *J. Nanobiology*, **6(2)**: 1-9.

Hanada, N., Ichikawa, T., and Fujii, H. (2005). Catalytic effect of nanoparticle 3d-transition metals on hydrogen storage properties in magnesium hydride $MgH_2$ prepared by mechanical milling, *J. Phys. Chem. B.*, **109**: 7188-7194

Hegrt, R., Dutz, S., M¨uller, R., and Zeisberger, M., (2006). Magnetic particle hyperthermia: Nanoparticle magnetism and materials development for cancer therapy, *J. Phys.: Condens Matter,* **18**:S2919-S2934.

Jordan, A., Scholz, R., Wust, P., Fahling, H. and Felix, R., (1999). Magnetic fluid hyperthermia (MFH): Cancer treatment with AC magnetic field induced excitation of

biocompatible superparamagnetic nanoparticles. *J. Magnetism Magnetic materials,* **201**: 413-419.

Kittelson, D.B., (2001). Recent measurements of nanoparticle emission from engines Current Research on Diesel Exhaust Particles, Japan Association of Aerosol Science and Technology, 9 January (Tokyo, Japan) and references therein

Laurent, S. et al. (2008). Magnetic Iron Oxide Nanoparticles: Synthesis, Stabilization, Vectorization, Physicochemical Characterizations, and Biological Applications. *Chem. Rev.* **108**: 2064-2110.

Lecommandoux, S., Sandre, O., Checot, F., and Perzynski, R. (2006). Smart hybrid magnetic self-assembled micelles and hollow capsules, *Prog. Solid State Chem.*, **34**: 171-179.

Lia, J., and Zhang, J.Z. 2009). Optical properties and applications of hybrid semiconductor nanomaterials, *Coordination Chem. Rev.*, **253**: 3015-3041.

Lu, A.H., Salabas, E.L., and Schuth, F., (2007). Magnetic nanoparticles: synthesis, protection, functionalization and application, *Angew. Chem. Int. Ed.* **46**:1222-1244 and references therein.

Mazzola, L. (2003). Commercializing nanotechnology. *Nature Biotechnology*, **21**:1137-1143

Murray, C.B., Kagan, C.R., Bawendi, M.G. (2000). Synthesis and characterisation of monodisperse nanocrystals and close-packed nanocrystal assemblies, *Annu Rev Mater Sci.*, **30:**545-610.

Pankhurst, Q.A., Connolly, J., Jones, S.K., Dobson, J. (2003**).** Applications of magnetic nanoparticles in biomedicine, *J Phys D: Appl Phys*, **36:**R167-R181.

Paull, R., Wolfe, J., Hebert, P., Sinkula, M. (2003). Investing in nanotechnology, *Nature Biotechnology*, **21:**1134-1147.

Puntes, V.F., Krishnan, K.M., and Alivisatos, A.P, (2001). Colloidal nanocrystal shape and size control: the case of cobalt. *Science* **291(5511)**: 2115-2117.

Salata, O.V., (2004). Application of nanoparticles in biology and medicine, *J Nanobiotechnlogy*, **2**:1-6.

The Cancer Genome Atlas Network (2012). Comprehensive molecular characterization of human colon and rectal cancer, *Nature*, **487**: 330-337.

Thomann, R., Nann, T. and Darbandi, M. (2205). Single quantum dots in silica spheres by microemulsion synthesis. *Chem. Mater.* **17**: 5720-5725.

Zsigmondy, R. (1909). "Colloids and the ultramicroscope: A manual of colloidal chemistry and ultramicroscopy", trans. by Alexander, J., Wiley, J. & Sons, New York.

# CHAPTER 2

## Literature Review

## 2.1 Nanomaterials

### 2.1.1 Does size matter?

This question reminded the author of her's thesis about first day of lectures she attended for her colloid chemistry class many years back. The professor asked the above question in his opening remark on the topic about the importance of surfaces for small particles. Clearly, the answer to this question is quite obvious: bigger things always dominate the smaller ones. But then, there is a saying that goes 'less is more'. According to the professor, this polemic can be clarified by considering the following task.

Consider a spherical particle, for example water, having a radius of 1.0 cm. Reapportion the particle by subdividing it, first, into an array of spheres, each with a radius half that of the original sphere. Then in the next subdivision, the radius of each of the spheres will be cut into half again. In the following subdivision, the radius will be halved again, and so on. The results of such reapportioning are shown in Table 2.1 (Hiemenz, 1986). It can be shown that after 25.62 halvings of all spheres, one water molecule per sphere is reached. From the Table 2.1 or by using equation 1, the radius of the water molecules after 25.62 halvings of the spheres can be evaluated. The radius is found to be 0.193 nm. However, the radius of a water molecule from the van der Waals b value is about 0.145 nm. The difference in value for the radius, points out the fact that the characterization of any material may be sensitive to the size of the sample.

**Table 2.1** The parameters after cutting a sphere of water each time by halves until n times (Hiemenz, 1986).

| Cut Number, n | Radius, $R_n$ (cm) | Number of water molecules per sphere | Total surface energy (J) |
|---|---|---|---|
| 0 | 1.0 | $1.38 \times 10^{23}$ | $9.07 \times 10^{-5}$ |
| 1 | $5 \times 10^{-1}$ | $1.75 \times 10^{22}$ | $1.81 \times 10^{-4}$ |
| 2 | $2.5 \times 10^{-1}$ | $2.18 \times 10^{21}$ | $3.62 \times 10^{-4}$ |
| 3 | $1.25 \times 10^{-1}$ | $2.73 \times 10^{20}$ | $7.27 \times 10^{-4}$ |
| . | . | . | . |
| n | $\left(\dfrac{1}{2}\right)^n R_o$ | $\dfrac{\frac{4}{3}\pi\,(R_n)^3\,6.02 \times 10^{23}}{18}$ | $2^n\,4\pi\,(R_o)^2\,72 \times 10^{-7}$ |

$$R_n = \left(\frac{1}{2}\right)^n R_o \qquad\qquad [1]$$

Another observation is using the definition of specific area of a substance, $A_{sp}$. For a uniform sphere, $A_{sp}$ is given by equation 2. This equation clearly shows the reciprocal effect of surface area with the radius. This also explains the increase in total surface energy of water when its radius is reduced (Table 2.1).

$$A_{sp} = \frac{A_{tot}}{m_{tot}} = \frac{n4\pi R^2}{n\frac{4}{3}\pi R^3 \rho} = \frac{3}{\rho R} \qquad\qquad [2]$$

Both of the phenomena, namely the difference in the radius of the water molecule and the inverse proportionality of the surface energy with the radius, answer the above question. Yes, size does matter and it is because of this point that nanomaterials, being in the nanometer scale, have received much attention by the scientific community.

## 2.1.2 What is a Nanomaterial?

Materials that are downsized into smaller components exhibit different properties from their bulk properties. A new group of materials or particles is encountered when the sizes are in the range of nano-scale. The interesting mesoscopic properties of this group of material have opened up a new frontier in science and especially in the field of colloidal science. Just how small is it? As a way of illustration, in order to appreciate the effect of the size difference, the sizes of several natural nanomaterials and biological components are compared as shown in Figure 2.1 (Buzea, 2007). From the figure, it can be visualised that a strand of hair (60 micrometer) must be cut or sliced about 60000 times in order for it to be equivalent to 1 nanometer.  Also a sheet of paper is about 100,000 nanometers thick. It is analogous to comparing the size of a marble to the size of the Earth. It is also noteworthy to observe, as will be shown later in Figure 2.9, that the smaller nanomaterials coincide with the size of those of proteins. This opens up new application of nanomaterials into biological systems.
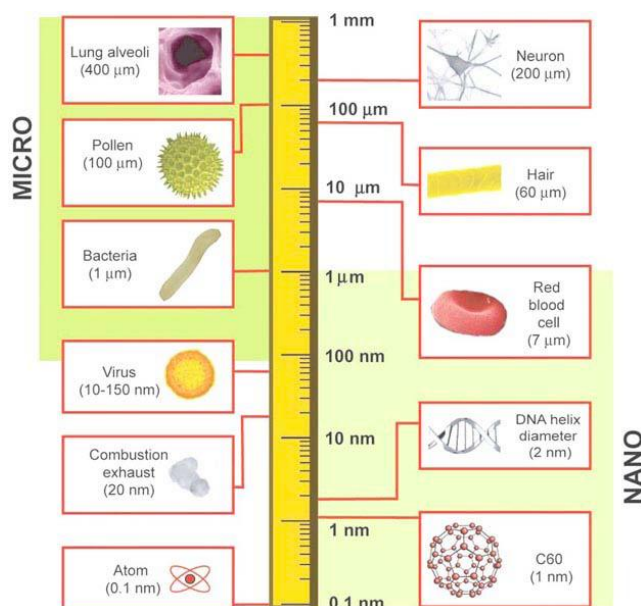


**Figure. 2.1** Size comparison of nanomaterials to biological components (extracted from Buzea, 2007)

Materials in the nano-scaled range have existed on earth for millions of years and have been used by mankind for thousands of years. Soot, for example is a product of the incomplete combustion of fossil fuels and vegetation. It has a particle size in the

nanometer-micrometer range and therefore falls partially within the nanoparticle domain. It is safe to say that every human has, in some way or another, been exposed to this kind of nanometer sized foreign particles. We inhale them with every breath and consume them with every food or drink. These inhaled nanomaterials (such as aerosols and dust) may or may not pose a potential health risk. If they do, we humans are lucky that our in-built bodily systems are there to fight and protect us from these potentially harmful materials. Initially, it may be thought that such nanoscaled materials, which are similar in size to viruses, would not pose any danger to the human body. It is because, unlike viruses, they lack the ability to replicate. However, some nanoparticles do penetrate the human skin and enter the circulatory and lymphatic systems just like viruses.

Nanoparticles formed the largest part of the nanomaterials group and can be made from many available materials with at least one dimension below 100 nm. The increasing uses of nanoparticles in scientific and industrial applications have not only led to a better understanding of their physical and chemical properties but also the invention of new equipment and techniques. The development of new equipment and techniques has made it possible to characterise and visualise nanometer sized structures which was impossible before. A major breakthrough was the invention of the electron microscope in the 1930s. Two such instruments are the scanning electron microscope (SEM) and transmission electron microscope (TEM).

.
Through SEM and TEM, the surface morphologies, shapes and sizes of nanoparticles can be elucidated to shed information about their behavioural pattern. In order to achieve any desired application properties, nanoscientists attempt to control and tailor the dimensions, shapes, structures, surfaces and interface properties of nanomaterials. These result in more engineered and functionalized nanomaterials. Figures 2.2 and 2.3 illustrate the beauty and complexity of the SEM and TEM images, respectively of this minute world of nanoparticles.
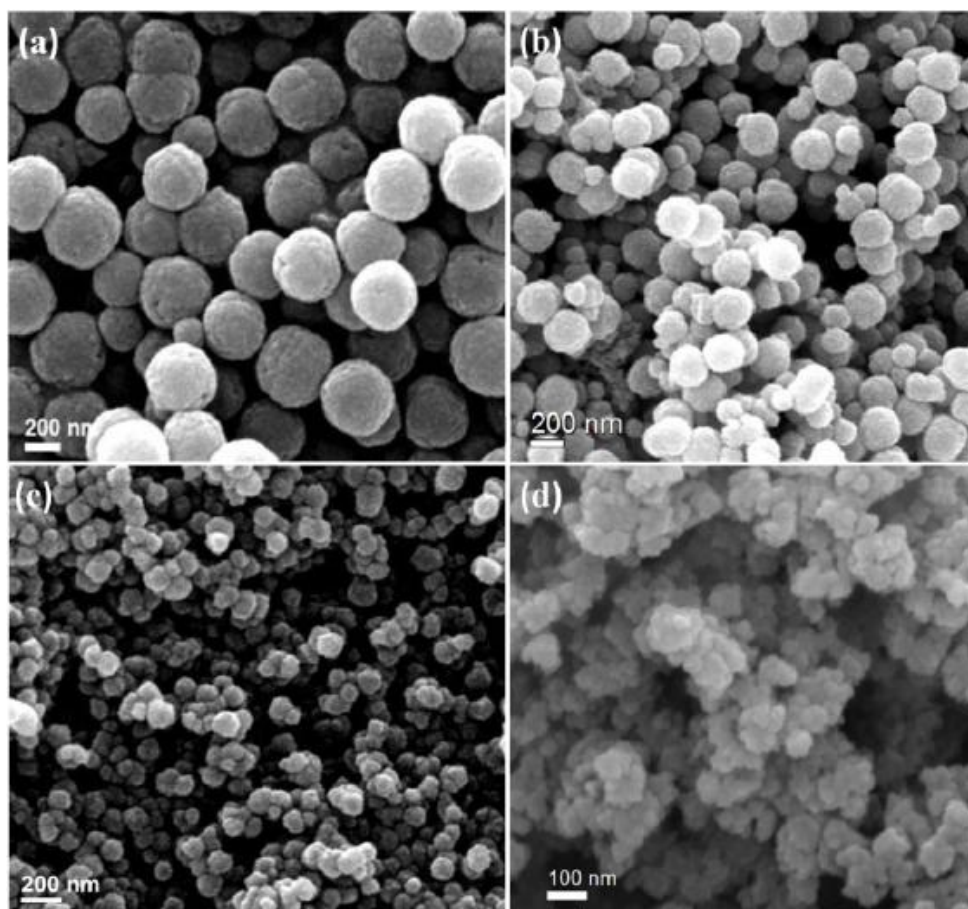
**Figure 2.2** SEM images of the $Fe_3O_4$@C core–shell nanomaterials prepared under various initial amounts of glucose: (a) 0 mmol, (b) 0.25 mmol, (c) 0.5 mmol and (d) 1.0 mmol (adapted from Zheng *et al.*, 2012).
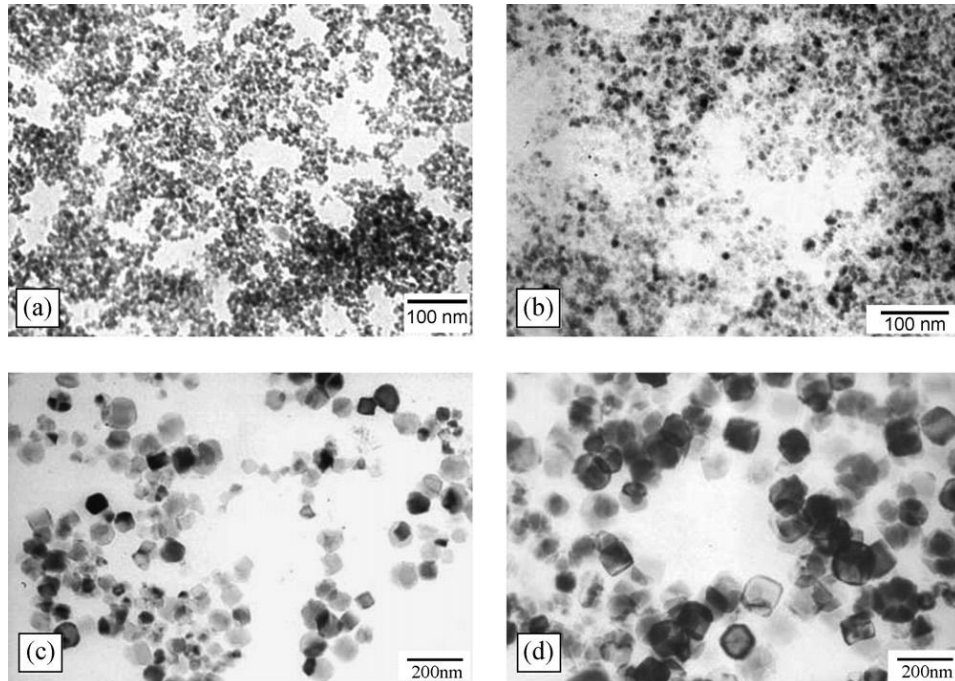
**Figure 2.3.** TEM images of different sized $Fe_3O_4$ nanoparticles (adapted from Ma *et al.*, 2004).

The benefits and positive effects of nanoscale particles, especially in drug delivery, will be described in the following section. But prior to that, understanding of the various types of nanoparticle that exist naturally or manmade becomes essential in order to facilitate understanding of their behaviour and benefits.

## 2.1.3 Forms of Nanomaterials

Nanoscaled materials can be separated into different structures and forms depending on the size, the material used, and purpose intended. These are biologic, polymer, silicon-based, carbon and metallic structures. Some of these forms are listed below:

- Liposomes
- Nanocapsules
- Dendrimers
- Micelles
- Nanotubes/Fullerenes
- Quantum dots

- Metal nanoparticles
- Magnetic nanoparticles

Table 2.2 shows some drug delivery technologies together with the materials and different forms of nanostructures that are associated with them (Hughes, 2005).

**Table 2.2**. Nanoscale drug delivery technologies (Hughes, 2005)

| Drug delivery technology | Materials | Nanostructure forms |
|---|---|---|
| Biologic | Lipids | Vesicles, nanotubes, rings; |
| | Peptides | Nanoparticles |
| | Nucleic acids | |
| | Polysaccharides | |
| | Viruses | |
| Polymeric | Poly(lactic acid) | Vesicles, spheres, nanoparticles |
| | Poly(glycolic acid) | Micelles, dendrimers |
| | Poly(alkylcyanoacrylate) | |
| | Poly(3-hydroxybutanoic acid) | |
| | Poly(organophosphazene) | |
| | Poly(ethylene glycol) | |
| | Poly(caprolactone) | |
| | Poly(ethylene oxide) | |
| | Poly(amidoamine) | |
| | Poly(L-glutamic acid) | |
| | Poly(ethyleneimine) | |
| | Poly(propylene imine) | |
| Silicon based | Silicon | Porous, nanoparticles |
| | Silicon dioxide | Nanoneedles |
| Carbon based | Carbon | Nanotubes, fullerenes |
| Metallic | Gold | Nanoparticles, nanoshells |
| | Silver | |
| | Palladium | |
| | Platinum | |

It is these structures that are responsible for their benefit and endless opportunity in many areas of research and fields of study. These structures have and will continue to generate a number of advancements throughout the years.

## 2.1.4 Application of Nanomaterials

The potential applications of nanomaterials are enormous. They include in the fields of electronic, biomedical, health care and agriculture. This vast potential has been meticulously illustrated by Tsuzuki (2009) as shown in Figure 2.4.
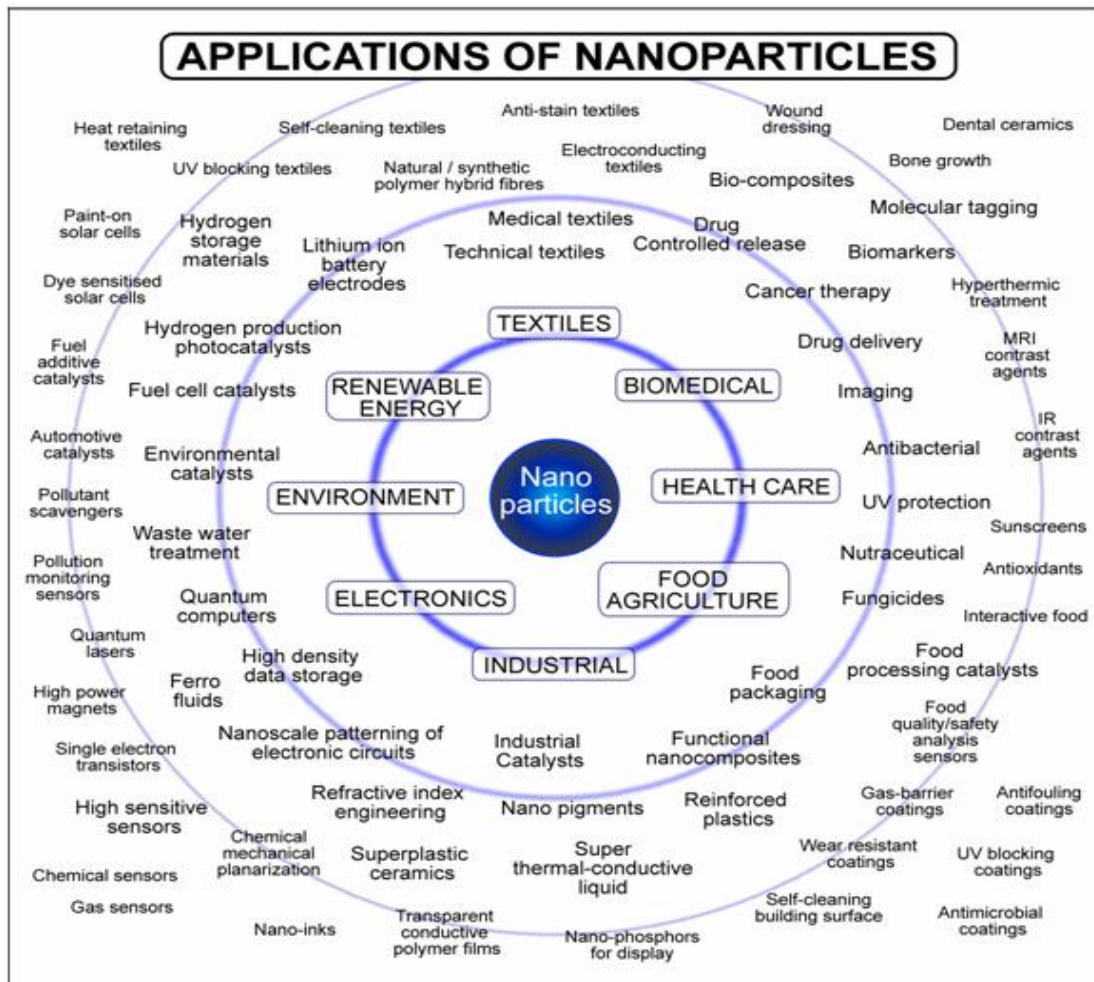


**Figure 2.4** Application of Nanoparticles (Tsuzuki, (2009).

## 2.1.5 Synthesis of Nanomaterials

Depending on the form of nanomaterials and their applications, numerous methodologies can be applied in order to synthesize them. The basic requirements are to obtain the appropriate size, shape and surface morphology in order for them to perform at their optimal level. Beija and co-workers (2012) have tabulated some of

the preparation methods involving some organic nanoparticles of relevance for drug delivery. The table is partially adopted here as shown in Table 2.3 for a quick view and way of illustration of the numerous preparation routes available.

**Table 2.3** The method of preparation for some nanoscaled particles (Beija *et al.*, 2012).

| Type | Method |
|---|---|
| Liposome | Film casting and rehydration of this film + extrusion |
| Polymersomes | Solvent switch method Film casting and rehydration of the film |
| Polymeric micelles | Direct organization or controlled aggregation in a solvent |
| Layer-by-Layer systems | Electrostatic interaction between oppositely charged polyelectrolytes |
| Solid Lipid Nanoparticle | Freezing of an emulsion of lipids heated above melting point of lipids |
| Polymer nanoparticle | Polymerization of monomers by emulsion process or starting from existing polymers, nanoprecipitation, gelation or emulsion process |
| Capsules | Nanocapsules: Interfacial polymerization of monomers or phase inversion process with emulsions of polymers |
| Dendrimers | Convergent or divergent synthesis |

Two of the most common and important synthetic preparation pathways, namely microemulsion polymerisation and coprecipitation, which are crucial in this thesis, will be elaborated. The literature review on magnetic iron oxide nanoparticle and its synthesis via co-precipitation process will be elaborated in this chapter, while the review on the preparation of nanocapsules using microemulsion polymerisation will be presented in Chapter 4.

## 2.2. Drug Delivery Systems

### 2.2.1 What is a drug delivery system?

A drug delivery system is simply a delivery system that carries a drug throughout the body. By this method, only a small amount of the drug reaches the affected area. A targeted drug delivery system is a delivery system that delivers and releases the drug at a preselected site in a controlled manner. As a consequence, targeted drug delivery may result in higher bioavailability of the drug at its preselected site, thus reducing both the total dose and the side effects associated with the drug. The ideal requirement of a drug delivery vehicle is that it must exhibit non-toxicity, biodegradability (Scott *et al.*, 2008), biocompatibility, non-immunogenicity, and also be able to avoid being recognised by the host's defence mechanisms (Bertrand & Leroux, 2012).

## 2.3 Nanoscaled Particles in Drug Delivery Systems

### 2.3.1 Benefit

The scientific community is seeking new avenues to utilise the unique properties of nanoparticles in order to understand their behaviour and applications. One of the major areas that has been investigated quite extensively is in the field of medicine. Some of the uses of nanoparticles in medicine (Figure 2.4) include drug delivery systems, cancer therapy, hyperthermic treatments and magnetic resonance imaging, MRI as contrast agents. Figure 2.5 illustrates how the unique properties of nanoparticles can be manipulated. By varying the composition, various types of nanoparticle can be prepared or synthesized with their corresponding physical properties. This is tuned by adding ligands (such as polymers and proteins) to the surfaces of the nanoparticles thus altering the surface properties and functionalities; they can then be utilized to target the affected sites or tumours.
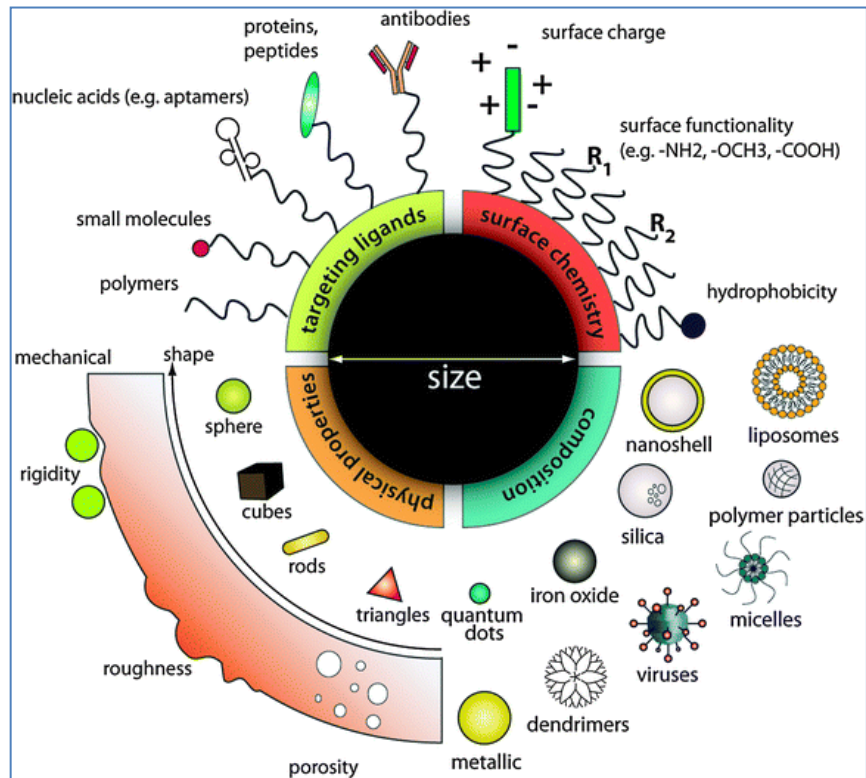
**Figure 2.5** Schematic of how properties and characteristic of nanoparticles can be manipulated while designing nanoparticles for biomedicine applications (Chou et al., 2011).

## 2.3.2 History and pioneers

Discussions on the historical background of the use of nanomaterials or nanoparticles for drug delivery should begin with Paul Ehrlich (1854-1915) for his concept of a 'magic bullet' (Witkop, 1999). Ehrlich's concept of a 'magic bullet' was a compound that targeted a specific pathogenic organism or cell without harming others. Hence, a 'magic bullet' would be created able to kill the targeted organism exclusively. Ehrlich's contribution in this area can be regarded as the beginning of targeted drug delivery. His first 'magic bullet' was an arsenic-based drug Salvarsan (or arsphenamine, or Ehrlich 606) which was used as a cure for syphilis as shown in Figure 2.6.
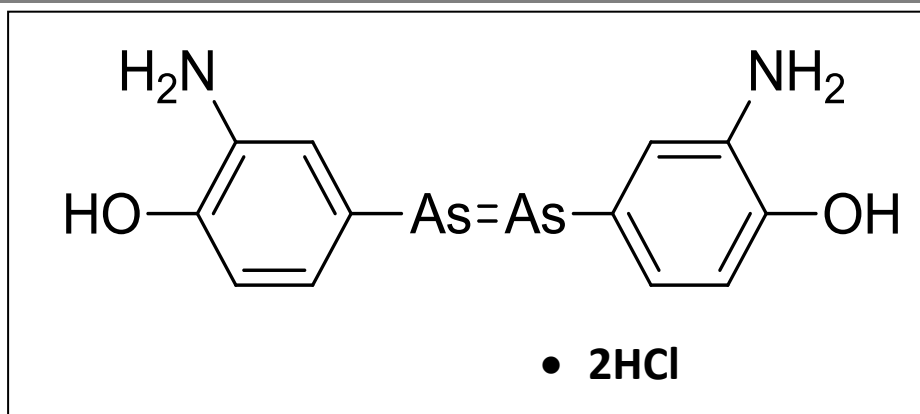
**Figure 2.6** The molecular structure for the first 'magic bullet', Salvarsan (Lloyd *et al.,* 2005)

With all the benefits offered, it is no surprise that one of the areas that has received much attention in the area of nanomedicine is drug delivery. This is shown by the exponential growth in the number of research articles published in the area of drug delivery as shown in Figure 2.7 (http://apps.webofknowledge.com. Date of search: October 2013. Search keyword 'drug delivery' and 'nanoparticles')

.
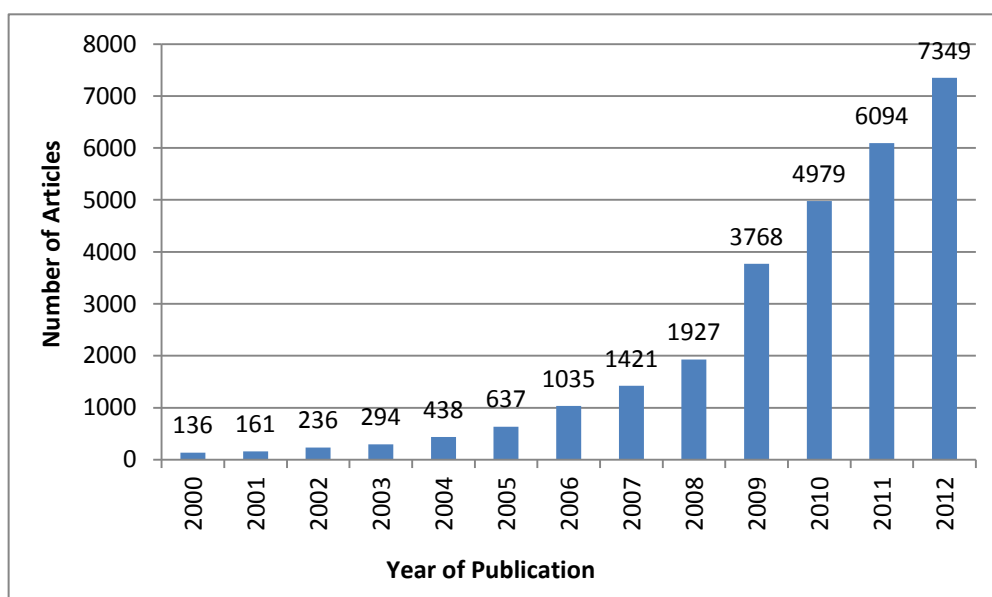


**Figure 2.7** Scientific publication involving drug delivery using nanoparticles from 2000 to 2012 (http://apps.webofknowledge.com. Date of search: October 2013. Search keyword: 'drug delivery' and 'nanoparticles')

Clearly from the figure, it shows a humble beginning with 136 articles published in 2000. This number however, rose exponentially to 7349 articles published in 2012. The advantages of using nanoparticles in a drug delivery system are due to their size, magnetic and electronic properties and can be conveniently broken down as follows:

- The size and surface characteristics of nanoparticles can be easily manipulated. Hence, from the delivery point of view, there is no limitation as the diameters of nanoparticles are well below that of the biological components (Figure 2.8). This enables them to mobilise freely and target specific locations in the body.
- Nanoparticles, through, their magnetic properties, can be made to control and sustain release of the drug during the transportation as well as the location of the release.
- A reduced amount of drug will be required to achieve a particular concentration at the targeted area.
- The amount of drug at non-target areas will also be reduced, thus minimizing severe side effects.
- Various forms of administration including oral, nasal and injection can be applied.
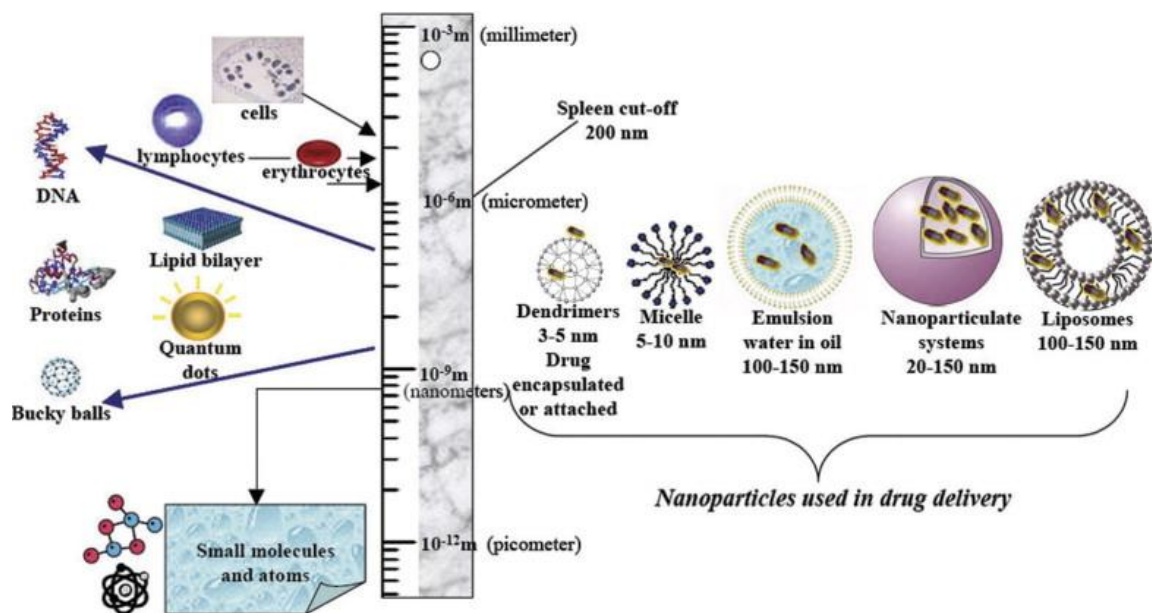


**Figure 2.8** Nanoparticle systems for drug delivery applications (Arruebo *et al.,* 2007).

The lamellae of swollen phospholipids known as lipid vesicles were the first nanotechnology drug delivery systems. These vesicles, which were later known as liposomes, have been in the literature for more than 40 years. The initial objective of that work was to look for a model for lysosomes (Bangham *et al.,* 1965; and Bangham, 1989). With that discovery, liposomes have gained wide acceptance not only as a model for a cell membrane but also as potential carriers for transporting drugs and macromolecules into the body which are useful for the pharmaceutical and healthcare industries. To date (Date of search: October 2013. Search keyword: 'liposomes'), a quick search online, show 55,511 articles were published involving liposomes since 1960 (http://apps.webofknowledge.com). Narrowing the search, within the same period, to liposome and drug delivery as keywords shows 12,169 articles were found in the literature. This indicates that more than 20 percent of the work done using liposomes was related to drug delivery.

As a result of the above findings, many polymeric or inorganic biomaterials for drug delivery were developed. In 1976 the first controlled release polymer system for delivery of macromolecules was described (Langer & Folkman, (1976). The work presented a simple method for incorporating various proteins and other macromolecules into non-inflammatory polymers. This is because there has been little success in the development of slow release agents for large molecular weight compounds. The polymers used in earlier studies, polyvinylpyrrolidone and polyacrylamide (Davis, 1972; 1974 and Gimbrone *et al.*, 1974), are often inflammatory in animal tissues and usually permit only brief periods of sustained release. In this work Hydron, a polymer of hydroxyethylmethacrylate was used. The result showed sustained release of protein and other macromolecules from polymeric carriers can be achieved over prolonged periods. In this case the sustained release of biochemically active macromolecules was achieved for periods exceeding 100 days. In addition, Hydron did not cause inflammation in the cornea. Indeed, it is the basic material used for most modern soft contact lenses.

So far, much of the work on drug delivery concentrated only on delivering drugs into the body. The main drawback with these is their inability to differentiate between a

normal and diseased cell. This leads to side effects such as stomach ulcers and at times hair loss. Because of this, targeting drug delivery systems becomes of high interest in order to overcome this drawback. Fortunately, the advancements in nanotechology and drug delivery have facilitated the targeting of specific tissues, The complex make up of the body system requires the scientific community to focus on more complex drug delivery systems capable of triggering drug release in the body in response to changes such as pH, colonic transit times and enzymic action (Yatvin *et al.*, 1980). The pioneering contributions to cell specific targeting of liposomes (Leserman *et al.*, 1980); Heath *et al.*, 1980) were first reported in 1980. Torchilin (2005) has schematically illustrated the evolution of liposomes from its beginning of discovery to their significant achievements in his review as shown in Figure 2.9.



Nature Reviews | Drug Discovery
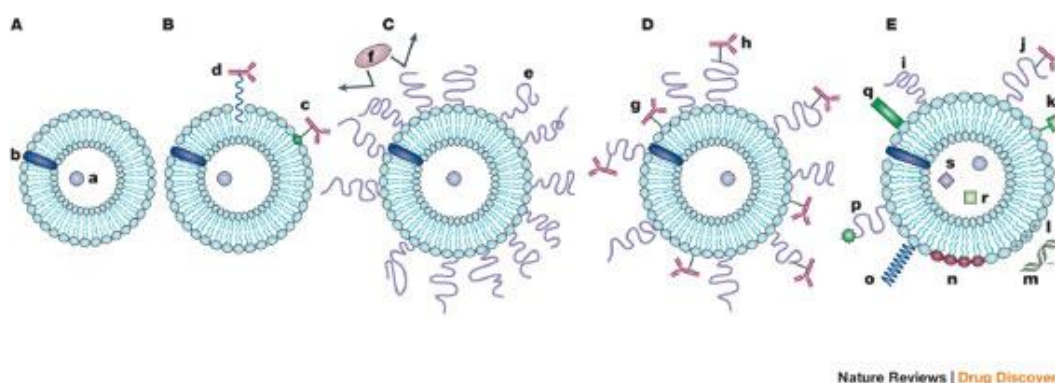
**Figure 2.9** Evolution of liposomes from first generation, A to new generation, E where (a) is hydrophilic drug; (b) is hydrophobic drug; (c), (d), and (g) are antibodies; (e) is PEG; (f) are proteins, (h) are antibody-grafted polymer; (i) protective polymer; (j) a protective polymer with antibody; (k) a diagnostic label; (l) positive charge lipid, (m) DNA; (n)stimuli-sensitive lipids; (o) stimuli-sensitive polymer; (p) cell-penetrating peptide; (q) viral components; (r) magnetic particles; and (s) gold/silver (Torchilin, 2005).

As mentioned earlier, during their early discovery until the late 80s liposomes have had their shortcomings. Therefore there arose a need to find an alternative to liposomes that offers better properties to achieve the desired goals.

Many drug carriers have been introduced as alternatives such as polymeric nanoparticles (Birrenbach and Speiser, 1976; Couvreur *et al.*, 1979) and albumin-

based nanoparticles (Marty *et al.*, 1978). These works pioneered by Peter Speiser (1976) are focussed on the development of nanomaterials for vaccination purposes. This nanomaterial is called a nanocapsule. To date (22/10/2013), a quick search online with nanocapsule as the search key word shows only 5454 articles were published since 1976 (http://apps.webofknowledge.com). About 4388 articles were published after 2005. The slow start from its first publication until 2005 shows that much less attention has been given to the topic compared with liposome research. Both liposomes and nanocapsules are nanovesicular drug delivery systems. Liposomes, as mentioned earlier, consist of layers of phospholipids, while nanocapsules comprise of a solid or liquid cavity enveloped by a single polymer membrane (Speiser, 1976). The liquid cavity can be oily or aqueous (please refer to Appendix A for schematic illustration of nanocapsule). Nanocapsules can be prepared by an interfacial polymerisation process of monomers or from preformed polymers involving oil-in-water (O/W) or water-in-oil (W/O) emulsions. Nanocapsules prepared by polymerisation require the polymerisation of the monomers to proceed rapidly. Alkycyanoacrylates have been proposed for preparation of oily and aqueous nanocapsules because of their rapid polymerisation, which is within seconds (Khouri *et al.*, 1986).

With that, nanomaterials prepared with polymer, poly(alkylcyanoacrylate) (PACA) have gained much interest as drug carriers. This is because of its biocompatibility and biodegradability (Couvreur *et al.*, 1986). Its ease of polymerisation (Al Khouri *et al.*, 1986)) and ability to entrap bioactive compounds such as insulin (Watnasirichaikul *et al.*, 2000) are other contributing factors. Nanocapsules of PACA were first developed by Couvreur and co-workers (1979). In that work, polymethyl and polyethycyanoacrylate were prepared by polymerisation. Monomers of methyl- or ethyl-cyanoacylate were added into a micellar (O/W) template comprising of Tween 20 in acidic condition (pH~3). SEM results showed spherical particles with a diameter of 200 nm were formed. The morphological appearance and size were not affected by the variation of Tween 20 concentrations. In another work by Al Khouri and co-workers (1986), a new process for manufacturing polyisobutylcyanoacrylate nanocapsules was developed using interfacial polymerisation with an average

diameter of about 200-300 nm. Poloxamer 188 was used as the surfactant component. Both of these approaches using micellar (O/W) template seemed to pose some unwanted reaction between the encapsulated drug and the monomers in the core of the micellar structure. For these reasons, attention has been directed to investigating the W/O emulsion as the template to prepare PACA nanocapsules (El-Samaligy *et al.*, 1986). However, the same issues as those faced by O/W emulsion were encountered. Later Gasco and Trotta (1986) proposed the use of W/O microemulsion as templates to overcome problems encountered using W/O emulsion as template. They successfully used isopropyl myristate, Aeosol-OT and butanol to prepare the microemulsion but the nanocapsules needed to be separated out from the medium due to biodegradability issues. The same procedure was later improved by using bicompatible microemulsion systems (Watnasirichaikul *et al.*, 2000). The use of biocompatible microemulsion as templates for the preparation of nanocapsules by interfacial polymerization are better than the use of size-reduced kinetically stabilized emulsions and it also eliminates the necessity of isolating the nanocapsules from the reaction medium (Vauthier *et al.*, 2003).

In the investigation by Watnasirichaikul and co-workers (2000), polyethylcyanoacrylate nanocapsules containing insulin was reported using biocompatible W/O microemulsions. The surfactants are mixtures of Crillet 4 and Crill 4. In this investigation the region of microemulsion composition was reported using phase diagrams. The nanocapsules formed have a mean particle size of 150.9 nm. Microemulsion polymerisation is a better choice over emulsion polymerisation. This is due to it being more thermodynamically stable and producing smaller and more uniform dispersions. It is also formed spontaneously. Just like the limitations faced by liposomes, nanocapsules also face the same challenges. The residues of monomers and oligomers from the polymerisation process and the possible unwanted reaction of the drug molecules with the monomers limit the development and potential of nanocapsules (Gallardo *et al.*, 1989).

One other alternative drug carrier that has a promising future and has caught the attention of the scientific community is dendrimers. After the amazing discovery by

various pioneers, namely Vogtle, Tomalia and Newcome through the 70's and 80's, these unique molecules, which are sometimes referred to as the polymers of the 21<sup>st</sup> century, have attracted much attention for their use in various application. The well defined structure, uniformity in size, surface functionalisation, and stability makes dendrimers an attractive polymeric nano-scaled structure for drug delivery compared to other nanomaterials, which have an average structure and a range of sizes.

The chemistry of these hyperbranched molecules/polymers, dendrimers, was introduced in 1978 by Vogtle and co-workers (Buhleier *et al.*, 1978). In this work, they took advantage of the existing iterative process of repeating-step principle used in the Host-Guest interaction (Cram *et al.*, 1975). This repetition of similar steps is used to construct large molecule cavities that are able to bind guest molecules. With this repeating step principle, they managed to bond successive arms or rings in the synthesis of noncyclic and cyclic polyaza compounds. They named the two synthetic pathways as cascade-like and nonskid-chain-like pathways, respectively.

With the first dendrimers prepared in 1978, it took about 7 years by another pioneer, led by Newcome (1985) to report the synthesis of other dendrimers. They named this new macromolecule as arborols. In this work they reported the synthesis and spectral characterization of [27]-arborol. The number 27 denotes the number of terminal OH groups. The synthetic pathways, as shown in Figure 2.10, started by nucleophilic substitution of 1-bromopentane by triethyl sodium methanetricarboxylate, $(NaC(CO_2Et)_3)$ in dimethylformamide and benzene. Lithium aluminium hydride was used to reduce the ester groups to a triol in a repeating step. The chain ends were activated by converting the alcohol groups to tosylate groups with tosyl chloride and pyridine. The tosyl groups then served as leaving groups in another reaction with the tricarboxylate, forming generation two. The sequence can be repeated to construct the next generation i.e. the [27]-arborol by treating the generation two compound with tris(hydroxymethyl)aminomethane, $(H_2NC(CH_2OH)_3)$ in DMSO at 70$^o$C.

Generation I

Generation II

Generation III ([27]-arborol)
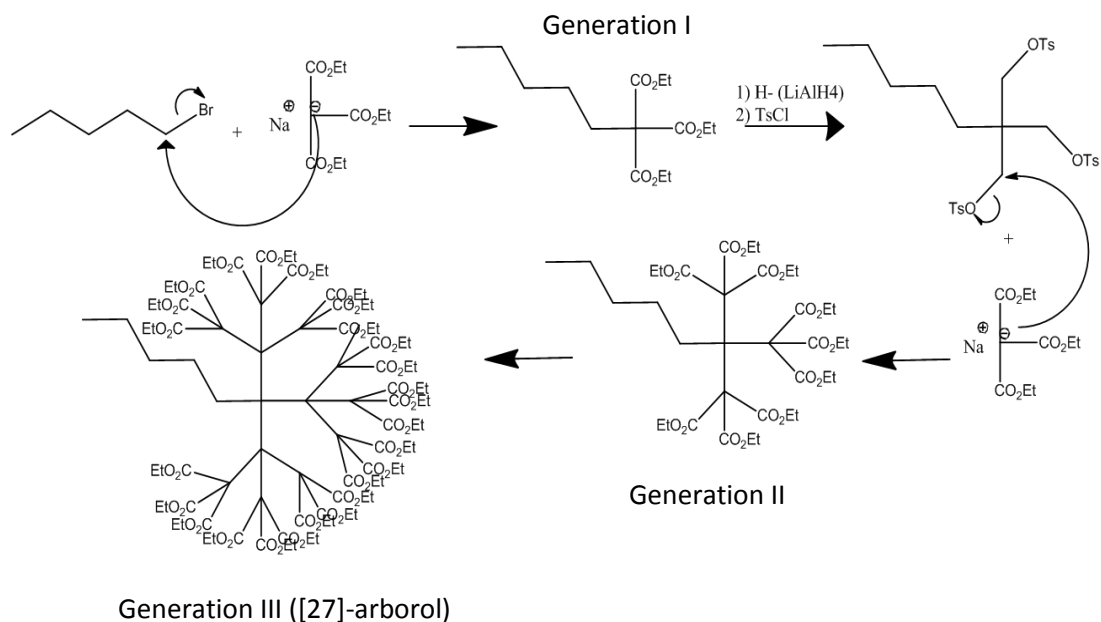
**Figure 2.10** The synthetic pathways for [27]-arborol (Newkome *et al.*, 1985).

At the same time, another pioneering group, Tomalia and co-workers (1985), have independently come up with a way of making batches of dendrimer with a uniform molecular weight and size. The group initially named this new class of polymers as starburst polymers. The first dendrimers they synthesised were polyamidoamines (PAMAMs) by first reacting ammonia with methyl acrvlate and then followed by an excess of ethylenediamine. The core molecule being ammonia possesses 3 hydrogens and therefore could exhibit three branches. At the end of each branch is a free amino group that can react with two more methyl acrylate monomers and then two more ethylenediamine molecules to make a generation one dendrimer. This process is repeated divergently for several generations. After generation nine the reaction kinetics drop suddenly and significantly. That is where the chains pack together to form a membrane-like globular structure, making it very difficult to grow further due to lack of space. This phenomenon is called the 'starburst effect'. The diameter of the globular structure was later determined to be 12.4 nm (Tomalia *et al.*, 1990),

As in any nano-sized carriers, the unique properties of dendrimers have found many applications such as nano reactors (Turro *et al.,* 1991), drug delivery carriers (Newkome *et al.,* 1991; Jansen *et al.*, 1994 and Mohammad *et al.*, 2006), MRI (Wiener *et al.*, 1994), immune diagnostics (Singh *et al.*, 1994), and gene delivery vectors (Haensler & Szoka, 1993). A quick search up to year 2012, showed that more than 20,000 papers were published regarding these amazing dendrimers (http://apps.webofknowledge.com). Even though dendrimers have enjoyed many successes and advantages, dendrimer-based drug delivery has still got a long way to go to enter into the market due to their cytotoxicity properties, the massive effort required for the synthesis and the cost implications. More effort and research is needed in order for dendrimers to match up to their promises. More recently, controlled methods to produce hyperbranched polymers have begun to offer a more synthetically-accessible alternative to dendrimers with some similar properties.

Another drug carrier that was adopted in 1999 is the polymersome. Polymersomes resembled liposomes in many ways but with increased stability and reduced permeability. The first publication on polymersomes by Discher and co-workers (1999) reported that polymersomes were 10 times less permeable to water than liposomes. In addition the polymersomes prepared from polyethyleneoxide-polyethylethylene ($EO_{40}$-$EE_{37}$), were not only reducing the water permeability but were also much tougher by a scale of one order of magnitude. Again, as any drug carriers, polymersomes also have their drawbacks. Because of being structurally huge and thick, they are not only difficult to add functional groups to but also involve tedious synthetic routes in order to form their derivatives.

In 2010, in pursuit of a new generation of smart drug carriers, another drug carrier was described. This time they are called dendrimersomes which are derived from Janus dendrimers (Borman, 2010; Percec, *et al.*, 2010). As described by Percec and co-worker (2010), dendrimersomes also exhibit the best of both worlds in term of stability and mechanical strength as those of polymersomes, but highly uniform in size, easy to prepare and functionalised. Time will tell whether these particles can deliver on their promise.

### 2.3.3 Recent Interest

As mentioned above, the work on drug delivery has been around for more than 40 years. But it is in the last decade that the research has really matured due to the merging of 3 interdisciplinary areas of science, engineering, and medicine (Gianchandani & Meng, 2012). Due to this merging, nanotechnology and nanofabrication techniques have allowed drug carriers to be further improved and developed. More novel approaches have been made. A quick internet search from the web of knowledge website (Date of search: October 2013. Search keyword: 'drug delivery') for 2010 to 2012 shows a total of 82,288 articles were published in the area of drug delivery (http://apps.webofknowledge.com). Narrowing it down to 2012, more than 29,704 articles were published or about 36 percent of the total publications. This number will surely continue to grow as the interest and impact is ever increasing. With all the literature becoming available, it is safe to say that the building blocks in designing any drug delivery systems, besides being biodegradable and biocompatible, are their ability to:

- Protect the drug
- Reduce degradation of the drug
- Reduce the accumulation of drug at healthy site by precisely target the drug
- Reduce its toxic level
- Be environment-responsive
- Improve stability
- Properly release the drug naturally or through initiation by external stimuli

Recently, numerous review papers have also been published pertaining to the development and design of drug delivery systems (Gianchandani & Meng, 2012; Kim *et al.*, 2012; Couvreur, 2013; Mitragotri, 2013; and Zhang *et al.*; 2013; and their references therein) which again shows the massive attention it has been given.

## 2.4 Colonic Targeted Drug Delivery Systems

Targeted drug delivery into the colon is highly desirable for local treatment of disorders of the large intestines such as ulcerative colitis, Crohn's disease, and colon cancer and systemic delivery of protein and peptide drugs (Oluwatoyin and John, 2005; Philip *et al.*, 2009). A colonic targeted drug delivery system is expected to protect the drug during the transit time in the GI tract and releases it only in the colon. This delivery system has the advantages of more effective therapy, a reduced dose and reduced undesirable side-effects often associated with high doses (Ashford, et al 1993 a, b),

### 2.4.1 GI tract

The GI tract (Figure 2.11) and its hindrances associated with oral drug delivery have been mentioned briefly in chapter 1. Therefore, an overview about it may facilitate basic understanding of what is going on in the tract and the digestive system. The GI tract can be divided into esophagus, stomach, small intestine and large intestine (colon). It can be further classified into upper (esophagus and stomach) and lower (small intestine and colon) GI tract.
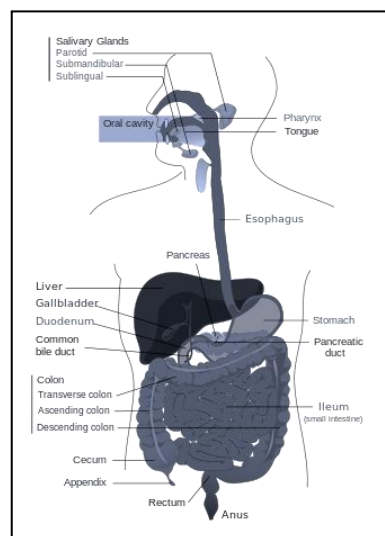


**Figure 2.11** The GI tract (Marieb and Hoehn, 2010)

Normally, the digestive system begins when food is consumed and chewed repeatedly together with the aid of secreted saliva in the mouth. The enzyme amylase produced by the salivary glands is able to break down starches into small sugar molecules. The salivary glands also produce the enzyme lipase to begin the digestion of fat components in the stomach. The digestion continues in the stomach by secreting a very strong acid called gastric juice. The acid denatures proteins and, together with the enzyme pepsin breaks them into amino acids. It also kills potential harmful microorganisms. It has been reported that the pH of the stomach is in the range of 1.0-3.7 depending on the state of the person i.e. fasted and fed state (Sonaje *et al.*, 2009; Vertzoni *et al.*, 2005). The digested food will then enter the small intestine.

The pH in the intestine has been reported to be in the range 6.0-7.0 (Fallingborg, 1999; Legen and Kristl, 2003). In the small intestine where absortion takes place, enzymes (Orienti *et al.*, 2001) such as trypsin, lactase and lipase, as well as bile salts, are present to further breakdown the digested food. Bile salts play an important role in the digestive system. Bile salts are sodium salts of the cholic acid. They are produced in the liver and stored in the gallbladder before secretion for the digestion of fats. They exhibit amphiphilic properties equivalent of surfactants, therefore spontaneously form micelles in aqueous environments (Kararli and Gupta, 1992). These micelles facilitate the breaking down of fatty materials in the small intestines. It has been reported that the absorption of some poorly soluble drugs increase in the presence of food (Charman *et al.*,1993; Crounce, 1961; Hamaguchi *et al.*, 1993). One of the two reasons given is due to increase of bile salts in the small intestine. It has been found in previous work that the concentration of bile salts in the duodenum and jejunum is 2-3 times more in the fed state (10-15 mM) as compare to the fasted (3 mM) state (Fausa, 1974; Tangerman, *et al.*, 1983). Later work by Mithani and co-worker (1996) proposes a model to predict the dependency of the solubility of drugs on the concentration of bile salts. An *in-vitro* model is then proposed that closely mimics the conditions *in-vivo* (Kostwicz *et al.*, 2002). The model provides the compositions of the gastrointestinal media that simulate the fed and fasted states as shown in Table 2.4.

**Table 2.4** The compositions of the simulated intestinal fluid (Kostwicz *et al.*, 2002).

| Chemical | Fasted State Simulated Intestinal Fluid (FaSSIF) | Fed State Simulated Intestinal Fluid (FeSSIF) |
|---|---|---|
| Sodium taurocholate | 3 mM | 15 mM |
| Lecithin | 0.75 mM | 3.75 mM |
| NaOH (pellets) | 0.174 g | 4.04 g |
| $NaH_2PO_4.H_2O$ | 1.977 g | - |
| Glacial Acetic Acid | - | 8.65 g |
| NaCl | 3.093 g | 11.874 g |
| Purified water qs | 500 mL | 1000mL |
| pH of resulting media | 6.5 | 5.0 |

After going through the small intestine pathway, the material is then passed down into the large intestine (colon). The colon is not only larger in size than the small intestine but it provides a suitable environment for the growth of most of the microflora found in the human intestine. The microflora is a collection of microbes colonising a host which in this case is the small intestine and colon (Savage, 1977). More than 500 bacterial species, mostly bacteroides, bifidobacterium, and lactobacillus, (Hooper *et al.*, 2002) inhabit the intestine and the number increases as it reaches the colon as shown in Figure 2.12. Depending on the different factors, the time needed for the transit through the GI tract, from the oesophagus to the colon, varies from 30-50 hours (Rubinstein, (1995). Finally, in the colon the water from the material is further absorbed back into the body and then awaits secretion through the anus when the need arises. Essentially, the digestive system is a long tube that runs from the mouth to the anus.
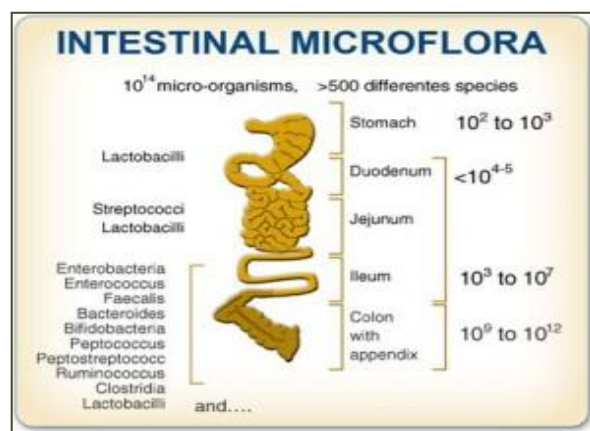


**Figure 2.12**. The microbial densities in the GI tract.
(http://www.customprobiotics.com/_images/intestinal-microflora-410.jpg)

## 2.4.2 Capsules

Oral drug delivery is by far the most popular drug delivery administration due to it being noninvasive and patient friendly. Tablets and gelatine capsules are widely used in oral drug delivery (La Wall, 1940). Capsule is derived from the Latin *Capsula* meaning small box.

There are two types of gelatine capsules namely soft and hard (Figure 2.13a and b, respectively) capsules (Augsburger, 1995). The soft gelatine capsules are one piece. A hard gelatine capsule shell (Figure 2.13b) comprises two sections i.e. the body and cap, which are fitted together. In oral drug delivery systems, the drug is filled into the body section and closed by using the cap. The shells of the hard capsules are mostly made from gelatine though other materials can be used for specialist applications or to satisfy religions or ethnic preferences. The standard shape is the traditional bullet shape and comes in various sizes. Table 2.5 lists the available sizes and volumes of the hard capsules in the market.



(a)                                    (b)
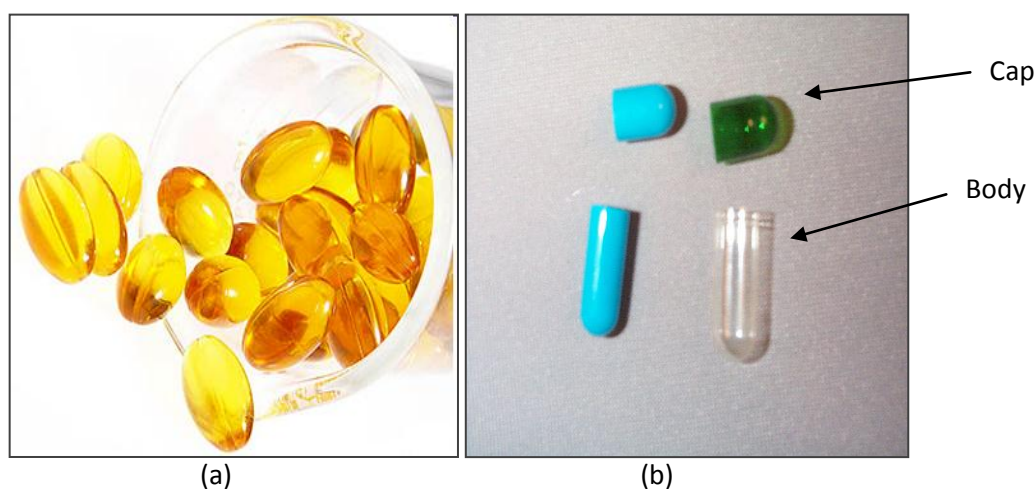
**Figure 2.13** Type of gelatine capsule (a) soft and (b) hard

**Table 2.5** Dimension of hard gelatine capsule (Stegemann and Bornem, (1999).

| Capsule Size | 000 | 00 | 0 | 1 | 2 | 3 | 4 | 5 |
|---|---|---|---|---|---|---|---|---|
| Capsule Volume, ml | 1.37 | 0.91 | 0.68 | 0.50 | 0.37 | 0. 30 | 0.21 | 0.10 |

The main advantages of hard gelatine capsules are their ease in swallowing, the shell is odourless and tasteless, faster dissolution and absorption in body fluids than pills and tablets and the drug can be easily released. Even though they have many advantages, they are still subjected to the harshness of the GI tract which warrant issues on stability, solubility and proper drug release to be addressed.

### 2.4.2.1 Capsules in the GI tract

Capsules, which are taken orally will travel the same path and encounter the same environment as the chewed food. The capsules, with the aid of saliva are, pushed through the throat into the esophagus and enter the stomach. At this stage, the capsules will encounter various enzymes and gastric acid at a low pH condition of 1.0-3.7. The capsules then enter the small intestine via the duodenum and then jejunum and exit through the ileum. Here the capsules will encounter more enzymes, microbes at higher pH values of 6.0-7.0. After going through the small intestine, the capsules (if still intact) exit the small intestine via the ileum and enter the colon. In the colon, the capsules will once again encounter more microbes.

The environment of the GI tract can then be partially summarized as shown in Table 2.6. From the table, it becomes obvious that the interaction between the capsules or any oral delivery formulations and the contents of the GI tract may lead to the degradation of the capsules due the different conditions existing in the GI tract. Consequently, in order to address this drawback, the makeup of capsules or any oral formulations need to be robust, resistant and stable in the GI tract in order to function effectively and efficiently. This is vital if the desired objective for the targeted oral drug delivery or drug-release system is to be achieved.

**Table 2.6** The different conditions in the GI tract

| GI tract | | pH | Microbial Densities/g | GI Transit, h | Length, m |
|---|---|---|---|---|---|
| Stomach | Fed | 2.0-3.7 | $10^2 - 10^3$ | more than 3 | |
| | Fasted | 1.0-1.9 | | less than 1 | |
| Small Intestine | | 6.0- 7.0 | $10^4 - 10^7$ | 3-4 | 6.0 |
| Colon | | 5.5-7.0 | $10^9 - 10^{12}$ | 20-40 | 1.5 |

One of the ways to overcome the drawback is by coating the capsule. Coated systems against the pH gradient and viscosity of the fluid in the GI tract have been well reported (Wilding, 2000). This can be achieved by enteric coating the capsules. They are designed to remain intact in the stomach in order to protect the active substance from the acidic gastric juice and then release the active substance at the target area in the intestine. The ingredients in enteric coating recipes usually comprise of enteric film formers, plasticizers, colourants and solubilisers. Polymers such anionic polymethacrylates (such as Eudragit L and S) (Hosny, *et al.*, 2002; Sonaje *et al.*, 2009) and cellulose based polymers (such as HPMC) (Cole *et al.*, 2002; Mohamad and Dashevsky, 2006) are widely used for the enteric film formers.

For instance, Sonaje and co-workers (2010) have developed an enteric coated capsule for oral delivery of insulin. In this work, hard gelatine capsules are used and insulin is filled into capsules. The capsules are then coated with Eudragit® S100 and L100-55. The dissolution study shows that both of the enteric coated capsules prevented the insulin from contacting the acidic medium of the stomach. As a way of illustration, the dissolution graph Figure 2.14 adapted from the study is adopted here. From the figure, clearly it shows that at lower pH values (1.2 or 2.5), insulin is released immediately by the uncoated capsules and continue to increase as it reaches higher pH values. However, for the enteric coated capsules, insulin is only released after a lapse of more than 100 and 200 min, for Eudragit L100-55 and S100, respectively
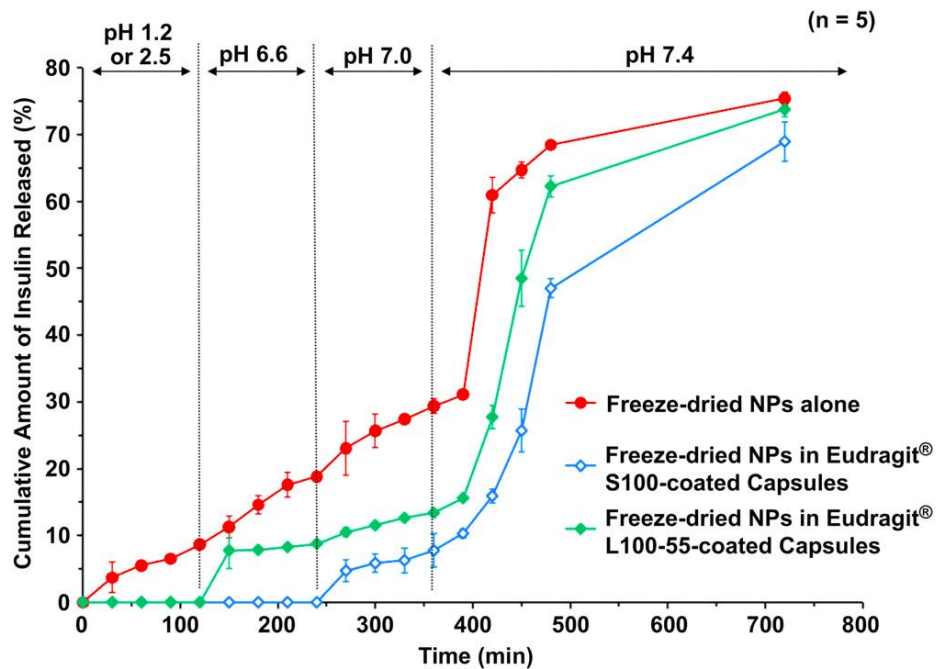
**Figure 2.14** Amount of insulin released from the freeze-dried nanoparticles (NPs) and in enteric-coated capsules at different pH values (Sonaje *et al.*, 2010).

Another recent review (Philip and Philip, 2010) has put forth two different existing approaches to withstand the harshness of the environment of the GI tract for colon specific drugs delivery (CDDS). They also make comparison between the two approaches. The approaches given are listed below:

1) Primary Approaches for CDDS

- pH Sensitive Polymer Coated Drug Delivery to the Colon
- Delayed (Time Controlled Release System) Release Drug Delivery to Colon
- Microbially Triggered Drug Delivery to Colon

2. Newly Developed Approaches for CDDS

- Pressure Controlled Drug-Delivery Systems
- Novel Colon Targeted Delivery System (CODESTM)
- Osmotic Controlled Drug Delivery (ORDS-CT)

## 2.5 Magnet, Magnetism and Magnetic Nanoparticles

### 2.5.1 Background

Permanent magnets are objects that produce their own magnetic field. Only certain classes of materials can do this. A phenomenon known as magnetism applied to most materials that produce magnetic field in response to an externally applied magnetic field. Therefore, magnetic materials are usually classified by their response to an externally applied magnetic field. Figure 2.15 shows the descriptions of orientations of the magnetic moments in a material in order to identify different forms of magnetism behaviour observed in nature. They are dependent on the structure of the material, and particularly on its electron configuration. Hence are characterized by the presence of magnetic dipoles generated by the spinning of some of their electrons. Each of these polarized electrons can be aligned in a parallel or anti-parallel fashion (Figure 2.15) with respect to the neighbouring ones in the crystal lattice. Five basic types of magnetism can be described: diamagnetism, paramagnetism, ferromagnetism, antiferromagnetism and ferrimagnetism (Matthew and Juang 2005). However, such behaviours are also strongly size-dependent and consequently at a particular temperature the magnetic behaviour of any material can be altered by tuning its size (Lima *et al.*, 2013).
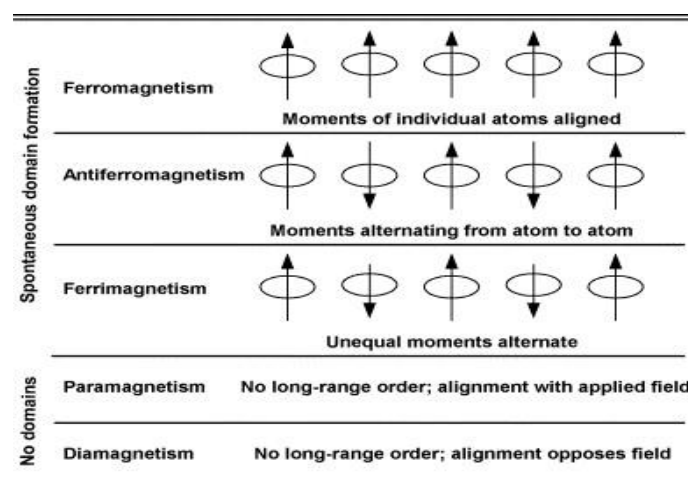


**Figure 2.15** A schematic representation of types of magnetic behaviour (Matthew and Juang 2005)

## 2.5.2 Magnetic nanoparticles

One other interesting development in the use of nanomaterials in drug delivery systems is the use of magnetic nanoparticle, and especially superparamagnetic iron oxide nanoparticles, (SPIONS). These magnetic nanoparticles are the focus of a large part of this thesis whereby they will be used to heat capsules that carry a drug.

As the name implies, magnetic nanoparticles are nanoparticles that exhibit magnetic properties. When a magnetic field of strength, H is applied to any magnetic material, its behaviour is well described by a hysteresis loop as shown in Figure 2.16 and is generated using the superconducting quantum interference device (SQUID) instrument. The magnetisation, M induced by a magnetic field strength, H is shown in Equation [1]

$$M = \chi H \qquad\qquad [1]$$

where $\chi$ is the magnetic susceptibility. From the curves of Figure 2.16, important parameters and properties can be extracted such as the coercivity, remanence, saturation magnetization and the type of magnetic material can be further classified.
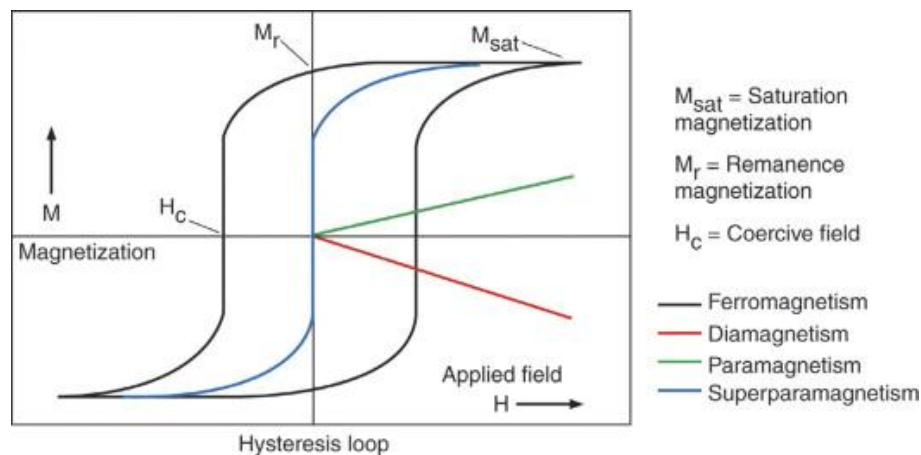


**Figure 2.16** Typical hysteresis loop of magnetization, B versus magnetic field of strength, H when applied to a magnetic material (Arruebo *et al.*, 2007).

Coercivity, Hc is a measure of the field needed to drive the magnetisation to zero after being saturated. This value can be obtained from the area or thickness of the curve. In fine particles such as nanomaterials, the coercivity is the property of most

interest in order to specify the types of magnetism. While, the remanence magnetization, $M_R$, which indicates the magnetisation at zero applied field. Finally, the saturation magnetization, $M_S$, is the maximum value of magnetization that the material can reach under the effect of sufficiently high magnetic fields. Depending on the values of the coercivity and remanence, the magnetic material can be further classified as below.

### 2.5.2.1 Diamagnetism

Material composed of atoms which have no net magnetic moments is called diamagnetic. It is due to the opposing behaviour of orbiting electrons when exposed to an applied magnetic field. In such materials all orbital shells are filled and there are no unpaired electrons. However, when exposed to a field, a negative magnetization is produced and thus the susceptibility is negative ($\chi < 0$). From the plot M vs H, a negative slope is observed (see red line of Figure 2.16) and magnetisation is zero when the no field, H is applied.

### 2.5.2.2 Paramagnetism

This class of materials have a net magnetic moment due to unpaired electrons in partially filled orbitals. The resulting magnetic field due to the upaired electrons does not contrast the applied field but it augments it. This results in a net positive magnetization and positive susceptibility ($\chi > 0$) (see green line of Figure 2.16). Here, again the magnetization is zero when the field is removed.

### 2.5.2.3 Ferromagnetism

The atomic moments in these materials make a phase transition to a state of spins aligned with parallel or anti-parallel orientations. This gives rise to strong interactions and magnetisation. It is called ferromagnetism (see black line of Figure 2.16). Ferromagnetic materials exhibit parallel alignment of moments resulting in large net magnetization even in the absence of a magnetic field (magnetisation remanence)..

### 2.5.2.4 Superparamagnetism

Some ferromagnetic materials exhibit superparamagnetism properties at nanoscale size domain or the single domain. The blue line of Figure 2.16 shows a superparamagnetism behaviour. For a superparamagnetic material, the coercivity, $H_c$ and remanence magnetisation, $M_R$ is equal to zero. Superparamagnetic materials do not present hysteresis meaning that they align immediately to an applied field and become randomly aligned when not in an applied field with no remanent magnetisation. Superparamagnetic nanomaterials are characterised by two modes of relaxations: the Néel and Brown relaxation which are accountable for the two different mechanisms of heat generation by magnetic nanoparticles when exposed to RF radiation (Brown, 1963).

### 2.5.2.4.1 Néel relaxation

Néel relaxation occurs when the magnetic nanoparticle remains stationary and the moment rotates within the crystal. The Néel relation time, $\tau_N$ is given by (Rosensweig 2002):

$$\tau_N = \frac{\frac{\sqrt{\pi}}{2\tau_0}\left(e^{\frac{KV_M}{k_BT}}\right)}{\sqrt{\frac{KV_M}{k_BT}}} \qquad [2]$$

### 2.5.2.4.2 Brown relaxation

Brownian relaxation occurs when a magnetic nanoparticle physically rotates within the medium, hindered by the viscosity of the medium, which tend to counter the rotation of particles. This resulted in heat dissipation through the frictional interaction between the particle and its surrounding medium. The Brownian relaxation time, $\tau_B$ is given by (Rosensweig 2002):

$$\tau_B = \frac{3\eta V_H}{k_BT} \qquad [3]$$

where $\eta$ is the viscosity of the medium, K the Boltzmann constant, T the absolute temperature. $V_H$ is the hydrodynamic volume of the particle, $V_M$ is the magnetic volume of the particle and K is the anisotropy constant

As mentioned above, magnetic nanoparticles offer excellent choice in drug delivery in various ways. Beside their sizes and the benefit that comes with it, their magnetic properties also offer another advantage. When a magnetic field is applied, they can be remotely controlled externally. In this way drug can be tagged along with the particle and can be transferred to a specific targeted site. The magnetic nanoparticles can be made to resonate by an external magnetic field, resulting in a remarkable heating effect. This can be applied to hyperthermia treatments and releasing of drug at the targeted area.

In most drug delivery systems, the drug that is administered is mostly nonspecific. This nonspecificity may lead to side effects as the drug, which is cytotoxic, is distributed all over the body, thus attacking not only the affected area but also the nonaffected area or healthy cells in the body. Therefore, there is a need to develop a delivery system that is more localized and reaches the targeted site so that the drug can be released at the affected site and at the right time. Magnetic nanoparticles, with their novel properties, are proposed to overcome such shortcomings. This prompted the scientific community to investigate the use of magnetic nanoparticles as carriers to target specific sites back in the late 1970s. Credit however, goes to much earlier contributions by Gilchrist and co-workers (1957), followed by Meyers and co-workers (1963) and Turner and co-workers (1975). Later in the 1970s more defined microstructure of magnetic materials were extensively investigated (Widder *et al.*, 1978; Zimmerman *et al.*, 1978; Mosbach & Schröder, 1979; Kato *et al.*, 1984; Gupta *et al.,* 1989; and Häfeli *et al.*, 1994). These investigations were all focussed only on magnetic carriers of micro-size, such as microspheres, with a two prong strategy namely reducing the drug distribution in order to reduce the side effects and localizing the drug at the targeted area more efficiently. In all of these studies the drug carriers in the form of ferrofluid were administered intravenously. In this way,

issues such as instability come into play due to aggregation and clogging. It is also known that bare magnetic materials are easily oxidised and loses their magnetism. By coating these magnetic materials with organic materials such as polymers and surfactants, or layers of inorganic material, it protects them from the surrounding environment and thus facilitates the stabilization of the magnetic materials (Mehta *et al.*, 1997). This enabled them have a longer circulating period.

Literature showed that Lübbe and co-workers (1996) were the pioneers in using magnetic nanoparticles in animal models. The magnetic nanoparticles used were ferrofluids prepared by wet chemical methods from iron oxides and hydroxides. Anhydroglucose polymers were then used to coat the nanoparticles in order to stabilize them. They concluded that the ferrofluid is not only safe but it can also be used for cancer treatment together with high-energy magnetic fields. Since then, many works followed suit such as in swine (Goodwin *et al.*, 1999; 2001; and Wiekhorst *et al.*, 2006), in rabbits (Alexiou *et al.*, 2000; 2006), in cats using magnetic liposomes (Kuznetsov *et al.*, 2001) and in human immune cells (Steinfeld *et al.*, 2006).

Due to several advantages of oral route administration over the parenteral route of administration, some development of the use of magnetic nanoparticles as oral delivery was also reported (Feng & Chien, 2003; Whitehead *et al.*, 2004; and Cheng *et al.*, 2006). This route is non-invasive, pain minimising, patient-friendly and does not require an expert to administer it (Feng & Chien, 2003). It is, however, subjected to the harsh proteolytic degradation of the gastrointestinal (GI) tract. Historically, the discovery of insulin in 1921 by Banting, a Nobel Prize winner in medicine, acted as an impetus to the research on delivering drugs orally. With that discovery, insulin became the first widely used injection drug. It later became the model drug for oral delivery (as used in Chapter 4).

With that in mind, Whitehead and co-workers (2004) described a method that used mucoadhesive intestinal patches to deliver insulin into the systemic circulation. The mucoadhesive patches, which protect the insulin from proteolytic degradation of the

GI tract, are filled in hard gelatine capsules (Figure 2.17a). Due to the size of the capsules, they are assessed by a jejunal administration method. The capsules then release the patches in the intestine (Figure 2.17b). The patches stick to the wall of the intestine and release the insulin (Figure 2.17c and d). The results show that the patches induce hypoglycemia.
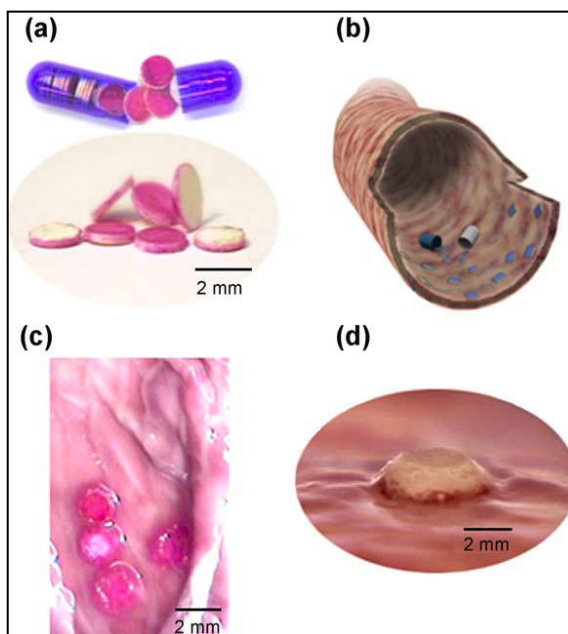


**Figure 2.17** The illustration of the patches (a) filled in the capsule, release in the intestine (b), stick to the wall of the intestine (c) and releasing the insulin (d) (Whitehead *et al*, 2004).

Later on in another related work, built on a previous finding (Chen and Langer, 1997) using a magnetic field on magnetite containing liposomes, Cheng and coworkers (2006) have prepared insulin and magnetic nanoparticles encapsulated with PLGA by an evaporation process in a double emulsion. It was then administered orally on mice. The results also showed improvement on the hypoglycemic effect, in the presence of an external magnetic field, of the mice that were administered orally.

### 2.5.3 Recent Interest

A quick internet search (Date of search: October 2013) on magnetic nanoparticles used as search keywords between 2010 and 2013 shows 22,137 articles have been published during that period(http://apps.webofknowledge.com). An equivalent search but with drug delivery shows 3,033 articles with 280 articles published in 2013.

Interestingly, the search for magnetic nanoparticles in oral delivery resulted in only 1 article published in 2010. The search results indicate that while the work on magnetic nanoparticles is still proliferating, the work on their application in drug delivery and especially in oral delivery is still much to be desired.

Recent interests are still focussing mainly on preparing the ideal or smart magnetic nanoparticle or carrier to address the drawback of magnetic nanoparticles for drug delivery (Chen *et al.*; Shaw *et al.*; and Qu *et al.*, 2013). Issues such as low stability, coating, bioavailabilty, pH sensitivity, stimuli responsiveness to electric field and temperature, cytotoxicity, mathematical modelling and commercialization are still being scrutinized. Amongst the investigations which address the issue of coating are by Gillich and co-workers (2013) and Wang and co-worker (2013) using dendrimers and polymers, respectively for coating the magnetic nanoparticles. In the latter work, Wang and co-workers (2013) have successfully prepared magnetic nanoparticles coated covalently with Pluronic 85 copolymers. They reported that magnetic nanoparticles obtained are smaller in size, better dispersed, more stable, have higher drug-loading capacity, and better sustained release. Curcumin was used as the model drug in their work.

In another related work, Wang and co-workers (2010), addresses not only the issue of coating but also the issue of pH-sensitivity with albendazole as the drug component. In this work, pH-sensitive magnetic hydrogels as the carrier are prepared from alginate-chitosan beads containing magnetic nanoparticles. Their swelling behaviour was studied and it was concluded that the pH-sensitive magnetic beads can be applied for drug targeting in the GI tract.

One pioneering contribution is the preparation of magnetic nanoparticles from natural resources. This work by Chamundeeswari and co-workers (2013) reported the preparation of iron nanoparticles, which are usually prepared from inorganic sources, from goat blood using an incineration method. Chitosan coupled with folic acid was then used to coat the nanoaprticles to form bionanocomposite. Physicochemical studies were done on the biocomposites. They concluded that for the treatment of

cancer this magnetic bionanocomposite may be an economical alternative compared to the already commercially available products which are mostly toxic.

The use of magnetic nanoparticles for oral delivery was also recently reported by Bakandritsos and co-workers (2010). By using self-emulsifying technology, they have prepared stable ferrofluid nanomaterials with a low value of the saturation magnetization of 4.1emu/g. The cytotoxicity studies on rodent fibroblasts show no affected cell activity over 24 h incubation. They concluded that such systems might have a potential use for oral delivery of poorly soluble compounds.

Finally, a solid lipid vehicle magnetised by the presence superparamagnetic iron oxide nanoparticles, SPIONS was reported for targeted and controlled lung drug delivery (Upadhyay *et al.*, 2012). In this report, the drug and melted glycerol behenate (lipid) were emulsified with Pluronic F-68 and heated to $90^{0}$C. The resulting samples were then freeze-dried and jet-milled to produce the desired particle size for inhalation delivery. The dried samples were then filled into hydroxypropyl methylcellulose (HPMC) capsules and placed into the Aeroliser Dry Powder Inhaler (DPI) device. Budesonide was used as the model drug. The results showed an accelerated drug release at the hyperthermia temperatures and the lipid system showed promise for controlled delivery as an effective drug carrier for lung cancer treatment.

## 2.6 Iron Oxide Nanoparticles, IONs

The advantages of using nanoscaled materials such nanoparticles in a drug delivery system have been described above. They are due to their unique size, optical, magnetic and electronic properties (Tari *et al.*, 1979; Masart, 1981; and Poizot *et al.*, 2000). Magnetic nanoparticles in particular, with diameter <20nm exhibit stable magnetic properties which can be utilised to control and sustain release of the drug during the transportation as well as the location of the release. It is therefore no surprise that magnetic nanoparticles have vast potential in application such as in

drug delivery, hyperthermia cancer treatment, and magnetic resonance imaging (MRI) (Crayton and Tsourkas, 2011; and Mahmoudi *et al.*, 2011).

IONs are the widely used magnetic nanoparticles and have captured significant scientific and industrial interest in recent years. They are the much sought nanoparticle ever since it was prepared by Massart (1981).They exist in two main forms namely magnetite ($Fe_3O_4$) and its oxidized form maghemite ($\gamma$-$Fe_2O_3$). Due to their importance, especially $Fe_3O_4$, vast effect has been focussed on developing the technique and processes for mass production and to obtain a monodispersed shape and size (Kotitz *et al.*, 1999; Kim and Park, 2005; and Amit et al., 2011). The main reason for their attraction is due to their superparamagnetic properties. Thus, IONs are also commonly known as superparamagnetic iron oxide nanoparticles or SPIONS. Other magnetic materials such as Cu, Co and Ni received limited attention because they suffer from being toxic in nature and more easily oxidised (Cho *et al.*, 2007).

Bare $Fe_3O_4$ nanoparticles are however easily subjected to oxidation to give maghemite ($\gamma Fe_2O_3$) as shown in the reaction below:

$$2Fe_3O_4 + \tfrac{1}{2}\,O_2 \rightarrow 3(\gamma\text{-}Fe_2O_3)$$
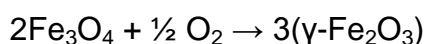
Both materials display superparamagnetic properties, however, they are also prone to aggregation due to their small sizes. These two phenomena resulted in poor magnetism and poor colloidal behaviour. In order to address this limitation, proper coating of the nanoparticles has shown improved properties. In addition, the coating also allows further functionalization of the nanoparticles to enhance their biological and medical application (Zhao *et al.*, 2005; and Xie *et al.*, 2006).

A few recent works are cited here such as the synthesis of pectin coated $Fe_3O_4$ nanospheres by a sonochemical method (Dai *et al.*, 2013), magnetic activated nanoparticles to respond to external stimuli for drug release (Kong, *et al.*, 2013), using amino acids as a linker and spacer between $Fe_3O_4$ and a fluorescent molecule, fluorescein isothiocyanate (Alireza *et al.*, 2013). An interesting development is the introduction of a new concept called nano metal oxide frameworks (MOFs) using iron,

that are able to entrap drugs that existing drug carriers could not (Horcajada *et al.*, 2010) is also cited here.

## 2.7 Synthesis of IONs

### 2.7.1 Chemical Co-Precipitation

Various approaches have been developed to prepare magnetic $Fe_3O_4$ nanoparticles such as via high-temperature decomposition of iron precursors such as iron acetate, acetyl acetate, carboxylate and carbonyl (Jeong *et al.*, 2007; Redl *et al.*, 2004; Sun *et al.*, 2002; 2004), sonochemical method (Dai *et al.*, 2013; Vijayakumar *et al.*, 2000) and involving ferrous and ferric ions co-precipitation (Massart, 1981; Kim *et al.*, 2001; and Harris *et al.*, 2003). The chemical co-precipitation method is the most conventional method to obtain $Fe_3O_4$ or $Fe_2O_3$ (Massart, 1981; and Massart *et al.*, 1995). This is because it is simple and very convenient to prepare, either at room or elevated temperature. Salt solutions (such as chlorides, nitrates, sulphates etc) of $Fe^{2+}$ and $Fe^{3+}$ in molar ratio of 1:2 are mixed together. The mixtures are then titrated with basic solutions (such as KOH, NaOH or $NH_4OH$) to achieve a pH value of 10 under inert conditions. The $Fe_3O_4$ nanoparticles formed in this way however suffer from being polydispersed and are not very stable. Willis and co-workers have shown that oleic acid is excellent in producing stable $Fe_3O_4$ nanoparticles (2005). Therefore, oleic acid is added to the above resulting mixtures.

By employing this method it has been reported that the values of the magnetization saturation, $M_s$, are found to be in the range of 30-50 emu/g, lower than the bulk value of 90 emu/g (Lu *et al.*, 2007). The large gap is due to the size, shape and composition of the nanoparticles prepared. Notwithstanding, the chemical co-precipitation has many advantages such as the ability to synthesise large quantities of nanoparticles, but at the expense of control over particle size and monodispersity.

## 2.8 Magnetic Nanoparticle Hyperthermia

What is hyperthermia? The term is derived from Greek words which mean 'overheating'. Hyperthermia is a promising approach to cancer treatment. It is a term used for the act of raising the whole body or certain parts of the body or tissues or organs to temperatures between 41 – 46 $^{o}$C (Hergt *et al.*, 2006). This can be achieved by heating in several ways such as water bath (Yatvin *et al.*, 1978), electrodes (Strohbehn, 1983) and microwaves (Franconi *et al.*, 2011). The problem encountered with the application of hyperthermic treatments is that it is difficult to heat the local tumour region without simultaneously killing the normal tissue. The higher temperatures can kill a great number of tumour cells, and in principle, tumour-specific hyperthermia can kill all types of tumour cells.

Some researchers have proposed the concept of intracellular hyperthermia and have developed submicron magnetic particles for inducing hyperthermia (Jordan *et al.*, 1993; Mitsumori *et al.*, 1996). This concept is based on the principle that under an alternating magnetic field (AMF), a magnetic particle can generate heat by hysteresis loss. Therefore, if magnetic nanoparticles are used to heat the subject, it is called magnetic nanoparticle hyperthermia. The IONs serve as mediators and help induce heat to the local tumours. When exposed to an external magnetic field, the mediators' magnetic moments oscillate, whereby the electromagnetic energy is converted into heat (magnetic entropy change) (Ito *et al.*, 2005) to destruct the tumour. In other words, the application of an external magnetic field of sufficient strength induces a magnetization in the nanoparticles and then, by applying a field alternating with high enough frequency, the magnetization of the particles is continuously reversed, which translates into a conversion from magnetic to thermal energy. This heat is released to the immediately surrounding diseased tissue. Brown and Néel relaxations are the dominant means of the thermal power dissipation. Both relaxations take place simultaneously but, to achieve high heating rates the Néel relaxation must not be allowed to dominate.

By considering Néel and Brown relaxations process to occur simultaneously, the effective relaxation time of $\tau$ is given by:

$$\frac{1}{\tau} = \frac{1}{\tau_N} + \frac{1}{\tau_B} \qquad [4]$$

Therefore, the power dissipation, P for a monodispersion in an RF field of amplitude, H and frequency, $f$ is given by:

$$P = \pi\mu_o\chi_o H_o^2 f \left[\frac{2\pi f\tau}{1 + (2\pi f\tau)^2}\right] \qquad [5]$$

where $\mu_o$ is the permeability of free space, $\chi_o$ is the magnetic susceptibility. By dividing Equation 5 with the mass of magnetic crystal, the specific power absorption (SPA) (also called the specific absorption rate, SAR) is obtained i.e.:

$$SPA = \frac{CV_S}{m}\frac{dT}{dt} \qquad [6]$$

where, C is the volumetric heat capacity of the sample, $V_S$ is the sample volume, and m is the mass of magnetic material in the sample. Figure 2.18 is adopted from Lima and co-workers (2013) to illustrate this phenomenon as variation of the particle size. It also should be noted that superparamagnetic materials are capable of generating higher levels of heat at lower fields. Hergt and co-workers (1998) reported a SPA value of 45Wg$^{-1}$ at 6.5 kAm$^{-1}$ and 300 kHz which extrapolates to 209 Wg$^{-1}$ for 14kAm$^{-1}$, compared to 75Wg$^{-1}$ at 14 kAm$^{-1}$ for the best ferromagnetic magnetite sample.
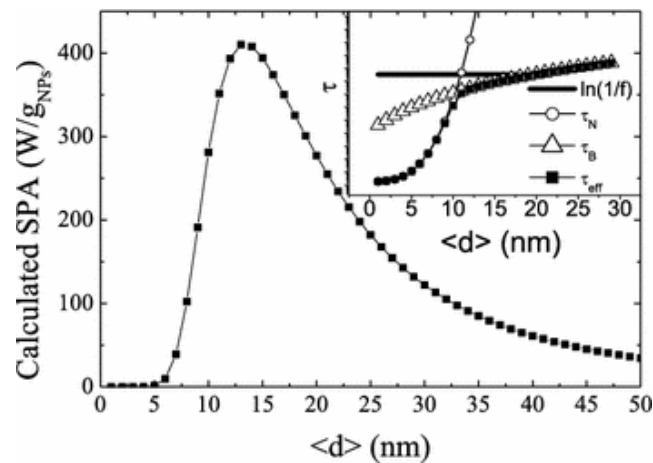


**Figure 2.18** Calculated SPA versus d curves of nanoparticles dispersed in toluene for an alternating magnetic field with $H_0$ = 13 kA/m and f = 250 kHz, and assuming the magnetic parameters characteristics of $Fe_3O_4$ nanoparticles with size dispersion of σ = 0.20 (Lima *et al.*, 2013).

Yatvin and co-workers reported the first work on treatment using hyperthermia (1978). In that study, liposomes containing dipalmitoyl phosphatidylcholine (DPPC) and distearoyl phosphatidylcholine with transition temperature, $T_C$, values of 41 and 54 $^o$C, respectively, were prepared at variable concentration. The basic strategy of the work is to exploit the liquid to crystalline $T_C$ of lipids. Lipid systems are very sensitive to temperature. This is due to their non-ionic nature that lead to spontaneous structural changes to isotropic, liquid crystal, gels etc upon temperature changes (Paphadjopoulus *et al.*, 1973). Earlier studies had shown that normal cells start to damage at about 42 °C (Crile, 1962). Therefore, in order to achieve the targeted therapeutic effect, just a few degrees above physiological temperature is required. The result showed that maximum killing of *E-coli* was seen with liposomes preincubated in the range 42 to 46 $^o$C. From that pioneering contribution, work on hyperthermia then explores other approaches to heating such as cathode, microwaves, ultrasound and lasers as reviewed by Guardia and co-workers (2012).

It has been mentioned earlier that credits for the early work on hyperthermia with magnetized microparticles being heated by an external magnetic field, goes to a much earlier contribution by Gilchrist and co-workers (1957). This was followed by Meyers and co-workers (1963) and Turner and co-workers (1975). More defined microstructures of magnetic materials were later extensively investigated in the late 1970s (Widder *et al.*, 1978; Zimmerman *et al.*, 1978; Mosbach and Schröder, 1979; Kato *et al.*, 1984; Gupta *et al.,* 1989).

In 1993, Jordan and co-workers were claimed to be the first group to report the safe H-field amplitudes and frequencies of RF radiation for excitation of magnetic nanoparticles for application in humans. At the same time, Chan and co-workers (1993) have also carried out similar research work which contributed to a thorough application of hyperthermia in the treatment of tumours. Most of the stated investigations above were carried out by using the parenteral route in administrating the active ingredient (drug). However, there are only limited studies of hyperthermia treatment via oral administration. One of the examples of hyperthermia with magnetised particles that was carried out via oral administration was performed by

Cheng and co-workers (2006). In this study, the result revealed a prolonged transit time of magnetic particles when an external field is applied to the intestine. This in turn extended the residence time in the small intestine and increased the absorption which led to improved delivery (Cheng *et al.*, 2006).

In the context of hyperthermia with magnetised nanoparticles iron oxides $Fe_3O_4$ (magnetite) and $\gamma$ -$Fe_2O_3$ (maghemite) are frequently employed. These materials have been regarded as safe to humans. In addition, the human tissues are also transparent to the magnetic field when RF radiation is applied to them (Tiihonen *et al.*, 1991). Nanoparticles absorb radiofrequency in the region of 100 kHz-1 MHz, and their SPA dictates the effectiveness of their heating (Hergt *et al.*, 2006) as explained earlier.

The limited study of orally-administered hyperthermia treatments with magnetic nanoparticles and the excellent safety profile of the used materials have paved a route for further exploration which serves as another main aim of this study, which is discussed in Chapters 5-7.

## 2.9 References

http://apps.webofknowledge.com

http://www.customprobiotics.com/_images/intestinal-microflora-410.jpg

Al Khouri, F.N., Treupel, L.R., Fessi, H., Devissaguet, J.P., and Puisieux, F. (1986). Development of a new process for the manufacture of polyisobutylcyanoacrylate nanocapsules, *Intern. J. Pharm.*, **28**: 125-132.

Alexey, M., Glushenkov, A.M., Stukachev, V.I., Hassan, M.F., Kuvshinov, G.G., Liu, H.K., and Chen, Y. (2008). A novel approach for real mass transformation from $V_2O_5$ particles to nanorods, *Crystal Growth & Design*, **8(10)**: 3661-3665.

Alexiou, C., Arnold, W., Klein, R.J., Parak, F.G., Hulin, P., Bergemann, C., Erhardt, W., Wagenpfeil, S., and Lübbe, A.S. (2000). Locoregional Cancer Treatment with Magnetic Drug Targeting, *Cancer Res.*, **60**: 6641-6648.

Alexiou, C., Schmid, R.J., Jurgons, R., Kremer, M., Wanner, G., Bergemann, C., Huenges, E., Nawroth, T., Arnold, W., and Parak, F.G. (2006). Targeting cancer cells: magnetic nanoparticles as drug carriers, *Eur Biophys J.*, **35**: 446-450.

Alireza E., Younes, G., Sara, R.A., Jaleh, B., and Soodabeh, D. (2013). Preparation of novel magnetic fluorescent nanoparticles using amino acids, *Colloids and surfaces. B, Biointerfaces*, **102**: 534-539.

Amit P. Khandhar, R. Matthew Ferguson, and Kannan M. (2011). Monodispersed magnetite nanoparticles optimized for magnetic fluid hyperthermia: Implications in biological systems, *J Applied Phys*, **109**: 07B310.

Arruebo, M., Pacheco, R.F., Ibarra, M.R., and Santamaria, J., (2007). Magnetic nanoparticle for drug delivery, *Nanotoday,* **2(3)**: 22-32

Ashford, M., Fell, J., Attwood, D., Sharma, H., and Woodhead, P. (1993a). An evaluation of pectin as a carrier for drug targeting to the colon, *J. Control. Rel*, **26**: 213-220

Ashford, M., Fell, J., Attwood, D., and Woodhead, P. (1993b). An in-vitro investigation into the suitability of pH dependent polymers for colon targeting, *Int. J. Pharm.* **91**: 241-245.

Augsburger, L.L. (1995). *"Hard and Soft Gelatin Capsules"*, Chapter 11 in Modern Pharmaceutics, 3rd Edition, Banker, G. and Rhodes, C.T. (Editors), Marcel Dekker, Inc., New York, NY.

Bakandritsos, A.,Zboril, R., Bouropoulos, N., Kallinteri, P., Favretto, M.E., Parker, T.L., Mullertz, A., and Fatouros, D.G. (2010). The preparation of magnetically guided

lipid based nanoemulsions using self-emulsifying technology, *Nanotechnology*, **21**: 055104-055112.

Bangham, A. D., Standish, M. M., and Watkins, J. C. (1965). Diffusion of univalent ions across the lamellae of swollen phospholipids. *J. Mol. Biol.*, **13**: 238–252.

Bangham, A. D., Standish, M. M. and Weissmann, G., (1965). The action of steroids and streptolysin S on the permeability of pospholipidstructures to cations. *J. Mol. Biol.,* **13**: 253-259.

Bangham, A.D. (1989). The first description of Liposomes, *Current Content*, **13**: 14.

Beija, M., Salvayre, R., Lauth-de Viguerie, N., and Marty, J-D. (2012). Colloidal systems for drug delivery: from design to therapy, *Trends in Biotechnology,* **30(9)**: 488-496.

Bertrand, N., and Leroux, J. C. (2012). The journey of a drug carrier in the body: an anatomo-physiological perspective, *J Controlled Release*, **161**: 152-163

Birrenbach, G. and Speiser, P. (1976). Polymerized micelles and their use as adjuvants in immunology, J. Pharm. Sci. 65 (1976) 1763–1766

Borman, S. (2010) Dendrimersomes Debut. Supramolecular Chemistry: Self-assembled dendrimer-based structures could deliver drugs, other substances, *Chem Engine News*, **88(12)**: 7.

Brown, W.F. (1963). Thermal Fluctuations of a Single-Domain Particle, *Phys. Rev.* **130**: 1677-1686

Buzea, C., Blandino, I.I.P., and Robbie, K. (2007). Nanomaterials and nanoparticles: Sources and toxicity, *Biointerphases,* **2(4)** : MR17 - MR172

Chamundeeswari, M., Sastry, T.P., Lakhsmi, B.S., Senthil, V., and Agostinelli, E. (2013). Iron nanoparticles from animal blood for cellular imaging and targeted delivery for cancer treatment, *Biochimica et Biophysica Acta*, **1830**: 3005-3010.

Charman, W.N., Rogge, M.C., Boddy, A.W., and Berger, B.M. (1993). Effect of food and a monoglyceride emulsion formulation on danazol bioavailability. *J. Clin. Pharmacol.* **33**: 381-386.

Chen, C., Jiang, X., Kaneti, Y.V., and Yu, A. (2013). Design and construction of polymerized-glucose coated Fe3O4 magnetic nanoparticles for delivery of aspirin *Powder Technol.,* **236**: 157-163.

Chen, H. and Langer, R.S.. (1997). Magnetically-Responsive Polymerized Liposomes as Potential Oral Delivery Vehicles, *Pharm. Res.*, 14: 537-540.

Cheng, F.Y., Su, C.H., Yang, Y.S., Yeh, C.S., Tsai, C. Y., Wu, C.L., Wu, M.T. and Shieh, D.B., (2005). Characterization of aqueous dispersions of $Fe_3O_4$ nanoparticles and their biomedical applications, *Biomaterials*, **26**: 729-738.

Cheng, J., Teply, B.A., Jeong, S.Y., Yim, C.H., Ho, D., Sherifi, I., Jon, S., Farokhzad, O.C., Khademhosseini, A., and Langer, R.S. (2006). Magnetically Responsive Polymeric Microparticles for Oral Delivery of Protein Drugs, *Pharm. Res.*, **23(3)**: 557-564.

Cho, S. J., Maysinger, D., Jain, M., Roder, B., Hackbarth, S., and Winnik, F. M. (2007). Long-term exposure to CdTe quantum dots causes functional impairments in live cells, *Langmuir*, **23**: 1974-1980.

Chou, L. Y. T., Ming, K., and Chan, W. C. W., 2011. Strategies for the intracellular delivery of nanoparticles, *Chemical Society Reviews* **40(1)**: 233-245.

Cole, E.T., Scott, R.A., Connor, A.L., Wilding, I.R., Petereit, H.U., Schminke, C., Beckert, T., and Cadé, D. (2002). Enteric coated HPMC capsules designed to achieve intestinal targeting, *Intern J Pharm*, **231**: 83-95.

Colon, G., Ward, B.C., and Webster, T.J. (2006). Increased osteoblast and decreased Staphylococcus epidermidis functions on nanophase ZnO and TiO2. *J Biomed Mater Res* A, **78A(3)**: 595–604.

Couvreur, P., Kanté, B., Roland, M., Guiot, P., Baudhuin, P., and Speiser, P. (1979). Polycyanoacrylate nanocapsules as potential lysosomotropic carriers: preparation, morphological and sorptive properties, *J. Pharm. Pharmacol.*, **31**: 331-332.

Couvreur, P., Grislain, L., Lenaerts, V., Brasseur, F., Guiot, P., and Biernacki, A. (1986). *Biodegradable polymeric nanoparticles as drug carriers for antitumor agents*, in: P. Guiot, P. Couvreur (Eds.), Polymer Nanoparticles and Microspheres, CRC Press, Boca Raton, FL, pp. 24- 94.

Couvreur, P. (2013). Nanoparticles in drug delivery: Past, present and future, *Adv. Drug Delivery Rev.*, **65**: 21-23.

Cram, D.J., Helgeson, R.C., Sousa, L.R., Timko, J.M., Newcomb, M., *et al.* (1975). Chiral recognition in complexation of guest by designed host molecules, *Pure Appl. Chem.*, **43**: 327-349.

Crayton, S.H., and Tsourkas, A., (2011). pH-titratable superparamagnetic iron oxide for improved nanoparticle accumulation in acidic tumor microenvironments. *ACS Nano*, **5**: 9592-9601.

Crile, G. (1962). Recent data obtained with E. coli auxotrophs requiring unsaturated fatty acids and with mammalian cells suggest that membrane fluidity may be a determining factor in hyperthermic cell death, *Ann. Surg.* **156**: 404

Crounce, R.G., (1961). Human pharmacology of griseofulvin: The effect of fat intake on gastrointestinal absorption. *J. Invest. Dermatol.* **37**: 529-532.

Dai, J., Wu, S., Jiang, W., Li, P., Chen, X., Liu, L., Liu, J., Sun, D., Chen, W., Chen, B., and Li, F. (2013). Facile synthesis of pectin coated $Fe_3O_4$ nanospheres by the sonochemical method, *J Magn. Magn. Mater.*, **331**: 62-66

Damge, C., Michel, C., Aprahamian, M., Couvreur, P., and Devissaguet, J.P. (1990). Nanocapsules as carriers for oral peptide delivery, *J Controlled Release,* **13**: 233-239.

Davis, B. K., (1972). Control of diabetes with polyacrylamide implants containing insulin, *Experientia*, **28**: 348.

Davis, B. K., (1974). Diffusion in polymer gel implants, *Proc. Natl. Acad. Sci. U.S.A.*, **71**: 3120–3123.

Discher, B.M., Won, Y-Y., Ege, D.S., Lee, J.C-M., Bates, F. S., Discher, D.E., and Hammer, D.A. (1999). Polymersomes: tough vesicles made from diblock co-polymers. *Science*, **284**:1143-1146.

Dumestre, F., Chaudret, B., Amiens, C., Respaud, M., Fejes, P., Renaud, P., and Zurcher, P. (2003). Unprecedented crystalline super-lattice of monodisperse cobalt nanorods, *Angew. Chem. Int. Ed.,* **42**, 5213-5214.

El-Samaligy, M.S., Rohdewald, P., and Mahmoud, H.A. (1986). Polyalkyl cyanoacrylate nanocapsules, *J. Pharm. Pharmaco.*, **38**: 216-218.

Fausa, O. (1974). Duodenal bile acids after a test meal, *Scand. J. Gastroent.*, **9**: 567-570.

Fallingborg, J. (1999). Intraluminal pH of the human gastrointestinal tract. *Dan Med Bull*, **46(3)**: 183-196.

Feng, S.S., and Chien, S. (2003). Chemotherapeutic engineering: Application and further development of chemical engineering principles for chemotherapy of cancer and other diseases, *Chem. Engine. Sci.,* **58(18)**: 4087-4114.

Franconi, C., Vrba, J., Micali, F. And Pesce, F. (2011). Prospects for Radiofrequency Hyperthermia Applicator Research. I - Pre-Optimised Prototypes of Endocavitary Applicators with Matching Interfaces for Prostate Hyperplasia and Cancer Treatments. *Int. J. Hyperthermia*, **27**: 187-198.

Gallardo, M.M., Treupel, R.L., Mahuteau, J., Genin, I., Couvreur, P., Plat, M. and Puisieux, F. (1989). Nanocapsules et nanosheres d-alkyl-cynoacrylate, interactions pioncipe actif/polymere, *Proc APGI, 5th Conference on Pharmeceutical technology,* Paris, 36-45.

Gasco, M.R., and Trotta, M. (1986). Nanoparticles from microemulsions, *Intern. J Pharm.*, **29** :267- 268.

Gianchandani, Y. and Meng, E. (2012). Emerging micro- and nanotechnologies at the interface of engineering, science, and medicine for the development of novel drug delivery devices and systems, *Adv. Drug Delivery Rev.*, **64**: 1545-1546.

Gilchrist, R.K., Medal, R., Shorey, W.D., Hanselman, R.C., Parrott, J.C., and Taylor, C.B., (1957). Selective inductive heating of lymph nodes. *Ann. Surg.* **146**: 596-606.
Gill, H.S., and Prausnitz, M.R. (2007). Coating formulations for microneedles, *Pharm. Res.*, **24**: 1369–1380.

Gillich, T., Acikgöz, C., Isa, L., Schlüter, A.D., Spencer, N.D., and Textor, M. (2013). PEG-stabilized core-shell nanoparticles: Impact of linear versus dendritic polymer shell architecture on colloidal properties and the reversibility of temperature-induced aggregation, *ACS Nano*, **7(1)**: 316-329.

Gimbrone, M. A., Jr, Cotran, R. S., Leapman, S. B., and Folkman, (1974). Tumor growth and neovascularization: An experimental model using the rabbit cornea, *J. Natl. Cancer Inst.*, **42**: 314–427.

Goodwin, S.C., Bittner, C.A., Peterson, C.L., and Wong, G. (2001). Single-dose toxicity study of hepatic intraarterial infusion of doxorubicin coupled to a novel magnetically targeted drug carrier. *Toxicol Sci.*, **60** : 177-183

Goodwin, S.C., Peterson, C., Hob, C., and Bittner, C. (1999). Targeting and retention of magnetic targeted carriers (MTCs) enhancing intra-arterial chemotherapy. *J Magn Magn Mater.*, **194**: 132-139

Guardia,P., Corato, R.D., Lartigue, L., Wilhelm, C., Espinosa, A., Garcia-Hernandez, M., Gazeau, F., Manna, L., and Pellegrino, T. (2012). Water-Soluble Iron Oxide Nanocubeswith High Values of Specific Absorption Rate for Cancer Cell, Hyperthermia Treatment, *ACS Nano*, **6(4)**: 3080-3091.

Gupta, P.K., Hung, C.T., and Rao, N.S. (1989). Ultrastructural disposition of adriamycin-associated magnetic albumin microspheres in rats. *J. Pharmacol. Sci.* **78**: 290-294.

Gwinn, M.R. and  Vallyathan, V. (2006). Nanoparticles: Health Effects—Pros and Cons Environmental Health Perspectives, **114(12)**: 1818-1825.

Haensler, J., and Szoka, F. Jr. (1993). Polyamidoamine cascade polymers mediate efficient transfection of cells in culture *Bioconjugate Chem.*, **4**: 372−379.

Häfeli, U.O., Sweeney, S.M., Beresford, B.A., Sim, E.H., and Macklis, R.M. (1994). Magnetically directed poly(lactic acid) 90Y-microspheres: novel agents for targeted intracavitary radiotherapy. *J. Biomed. Mater. Res.* **28**: 901-908.

Hamaguchi, T., Shinkuma, D., Irie, T., Yamanaka, Y., Morita, Y., Iwamoto, B., Miyoshi, K., and Mizuno, N. (1993). Effect of a high-fat meal on the bioavailability of

phenytoin in a commercial powder with a large particle size. *Int. J. Clin. Pharmacol. Ther. Toxicol.* **31(7)**: 326-330.

Harris, L.A., Goff, J.D., Carmichael, A.Y., Riffle, J.S, Harburn, J.J., St. Pierre, T.G., and Saunders, M. (2003). Magnetite nanoparticle dispersions stabilized with triblock copolymers, *Chem Mater*, **15**: 1367-1377.

Heath, T. D., Fraley, R. T. and Papahdjopoulos, D. (1980). Antibody targeting of liposomes: Cell specificity obtained by conjugation of F(ab')2 to Vesicle Surface, Science, **210**: 539–541.

Hergt R, Andra W, d'Ambly CG, Hilger I, Kaiser WA, Richter U, and Schmidt, H.G. (1998). Physical limits of hyperthermia using magnetite fine particles. *IEEE Trans Magn*, **34**: 3745-3754.

Hegrt, R., Dutz, S., M¨uller, R., and Zeisberger, M., (2006). Magnetic particle hyperthermia: Nanoparticle magnetism and materials development for cancer therapy, *J. Phys.: Condens Matter,* **18**: S2919-S2934.

Hiemenz, P.C. (1986). Principles of colloid and surface chemistry, 2$^{nd}$ Ed, Ch 1, pp 5-7, Marcel Dekker, Inc., New York.

Hooper, L.P., Midtvedt, T., and Gordon, J.I. (2002).  How host-microbial interactions shape the nutrient environment of the mammalian intestine, *Annu. Rev. Nutrition*, **22**: 283-307.

Horcajada, P., Chalati, T., Serre, C., Gillet, B., Sebrie, C., Baati, T., Eubank, J.F., Heurtaux, D., Clayette, P., Kreuz, C., Chang, J-S., Hwang, Y., Marsaud, V., Bories, P., Cynober, L., Gil, S., Férey, G., Couvreur, P., and Gref, R. (2010). Porous metal-organic-framework nanoscale carriers as a potential platform for drug delivery and imaging *Nat. Mater.*, **9**: 172-178.

Hosny, E.A., Al-Shora, H.I., and Elmazar, M.M.A. (2002). Oral delivery of insulin from enteric-coated capsules containing sodium salicylate: effect on relative hypoglycaemia of diabetic beagle dogs, *Intern. J Pharm,* **237**: 71-76.

Hughes, G.A. (2005). Nanostructure-mediated drug delivery, *Nanomedicine: Nanotechnology, Biology, and Medicine*, **1** : 22-30.

Ito, A., Shinkai, M., Honda, H., and Kobayashi, T. (2005). Medical application of functionalized magnetic nanoparticles, *J. Biosci. Bioeng.*, **100(1)**: 1-11.

Jain, R. K. (1994). Barriers to drug-delivery in solid tumors. *Sci. Am.,* **271**: 58-65.

Jansen, J. F. G.A.,de Brabander van den Berg, E. M. M. and Meijer, E. W. (1994). Encapsulation of guest molecules into a dendritic box, *Science,* **266**: 1226−1229.

Jeong, U., Teng, X., Wang, Y., Yang, H., and Xia, Y. (2007). Superparamagnetic Colloids: Controlled Synthesis and Niche Applications, *Adv. Mater.* **19**: 33-60.

Jiles, D. (1991). *Introduction to magnetism and magnetic materials*, Chapman and Hall, London.

Jordan, A., Wust, P., Fähling, H., John, W., Hinz, A., and Felix, R. (1993). Inductive heating of ferrimagnetic particles and magnetic fluids: physical evaluation of their potential for hyperthermia. *Intern. J. Hyperthermia*, **9**: 51-68.

Joshi, R.K., Krishnan, S., Yoshimura, M., and Kumar, A. (2009). Pd Nanoparticles and Thin Films for Room Temperature Hydrogen Sensor, *Nanoscale Res Lett.*, **4(10)**: 1191–1196.

Kararli, T.T. and Gupta, V.W. (1992) Solubilization and dissolution properties of a leucotriene-$D_4$ antagonist in micellar solutions. *J. Pharm. Sci.*, **81**: 483-485.

Kato, T., Nemoto, R., Mori, H. (1984). Magnetic microcapsules for targeted delivery of anticancer drugs. *Appl. Biochem. Biotechnol.* **10**: 199-211.

Kim, D.K., Zhang, Y., Voit, W., Rao, K.V., and Muhammed, M. (2001). Synthesis and characterization of surfactant-coatedsuperparamagnetic monodispersed iron oxide nanoparticles, *J Magn Magn Mater*, **225**: 30-36.

Kim, K.S. and Park, J.K. (2005). Magnetic force-based multiplexed immunoassay using superparamagnetic nanoparticles in microfluidic channel. *Lab Chip*, **5(6)**: 657-664.

Kim, Y.C., Park, J.H., and Prausnitz, M.R. (2012). Microneedles for drug and vaccine delivery, *Adv. Drug Delivery Rev.*, **64**: 1547-1568.

Kipp, J.E. (2004). The role of solid nanoparticle technology in the parenteral delivery of poorly water-soluble drugs. *Int. J. Pharm.*, **284**:109-122.

Kong, S.D., Sartor, M., Jack Hu, C.H., Zhang, W., Zhang, Z., and Jin, S. (2013). Magnetic field activated lipid-polymer hybrid nanoparticles for stimuli-responsive drug release, *Acta Biomaterialia*, **9(3)**: 5447-5452.

Kotitz, R., Weitschies, W., Trahms, L., Brewer, W., and Semmler, W. (1999). Determination of the binding reaction between avidin and biotin by relaxation measurements of magnetic nanoparticles. *J Magn Magn Mater*, **194(1-3)**: 62-68.

Kostwicz, E. S., Brauns, U., Becker, R., and Dressman, J. B. (2002). Forecasting the oral absorption behavior of poorly soluble weak bases using solubility and dissolution studies in biorelevant media. Pharm. Res., **19(3)**: 345–349, 2002.

Kuznetsov, A.A.,Filippov, V.I., Alyautdin, R.N., Torshina, N.L., and Kuznetsov, O.A. (2001). Application of magnetic liposomes for magnetically guided transport of muscle relaxants and anti-cancer photodynamic drugs, *J Magn Magn Mater*, **225**: 95-100

Langer, R. and Folkman, J. (1976). Polymers for the sustained release of proteins and other macromolecules. *Nature*, **263**: 797–800.

La Wall, C. H., (1940). *4000 years of pharmacy, an outline history of pharmacy and the allied sciences*, J. B. Lippincott Comp., Philadelphia/London/Montreal.

Lee, J.W., Park, J.H., and Prausnitz, M.R. (2008). Dissolving microneedles for transdermal drug delivery, *Biomaterials*, **29**: 2113–2124.

Legen, I., and Kristl, A. (2003). Factors affecting the microclimate pH of the rat jejunum in Ringer bicarbonate buffer, *Biol Pharm Bull*, **26(6)**: 886-889.

Leserman, L. D. Barbet, J. Kourilsky,F. and Weinstein, J. N. (1980). Targeting to cells of fluorescent liposomes covalently coupled with monoclonal antibody or protein A, *Nature,* **288**: 602–604.

Lima, E., Torres, T.E., Rossi, L.M., Rechenberg, H.R., Berquo, T.S., Ibarra, A., Marquina, C., Ibarra, M.R., and Goya, G.F. (2013). Size dependence of the magnetic relaxation and specific power absorption in iron oxide nanoparticles, *J. Nanopart. Res.,***15**: 1654-1665.

Liu, Z.L., Liu, Y.J., Yao, K.L., Ding, Z.H., Tao, J., and Wang, X. (2002). Synthesis and magnetic properties of $Fe_3O_4$ nanoparticles, *J. Mater. Synth. Proc.* **10(2)**: 83-87.

Lloyd, N. C., Morgan, H. W., Nicholson, B. K., and Ronimus, R. S. (2005). The Composition of Ehrlich's Salvarsan: Resolution of a Century-Old Debate, *Angew. Chem. Int. Ed.*, **44**: 941-944.

Lu, A.H., Salabas, E.L., and Schüth, F. (2007). Magnetic Nanoparticles: Synthesis, Protection, Functionalization, and Application, *Angew. Chem. Int. Ed.* **46**: 1222-1244.

Lübbe, A.S., Bergemann, C., Huhnt, W., Fricke, T., Riess, H., Brock, J.W., and Huhn, D. (1996). Preclinical experiences with magnetic drug targeting: tolerance and efficacy. *Cancer Res.,***56**: 4694-4701.

Luo, D., Han, E., Belcheva, N., and Saltzman, W., M. (2004). A self-assembled, modular DNA delivery system mediated by silica nanoparticles *J. Control. Rel.*, **95**: 333-341.

Ma, M., Wu, Y., Zhou, H., Sun, Y.Kk., Zhang, Y., and Gu, N. (2004). Size dependence of specific power absorption of Fe3O4 particles in AC magnetic field, *J Magn Magn Mater.*, **268**: 33-39.

Ma, P. X., (2008). Biomimetic materials for tissue engineering, *Adv. Drug Delivery Rev.*, **60**: 184-198.

Mahmoudi, M., Sant, S., Wang, B., Laurent, S., and Sen, T., (2011). Superparamagnetic iron oxide nanoparticles (SPIONs): development, surface modification and applications in chemotherapy, *Adv. Drug Deliv. Rev.*, **63**: 24-46.

Marieb, E.N. and Hoehn, K. (2010). *Human anatomy & physiology*, San Francisco: Benjamin Cummings

Massart, R. (1981). Preparation of Aqueous Magnetic Liquids in Alkaline and acidic media, *IEEE Trans Magnetics*, **17(2)**: 1247-1248.

Massart, R., Roger, J., and Cabuil, V. (1995). New Trends in Chemistry of Magnetic Colloids: Polar and Non Polar Magnetic Fluids,Emulsions, Capsules and Vesicles, *Brazilian J, Phys.*, **25**: 135-141.

Marty, J.J., Oppenheim, R.C. and Speiser, P. (1978). Nanoparticles-A new colloidal drug delivery system, Pharm. Acta Helv. 53 (1978) 17–23.

Mathew, D.S., and Juang, R.S. (2005). An overview of the structure and magnetism of spinel ferrite nanoparticles and their synthesis in microemulsions, *Chem. Engine. J.*, **129**: 51-65.

Mehta, R. V., Upadhyay, R. V., Charles, S. W., and Ramchand, C. N. (1997). Direct binding of protein to magnetic particles *Biotechnol. Techn.* **11**: 493-496.

Meyers, P.H., Cronic, F., and Nice, C.M., (1963). Experimental approach in the use and magnetic control of metallic iron particles in the lymphatic and vascular system of dogs as a contrast and isotopic agent, *Am. J. Roentgenol. Radium Ther. Nucl. Med.*, **90**: 1068-1077.

Misra, R., Acharya, S., and Sahoo, S.K. (2010). Cancer nanotechnology: application of nanotechnology in cancer therapy, *Drug Discovery Today*, **15(19&20)**: 842-850.

Mithani, S.D., Bakatselou, V., TenHoor, C.N., and Dressman, J.B. (1996). Estimation of the increase in solubility of drugs as a function of bile salt concentration. *Pharm Res.*, **13(1)**: 163-167.

Mitragotri, S. (2013). Devices for overcoming biological barriers: The use of physical forces to disrupt the barriers, *Adv. Drug Delivery Rev.*, **65**: 100-103.

Mitsumori, M. Hiraoka, M., Shibata, T., Okuno, Y., Nagata, Y., Nishimura, Y., Abe, M., Hasegawa, M., Nagae, H., and Ebisawa, Y. (1996). Development of intra-arterial hyperthermia using a dextran-magnetite complex. *Hepatogastroenterology*, **43**: 1431-1437.

Mohamad, A., and Dashevsky, A. (2006). pH-independent pulsatile drug delivery system based on hard gelatin capsules and coated with aqueous dispersion Aquacoat®ECD, *European J Pharm Biopharm*, **64**: 173-179.

Mohammad, N., Freeman, S., Attwood, D., and D'Emanuele, A. (2006). Synthesis, characterization and stability of dendrimer prodrugs, *Intern. J. Pharmaceutics*, **308**: 175-182.

Mosbach, K. and Schroder, U. (1979). Preparation and application of magnetic polymers for targeting of drugs *FEBS Lett.* **102** 112-116.

Newkome, G. R., Yao, Z., Baker, G. R., and Gupta, V. K. (1985). Micelle. Part 1. Cascade Molecules: A New Approach to Micelles. A [27]-Arborol, *J. Org. Chem.*, *50***(11)**: 2003-2004.

Newkome, G. R., Moorefield, C. N., Baker, G. R., Saunders, M. J. and Grossman, S. H. (1991). Unimolecular micelles, *Angew. Chem. int. Edn Engl.*, **30**, 1178−1180.

Oluwatoyin, A.O., and John, T.F. (2005). In vitro evaluation of khaya and albizia gums as compression coating for drug targeting to the colon. *J Pharm Pharmacol.*, **57**: 1-6.

Orienti, I., Trere, R., and Zecchi, V. (2001). Hydrogels Formed by Cross-Linked Polyvinylalcohol as Colon-Specific Drug Delivery Systems, *Drug Develop Indus. Pharm.*, **27(8)**: 877-884.

Papahadjopoulos, D., Jacobson, K., Nir, S., and Isac, T. (1973). Phase Transitions in Phospholipid Vesicles: Fluorescence Polarization and Permeability Measurements. Effect of Temperate and Cholesterol, *Biochim. Biophys. Acta*, **311**, 330-348.

Percec, V., Wilson, D.A., Leowanawat, P., Wilson, C.J., Hughes, A.D., Kaucher, M.S., Hammer, D.A., Levine, D.H., Kim, A.J., Bates, F.S., Davis, K.P., Lodge, T.P., Klein, M.L., DeVane, R.H., Aqad, E., Rosen, B.M., Argintaru, A.O., Sienkowska, M.J.,

Rissanen, k., Nummelin, S., and Ropponen, J. (2010). Self-Assembly of Janus Dendrimers into Uniform Dendrimersomes and Other Complex Architectures, *Science*, **328**: 1009-1014.

Poizot, P., Laruelle, S., Grugeon, S., Dupont, L., and Tarascon, J.M. (2000). Nano-sized transitionmetaloxides as negative-electrode materials for lithium-ion batteries, *Nature*, **407**: 496–499.

Philip, A.K., Dabas, S., and Pathak, K. (2009). Optimized prodrug approach: A means for achieving enhanced anti-inflammatory potential in experimentally induced colitis, *J Drug Target*, **17**: 235-241.

Philip A.K. and Philip, B. (2010). Colon Targeted Drug Delivery Systems: A Review on Primary and Novel Approaches, *Oman Med. J.*, **25**: 70-78.

Prabha, S., and Labhasetwar, V. (2004). Critical determinants in PLGA/PLA nanoparticle-mediated gene expression. *Pharm. Res.*.**21(2)**: 354-364.

Qu, J.B., Shao, H.H., Jing, G.L., and Huang, F. (2013). PEG-chitosan-coated iron oxide nanoparticles with high saturated magnetization as carriers of 10-hydroxycamptothecin: Preparation, characterization and cytotoxicity studies, *Colloids Surfaces B: Biointerfaces*, **102**: 37-44.

Redl, F. X., Black, C.T., Papaefthymiou, G.C., Standstrom, R.L., Ying, M., Zeng H.,Murray, C.B. and O'Brien, S.P. (2004). Magnetic, Electronic and Structural Characterization of Non-stoichiometric Iron Oxides at the Nanoscale, *J. Am. Chem. Soc.* **126**: 14583

Rosensweig, R.E. (2002). Heating magnetic fluid with alternating magnetic field, *J.I of Magn. Magn Mater.*, **252**: 370-374.

Rubinstein, A. (1995). Approaches and opportunities in colon-specific drug delivery, *Crit. Rev.Ther. Drug Carrier Syst.*, **12**: 101-149.

Savage DC. 1977. Microbial ecology of the gastrointestinal tract. *Annu. Rev. Microbiol*, **31**: 107-133.

Scott, R. C., Crabbe, D., Krynska, B., Ansari, R., and Kiani, M. F. (2008). Aiming for the heart: targeted delivery of drugs to diseased cardiac tissue, *Expert Opinion on Drug Delivery,* **5(4)**: 459–470.

Shaw, S., Murthy, P.V.S.N., and Sibanda, P. (2013). Magnetic drug targeting in a permeable microvessel, *Microvascular Res.*, **85**: 77-85.

Singh P, Moll, F. 3rd, Lin, S.H., Ferzli, C., Yu, K.S., Koski, R.K., Saul, R.G., and Cronin, P. (1994). Starburst dendrimers: enhanced performance and flexibility for immunoassays, *Clin. Chem.,* **40**: 1845−1849.

Sonaje,K., Chen, Y.J., Chen, H.L., Wey, S.P., Juang, J.H., Nguyen, H.N., Hsu, C.W., Lin, K.J. and Sung, H.W. (2010). Enteric-coated capsules filled with freeze-dried chitosan/poly(g-glutamic acid) nanoparticles for oral insulin delivery, *Biomaterials*, **31**: 3384-3394.

Speiser, P. (1976). Controlled release of drugs from microcapsules and nanocapsules, *Acta Pharmaceutica Suecica*, **13**: 35

Stegemann, S. and Bornem, C. (1999). Hard gelatin capsules today – and tomorrow. Capsugel Library, **1**: 1-23 and references therein.

Steinfeld, U., Pauli, C., Kaltz, N., Bergemann, C., and Lee H. (2006). T lymphocytes as potential therapeutic drug carrier for cancer treatment, *Int. J. Pharm.* **311**; 229-236.

Strohbehn, J.W. (1983). Temperature distributions from interstitial RF electrode hyperthermia systems: Theoretical predictions, *Intern J Radiation Oncology*Biology*Physics*, **9(11)**: 1655-1667.

Sun, S., and Zeng, H. (2002). Size-controlled synthesis of magnetite nanoparticles, *J Am. Chem. Soc.*, **124**: 8204-8205.

Sun, S., Zeng, H., Robinson, D. B., Raoux, S. Rice, P. M., Wang, S. X., and Li, G. X. (2004). Monodisperse $MFe_2O_4$ (M = Fe, Co, Mn) nanoparticles, *J. Am. Chem. Soc.* **126**: 273-279.

Suslick, K.S., Choe, S.B., Cicholas, A.A., and Grinstaff, M.W. (1991). Sonochemical synthesis of amorphous iron, *Nature*, **353**: 414-417.

Tangerman, A., vanSchaik, A., and vander Hook, V.W. (1986) Analysis of conjugated and unconjugated bile acids in serum and jejunal fluid of normal subjects. *Clin. Chem. Acta.* **159:**123-132.

Tari, A., Chantrell, R.W., Charles, S.W. and Popplewell, J. (1979). Magnetic-properties and stability of a ferrofluid containing $Fe_3O_4$ particles, *Physica B & C*, **97 (1)**: 57-64.

Tiihonen, J., Hari, R., Kajola, M., Karhu, J., Ahlfors, S., and Tissari, S. (1991). Magnetoencephalographic 10-Hz rhythm from the human auditory cortex, *Neurosci. Lett.*, **129**: 303-305.

Tomalia, D. A., Baker, H., Dewald, J., Hall, M., Kallos, G., Martin, S., Roeck, J., Ryder, J., and Smith, P. (1985). A New Class of Polymers: Starburst-Dendritic Macromolecules, *Polym. J.*, **17(1)**: 117-132.

Tomalia, D.A., Naylor, A.M. & Goddard III, W.A. (1990) Starburst dendrimers: Molecular-level control of size, shape, surface chemistry, topology, and flexibility from atoms to macroscopic matter. *Angew. Chem., Int. Edn.*, **29**: 138–175.

Torchilin, V. P. (2007). Micellar nanocarriers: pharmaceutical perspectives, *Pharm. Res.*, **24**: 1-16.

Tsuzuki, T. (2009). Commercial scale production of inorganic nanoparticles, *Intern. J. Nanotechnology*, 6:567-578.

Turner, R.D., Rand, R.W., Bentson, J.R., and Mosso, J.A., (1975). Ferromagnetic silicone necrosis of hypernephromas by selective vascular occlusion to the tumor: a new technique. *J. Urol.* **113**: 455-459.

Turro, N. J.; Barton, J. K.; Tomalia, D. A. (1991). Molecular recognition and chemistry in restricted reaction spaces. Photophysics and photoinduced electron transfer on the surfaces of micelles, dendrimers and DNA. *Acc. Chem. Res.*, , **24**: 332–340.

Upadhyay, D., Scalia, S., Vogel, R., Wheate, N., Salama, R.O., Young, P.M., Traini, D., and Chrzanowski, W. (2012). Magnetised Thermo Responsive Lipid Vehicles for Targeted and Controlled Lung Drug Delivery, *Pharm Res.*, **29**: 2456-2467.

Vauthier, C., Dubernet, C., Fattal, E., Pinto-Alphandary, H., Couvreur, P., (2003). Poly(alkylcyanoacrylates) as biodegradable materials for biomedical applications. Adv. Drug Deliv. Rev. 55, 519-548, 2003.

Vertzoni, M., Dressman, J., Butler, J., Hempenstall, J., and Reppas, C. (2005). Simulation of fasting gastric conditions and its importance for the in vivo dissolution of lipophilic compounds, *European J Pharm Biopharm*, **60(3)**: 413-417.

Vijayakumar, R., Koltypin, Y., Felner, I., and Gedanken, A. (2000). Sonochemical synthesis and characterization of pure nanometer-sized $Fe_3O_4$ particles. *Mater Sci Eng A*, **286**: 101-105.

Wang, F.Q., Li, P., Zhang, J.P., Wang, A.Q., and Wei, Q. (2010). A novel pH-sensitive magnetic alginate–chitosan beads for albendazole delivery Magnetic Alg/CS beads for ABZ delivery, *Drug Develop Indus Pharm*, **36(7)**: 867-877.

Wang, N., Guan, P., Yang, L., Jia, L., Wei, X., Liu, H., and Guo, C. (2013). Magnetic nanoparticles (MNPs) covalently coated by PEO–PPO–PEO block copolymer for drug delivery, *J Colloid Interface Sci.*, **395**: 50-57.

Watnasirichaikul, S., Davies, N.M., Rades, T., and Tucker, I.G. (2000). Preparation of biodegradable insulin nanocapsules from biocompatible microemulsions, *Pharm. Res.*, **17**: 684-689.

Weinstein, J.N., Blumenthal, R., Sharrow, S.O., and Henkart, P. (1978). Antibody-mediated targeting of liposomes: Binding to lymphocytes without incorporation of vesicle contents into the cells. *Biochim. Biophys. Acta*, **509**: 272-288.

Weissmann, G., Bloomgarden, D., Kaplan, R., Cohen, C., Hoffstein, S., Collins, T., Gottlieb, A., and Nagel, D, (1975). A general method for the introduction of enzymes, by means of immunoglobulin-coated liposomes into lysosomes of deficient cells.*Proc Natl Acad Sci USA*, **72**: 88–92.

Whitehead, K., Shen, Z.C., and Mitragotri, S. (2004). Oral delivery of macromolecules using intestinal patches: applications for insulin delivery. J. Control. Release 98:37-45.

Widder, K. J., Senyei, A. E., and Scarpelli, D. G. (1978) Magnetic microspheres: a model system for site specific drug delivery *in vivo Proc. Soc. Exp. Biol. Med.* **58** 141-146.

Wiekhorst, F., Seliger, C., Jurgons, R., Steinhoff, U., Eberbeck, D., Trahms, L., and Alexiou, C. (2006). Quantification of magnetic nanoparticles by magnetorelaxometry and comparison to histology after magnetic drug targeting. *J Nanoscience Nanotechnology.* **6(9-10)**: 3222-3225.

Wiener, E. C., Brechbiel, M. W., Brothers, H., Magin, R. L., Gansow, O. A., Tomalia, D. A., and Lauterbur, P. C. (1994). Dendrimer-based metal chelates: a new class of magnetic resonance imaging contrast agents *Magn. Resonance Med.*, **31**: 1−8.

Wilding, I.R., 2000. Site-Specific drug delivery in the gastrointestinal tract. *Crit. Rev. Ther. Drug Carr. Syst.*, **17**: 557–620.

Willis, A.L., Turro, N.J., and O'Brien, S., (2005) Spectroscopic Characterization of the Surface of Iron Oxide Nanocrystals, *Chem. Mater.*, **17**: 5970-5975.

Witkop, B. (1999). Paul Ehrlich and His Magic Bullets- Revisited, *Proc. American Philosophical Soc.*, **143(4)**: 540-557.

Xie, J., Xu, C., Xu, Z., Hou, Y., Young, K.L., Wang, S., Pourmond, N., and Sun, S. (2006). Linking hydrophilic macromolecules to monodisperse magnetite ($Fe_3O_4$) nanoparticles via trichloro-s-triazine, *Chem Mater.*, **18(23)**: 5401-5403.

Xuan, S., Hao, L., Jiang, W., Gong, X., Hu, Y., and Chen, Z. (2007). A facile method to fabricate carbon-encapsulated $Fe_3O_4$ core/shell composites *Nanotechnology*, **18**: 035602-035608.

Yatvin, M. B., Weinstein, J.N., Dennis, W.H., and Blumenthal, R. (1978). Design of liposomes for enhanced local release of drugs by hyperthermia, *Science*, **202**: 1290-1293.

Yatvin, M. B., Kreutz, W., Horwitz, B. A., and Shinitzky, M. (1980). pH-Sensitive Liposomes: Possible Clinical Implications. *Science*, 210: 1253–1255.

Zhang, Y., Chan, H.F., and Leong, K.W. (2013). Advanced materials and processing for drug delivery: The past and the future, *Adv. Drug Delivery Rev.*, **65**: 104-120.

Zhao, G., Feng, J. J. Zhang, Q. L. Li, S. P. and Chen, H. Y. (2005). Synthesis and Characterization of Prussian Blue Modified Magnetite Nanoparticles and Its Application to the Electrocatalytic Reduction of $H_2O_2$, *Chem. Mater.*, **17**: 3154-3159.

Zheng, J., Liu, Z.Q., Zhao, X.S., Liu, M., Liu, X., and Chu, W. (2012). One-step solvothermal synthesis of $Fe_3O_4$@C core–shell nanoparticles with tunable sizes, *Nanotechnology,* **23**: 165601-165608.

Zimmermann, U., Pilwat, G., and Esser, B. (1978). The Effect of Encapsulation in Red Blood Cells on the Distribution of Methotrexate in Mice, *J. Clin. Chem. Clin. Biochem.* **16**: 135-144.

# CHAPTER 3

## Materials, Equipment and Methodologies

### 3.1 Materials

**Table 3.1** List of chemicals

| Experiment | Substances | Source |
|---|---|---|
| Microemulsion | n- Hexane | Sigma Aldrich |
| | Cyclohexane | Sigma Aldrich |
| | Toluene | Sigma Aldrich |
| | Methyl Acetate | Sigma Aldrich |
| | Ethyl Oleate | Sigma Aldrich |
| | SPAN 20 | Sigma Aldrich |
| | TWEEN 80 | Sigma Aldrich |
| | Insulin | Sigma Aldrich |
| | Sucrose | Sigma Aldrich |
| | 1-Butanol | Sigma Aldrich |
| | Iron (II) Sulphate Heptahydrate | Alfa Aesar |
| | Iron (III) Chloride Hexahydrate | Alfa Aesar |
| | Ammonium hydroxide | Sigma Aldrich |
| | Oleic Acid | Sigma Aldrich |
| | Ethanol | Sigma Aldrich |
| | Hydrochloric Acid | Sigma Aldrich |
| DLS | Toluene | Sigma Aldrich |
| TEM | Chloroform | Sigma Aldrich |
| SEM | Ethanol | Sigma Aldrich |
| DSC | n-Octadecane | Sigma Aldrich |
| | Indium | Sigma Aldrich |
| Dissolution Test | Paracetamol | Sigma Aldrich |
| | Sodium Cholate | Sigma Aldrich |
| | Sodium Taurocholate | Sigma Aldrich |
| | Sodium dihydrogen phosphate | Sigma Aldrich |
| | Sodium Chloride | Sigma Aldrich |
| | Sodium Hydroxide (pellets) | Sigma Aldrich |
| | Hydrochloric Acid | Sigma Aldrich |
| UV & FTIR | Acetone | Sigma Aldrich |
| HPLC | Sodium dihydrogen phosphate | Sigma Aldrich |
| | Acetonitrile | Sigma Aldrich |
| | Orthophosphoric Acid | Sigma Aldrich |
| | C18 (2) column | Phenomenex |

## 3.2 Equipment and methodology

### 3.2.1 Introduction

The term microscope derives from Ancient Greek language: small (*mikros*) and to look or see (*scopein*). It has been around for several centuries. The first microscope invented was the optical or light microscope. It uses visible light (located at the bottom of the instrument) which is passed through the object. Glass lenses are used to focus the light that is passed through the platform (sample stage) where the object is placed on a glass slide covered with a glass cover. The image of the object is observed through the eyepiece or ocular of the microscope. Since the optical microscope uses visible light, what is observed is dependent on the wavelength of the light. This limits the range and clarity of the images especially at high magnification when an object is observed under an optical microscope. For practical purposes, the diffraction limit means that the smallest objects that can be observed are about 0.5-1 µm. This prompted the introduction of the electron microscope in 1931 by Max Knoll and Ernst Ruska (www.nobelprize.org/nobel_prizes/physics/laureates/1986/ruska-bio.html).

### 3.2.1.1 Transmission electron microscope, TEM

In TEM (Figure 3.1), the same principle as in an optical microscope is applied but it uses electrons instead of light. As the name implies, electrons are transmitted through the sample materials, usually nanomaterials, or thin films. TEM provides information on the morphology and size of the samples investigated. An electron source, located on top of the instrument, emits electrons. The electrons then travel through evacuated chambers. The electrons in the chambers are focussed by using electromagnetic lenses thus creating a beam that accelerates further down through the object. After passing through the object, the unscattered (or transmitted) electrons hit the fluorescent screen at the bottom of the instrument and produce the desired image. The lower wavelength of electrons compared with visible light allows better resolution than with an optical microscope, and especially at higher

magnification, allowing objects to be imaged down to the nanoscale and in the best HR TEM instruments right down to atomic resolution.
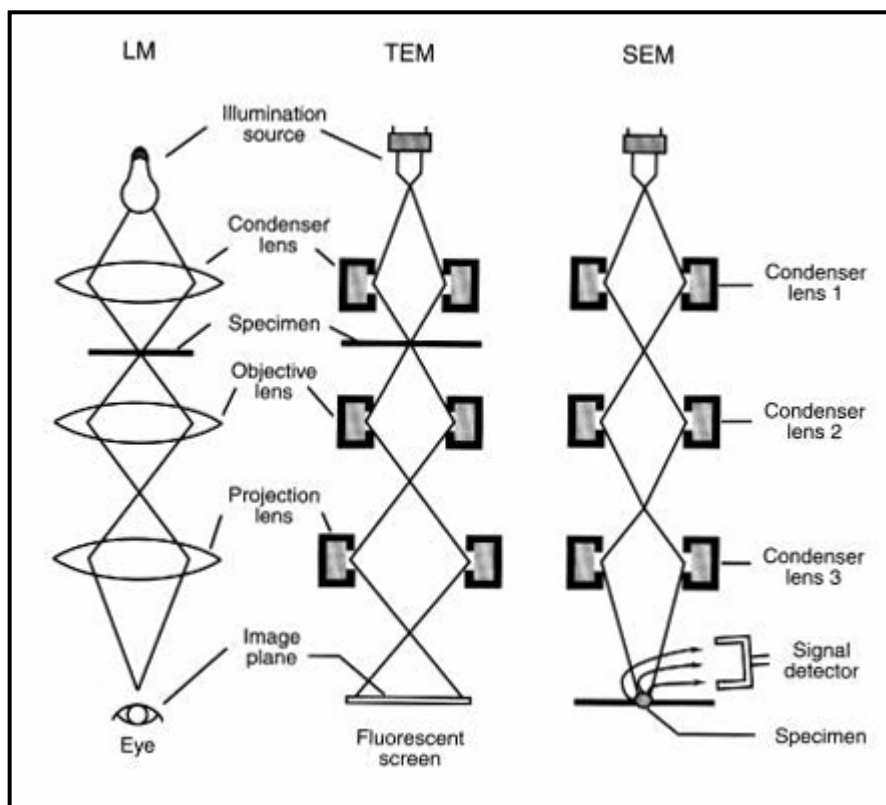


**Figure 3.1** Comparison of light microscope, LM, transmission, TEM and scanning electron microscope, SEM (http://cmrf.research.uiowa.edu/transmission-electron-microscopy)

In this work, samples containing IONs in chloroform are dropped carefully onto a circular cooper grid. The grid is then placed onto a sample holder and inserted into the electron beam, between the condenser and apertures, through a vacuum seal. The samples then interact with electrons and the images appear on a fluorescent screen. The images are captured with a digital camera. The morphology and size of the synthesized particles were observed using transmission electron microscope (TEM, Jeol-JEM 2000EX).

### 3.2.1.2 Scanning electron microscope, SEM

The invention of the scanning electron microscope, SEM soon followed after the invention of TEM. As the name implies, SEM uses an electron beam to scan the surface of the samples. It uses a focused beam of electrons to generate a variety of signals at the surface of solid samples. The signals that derive from electron-sample interactions, provides information on the samples surface morphology. Electrons impacting onto a material result in a number of interactions with the atoms of the target sample. Accelerated electrons can pass through the sample without interaction, undergo elastic scattering and can be in elastically scattered as shown in Figure 3.2.
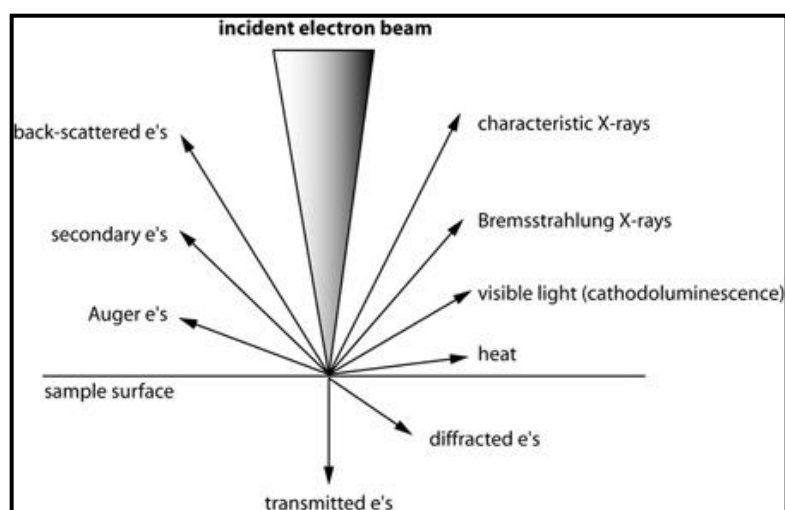


**Figure 3.2** When the incident energy of the electron beam collide with a sample, a variety of electrons (auger, secondary and back-scattered), X-rays (characteristic and Bremsstrahlung), light (cathodoluminescence) and heat (phonons) are emitted. (http://serc.carleton.edu/research_education/geochemsheets)

In SEM, back scattered electrons, secondary electrons, characteristic X-ray and chathodoluminescence produced after collision with the samples are used for the imaging of samples to get its surface morphology and 3D-impression. In most applications, data are collected over a selected area of the surface of the sample with areas in micro-scale, approximately 1 cm to 5 microns, in width. Unlike TEM, atomic scale imaging cannot be done using SEM, due to their lower magnification. The resolution of SEM is 0.4 nanomaters while TEM is 0.05 nanometers.

In this work, all the samples, after being properly cleaned, rinsed, dehydrated, and dried were coated with gold (thickness of 15nm) by a Polaran SC7640 sputter gold coater (Quorum Technologies) at an accelerating voltage of 2.2 kV prior to imaging. Care was taken by using disposable gloves and tweezers to prevent unwanted deposits. The sample was sprinkled on a carbon tape mounted on an aluminium SEM stub. After coating, the sample specimens were imaged in the high vacuum sample chamber equipped with electron optic column and electronics console. The SEM instrument employed was a JEOL JSM - 5900LV Scanning Electron Microscope (JEOL Ltd, Japan) fitted with a Tungsten filament.

### 3.2.2 DLS particle size analyzer

Dynamic Light Scattering (sometimes referred to as Photon Correlation Spectroscopy) is one of the most popular methods for measuring the size of particles. It is about the measurement made from particles suspended within a liquid. When a light (usually a laser) is passed through the liquid placed in a sample cell, it is scattered in all directions (Figure 3.3) (Hiemenz, 1986). This is known as Rayleigh scattering. The scattered light is measured by a detector.
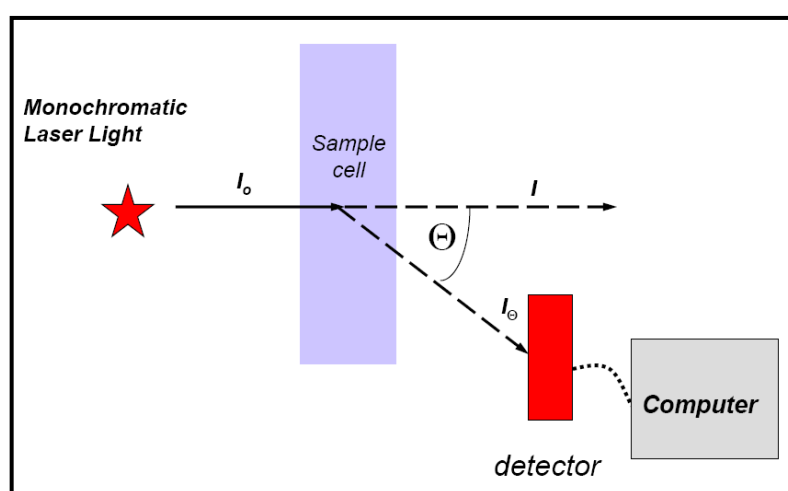


**Figure 3.3** A schematic illustration of DLS setup

When the light is scattered in all directions from many different particles, some waves are bound to cancel each other and some may constructively interfere with each other. This phenomenon is called destructive and constructive interference as shown

in Figure 3.4A and B, respectively. If the interference is a destructive one, the net intensity detected is reduced (Figure 3.4A). If they interfere constructively, the intensity is enhanced.
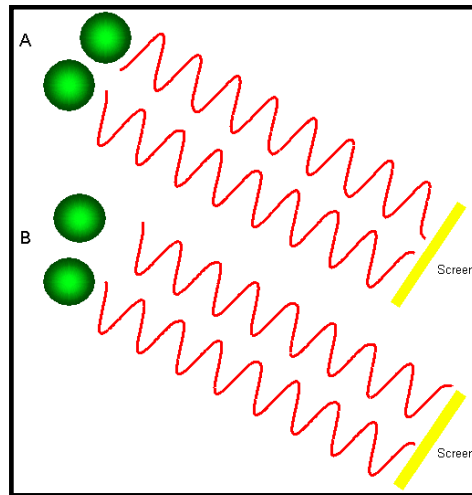


**Figure 3.4** Illustration of (A) destructive and (B) constructive interference resulting in the variation of the intensity detected (http://www3.nd.edu/~rroeder/ame60647/slides/dls.pdf).

The intensity of the scattered light by a single small particle is expressed as a ratio i.e. $I/I_o$, where I is the intensity of scattered light and $I_o$ is the intensity of the incident light. This ratio is called the Rayleigh ratio, $R_\theta$ is given by:

$$R_\theta = \frac{I}{I_o} = \frac{1 + \cos^2\theta}{2R^2} \left[ \left(\frac{2\pi}{\lambda}\right)^4 \left(\frac{n^2 - 1}{n^2 + 2}\right)^2 \left(\frac{d}{2}\right)^6 \right] \qquad [1]$$

where,

λ = wavelength of the light.

R = distance to the particle

n = refractive index of the medium

d = diameter of the particle

The Rayleigh approximation shows that the intensity of the scattered light varies directly with the sixth power of d and inversely with the fourth power of λ. What this

means is that in a mixture with large differences in particle size, the contribution of the smaller size to the total light scattered is very small. This makes it difficult for DLS to perform accurate measurement in polydisperse samples. Also a higher scattering intensity is observed when the wavelength of the light is reduced.

The correlation function, $G(\tau)$ of the scattered intensity is the exponential decaying function of the correlator time delay $\tau$. The equation is given below;

$$G_{(\tau)}) = \; < I(t).I(t+\tau) > \qquad [2]$$

where $\tau$ is the time difference of the correlator. For monodisperse and polydisperse samples, $G(\tau)$ is expressed as Equation 3 and 4, respectively

$$G_{(\tau)} = \; A\,[1 + B\;\exp[-2D\,(\frac{4\pi n}{\lambda_o}\sin\,(\frac{\theta}{2})^2\tau)] \qquad [3]$$

$$G_{(\tau)} = \; A\,[1 + B\,g_1(\tau)^2] \qquad [4]$$

where,

A = the baseline of the correlation function

B = intercept of the correlation function

D = translational diffusion coefficient which is the velocity of Brownian motion

$g_1(\tau)$ = the sum of all the exponential decays contained in the correlation function

n = refractive index of dispersant

$\lambda_o$ = wavelength of the laser

$\theta$ = scattering angle

Therefore, the size of the particle is obtained from the translational diffusion coefficient, D from the correlation function Equation 3 by using the Stokes-Einstein

equation. Assuming spherical particles, the translational diffusion coefficient is shown as;

$$D = \frac{k_b T}{3\pi\eta d}$$ [5]

where,

$K_b$ = Boltzmann constant

T = Temperature

ŋ = viscosity

d = hydrodynamic diameter of the particle

The size distribution obtained is a plot of the relative intensity of light scattered by particles in various size classes. It is often represented in terms of number, volume and intensity percent as shown in Figure 3.5.
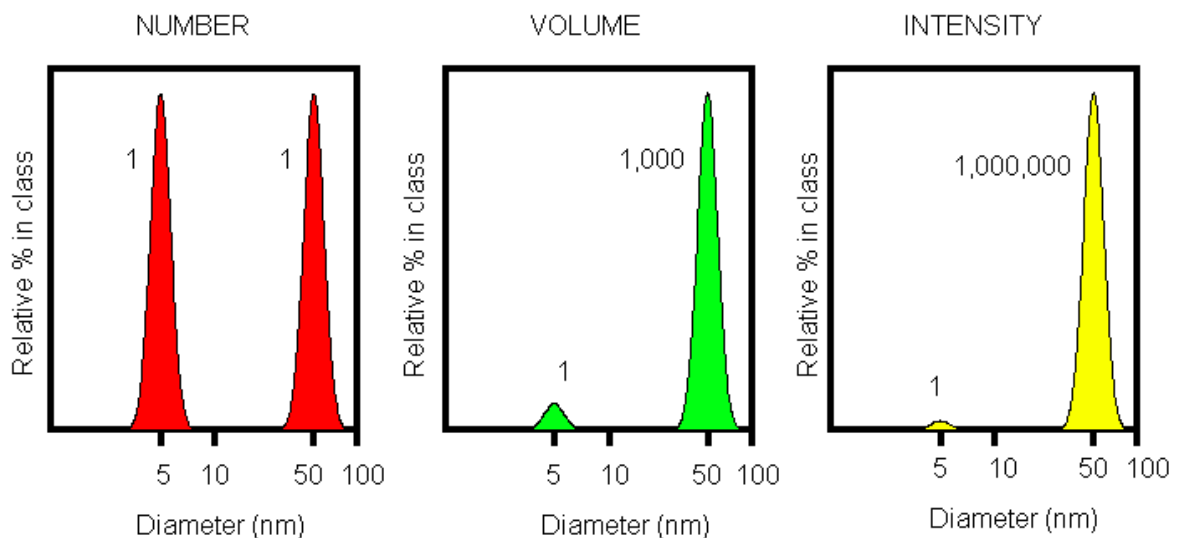


**Figure 3.5** Illustration of the number, volume and intensity distributions of a mixture of two different particle sizes present in equal numbers (http://www.nbtc.cornell.edu)

In this work, the nanoparticle size distributions were measured using the supplied software Particle Size Analyzer (ZETA-SIZER, MALVERN Nano-ZS90) with HeNe 5 mW laser at 173°. The nanoparticles were dispersed in toluene and filled into a

cuvette. The cuvette was placed into the holder and illuminate by a laser beam. The scattered light was measured by a detector.

### 3.2.3 X-ray powder diffraction

When William Conrad Rontgen first discovered x-rays, nothing was known about their exact nature (1895). It was initially thought that they would exhibit wave-like nature. It wasn't until 1912, Friedrich and co-workers performed the first diffraction experiment using a copper sulphate single crystal. They obtained a diffraction pattern and concluded that x-rays must be electromagnetic radiation.

Bragg diffraction was first proposed by William Lawrence Bragg (1912) when they discovered the principle of constructive interference of X-rays which have been scattered from a set of parallel lattice planes. Figure 3.6 shows X-rays are diffracted by the crystal planes an angle (glancing angle) twice the angle of incidence, θ.
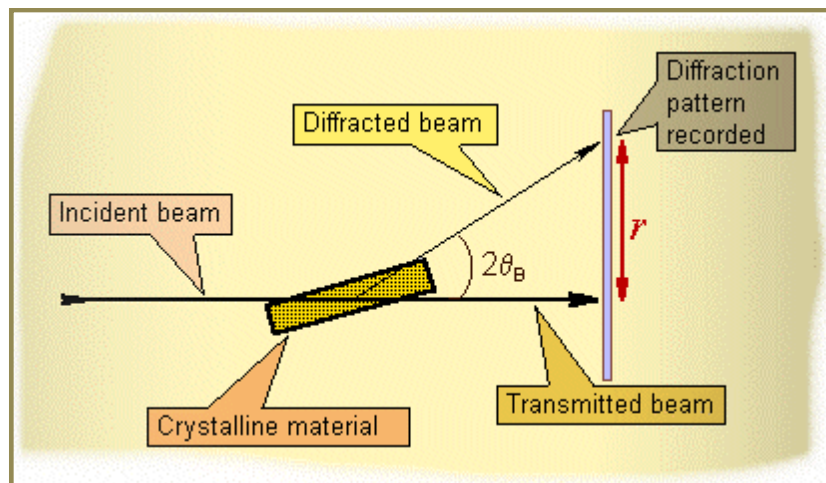


**Figure 3.6** X-ray are diffracted by a crystal lattice at an angle (glancing angle) twice the angle of incidence, θ.

Consider an incoming X-ray beam will be scattered by lattice point A as shown in Figure 3.7a.
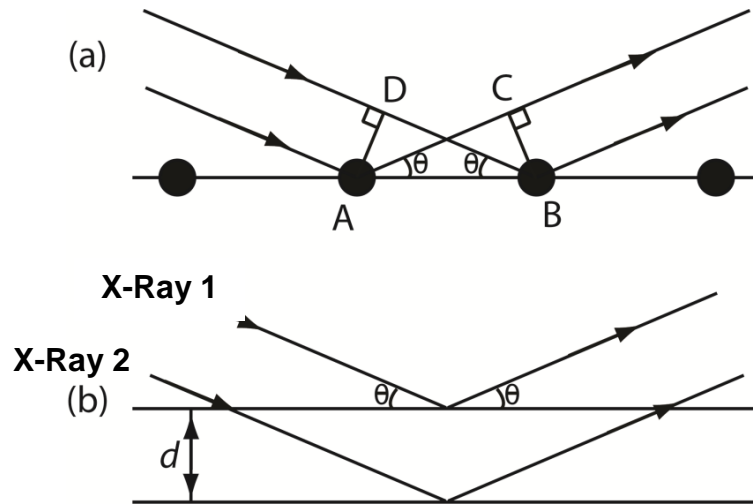


**Figure 3.7** X-ray diffraction by a crystal lattice. (a) An incoming X-ray will be scattered by lattice point A at an angle twice the glancing angle ($\theta$). (b) Multiple lattice planes with spacing d will scatter incoming X-rays by an angle $\theta$ according to Bragg's Law (Equation 1).

Constructive interference occurs between waves at points A and B if the distances AC and DB are equal. Successive planes also scatter in phase (Fig 3.7b) on the condition that the path difference is an integral number of wavelengths, i.e. obeys the equation:

$$n\lambda = 2d\sin\theta \qquad\qquad [1]$$

which is the Bragg's Law, where d is the spacing of the planes, $\theta$ is angle, $\lambda$ is the wavelength of the scattered X-ray and n is an integer. Diffraction from any set of lattice planes can only occur at the angles predicted by Bragg's law. The peaks (referred to as reflections) observed in diffraction patterns are labelled using Miller indices (h k l). As a way of illustration Figure 3.8 shows the shaded region of Miller indices.
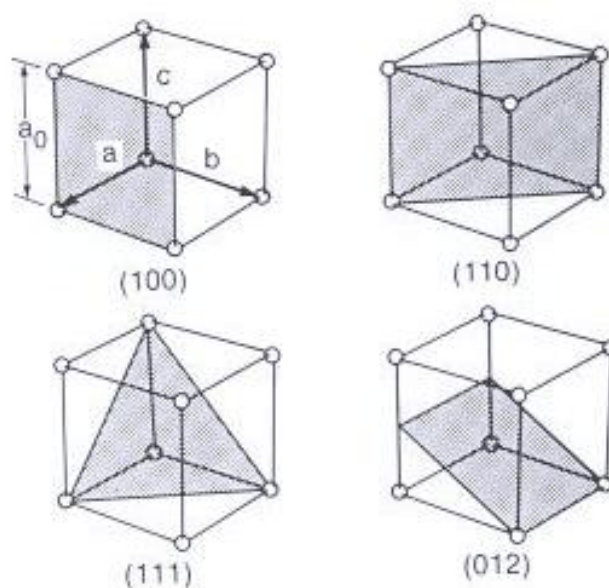
**Figure 3.8** Several atomic planes shown by the shaded region in a simple cubic crystal

In this work, the IONs were analyzed for phase composition using a XRPD, Thermo ARL Xtra model (Switzerland) using using Cu-Kα radiation ($\lambda = 1.540562$ Å). The samples were pressed into a sample holder to generate a flat and smooth plane surface. The samples were then exposed to an X-ray beam with voltage of 45 kV and a current 40 mA. All XRPD experiments were performed at step scan of $0.01^\circ$ and 1 second for every step.

## 3.2.4 UV-visible spectroscopy

Figure 3.9 shows the full electromagnetic spectrum. However, our eyes can only see the visible light. Passing visible light through a prism, a typical rainbow is observed namely VIBGYOR (violet, indigo, blue, green, yellow, orange, red) which consists of seven different colours. Each colour has a different wavelength ranging from 400-800 nm.
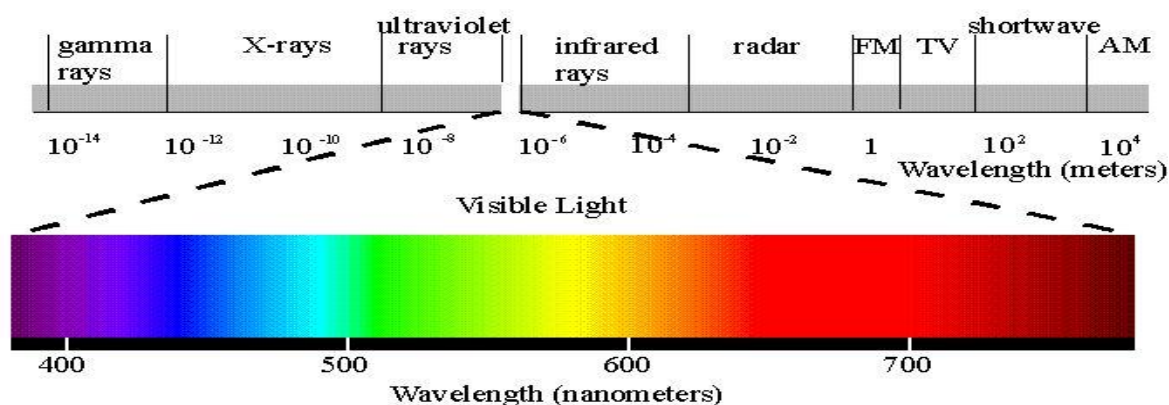
**Figure 3.9** The electromagnetic spectrum of light

The UV region ranges from 190 to 400 nm. The UV-visible spectrometer is the equipment that is used to measure the absorption of UV or visible light. The absorption of light in the UV-visible region, depending on the amount of energy, can cause the excitation of electrons from lower to higher energy levels within molecular orbitals. The shape of the spectrum depends on the properties of the molecule.

UV-visible spectroscopy is also use to determine the concentration of substances by using the Beer-Lambert law. According to the law, the absorbance is proportional to the concentration of the substance in solution and is expressed in the form of the following equation:

$$A = \varepsilon cl \qquad\qquad [5]$$

where,

A = absorbance
l = optical path length, i.e. dimension of the cell or cuvette
c = concentration of solution
$\varepsilon$ = molar extinction, which is constant for a particular substance at a particular wavelength

From the equation, a calibration curve of absorbance versus concentration is plotted and the concentration of an unknown substance can be determined by measuring its absorbance. Nowadays, this technique is widely used for dissolution testing of tablets and capsules in the pharmaceutical industry. It was used for this purpose in Chapter 7.

In this work, the drug used in the dissolution studies was paracetamol. In order to quantify the drug content in a medium sample, each sample was scanned at a wavelength of 243 nm. Prior to quantifying the drug content, calibration curves were constructed by using standard solutions of drug in the corresponding medium or buffer. The drug was weighed accurately in a weighing boat then transferred into a dry volumetric flask. Then the solution was made up to the desired volume. Once the drug solution (stock solution) was prepared, 1, 2, 3, 4, 5 ml aliquots of the stock solution were transferred into separate 10 ml volumetric flasks for dilution. A further amount of medium was added to each volumetric flask to obtain a series of 10 ml solutions for the calibration.

The series of solutions were analyzed with a Perkin-Elmer Lambda XLS UV/VIS spectrophotometer (USA). The average absorbance readings were plotted against the respective drug concentrations to get a calibration line. Each point in the calibration line was an average value of three measurements as shown in Appendix B.

### 3.2.5 FTIR spectroscopy

Fourier Transform Infrared spectroscopy, FTIR is the IR spectroscopy of choice. Just as in many spectroscopy techniques, IR radiation is used to pass through a sample. Some of the IR radiation is absorbed by the sample and some may just transmit. The pattern of absorption and transmission results in a spectrum and creates a molecular fingerprint of the sample. As the name implies, no two compounds produce the exact same IR spectrum.

IR radiation is another form of radiation found in the electromagnetic spectrum with a wide range of 13,000 to 10 $cm^{-1}$, or wavelengths from 0.78 to 1000 μm. It is further divided into three smaller areas; near, mid and far IR. The most frequently used in much experimentation is the mid IR ranging from 4000 to 400 $cm^{-1}$. The main objective of IR spectroscopic analysis is to determine the functional groups in the sample

In a molecule the total energy is the sum of the contributing energies due to the movement or motion of bonds in the molecule i.e.,

$$Energy_{total} = E_{elec} + E_{vib} + E_{rot} + E_{trans} \qquad [6]$$

Theoretically, all atoms in the molecule are in continuous vibration. The major types of molecular vibrations are stretching and bending as shown in Figure 3.10 for the $CH_2$ group (Silverstein *et al.*, 1981). These stretching and bending motions, together with rotational motions lead to the absorption peaks observed in the spectrum. An example of these absorption peaks together with their respective wavenumber is shown in Figure 3.11 (Lu *et al.*, 2012).
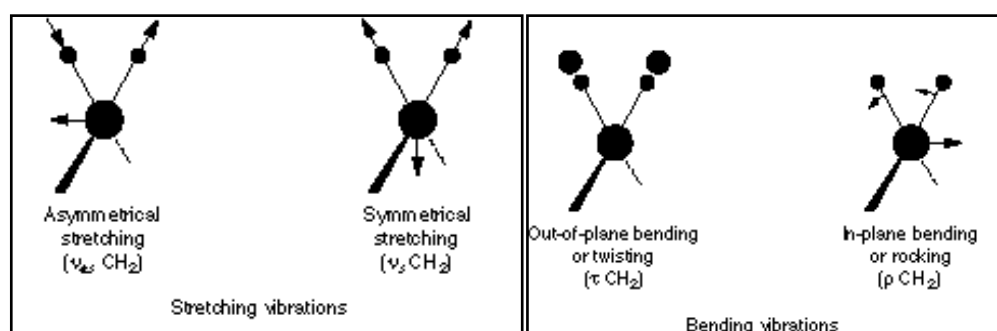


**Figure 3.10** The vibrational modes for a nonlinear group, $CH_2$ (Silverstein *et al.*, 1981).
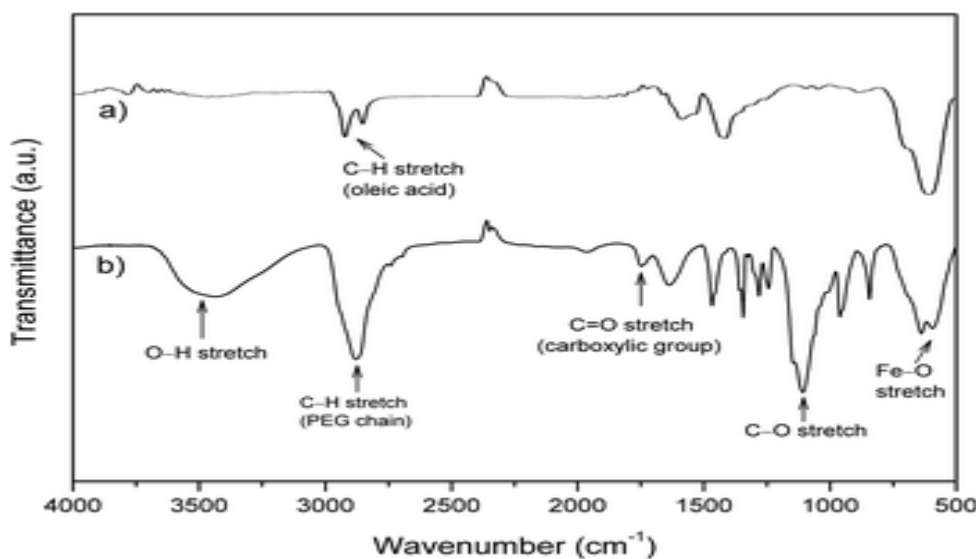
**Figure 3.11** FT-IR spectra of 6 nm (a) oleic-acid-capped $Fe_3O_4$ nanoparticles, and (b) carboxyl–PEG–phosphoric-acid-stabilized $Fe_3O_4$ nanoparticle (Lu *et al.*, 2012).

In this work, the measurement was carried out on a Fourier transform infrared spectrometer (BRUKER IFS 66/S) in the range 4000-500 cm$^{-1}$ (wavenumber), with 16 scans at a resolution of 2 cm$^{-1}$. The samples of the synthesised magnetic nanoparticle were dried *in vacuo* and analysed as a solid powder. Acetone was used to clean the crystal area of the ATR plate. The powdered samples were then placed directly onto the ATR crystal.

### 3.2.6 Superconducting quantum interference device, SQUID

Magnetic nanoparticles are nanoparticles that exhibit magnetic properties just like in any magnet, such as the magnetic flux which flows through space. A SQUID is the most sensitive magnetometer for detecting the magnetic flux. The device has been used to detect weak magnetic field, current, voltage, and magnetic susceptibility. It consists of a loop of superconductor with one or more Josephson junctions, called weak links. British physicist Brian David Josephson, now a retired professor at the University of Cambridge, discovered the Josephson effect, invented the Josephson junction, and SQUID in 1962. He was later awarded the 1973 Nobel Prize for his discovery. Josephson junctions are barriers between two superconductors where electric current (known as Josephson current) can flow through them.

From the SQUID instrument, magnetic curves (such as in Figure 3.12) are generated and important parameters and properties can be extracted such as the coercivity, remanence, saturation magnetization and the type of magnetic material can be further classified.
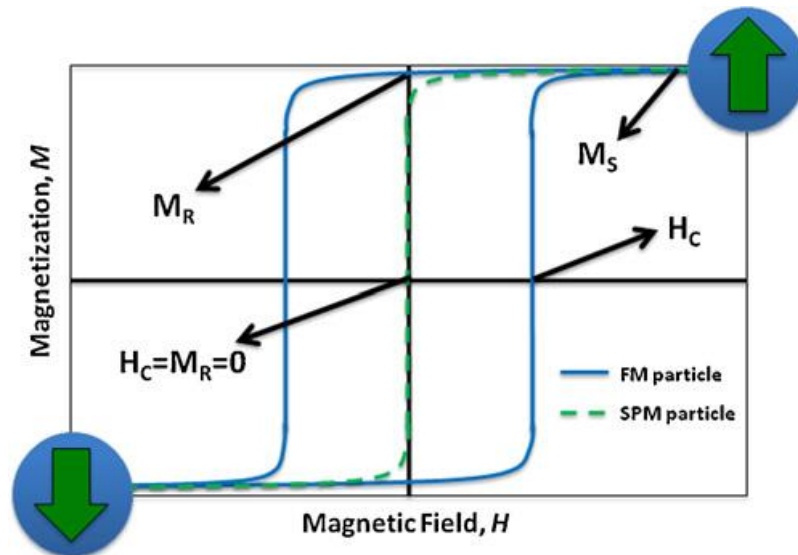


**Figure 3.12** Hypothetical magnetization versus magnetic field curve for superparamagnetic (SPM) and ferro- or ferromagnetic nanoparticles (FM) where the coercive field ($H_C$), the saturation magnetization ($M_S$) and the remanent magnetization ($M_R$) parameters are indicated (Figuerola *et al.*, 2010).

Upon application of a magnetic field to a ferromagnetic material, the resulting curve is well described by a hysteresis loop (shown as blue lines in Figure 3.12). This loop is characterised by three distinct parameters: coercivity, remanence magnetisation and saturation magnetisation. The first parameter i.e. coercivity, Hc is related to the area or thickness of the curve. In fine particles such as nanomaterials, the coercivity is the property of most interest. It has been found that as the particle size is reduced, the coercivity increases to a maximum and then decreases toward zero as shown in Figure 3.13 (Akbarzadeh *et al.*, 2012). When the coercivity becomes zero such particles become superparamagnetic and have no hysteresis.
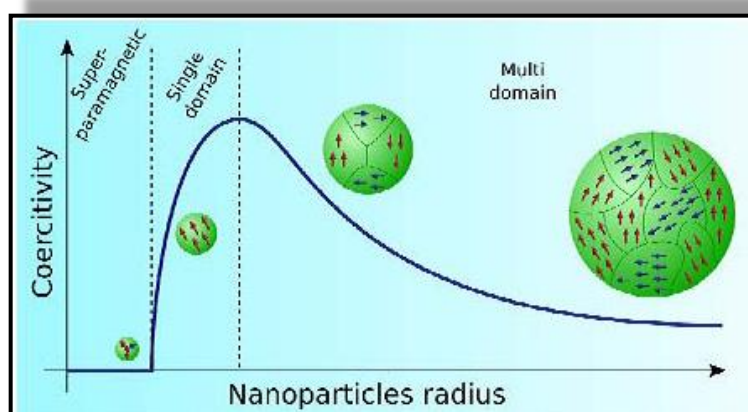
**Figure 3.13** Schematic repsentation of the coercivity-size relations of small particles (Akbarzadeh *et al.*, 2012).

The second parameter is the remanent magnetization, $M_R$, which indicates the magnetisation at zero applied field. The third is the saturation magnetization, $M_S$, which is the maximum value of magnetization that the material can reach under the effect of sufficiently high magnetic fields. For a super paramagnetic material, $H_c$ and $M_R$ is equal to zero.

In this work, magnetisation data was taken using a Quantum Design MPMS SQUID VSM Magnetometer (San Diego, USA) at 300 K using a field range of ±7 T. The equipment is located at University College of London. The samples of the synthesised magnetic nanoparticle were dried *in vacuo* and analysed as a solid powder.

### 3.2.7 Differential Scanning Calorimetry, DSC

The law of conservation of energy states that energy can neither be created nor destroyed, but can be transferred into different forms. One of the forms is heat, q. Thermodynamics is the subject that deals with thermal transfer of energy. If heat is absorbed, the process is called endothermic. If heat is released, it is called exothermic.

DSC is a reliable method for measuring the above as well as the thermal transitions and other thermodynamics properties of materials. In DSC the material is subjected

to continuous heating and at some points its phase changes. A classic example is ice. Upon heating, it melts at a transition temperature of $0^o$C and further heating, it vaporized at a transition temperature of $100^o$C. These two transition temperatures are called the melting and boiling point, respectively. Melting point is often measured using a simple melting point apparatus. However, the value is not precise and difficult to reproduce. By using DSC, the melting points are obtained from a calibrated and highly precise system. In addition, it also provides more information about the sample. Besides the changes in the transition temperature, it should also be noted that changes in the phases also occur from solid to liquid to gaseous phase. Data from DSC also allows other thermodynamic properties such as the latent heat, heat capacity, heat of transitions, heat of polymerization etc to be elucidated. The data from DSC, the heat flow, ($\Delta q/\Delta t$) is plotted against temperature, T.

Figure 3.14 shows typical transitions and phase changes when an amorphous material is subjected to continuous heating. The material undergoes a glass transition, followed by crystallization, melting and finally at higher temperature, it may undergo oxidation or decomposition
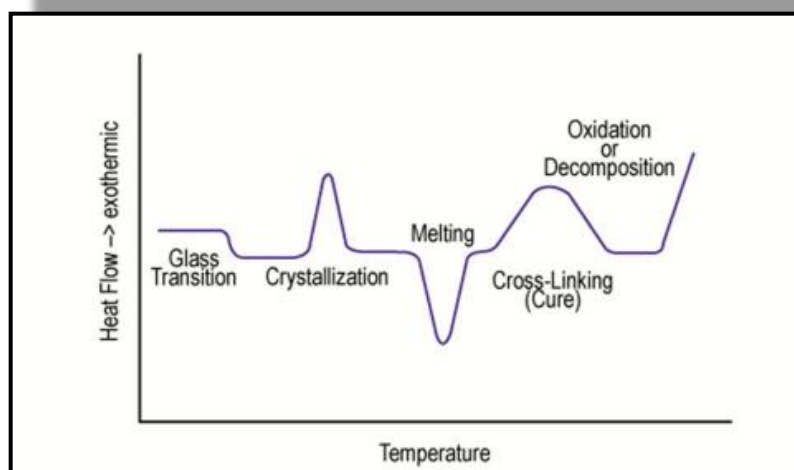


**Figure 3.14** DSC curves when an amorphous material is heated continuously.

Usually in a standard DSC, the temperature of the furnace is raised and lowered in a linear fashion. This has certain issues of overlapping peaks and it is difficult to interpret the data. These issues can be corrected by using a Modulated Temperature

DSC (Gill et al., 1993). Modulated Temperature DSC, MT-DSC is for DSC techniques where a non-linear heating or cooling rate is applied to the sample. This is to separate the kinetic from the thermodynamic data, and therefore removes the kinetic noises and the overlapping of peaks.

In this work, thermograms were recorded with a modulated temperature DSC (Q2000, TA Instrument, Newcaslte USA) at a preselected uniform scan rate of $2^{o}C$ $min^{-1}$, 60 sec for the modulation period and $\pm$ $0.318^{o}C$ for the amplitude (unless otherwise specified).

Samples of the coatings were weighed (1 to 3 mg) into pinhole aluminium pans (Perkin Elmer) to allow the removal of excessive moisture in the sample in order to minimize influence of water content on the sample's properties. Temperature and cell constant calibration of DSC were performed using indium, n-octadecane and tin. The transition temperature was determined as onset temperature by extrapolation to the baseline of the peaks as a function of temperature. The latent heat was determined from the area under the transition peak by comparison with a known standard namely indium.

## 3.2.8 Thermogravimetric Analysis, TGA

Thermogravimetric Analysis (TGA) measures the changes in the sample weight of a material caused by the chemical or physical processes as a function of temperature or time in a controlled atmosphere. Measurements are used primarily to determine the composition of materials and to predict their thermal stability at temperatures up to 1000°C. The technique can characterize materials that exhibit weight loss or gain due to decomposition, oxidation, or dehydration.

In this work, samples were heated from room temperature up to $100^{o}C$ at heating rate of $10^{o}C$ per minute and held isothermally for at least 15 minutes before continuing the heating ramp up to $700^{o}C$. The instrument used was a TGA Q5000 (TA Instruments, Newcastle, USA).

### 3.2.9 Hyperthermia studies

### 3.2.9.1 Magnetherm system

Figure 3.15 shows the schematic representation of the set up for hyperthermia studies (www.nanotherics.com).
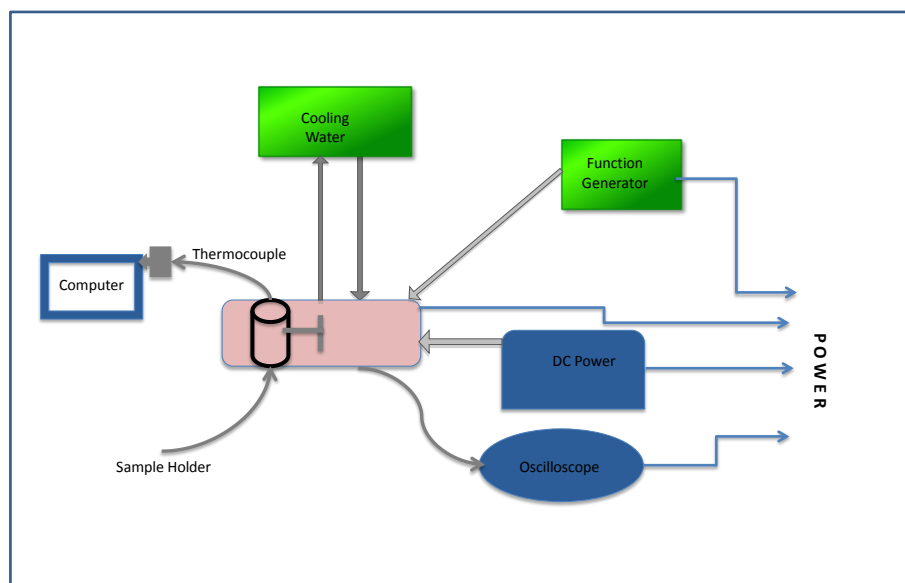


**Figure 3.15** Schematic representation of hyperthermia system setup (www.nanotherics.com)

The Magnetherm is a device used to measure the heating effects of magnetic nanoparticles for hyperthermia applications. It is portable and only requires a water bath for cooling purposes. This device also offers a wide range of heating frequencies. Five different capacitor blocks and two coils (lengths 3 and 5 cm) provide for 10 different frequency options ranging from 100 – 1000 kHz. The frequencies are nominally: 110 (25), 168 (17), 176 (23), 262 (23), 335 (17), 474 (11), 523 (20), 633 (9), 739 (16), 987 (12) kHz. The numbers in brackets are the maximum field strength for each frequency and are given in mT. These values are within the accepted literature values for successful hyperthermia and are reported to be safe for humans - in the range 0.1-1 MHz (Atsumi *et al.*, 2007).

The temperature of the setup was maintained at 37$^o$C which is the temperature of human body. This was done in anticipation of the experimentation to be performed mimicking the GI tract later in the thesis.It was observed that when in use there was a general  heating effect resulting from the RF coil. This could be balanced via the cooling effect of a recirculating water bath, the temperature of which was adjusted by trial and error until a stable equilibrium temperature of 37$^o$C was achieved. This was repeated at each different frequency/power setting and the results tabulated for future reference (Table 3.2)

- With the circulating water bath set at 30.5$^o$C and the RF coil on full power (6 scope divisions Vp/p for 164.8 kHz) the resulting steady-state temperature of 37$^o$C was achieved inside the polystyrene insulating chamber after 15 minutes. This was measured using the type T-thermocouple and  meter provided with the instrument (Rapid 328DMM)

- The sample heated to 37$^o$C using a second water bath and measured using a second type T-thermocouple

- When the sample and polystyrene insulating chamber were fully equilibrated to 37$^o$C, the power to the RF coil was turned down to minimum using the Course Voltage knob and the sample quickly transferred and inserted in the insulating chamber. The RF coil power was then adjusted back to the desired power setting.

**Table 3.2** The temperature of the circulating water bath needed to maintain a steady temperature of 37$^o$C at different frequencies.

| Frequency, kHz | Temperature set at circulating wath bath, $^o$C |
|----------------|--------------------------------------------------|
| 109.9 | 20.0 |
| 164.8 | 30.5 |
| 329.6 | 10.0 |
|  |  |
| 173.9 | 35.0 |
| 521.3 | 17.5 |
| 737.5 | 20.0 |

### 3.2.9.1.1 Heating effect of ferrofluid

The experimental setup for this work is shown in Figure 3.16. In this work, the same amounts of IONs with different particle sizes in the ferrofluid were poured into the eppendorf vial. A type T-thermocouple probe is inserted into the vial and the other end of the thermocouple terminal was attached to a computer via the thermocouple input of a 'MyPCLab' AD converter module. This was read using a custom-written LabView data logging routine, which displayed the data in real time and also wrote it to a DAT file for future use. This was imported to Excel for display and data processing.
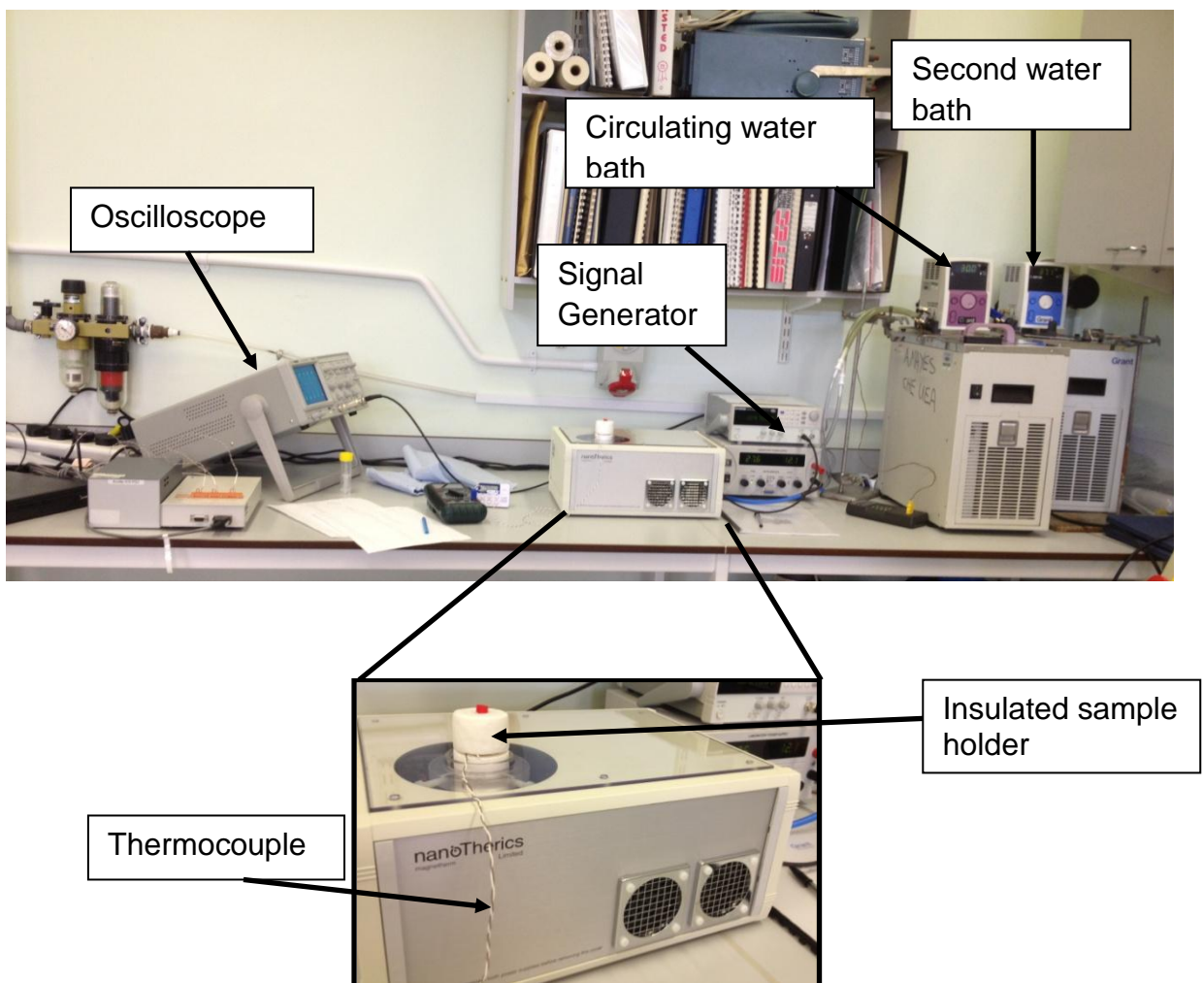


**Figure 3.16** The magnetherm setup for hyperthermia studies.

The eppendorf vial was then inserted into an insulated holder and placed directly into the sample aperture. The sample aperture was 44 mm in diameter. Care was taken to make sure the centre of the sample was located at the center of the coil (where the magnetic flux is highest). The temperature was set at 37$^{o}$C by a circulating water bath. The thermal heating effect, due to the IONs, was monitored for 600 seconds. The experiment was done at 6 different frequencies using 2 different coils.

### 3.2.9.1.2 Heating effect of IONs embedded in coatings

In this work, IONs with a particle size 10 nm were mixed with the coating materials in a beaker. The resulting mixtures were heated slightly above the respective melting point of the coating materials and the molten mixtures were then homogenised using a Ultra-Turrax T8 micro homogeniser with a S8N-5G dispersing tool for 10 min. The homogenised mixtures were placed in a water bath controlled between 40- 45$^{o}$C. To investigate the effect of ION loading, samples of 0.5 ml coating containing IONs at 2, 4, 6, 8 and 10 percent by weight, were filled into eppendorfs vials. The vials are then inserted into the insulated sample holder and the resulting heating effect was monitored as described in 3.1.8.1.

### 3.2.10 Dissolution studies

Dissolution is a process whereby a solid solute enters a solution. Therefore, drug dissolution by definition is the amount of drug that enters the solution under standardized temperature and solvent composition (Qureshi and McGilveray, 1999). It is crucial for the development of drugs and is also an essential tool for quality control. The pioneers in this work were Noyes and Whitney (1897) more than a century ago. The salts used were benzoic acid and lead chloride as the solid solutes. The molten salts were poured into test tubes containing glass rods. From the results, they then proposed a relationship for the dissolution rate of solid solutes i.e.

$$\frac{\partial c}{\partial t} = k(Cs - C) \qquad\qquad [1]$$

where $\partial c/\partial dt$ represents the rate of dissolution, k is a constant, Cs is the equilibrium solubility of the solid and C is the concentration of solid in equilibrium at time t.

Dissolution testing is an official test used by pharmacopeia's for evaluating drug release. It was introduced as a USP method in the 1970s for oral tablets and capsules (Cohen et al., 1990). The basket method (USP apparatus I) became the first official dissolution test in 6 monographs of the USP. This was later followed by the paddle method (apparatus II), the reciprocating cylinder (apparatus III) and the flow-through cell (apparatus IV) in 1978, 1991, and 1995, respectively (Maddineni *et al.*, 2012).

In this work, a model drug, paracetamol, was filled inside hard gelatine capsules. The capsules were then coated with fatty acid (or paraffin) embedded with IONs. The capsules are then subjected to various dissolution media at variable pH values and temperatures. The pH of the dissolution media was prepared at pH 1.2 and 7.4, using 0.1 M HCl and phosphate buffer, respectively. The medium at pH 1.2 represents the acidic conditions in the stomach and phosphate buffer pH 7.4  mimics conditions in the intestine. The temperature of the dissolution bath was set at 37 ± 0.5$^{o}$C at 50 rotations per minute. The dissolution test was performed for 2 h at pH 1.2. After the end of 2 h, the medium was changed to pH 7.4 and the test  continued. At certain intervals throughout the test period, 10 ml of medium was taken out for analysis and replenished with a fresh 10 ml medium. An aliquot of the removed dissolution medium was then used to determine the concentration of the drug. The drug concentration was determined by using a Perkin-Elmer Lambda XLS UV/VIS spectrophotometer (USA) at 243 nm (please refer to section 3.1.4 for the methodology).

Dissolution tests were performed using BP Apparatus I (D8000, Copley Scienfitic Ltd., Nottingham, UK) with the basket method as shown in Figure 3.17. All dissolution tests were carried out in triplicate.
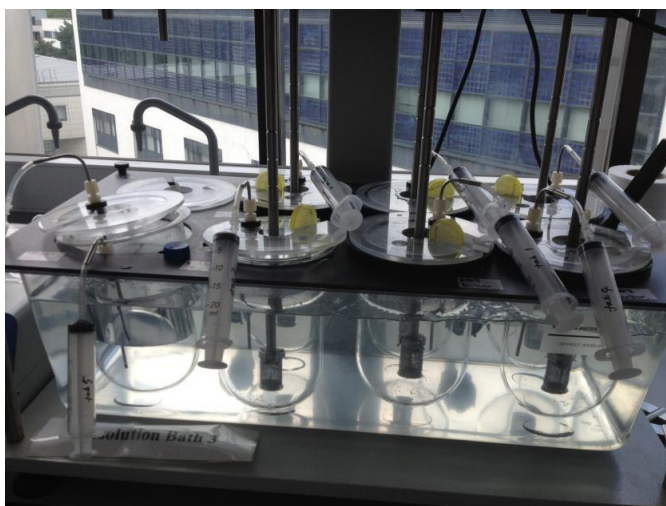
**Figure 3.17** The BP Apparatus I using basket method.

### 3.2.11 High Performance Liquid Chromatography, HPLC

HPLC is a specialised separation technique using the chromatography process in order to separate components in a mixture. Figure 3.18 shows the setup of a basic HPLC system (Bird, 1989). Its components include a solvent(s) reservoir, pump, syringe (injector), injection valve, column, detector and recorder.
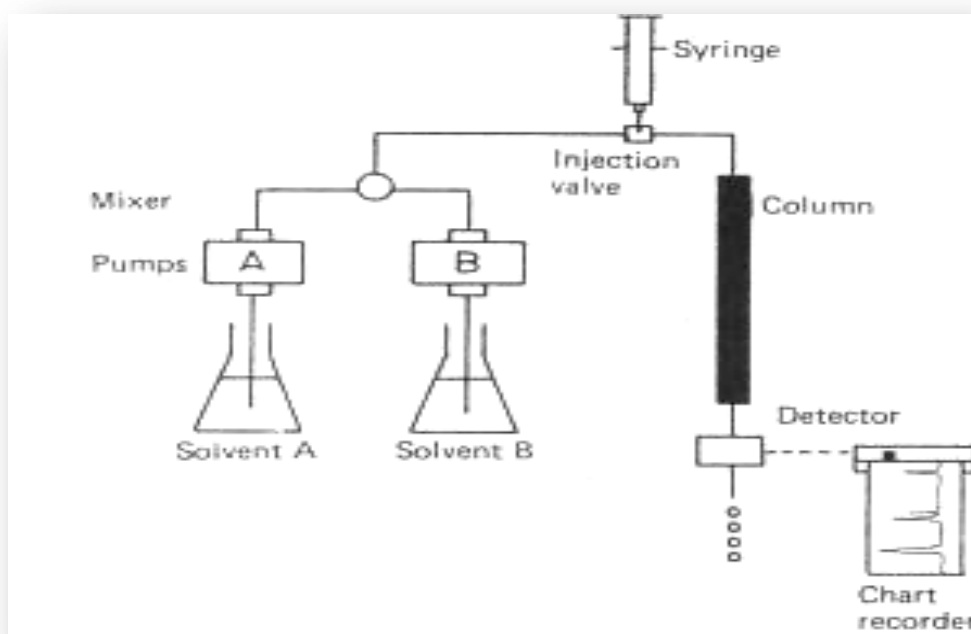


.**Figure 3.18** A typical set up of HPLC system (Bird, 1989).

A liquid solvent(s) or eluent(s) is driven throughout the system by a high pressure pump. The procedure starts by injecting a liquid sample through the sample injection valve. The injected sample flows together with the eluent over a column packed with a solid adsorbent material called the stationary phase. Each substance eluted from the column is then detected by a detector. How well an analyte in the sample is separated depends on the interaction of each of the analytes with the stationary phase and the eluent. If the interaction is weak, the analytes flow off the column in a short amount of retention time. If the interaction is strong, then the retention time is long.

The equipment used was either Beckman System gold (Beckman Coulter, Inc, USA) comprising 507e-autosampler, 126-solvent module, and 168-diode array detector or a Perkin Elmer 200 series comprising autoinjector, quaternary pump and 785 UV detector. In-line solvent degassers were used on both systems.

### 3.2.12 Dip coating of capsules

The experimental setup for the dip coating process is shown in Figure 3.19. In this work, 10 % by weight of IONs were mixed with the coating materials in a beaker.
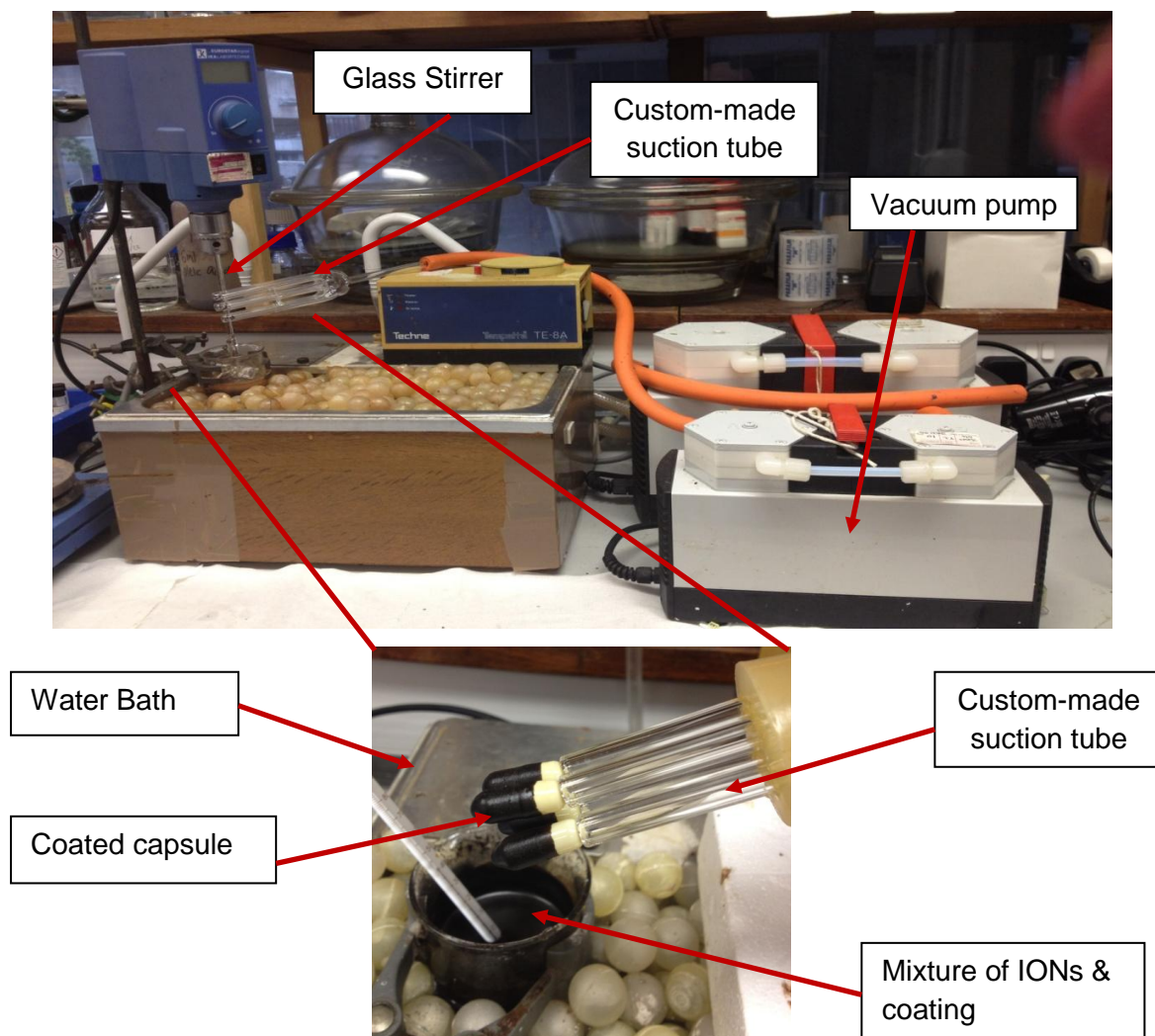
**Figure 3.19** The experimental setup for the dip coating process. (Inset: capsules dipped into the mixture using custom-made suction tube).

The resulting mixtures were heated slightly above the respective melting point of the coating materials and the molten mixtures were then homogenised using a Ultra-Turrax T8 micro homogeniser with a S8N-5G dispersing tool for 10 min. The homogenised mixtures were placed in a water bath controlled between 40- 45°C. Using custom-made suction tubes (see inset of Figure 3.19), the capsules were sucked at the end of the suction tube using a membrane type vacuum pump. The capsules were then dipped layer by layer into the mixtures reversing the capsules to complete coating. The coated capsules were then allowed to harden overnight at room temperature.

From the above results, the thickness of each layer is measured and its amount of IONs is weigh and tabulated in Table 3.3.

**Table 3.3** The thickness of the layers and the amount of IONs for each dipping.

| Layer/Dip | Thickness, mm | | | Amount of IONs, mg | | |
|---|---|---|---|---|---|---|
| | Mixed FA* | Eicosane | Mixed E:D** | Mixed FA* | Eicosane | Mixed E:D** |
| 1 | 0.82 | 1.02 | 0.67 | 8.81 | 8.81 | 9.28 |
| 2 | 1.17 | 1.17 | 1.01 | 10.67 | 10.41 | 13.41 |
| 3 | 1.52 | 1.87 | 1.72 | 16.72 | 16.52 | 17.52 |

*FA = Fatty Acid; **E:D = Eicosane:Docosane

# 3.3 References

http://cmrf.research.uiowa.edu/transmission-electron-microscopy

http://nbtc.cornell.edu

http://serc.carleton.edu/research_education/geochemsheets

http://www3.nd.edu/~rroeder/ame60647/slides/dls.pdf

Akbarzadeh, A., Samiei, M., and Davaran, S. (2012). Magnetic nanoparticles: preparation, physical properties, and applications in biomedicine, *Nanoscale Research Letters*, **7**: 144-157.

Atsumi, T., Jeyadevan, B., Sato, Y. and Tohji, K. (2007). Heating efficiency of magnetite particles exposed to AC magnetic field. *J. Magnetism and Magnetic Materials* **310**: 2841-2843.

Bird, I.M. (1989). High performance liquid chromatography: principles and clinical applications. BMJ, **299(6702)**: 783-787.

Bruner, L., and Tolloczko, S. (1900). Uber die Auflosungsgeschwindigkeit Fester Korper. Zephyrs., *Chem.* **35**: 283-290.

Brunner, E. (1904). Reaktionsgeschwindigkeit in heterogenic systemen., *Z. Phys.Chem.*, **43**: 56-102.

Coey, J.M.D. Magnetism and Magnetic Materials. (Cambridge University Press: 2010).

Cohen, J.L., Hubert, B.B., Leeson, L.J., Rhodes, C.T., Robinson, J.Rr, Roseman, T.J., Shefter, E. (1990). The development of USP dissolution and drug release standards, *Pharm Res.* **7(10)**: 983-987.

Figuerola, A., Corato, R.D., Manna, L., and Pellegrino, T. (2010). From iron oxide nanoparticles towards advanced iron-based inorganic materials designed for biomedical applications, *Pharm. Res.,* **62**: 126-143.

Friedrich, W., Knipping, P., and Laue, M. (1912) *"Interferenz- Erscheinungen bei Röntgenstrahlen (Interference appearances in X-rays)"*, Proceedings of the Bavarian Academy of Sciences (Sber. Bayer. Akad. Wiss.): 303-322; reprinted in: Annalen der Physik **41**: (1913) 971-988.

Gill, P.S., Sauerbrunn, S. R. & Reading, M. 1993. Modulated differential scanning calorimetry. *JThermal Anal,* **40**: 931-939.

Hiemenz, P.C. (1986). Principles of colloid and surface chemistry, 2nd Ed, Ch 5, pp 223-282, Marcel Dekker, Inc., New York.

Hixson, A.W., and Crowell, J.H., (1931). Dependence of reaction velocity upon surface and agitation, *Ind. Eng. Chem.*, **23**: 923-993

Körner, S., Niemz, P., Wienhaus, O., and Henke, R. (1943). Orientierende Untersuchungen zum Nachweis des Klebstoffantiels auf Holzpartikeln mit Hilfe der FTIR-Spektroskopie | [Orientating tests for detecting the glue portion/wood particles ratio by means of FTIR-spectroscopy], *Holz als Roh- und Werkstoff*, **6(1)**: 67-72.

Lu, C, Bhatt, L.R., Jun, H.Y., Park, S.H., and Chai, K.Y. (2012). Carboxyl–polyethylene glycol–phosphoric acid: a ligand for highly stabilized iron oxide nanoparticles, *J. Mater. Chem.*, **22**: 19806-19811.

Maddineni, S., Chandu, B.R., Ravilla, S., and Nama, S. (2012). Dissolution research- A predictive tool for conventional and novel dosage forms, *Asian J Pharm Life Sci.*, **2 (1)**: 119-134.

Nernst, W. (1904). Theories der Reaktionsgeschwindigkeit in heterogenic systemen. *Z. Phys.Chem.*, **47**: 52-55.

Noyes, A.A., and Whitney, W.R. (1897). The rate of solution of solid substances in their own solution, *J. Am. Chem. Soc.*, **19(12)**: 930-934.

Qureshi, S.A. and McGilveray, I. J (1999). Typical variability in drug dissolution testing: study with USP and FDA calibrator tablets and a marketed drug (glibenclamide) product, *European J Pharm Sci*, **7:** 249–258.

Röntgen, W.C. (1895). "*U¨ber eine neue Art von Strahlen Vorla¨ufige Mitteilung*". In: Sitzungsberichte der physikalisch-medicinischen Gesellschaft zu W¨urzburg, Sitzung **30**, 132-141.

Silverstein, R.M., Bassler, G.C. and Morrill, T.C. (1981). Spectrometric Identification of Organic Compounds, 4th edition. New York: John Wiley & Sons.

Warren, B.E. (1990). *X-ray Diffraction*, Dover, Canada.

# CHAPTER 4

## Microemulsions as Template for the Preparation of Poly (alkylcyanoacrylate) Nanocapsules for Drug Delivery System via Microemulsion Polymerisation Method

## 4.1 Introduction

This chapter describes our initial attempt to prepare poly (alkylcyanoacrylate) nanocapsules via microemulsion polymerization. A region of water-in-oil microemulsion stabilised by non-ionic surfactant was identified and used as a template. Monomers were added into the microemulsion template in order to obtain nanocapsules. The prepared nanocapsules were intended for use in the delivery of drugs. In addition, the use of pseudoternary phase diagrams to locate the microemulsion region and the compositions of the template will also be described in this chapter.

## 4.2 Surfactant

Surfactants or surface active substances are a group of compounds with amphiphatic structures that is they contain in one structure, both hydrophilic groups (normally called their heads) and hydrophobic groups (normally called their tails). Compounds with these amphipathic structures are among the most demanded products in the chemical industries such as pharmaceuticals, cosmetics, detergents, paints, dye stuffs, pesticides, fibers and plastics (Rosen, 1978). Figure 4.1 shows a typical surfactant having both hydrophilic head and hydrophobic tail. In industry, surfactants are used either as essential additives or processing aids or in many cases as only a minor part of particular systems or formulations, although can have a dramatic effect on properties.
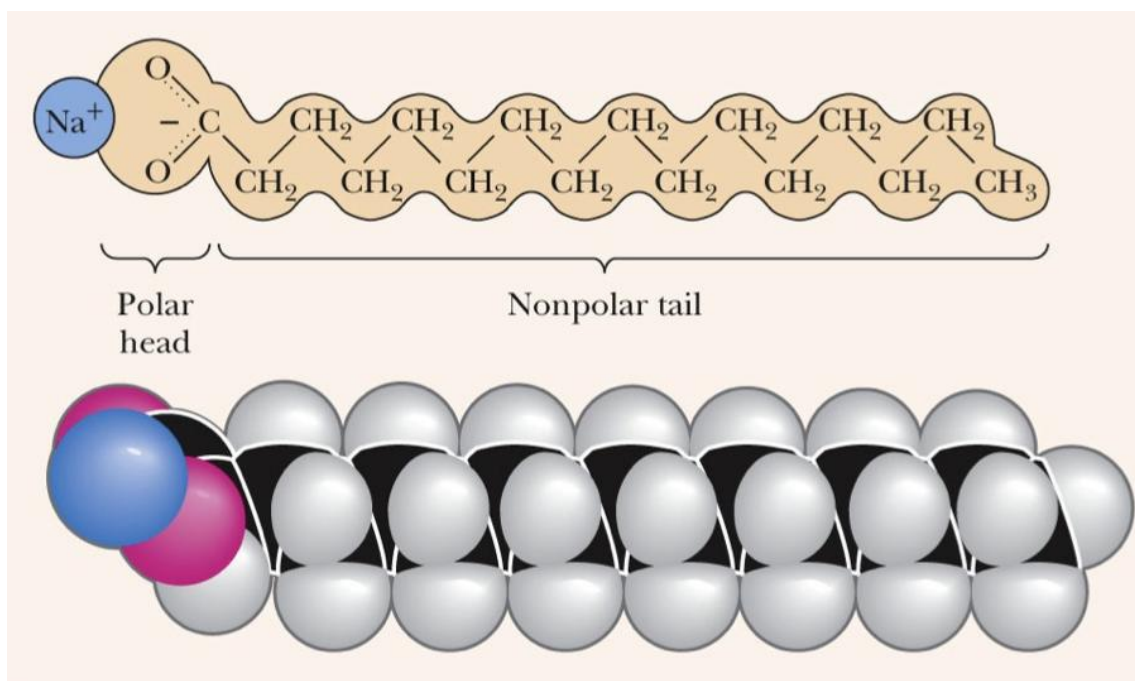
**Figure 4.1.** Structure of a typical surfactant (in this case a sodium palmitate ($Na^{+-}OOC(CH_2)_{14}CH_3$)) (http://oregonstate.edu/instruct/bb350/textmaterials/02/Slide08.jpg)

### 4.2.1 Types of Surfactants

Surfactants are generally categorized, depending on the nature of their polar head group into four types (Kalyanasundaram & Thomas, 1977):

I.   Anionic – a surfactant molecule that can dissociate to yield a surfactant ion whose polar group is negatively charged. Example: Sodium dodecyl sulphate ($C_{12}H_{25}SO_4^-Na^+$)

II.  Cationic – a surfactant molecule that can dissociate to yield a surfactant ion whose polar group is positively charged. Example: Dodecyltrimethylammonium bromide ($C_{12}H_{25}N^+Me_3Br^-$)

III. Nonionic – a surfactant molecule whose polar group is not electrically charged. Example: Dodecylalcohol ethoxylate

IV. Amphoteric – a surfactant molecule for which the ionic character of the polar group depends on solution pH. Example: Sulfobetaines

Mostly, surfactants have crystalline structures and when a solvent, commonly water is added to the surfactant molecule, the crystalline molecules create their own interface by forming monolayers, micelles, vesicles and lyotropic liquid crystal in order to remove a portion of their structure from contact with the solvent (Kalyanasundaram & Thomas, 1977). Surfactant aggregates, on the other hand, can form separate thermodynamic phases such as emulsions or microemulsions.

## 4.2.2 Microemulsion

Microemulsions are colloidal dispersions of either water-in-oil and oil-in-water stabilised by amphiphiles (surfactants). They are transparent, homogenous, and isotropic dispersions. Microemulsions were brought to the attention of the scientific community beginning in the late 1940's by Schulman and a series of collaborators (Hoar & Schulman, 1943; Schulman *et al.*, 1948, 1949). Since then numerous attempts have been made to investigate various aspects of microemulsions from the treatment of microemulsions as colloidal systems (Adamson, 1969; Ahmad *et al.*, 1974) to more theoretical contributions (Reiss, 1975). Recent contributions have been directed towards industrial application, due to its unique properties, including encapsulation and controlled drug delivery, preparation of bactericidal and vaccine formulations (Boman *et al.*, 1996) as well as for the preparation of cosmetics and pharmaceutical products (Bangham, 1995;  Talsania et al., 1997).  Microemulsions have merits over other vehicles or solvents due to their improved stability, solubilisation characteristics and ease in preparation. Microemulsions require only a minimal input of energy for their formation compared to size-reduced kinetically stabilised water-in-oil emulsions.

Figure 4.2 shows a schematic illustration of typical microemulsions. They are categorised into 3 types namely oil-in-water (O/W), bicontinuous and water-in-oil (W/O) (http://www.google.co.uk/imagesTYPESofmicroemulsion).
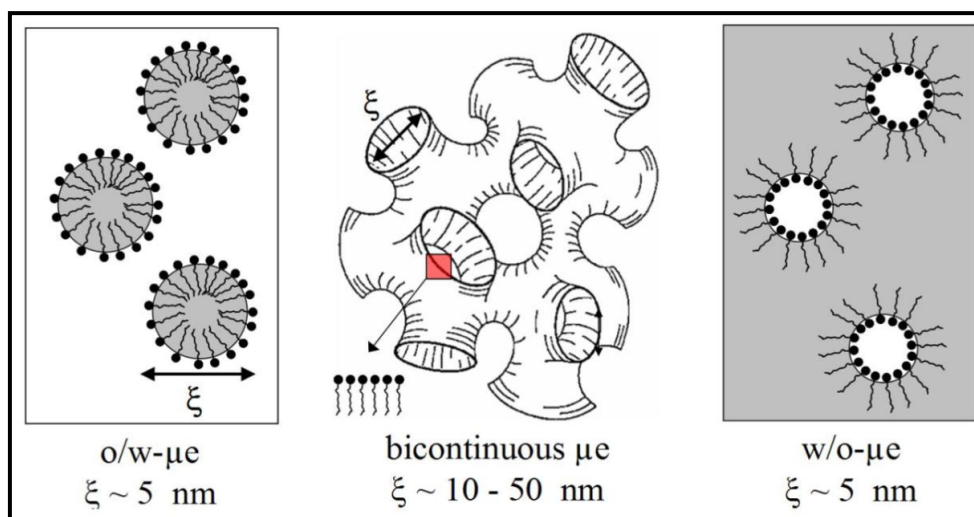


**Figure 4.2** Types of microemulsion
(http://google.co.uk/imagesTYPESofmicroemulsion)

These colloidal dispersions are also sometimes called nanoreactors. They can be used to carry out chemical reactions and, in particular, to synthesise nanomaterials. By controlling the parameters of the synthesis, these nanoreactors can be used as template to produce tailor-made products down to a nanoscale level with new and special properties (Eastoe and Warne, 1996; Lopez-Quintela, 2003). One such example is microemulsion polymerisation. Due to their small and uniform droplet size, they can form nanomaterials via polymerisation processes (Watnasirichaikul et al 2000). In addition, if biocompatible oils and surfactants are used for the formation of the microemulsion, the need to separate the nanomaterials from the reaction medium following polymerisation when emulsion systems are used may be eliminated (Vauthier *et al.*, 2003).

**4.2.2.1 Nonionic microemulsion system**

In this work, the phase behaviour of stable W/O microemulsion regions formed by non-ionic surfactants was investigated. Non-ionic surfactant is an attractive choice due to its mild effect and low cost as compared to other types of surfactants. The W/O microemulsion region was chosen due to its vast potential in the pharmaceutical industry and because it's potential has not been getting the attention it deserves compared to the O/W systems. We were particularly interested in its potential to incorporate biological molecules into the aqueous phase. It is also well known that non-ionic surfactants with the right combination of water and oil produce microemulsion regions without the need of using co-surfactant in some cases which would probably be beneficial to minimise protein denaturation in such systems.

Candau and co-workers (1999) reported that microemulsion regions were found in a hydrophilic-lipophilic balance, HLB domain ranging from 8 to 11 using non-ionic surfactants such as Arlacel 83 and G1096.  Recently, it has been reported that a mixture of non-ionic surfactants with a lower HLB value of about 7.1 produce a stable W/O microemulsion region (Wan et al., 2010). The nonionic surfactants used were Tween 80 and Span 80.  Similar HLB values (7-8) with cosurfactant were favourable in order to produce a balanced microemulsion using sorbitan monolaurate (Crill 1) and polyoxyethylene (20) monooleate (Crillet 4 Super) (Alany et al., 2000).

## 4.3 What is microemulsion polymerization?

As the name implies, microemulsion polymerisation is the polymerisation reaction taking place in a microemulsion system. Basically, polymerisation reactions can be carried out by adding monomers to an acidic aqueous solution medium containing surfactant under mechanical stirring. The system is left for polymerisation under increasing pH of the medium until the desired products are obtained. The reaction proceeds through anionic mechanism since it is initiated in the presence of nucleophilic initiators like $OH^-$, $CH_3O^-$, $CH_3COO^-$ and $CN^-$. The nanocapsules are then collected by centrifugation. Depending on the type of aqueous solution of

surfactants (polymerisation medium) used the process is called emulsion or microemulsion polymerisation.

As mentioned above, polymerisation may be achieved by incorporating a monomer in either the dispersed or continuous phase of the microemulsion. If this reaction takes place at the interface between the two phases, this process is called interfacial polymerisation. The interfacial polymerisation technique is the method use to prepare oily and aqueous-type nanocapsules surrounded by polymer membrane.

### 4.3.1 Oily nanocapsules

If the acidic polymerisation medium is an O/W system with an additional water-miscible organic solvent such as ethanol or acetone, then oily-type nanocapsules will be produced (Chouinard *et al.*, 1991; Gallardo *et al.*, 1993; Yordanov and Bedzhova, 2011). This type is preferred as carriers of lipophilic and oil-soluble molecules. Work by Chouinard and co-workers (1991), reported the production of nanocapsules with diameter of 200 nm by interfacial polymerization of isohexylcyanoacrylate (IHCA) monomer in an oil-in-water system. The effect of various parameters on the size of the nanocapsules was also reported.

### 4.3.2 Aqueous nanocapsules

As stated earlier in Chapter 2, Gasco and Trotta (1986) were the first to propose an interfacial polymerisation in W/O microemulsion systems which resulted in the production of aqueous nanocapsules. This was later improvised by using biocompatible W/O microemulsions using ethylcyanoacrylate as a monomer Watnasirichaikul *et al.*, 2000). This type of aqueous nanocapsule is preferred for hydrophilic and water-soluble compounds such as many materials of bio origin like DNA, proteins etc. This is because the delivery of these materials is associated with low bioavailabilty due to proteolytic degradation (Zhou and Wan Po, 1991). Encapsulation is therefore important because it has been demonstrated that encapsulation within particulate delivery systems could protect peptides from

proteolytic enzymes (Damge *et al.*, 1997). Hillaireau and co-workers (2007) used poly (isobutylcyanoacylate) aqueous nanocapsules to encapsulate mono- and oligo-nucleotides. They also showed that the presence of cationic polymers facilitated the encapsulation of the hydrophilic nucleotides.

## 4.4 Objective

The main objective of the work was to locate and characterise a microemulsion region, especially for W/O systems, that could be used to design a potential microemulsion polymerization to form nanocapsules. With that in mind, preliminary studies of the microemulsion region stabilised by nonionic surfactants were undertaken by;

1. Constructing typical phase diagrams consisting of water/non-ionic surfactant with various oils as the third component.
2. Assessing a suitable composition from the phase diagram and investigating the particle sizes and stability.
3. Selecting a microemulsion template system for further investigation into microemulsion polymerization.
4. Preparation of poly (alkycynoacrylate) nanocapsules using the selected microemulsion template.
5. Incorporation of a model protein drug into the system and assessment of encapsulation and release

## 4.5   Methods

The overall experimentation for the preparation of nanocapsules using W/O microemulsion as a template is shown in Figure 4.3.

```
┌─────────────────────────────────────────────────────┐
│   SYNTHESIS OF POLY (ALKYLCYANOACRYLATE)             │
│   NANOCAPSULES USING W/O MICROEMULSION AS TEMPLATE   │
└─────────────────────────────────────────────────────┘

┌──────────────────────────┐   ┌──────────────────────────┐
│  NONIONIC SURFACTANT A    │ + │  NONIONIC SURFACTANT B    │
└──────────────────────────┘   └──────────────────────────┘

            ┌──────────────────────────────┐
            │  CONSTRUCTION OF PHASE        │
            │  DIAGRAMS                     │
            └──────────────────────────────┘

            ┌──────────────────────────────┐
            │  IDENTIFICATION OF W/O        │
            │  MICROEMULSION REGION         │
            └──────────────────────────────┘

            ┌──────────────────────────────┐
            │  DLS STUDY OF SELECTED        │
            │  W/O MICROEMULSION            │
            └──────────────────────────────┘

            ┌──────────────────────────────┐
            │  SYNTHESIS OF                 │
            │  NANOCAPSULES                 │
            └──────────────────────────────┘

            ┌──────────────────────────────┐
            │  ENTRAPMENT OF INSULIN BY     │
            │  NANOCAPSULES                 │
            └──────────────────────────────┘

            ┌──────────────────────────────┐
            │  ASSESSMENT OF RESULTS        │
            └──────────────────────────────┘
```
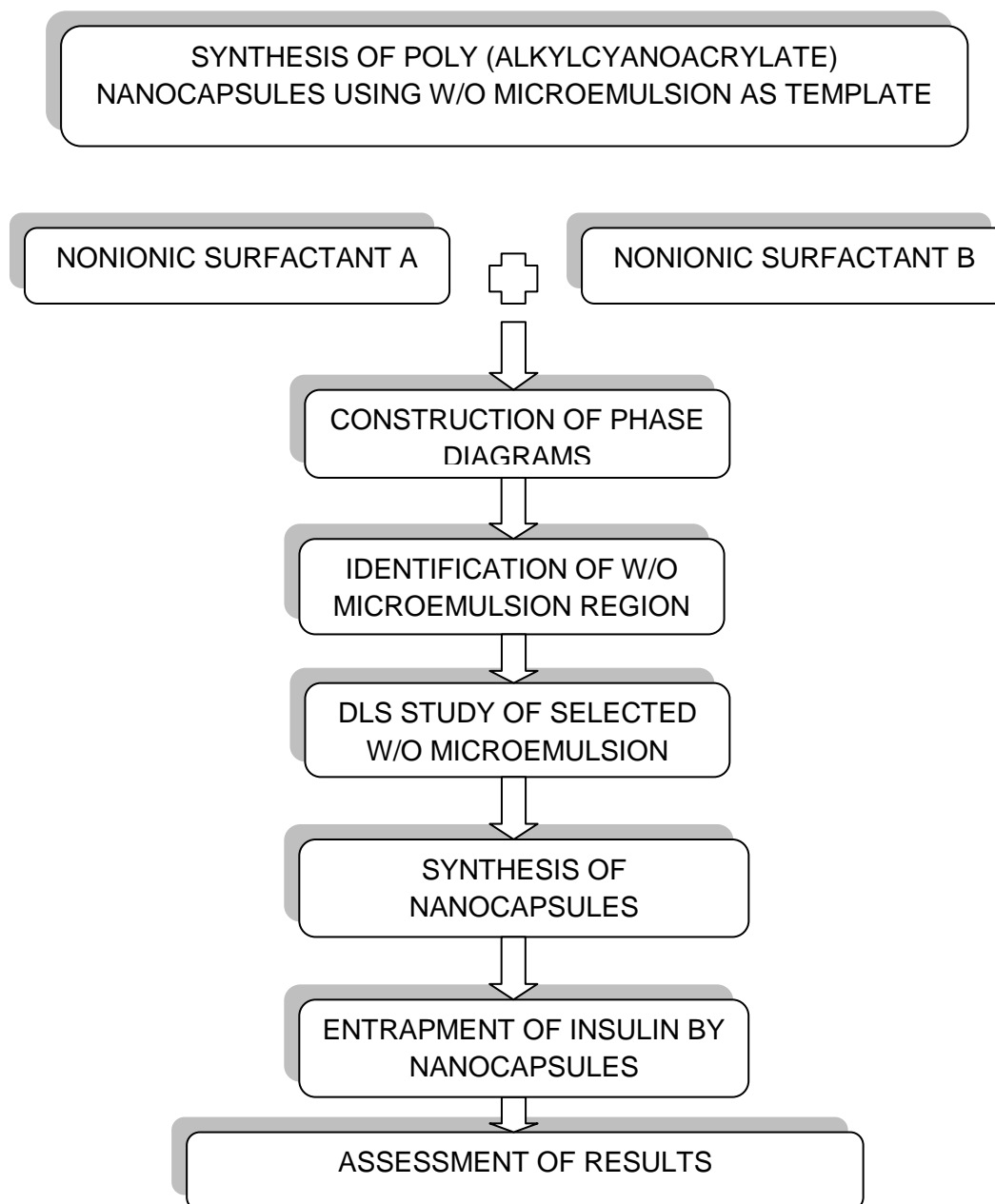
**Figure 4.3** Experimental flow chart

## 4.5.1 Construction of phase diagrams

The basic idea is to understand and predict what phases will be stable in a system when the temperature, pressure, and composition are defined and how those stability relations will change as the prescribed parameters are varied. Ternary or three-component phase diagrams are essentially equilateral triangles. This triangle is a section cut from a three-dimensional figure. As a way of illustration, Figure 4.4 shows a typical three-component phase diagram consisting of compound A, B and C.
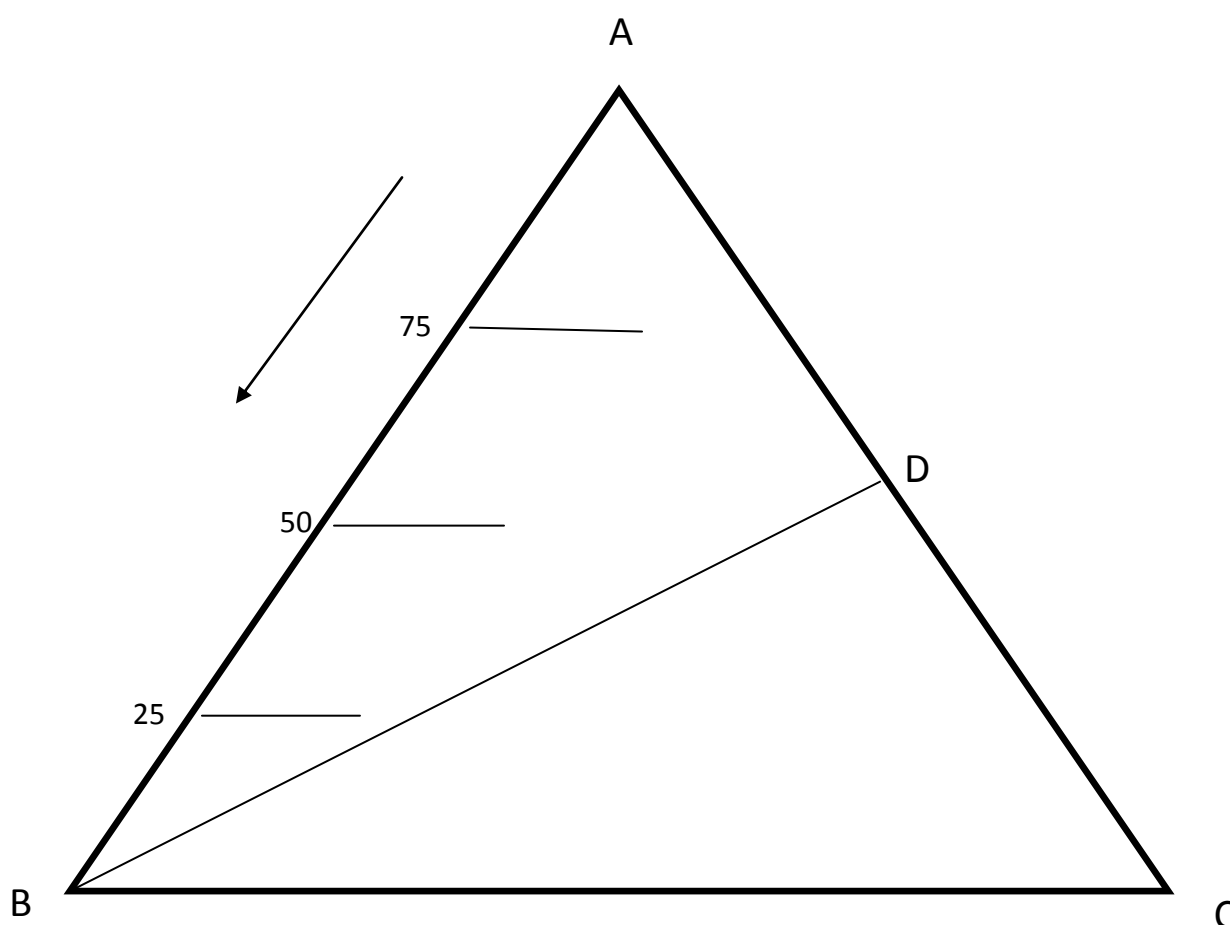


**Figure 4.4** A typical 3-component phase diagram with component A, B and C

At any point in the triangle, the compositions of A, B, and C must add up to 100 percent. At any apex, one component is 100 percent, while both others are zero. Along the line connecting A and C, the composition of B must be zero. The line AC is

also referred to as B-free axis. The point D shows the ratio of A to C and moving along the line from D to B indicates that the ratio of A to C is kept constant throughout the line, but with increasing proportion of B added. Note the arrow moving from A to B, the composition of A is decreasing as it approaches B and vice versa if the arrow moves from B to A.

In this work, the phase diagrams were determined on a clear/turbid criteria basis by mixing two of the components and titrating with the smallest amount of the third component. The samples were then thoroughly mixed to homogeneity with a vortex mixer, centrifuged and then allowed to reach equilibrium at a specific temperature in a water bath. The phases were then examined by visual inspection between cross polarisers. An estimated region of the phases can then be made by this method by noting the turbid and clear compositions.

### 4.5.2 Dynamic light scattering measurements

In this work, 2 ml of selected microemulsion samples were prepared and kept in the water bath at $25^{o}$C overnight to equilibrate. A Zetasizer Nano Series (Malvern Instruments, Worcestershire, UK) set at $25^{o}$C were used to measure the droplet size. The measurement were made in triplicate.

### 4.5.3 Preparation of poly (ethyl 2-cyanoacrylate) PECA nanocapsules by interfacial W/O microemulsion

In this work, the PECA nanocapsules were prepared following the method used by Watnasirichaikul and co-workers (2000). 200 mg of ethyl 2-cyanoacrylate monomer is dissolved in 600 mg of chloroform. The mixture was then mixed with 10 ml of selected microemulsion template and mechanically stirred at 700 rpm overnight at 4 $^{o}$C for the polymerisation process to take place. The nanocapsules were then isolated from the microemulsion medium by repeated washing in ethanol. The nanocapsules

were centrifugated to remove residual oil and surfactant and were then freeze-dried for 48 hours. The mechanism referring to the polymerisation is shown in Figure 4.5 (Yordanov and Bedzhova, 2011).
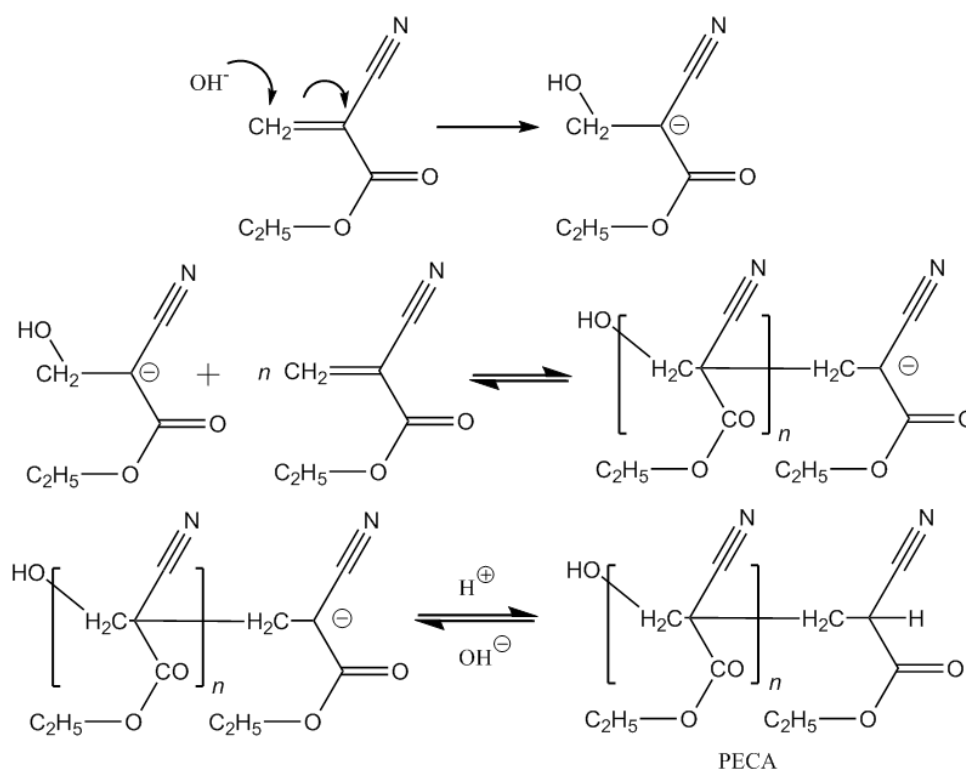


**Figure 4.5** The mechanism of poly (ethyl 2-cyanoacrylate) PECA polymerisation (Yordanov and Bedzhova, 2011).

## 4.5.4 Preparation of poly (ethyl 2-cyanoacrylate) nanocapsules containing insulin

In this work, the nanocapsules containing insulin were prepared following the same method as above (4.5.4) but, for this work, the aqueous component of the microemulsion template was replaced with an aqueous solution of insulin having a concentration 100 units/ml and a pH 7.4.

### 4.5.5 Assessing level of insulin entrapment

In this work, 1.6 g of the polymerised insulin microemulsion was diluted with 10 ml of water. The pH is adjusted to pH 2.5 using hydrochloric acid. 300 µl of this dispersion were mixed with 300 µL of solution containing methanol and water at 80:20 (v:v) at pH 2.5. The mixture was then centrifuged. The supernatant was then injected into the HPLC equipment using a C18 column (Luna $5\,\mu$m C18 (2), 150 mm x 3.0 mm; Phenomenex). The mobile phase used contained a mixture of acetonitrile and sodium dihydrogen phosphate at a weight ratio of 23.5 % by weight. The pH was adjusted to 2.5 using orthophosphoric acid. The column was maintained at $50^{o}$C and the flow rate at 0.5 ml/min. The eluent was monitored at a wavelength of 214 nm. The percent entrapment of insulin was calculated from the difference between the total amount of insulin added to the polymerisation template and the untrapped amount measured in the supernatant.

### 4.5.6 *In Vitro* release study

A previously reported method to determine *in vitro* release of insulin was adopted in this work (Watnasirichaikul *et al.*, 2002). The release of insulin from the polymerised material was carried out by diluting 63.0 mg of dry polymer with encapsulated insulin to 20 ml with PBS (pH 6.8) which was subsequently stirred at 50 rev/min in a water bath ($37^{o}$C). Samples of 200 ul were removed at various times and released insulin was analysed by HPLC as described above for the determination of encapsulated insulin. The release was monitored for 8 h at this pH. Release was also studied as described above at pH 1.2 (mimicking the GI tract condition) for 2 hours.

## 4.6 Results and Discussion

The results and discussion will be presented in 4 parts. The first part covers the investigation of microemulsion region stabilized by non-ionic surfactants by construction of phase diagrams. The second part, the dynamic light scattering measurements are presented. The third part, characterisation of poly(ethyl-2-

cyanoacrylate) nanocapsules. Finally, insulin entrapment and release were discussed.

## 4.6.1 Phase Diagrams

In order to understand the association behaviour of microemulsions, a preliminary investigation of the phase behaviour employing solvent/non-ionic surfactants with different types of oil as the third component was carried out. The solvents were water and insulin solution. The following results and discussion of the phase diagrams were reported in all of the three solvents.

### 4.6.1.1 Water/Nonionic Surfactant systems

In these investigations, two nonionic surfactants with similar HLB values as Crill 1 and Crillet 4 super were employed. The nonionic surfactants were Tween 80 and Span 20. Crill and Crillet are suitable for topical preparation, while Tween and Span are usually used for preparation of food products. Tween 80 (HLB = 15) and Span 20 (HLB = 8.5) were chosen since they have been previously described in the literature (Constantinides and Scalart, 1997; Hickey *et al.*, 2010). They are readily available and their colloidal structures have been characterized by many groups (Aizawa, 2009; Alany et al. 2001; Krauel et al. 2005; Shukla *et al.*, 2004). Figure 4.6 shows the location of the one phase isotropic region for water/Span20/Tween 80. It was observed that both of the Tween 80 and Span 20 were completely miscible in each other. The isotropic solution region was found to be extending fully from the water-free axis towards the water apex. A maximum water solubility of 24 weight percent of water was observed at Tween 80/Span 20 weight ratio of 60/40. This observation is in agreement with the previously reported result (Alany et al. 2001).
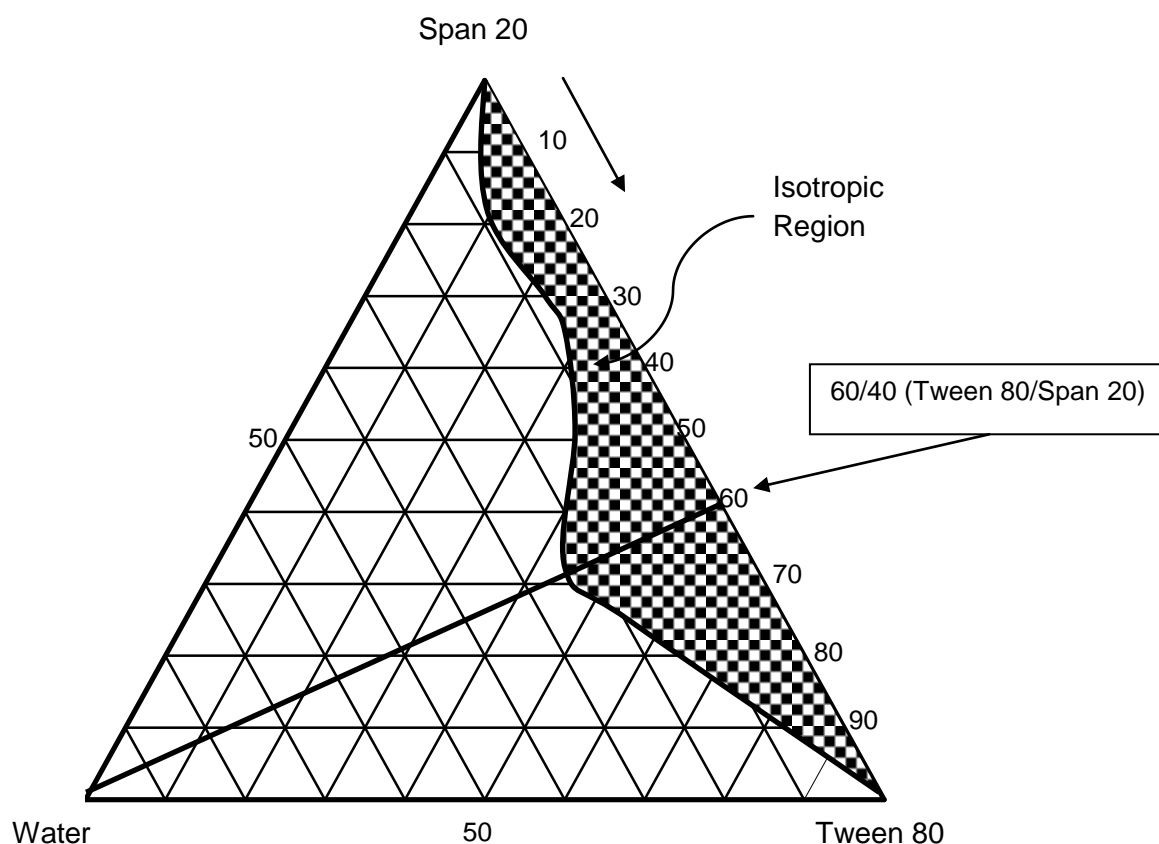
**Figure 4.6** Pseudoternary diagram for water/Span 20/Tween 80 systems showing the isotropic region.

### 4.6.1.2 Water/Span 20:Tween 80/1-Butanol  systems

The ratio (i.e. 60/40 of Tween 80/Span20) was then used as the mixed nonionic surfactant apex and titrated with a third component containing 1-butanol as shown in Figure 4.7. The figure showed a similar pattern of the isotropic region to that of the water/Tween 80/Span 20 system (Figure 4.6) but, with a slightly reduced amount of the maximum water solubility of 20 weight percent. The maximum water solubility occurs at 1-butanol/Tween 80:Span 20 (60:40) weight ratio of 30/70. This suggested that a higher amount of mixed surfactant was required to achieve the maximum water solubility and to form the colloidal structures.
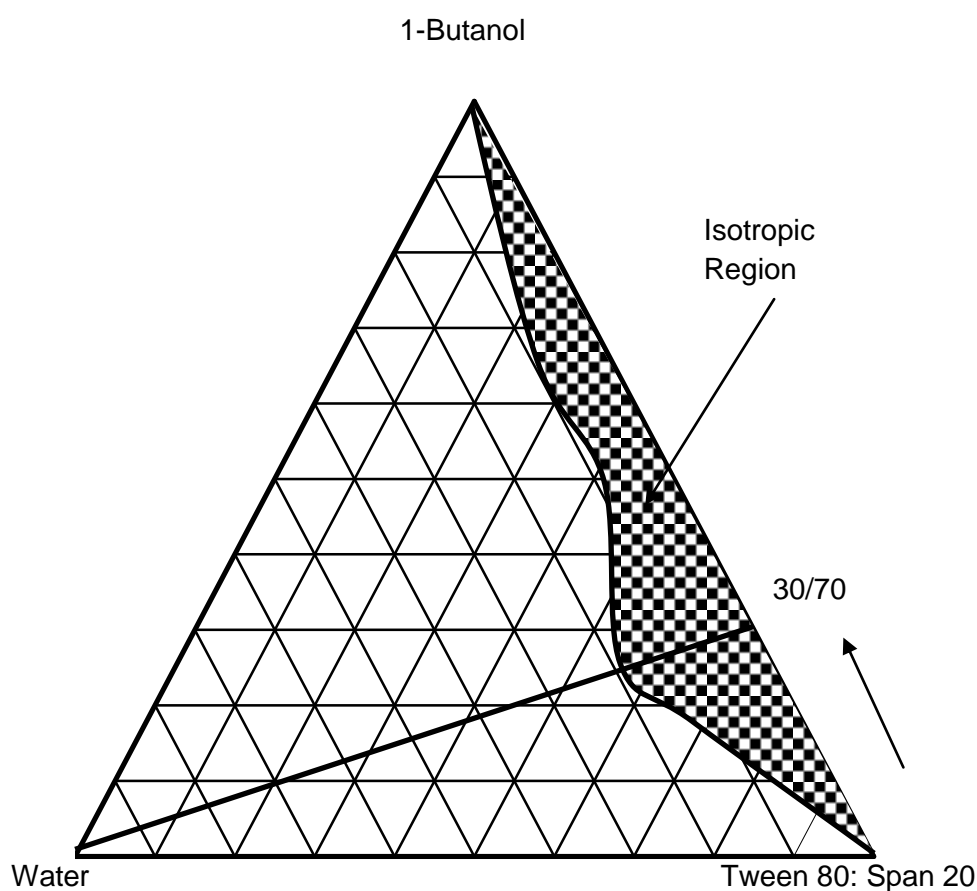
**Figure 4.7** Pseudoternary diagram for water /Tween 80:Span 20/1-Butanol systems

## 4.6.1.3 Water/Span 20:Tween 80/1-Butanol/Oil system

For the formation of W/O microemulsion, methyl acetate and ethyl oleate were then added separately as the oil component in systems containing water and Tween 80/Span20 (60/40):1-butanol (70:30) as shown in Figure 4.8. The system with methyl acetate (solid line, Figure 4.8) showed a total miscibility of the mixed surfactant and 1-butanol component in both of water and methyl acetate. The microemulsion region was seen to be projecting in an inwards manner from the mixed surfactant/1-butanol-free axis starting from both water and methyl acetate apices.
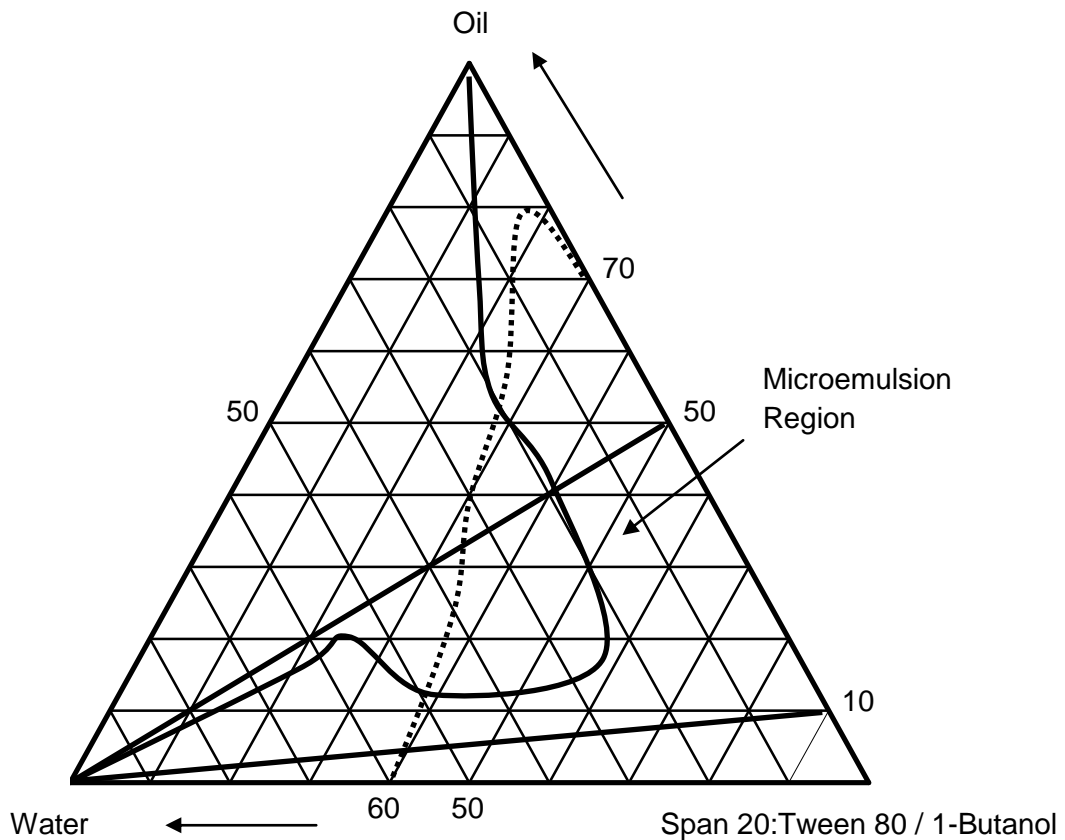
**Figure 4.8**    Pseudoternary diagram for water/Span 20:Tween 80/1-Butanol /Oil systems ( methyl acetate, ___ and ethyl oleate, **.......**)

The microemulsion region for ethyl oleate (dotted line, Figure 4.8) however showed a different behaviour.   The region seemed to cover almost two thirds of the mixed surfactant/1-butanol apex and projecting upwards from the ethyl oleate-free axis with a maximum ethyl oleate solubility of 80 percent by weight. The figure also showed a partial miscibility of the mixed surfactant/1-butanol component in both water (60 %) and ethyl oleate (70 %).

**4.6.1.4 Insulin/Span 20:Tween 80/1-Butanol/Ethyl Oleate system**

The dotted line of Figure 4.9 showed a microemulsion region when water was replaced with insulin solution. The region was observed to shrink towards the solvent-free axis with a maximum insulin solution solubility of about 20 % by weight. It

occurred at an ethyl oleate/(Tween 80:Span/1-butanol) weight ratio of 50/50. It was also observed that the solubility region at the ethyl oleate-free axis did not occur in this system. This suggests that the presence of ethyl oleate is vital for the formation of microemulsion when insulin is present.

Ethyl Oleate

Microemulsion
Region

50:50

Water, _____
Insulin Solution, _._._

Span 20: Tween 80 / 1-Butanol
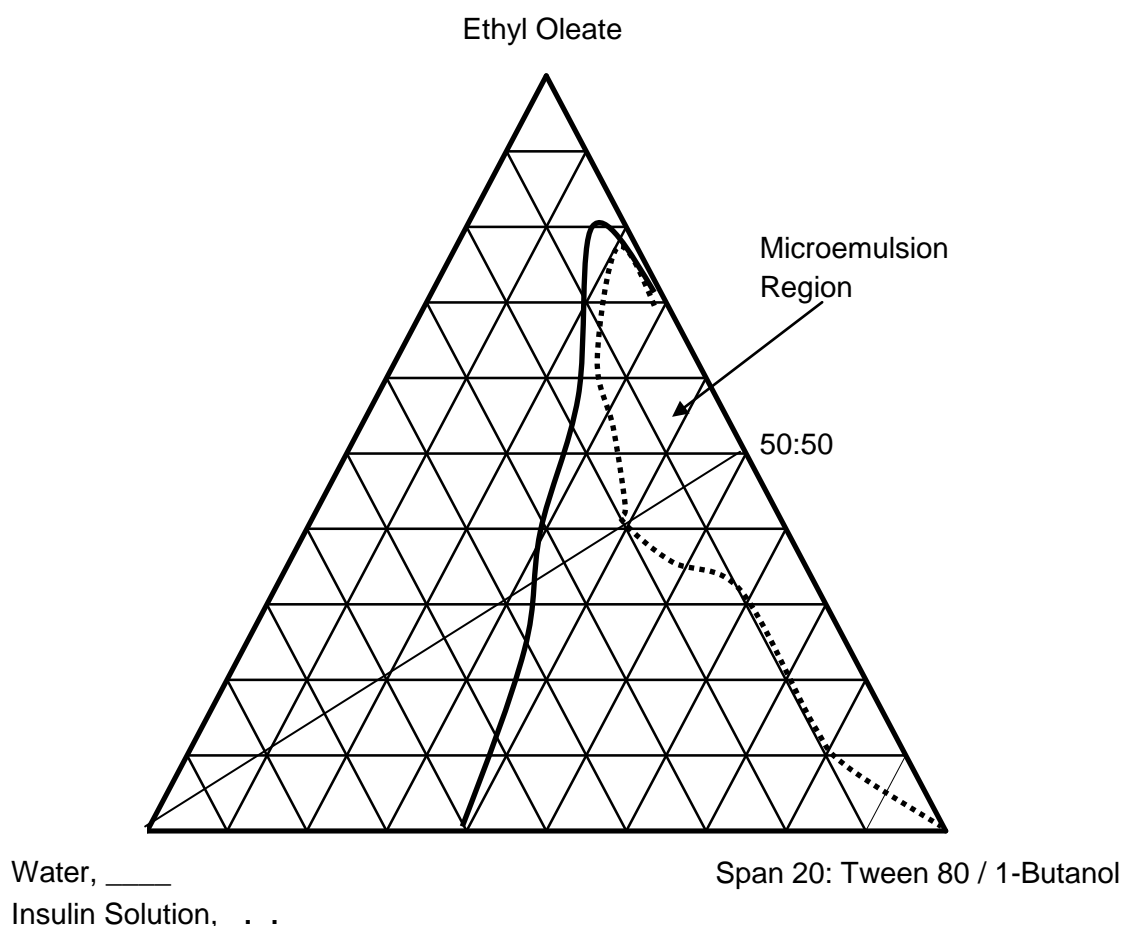
**Figure 4.9** Pseudoternary diagram for solvent/Span 20:Tween 80/1-Butanol/Ethyl oleate systems. The solvents are water, ___ , and insulin solution, **......**

Overall, it may be summarised that the solubility area of the microemulsion regions have been located in the systems studied. The region with the presence of insulin however, has some detrimental effect on the solubility area of the microemulsion region. This is expected due the large size of the insulin structure. Therefore, ethyl oleate is needed if insulin is to form a microemulsion in this system.

## 4.6.2 Dynamic light scattering measurements

In order to elucidate the different types of colloidal structures present in the prepared microemulsion, DLS measurements were carried out to determine the particle size and distribution. For the light scattering measurements of these mixed non-ionic surfactant microemulsion systems, two lines at a constant weight ratio of surfactant/oil of 50/50 and 90/10 were taken. The line at the 50/50 weight ratio shows limited solubility in water of less than 20 percent, while the other line at the 90/10 shows complete miscibility in water (see Figure 4.8). The droplet size of each of the composition is obtained from the particle size distribution described as intensity percent from the DLS measurements. To illustrate this, Figure 4.10 showed the droplet size distribution described as intensity percent for sample at 50:50 (mixed surfactant/1-Butanol:Methyl Acetate) for $H_2O$/Tween 80:Span 20/1-Butanol/Methyl Acetate containing at 5 weight percent of water. Similar exercises were used for the other compositions and their droplet size with the variation of water content is shown in Figure 4.11.
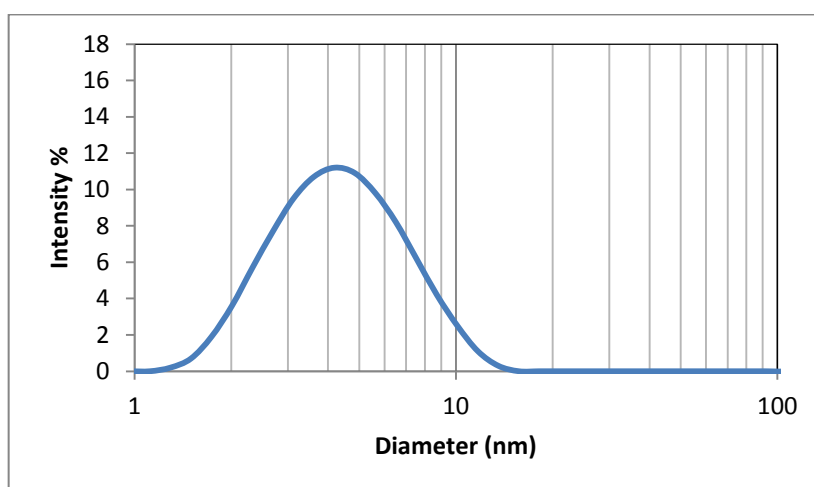


**Figure 4.10** The particle size distribution by DLS of microemulsion droplet described as intensity percent (%) at 5 weight % of water.

The solid line of Figure 4.11 shows the variation of the droplet size with the weight percentage of water for the methyl acetate system at the weight ratio of 50/50. The sizes of the droplets showed an upward trend from 4.5 to 7.5 nm with the increment of water content. These values are in agreement with the previously reported result i.e. from 3.9 to 13.1 nm for systems containing mixtures of Tween 80 with soya bean

oil (Constantinides and Scalart, 1997). For the 90/10 weight ratio (dotted line, Figure 4.11), showed a similar increasing trend but a marked increase in the values of the droplet size of more than 100 nm.
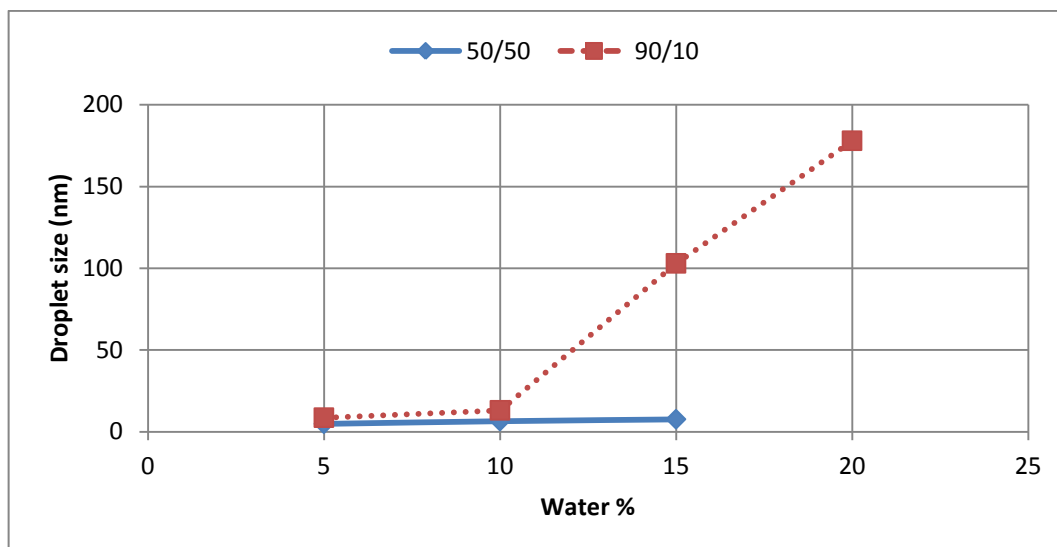


**Figure 4.11** Droplet size for 50:50 ( ___ ) and 90/10 ( **......** ) (mixed surfactant/1-But:MeAc) for  $H_2O$/Tween 80/Span 20/1-Butanol/Methyl Acetate systems.

It is also worth mentioning of the sudden increase in the value of the particle size occurring at 10 percent for both systems. The sudden increase in the value of the particle size at 10 percent of water is satisfying since similar observations were made by previous workers (Shah & Hamlin, 1971; Friberg & Buraczewska, 1978). They suggested that at that concentration of water, the first inverse micelles are formed or the increase in size shows a change in association behaviour to form a bicontinuous system. This is further substantiated by Krauel and coworkers (2005) and Hickey and co-wokers (2010) whom reported that at water percentage between 5 to 10 percent, W/O microemulsion was formed. However, as the water content was further increased the W/O microemulsion changes to that of bicontinuous type.

### 4.6.3 Characterisation of poly (ethyl- 2-cyanoacrylate) nanocapsules

Finally from the above results, the phase diagrams using W/O microemulsion stabilised by non-ionic surfactants were further used as microemulsion templates for the interfacial polymerisation of poly (ethyl - 2-cyanoacrylate) nanocapsules. This is

due to the biocompatibility of the oil (ethyl oleate) and surfactants (Tween 80 and Span 20) used as reported by Damge and co-workers (1987). In this system it consisted of a mixture of Tween 80:Span 20 (60:40/w:w), ethyl oleate and water as the aqueous component. The locations and compositions of the selected microemulsion used for further characterisations are shown as dots at points $P_1$, $P_2$, and $P_3$ in Figure 4.12 and Table 4.1, respectively.
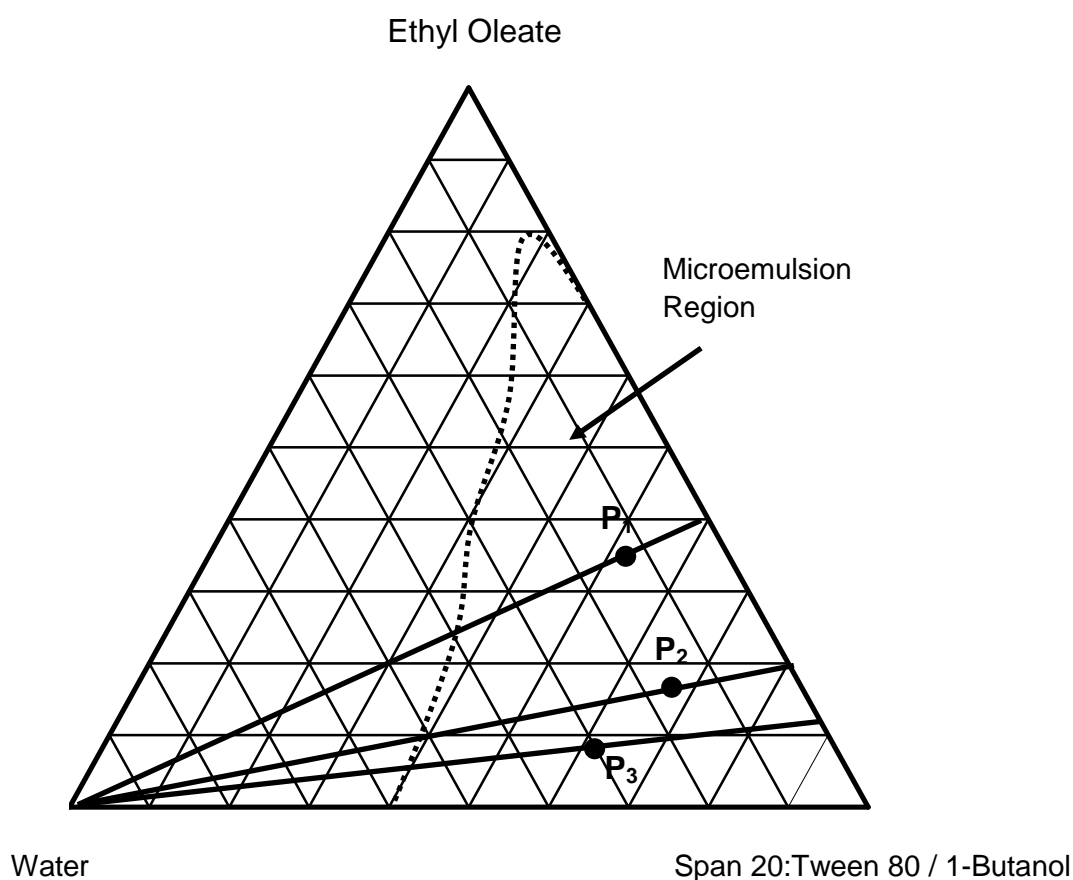


**Figure 4.12** The points $P_1$, $P_2$, and $P_3$ selected as templates for interfacial cyanoacrylate polymerisation.

**Table 4.1** The compositions of selected points $P_1$, $P_2$ and $P_3$.

| | Percent by Weight | | |
|---|---|---|---|
| | Water | Mix Surfactant:1-Butanol | Ethyl Oleate |
| $P_1$ | 13 | 52 | 35 |
| $P_2$ | 16 | 66 | 18 |
| $P_3$ | 30 | 62 | 8 |

Figure 4.13 shows the FTIR spectrum of the prepared poly (ethyl 2-cyanoacrylate) nanocapsules after washing and freeze drying.
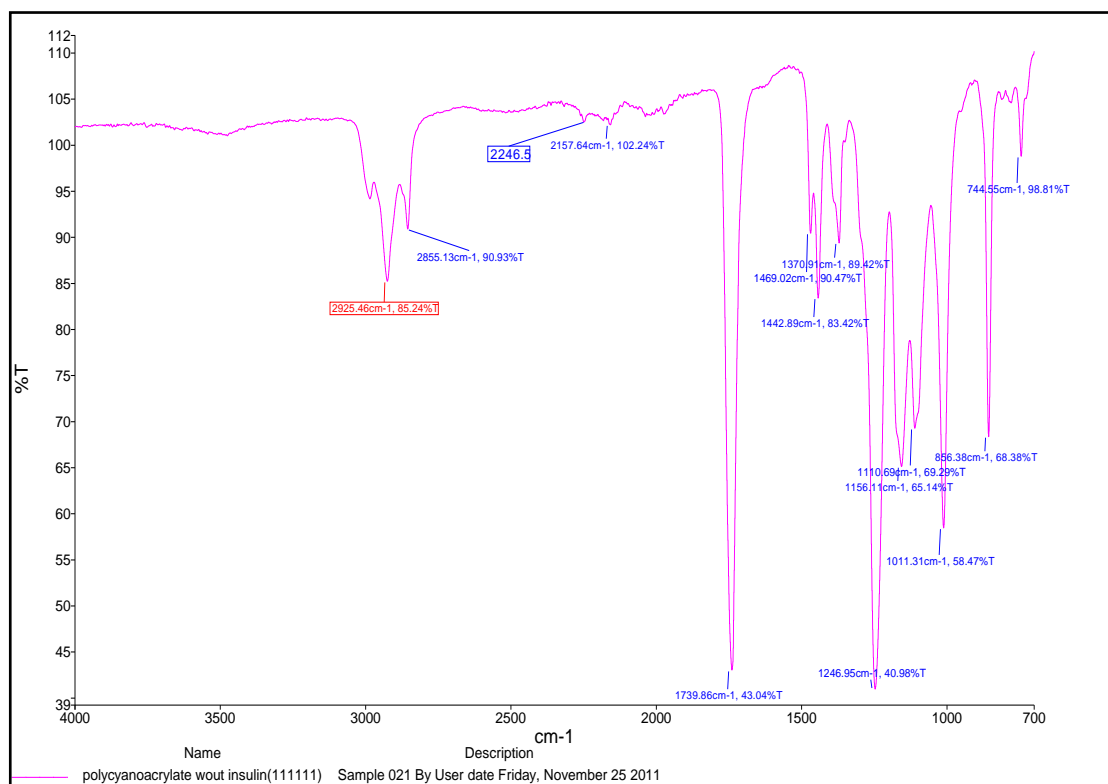


**Figure 4.13**   FTIR spectrum of poly (ethyl 2-cyanoacrylate).

The observed FTIR spectrum is similar to those reported in the literature for this material (Ariasa *et al.*, 2001; Han *et al.*, 2008). It shows the typical absorption peaks for the carbonyl C=O ester (1739 cm$^{-1}$), C≡N groups (weak, 2246 cm$^{-1}$) and C-H (2855-2988 cm$^{-1}$). The rest of the peaks observed at lower wavenumbers were due to C-H bending (1370-1669 cm$^{-1}$) and the stretching and bending of the C-CO-C group

(1110-1246 cm$^{-1}$). One striking observation was the absence of prominent absorption peaks at around 1600-1650 cm$^{-1}$. These peaks would be due to the presence of C=C functional group. This is satisfying because this functional group is only observed in the ethyl 2-cyanoacrylate monomer and disappears in the poly (ethyl - 2-cyanoacrylate) due to the formation of polymer chain as reported by Han and co-workers (2008). From the FTIR results, it may therefore be concluded that the polymerisation of ethyl - 2-cyanoacrylate was completed.

Figure 4.14 shows the morphologies of the prepared nanocapsules at points $P_1$, $P_2$, and $P_3$. All of the three compositions showed a porous honeycomb structure indicative of a bicontinuous type of microemulsion rather than a high yield of discrete nanocapsules, although some nanoscale product was also evident. The size presented by intensity percent for the microemulsion template and the prepared nanocapsules at different compositions $P_1$, $P_2$ and $P_3$ is tabulated as shown in Table 4.2.
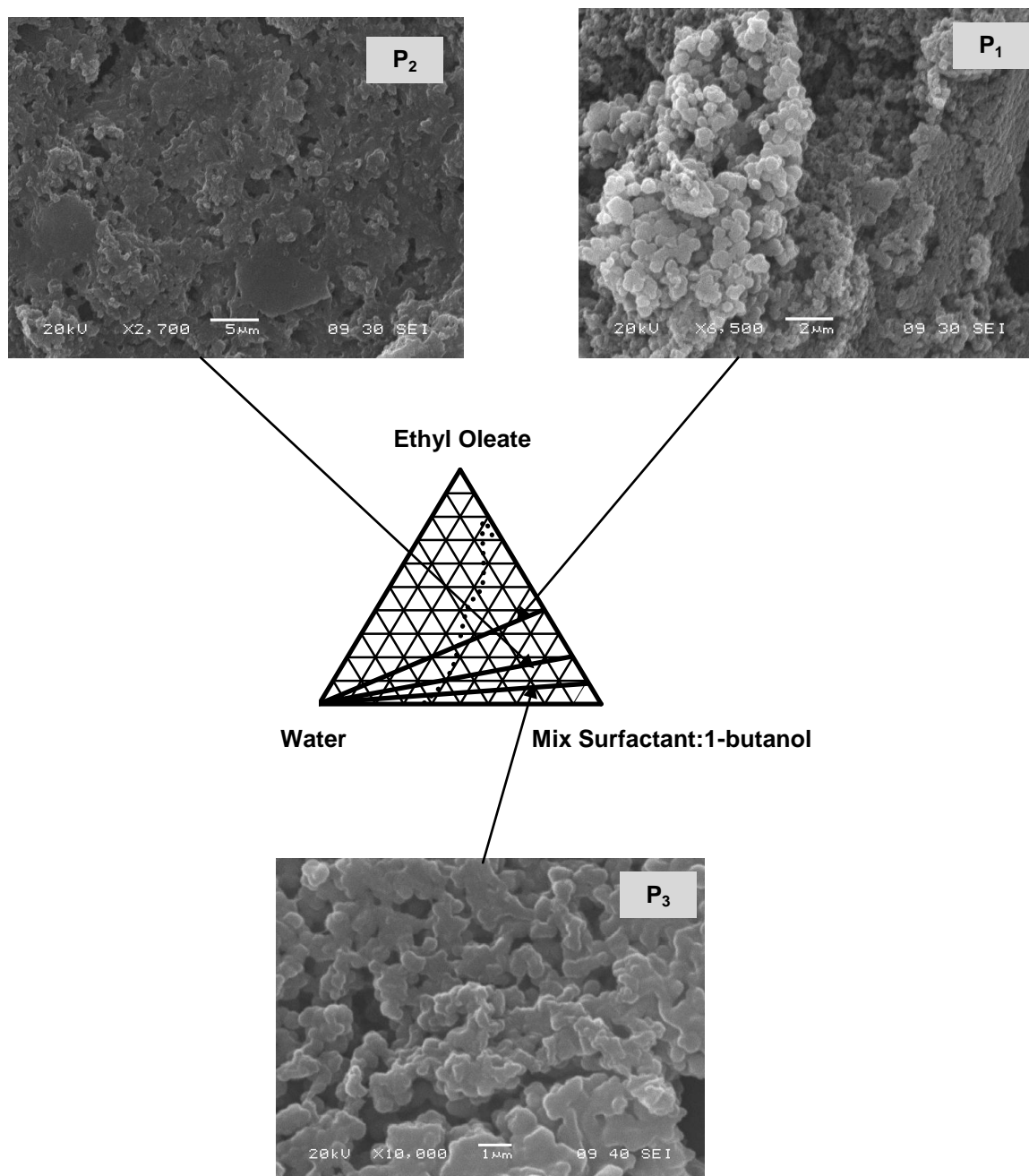
**Figure 4.14** SEM images of nanocapsules at compositions $P_1$, $P_2$ and $P_3$ showing porous structures at magnifications 6500, 2700 and 10000x, respectively.

From the table, the size of the microemulsion template measured by DLS was found to be more than 300 nm. This again suggested that a bicontinuous type of microemulsions was formed. The size of the prepared nanocapsules was found to be large (> 140 nm). The value of 140 nm is close to the reported value of 150 nm (Watnasirichaikul *et al.*, 2000) using Crillet 4 and Crill 4 as the non-ionic surfactants.

The observed value is however smaller compared to the reported average value of 250 nm (Krauel *et al.*, 2005) using Crill 1 and Crillet 4 super. This may be due to different non-ionic surfactants used namely Crill 1, Crill 4, Crillet 4 and Crillet 4 super. In this work, Span 20 and Tween 80 were used. It is known that non-ionic surfactants are sensitive to temperature. Therefore, the differences may be attributed to a difference in temperature at which the samples were measured.

**Table 4.2** The mean diameter, in nm, of the templates and nanocapsules from DLS measurement extracted from the scattering data using intensity calculation from the Malvern software. S.D. = standard deviation.

| Compositions | Microemulsion Size (nm) | S.D. | Nanocapsules Size (nm) | S.D. |
|:---:|:---:|:---:|:---:|:---:|
| **P1** | 393 | 5.4 | 147 | 4.2 |
| **P2** | 381 | 0.5 | 190 | 0.9 |
| **P3** | 336 | 2.3 | 178 | 2.7 |

### 4.6.4 Characterisation of poly (ethyl 2-cyanoacrylate) nanocapsules with insulin

The same composition at point $P_1$ (Figure 4.12) was chosen to prepare nanocapsules with insulin. From the DLS measurement, the size of the nanocapsules with insulin was found to be 178 nm. To determine the amount of insulin entrapped in the nanocapsules, reversed phase HPLC was carried out on the combined washings from the synthesis. Figure 4.15 shows the chromatogram for insulin in the supernatant (free drug). From the HPLC study, the concentration of insulin in the supernatant was found from the area of the peak at the retention time 4.33 min.
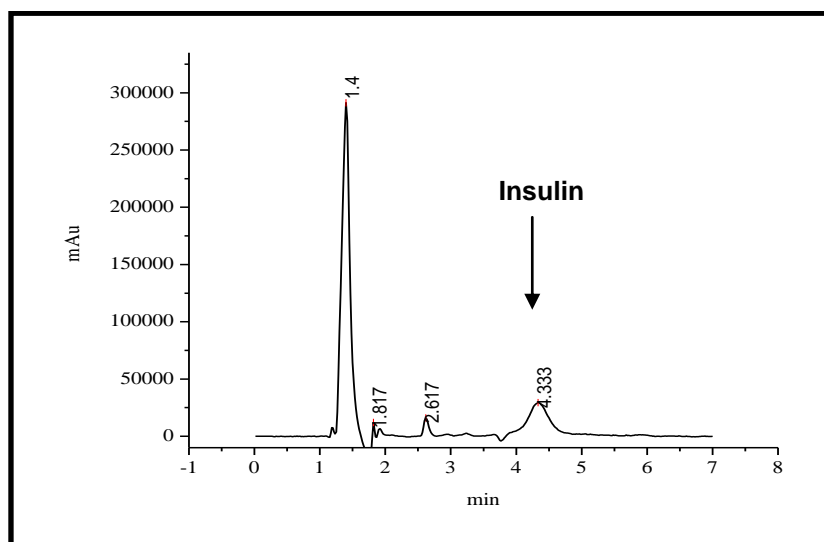
**Figure 4.15** HPLC chromatogram for insulin in the supernatant separated by C18(2) column at an elution rate of 0.5 ml/min, 50°C, 214 nm.

Using the calibration graph for pure insulin (Figure 14.16), by using this formula:

$$\% \text{ Insulin Entrapped} = \frac{(\text{Total Drug} - \text{Free Drug})}{\text{Total Drug}} \text{ x } 100\%$$

it was found that more than 85 % of the insulin was entrapped in the polymer during synthesis.
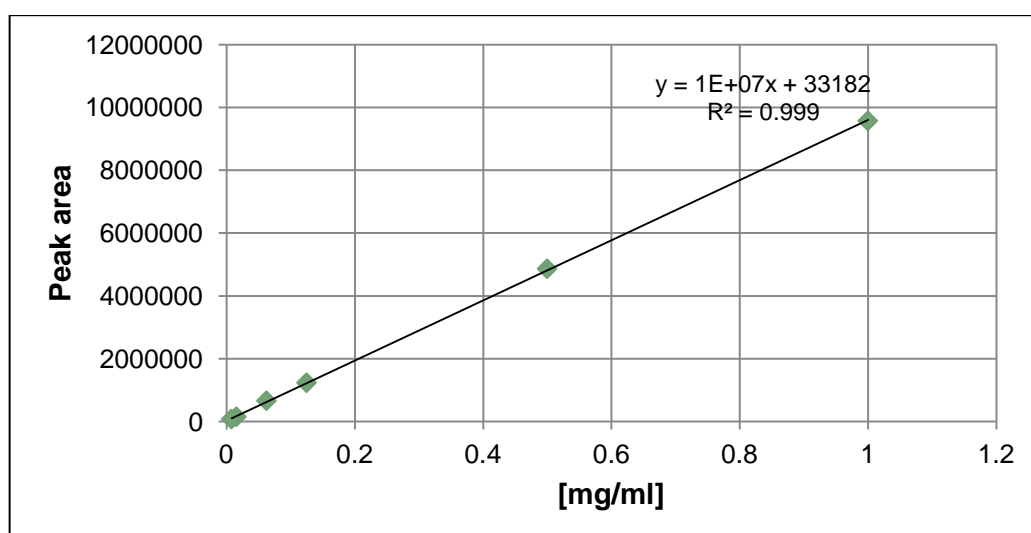


**Figure 4.16** Calibration curve for pure insulin

Figure 4.17 a and b shows the percent drug release of insulin entrapped in the cyanoacrylate polymer at pH values of 1.2 and 6.8, respectively. The result showed that the percent of drug release reached more than 50 % after 30 min elapsed in the pH 1.2 medium, while a release of more than 80 % entrapped insulin in less than 60 min for the pH 6.8 medium. These suggested that while the polymer was able to entrap a good amount of insulin, they were not able to prolong the release of drug for long at both pHs. The polymer was quite unstable, even under these mild conditions, and degraded to liberate the insulin. It is likely that this was greatly assisted by the honeycomb nanostructuring of materials produced. This might have some future interest for drug delivery applications, even though it was not the discrete nanocapsule structure sought in this work.
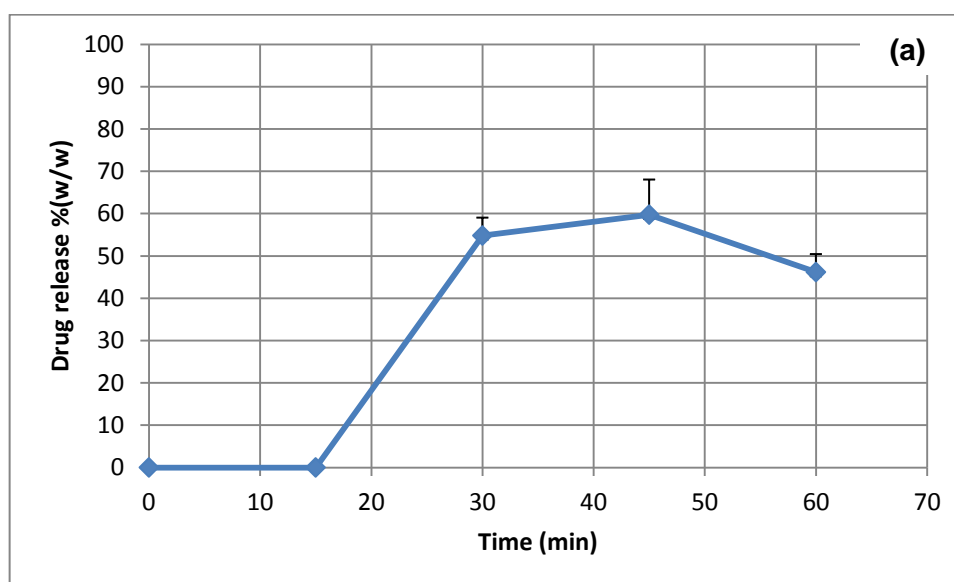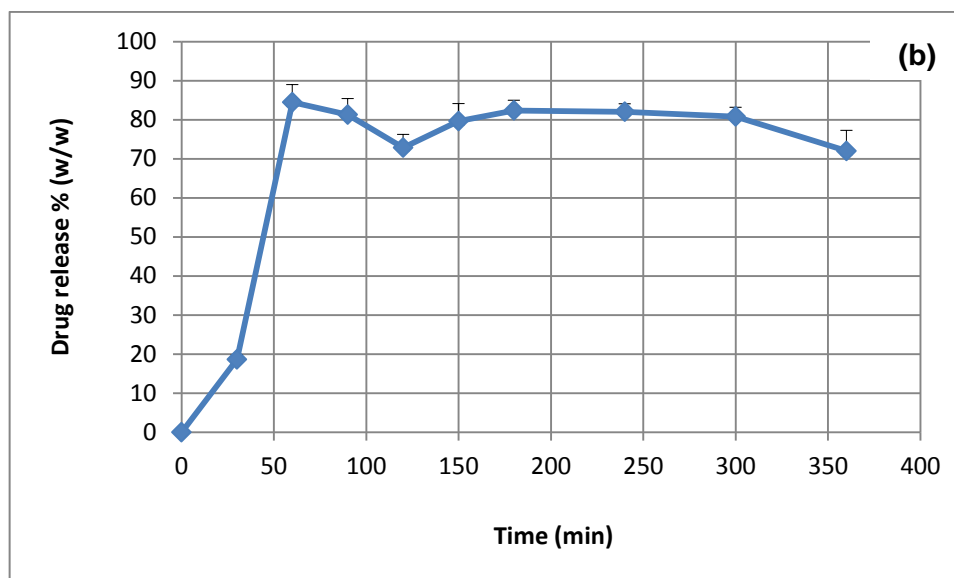
**Figure 4.17** The drug release curve for insulin entrapped in the cyanoacrylate polymer measured at 37 $^{o}$C in (a) pH 1.2 and (b) PBS buffer (pH 6.8). The values represent mean ± S.D. in triplicate measurements.

## 4.7 Conclusion

From the above results, it can be concluded that the microemulsion templates are most likely of bicontinuous type. This resulted in the production of large nanocapsules and a large amount of nanostructured honeycomb type material. These results did not meet the targeted objectives of this work, namely smaller particle size and high yield of clearly defined capsules.

From the *In Vitro* release study, it has showed that the majority of entrapped insulin can be released quite rapidly from the highly porous nanostructured solids. Their inability to prolong drug release in both of pH media rendered it unfavourable for application as a drug delivery material in the GI tract.  With that, this part of the work was halted in favour of a different drug delivery approach using magnetic hyperthermia (though staying within the general theme of nanomaterials for drug delivery). A new project has started by using superparamagnetic iron oxide nanoparticles (IONs) to cause heating when exposed to RF frequency magnetic fields. We are attempting to use this to control drug delivery so that a drug could be delivered "on demand" by exposure to magnetic fileds triggerinf release. This

required the synthesis of IONs via a co-precipitation method and will be presented in the next chapter.

## 4.8 References

http://oregonstate.edu/instruct/bb350/textmaterials/02/Slide08.jpg

http://google.co.uk/imagesTYPESof microemulsion

Adamson, A.W. (1969). Model for micellar emulsions, *J Colloid Interface Sci.*, **29**: 261-267.

Ahmad, S.I., Shinoda, K. and Friberg, S.E. (1974). Microemulsion and phase equilibriums. Mechanism of the formation of so-called microemulsions studied in connection with phase diagram, *J Colloid Interface Sci.*, **47**: 32-37.

Aizawa, H. (2009). Morphology of polysorbate 80 (Tween 80) micelles in aqueous 1,4-dioxane solutions, *J. Appl. Cryst.*, **42**: 592-596.

Alany R.,G, Rades, T., Agatonovic-Kustrin, S., Davies N.M. and Tucker I.G. (2000). Effects of alcohols and diols on the phase behaviour of quaternary systems, *Int J Pharm.*, **196(2)**:141-145.

Alany, R.G., Tucker, I.G., Davies, N.M. and Rades,T. (2001). Characterizing Colloidal Structures of Pseudoternary Phase Diagrams Formed by Oil/Water/Amphiphile Systems, *Drug Development and Industrial Pharmacy*, **27(1)** : 31-38

Ariasa, J.L., Gallardob, V., Go´mez-Loperaa, S.A., Plazaa, R.C., and Delgadoa, A.V. (2001). Synthesis and characterization of poly (ethyl-2-cyanoacrylate) nanoparticles with a magnetic core, *J. Controlled Release* **77**: 309-321.

Bangham, A. D. (1995). Surrogate cells or trojan horses. The discovery of liposomes *BioEssays*, **17**: 1081-1088.

Boman,N.L., Tron, V.A., Bally, M.B. and Cullis, P.R. (1996). Vincristine-induced dermal toxicity is significantly reduced when the drug is given in liposomes, *Cancer Chemoter Pharmacol*, **37**: 351-355

Candau, F., Pabon, M and Anquetil, J.Y. (1999). Polymerizable microemulsions: some criteria to achieve optimal formulation, *Colloids and Surfaces*, **153**: 47-59

Chouinard, F. I., Frederick W.K.K., Leroux, J.C., Foucher, C. and Lenaerts, V. (1991). Preparation and purification of polyisohexylcyanoacrylate nanocapsules, *Intern. J. Pharm*, **12**: 211-217.

Constantinides, P.P., and Scalart, J.P. (1997). Formulation and physical characterization of water-in-oil microemulsions containing long- versus medium-chain glycerides, *Intern. J. Pharm.*, **158**: 57-68.

Damge, C., Aprahamian, M., Balboni, g., Hoeltzel, A., Andrieu, V., and Devissaguet, J.P. (1987). Polyalkylcyanoacrylate nanocapsules increase the intestinal absorption of a lipophilic drug, *Intern. J. Pharm.*, **36**: 121– 125.

Damge, C., Vranckx, H., Balschmidt, P., and Couvreur. P. (1997). Poly(alkyl cyanoacrylate) nanospheres for oral administration of insulin, *J. Pharm. Sci.* **86**: 1403-1409.

Eastoe, J., and Warne B. (1996). Nanoparticle and polymer synthesis in microemulsions. *Curr Opin Colloid Interface Sci.*, **1** :800-805.
Friberg, S.E. and Buraczewska, J. (1978). Microemulsion in the water-potassium oleate-benzene system, *Progr Colloid Polym Sci.*, **63**: 1-9.

Gallardo, M., Couarraze, G., Denizot, B., Treupel, L., Couvreur, P., and Puisieux, F. (1993). Study of the mechanisms of formation of nanoparticles and nanocapsules of polyisobutyl-2-cyanoacrylate, *Intern. J. Pharm.,* **100**: 55-64.

Gasco, M.R., and Trotta, M. (1986). Nanoparticles from microemulsions, *Intern. J Pharm.*, **29** :267- 268.

Ariasa, J.L., Gallardob, V., Go´mez-Loperaa, S.A., Plazaa, R.C., and Delgadoa, A.V. (2001). Synthesis and characterization of poly(ethyl-2-cyanoacrylate) nanoparticles with a magnetic core, *J. Controlled Release* **77**: 309-321

Han, M.G., Kim, S., and Liu, S.X. (2008). Synthesis and degradation behaviour of poly(ethyl cyanoacrylate), *Polymer Degradation and Stability* **93**: 1243-1251.

Hickey, S., Hagan, S.A., Kudryashov, E., and Buckin, V. (2010). Analysis of phase diagram and microstructural transitions in an ethyl oleate/water/Tween 80/Span 20 microemulsion system using high-resolution ultrasonic spectroscopy, *Intern. J. Pharm*, **388**: 213-222.

Hillaireau, H., Le Doana, T., Chacun, H., Janin, J. and Couvreur, P. (2007). Encapsulation of mono- and oligo-nucleotides into aqueous-core nanocapsules in presence of various water-soluble polymers, *Intern. J. Pharm.*, **331**: 148-152.

Hoar, T.P and Schulman, J.H. (1943). Transparent water-in-oil dispersion-oleophatic hydromicelle, *Nature* (London), **152**: 102-103.

Kalyanasundaram, K. and Thomas, J.K. (1977). Environmental effects on vibronic band intensities in pyrene monomer fluorescence and their application in studies of micellar aggregates, *J. Am. Chem. Soc*, **99 (7):** 2039-2044.

Krauel, K., Davies,N.N., Hook, S. and Rades, T. (2005). Using different structure types of microemulsion for the preparation of poly(alkylcyanoacrylate) nanoparticles by interfacial polymerization, *J Controlled Release*, **106:** 76-87.

Lambert, G.S., Fattal, E., Pinto-Alphandary, H., Gulik, A., and Couvereur, P. (2001) Polyisobutylcyanoacrylate nanocapsules containing an aqueous core for the delivery of oligonucleotides, *Intern. J. Pharm.*, **214**: 13-16.

Lopez-Quintela, M.A. 2003. Synthesis of nanomaterials in microemulsions: formation mechanism and growth control, *Curr. Opin. Coll. Int. Sci.*, 8, 137-144

Reiss, H., (1975). Entropy-induced dispersion of bulk liquids, *J. Colloid Interface Sci.*, **53**: 61-70.

Rosen, M.J. (1978). Surfactant and Interfacial Phenomenon, John Wiley and Son, New York.

Schulman, J.H. and Riley, D.P. (1948). Structure of transparent water and oil dispersions, *J Colloid Interface Sci.*, **3**: 383-405.

Schulman, J.H. and Friend, J.A. (1949). Light scattering investigation of the structure of transparent oil-water disperse systems, *J Colloid Interface Sci.*, **4**: 497-509.

Shah, D.O. and Hamlin, R.M. (1971). Structure of water in microemulsion: electrical, birefringence and nuclear magnetic resonance studies, *Science*, **171**: 483-485

Shukla, A., Kiselev, M.A., Hoell, A. and Neubert, R.H.H. (2004). Characterization of nanoparticles of lidocaine in w/o microemulsions using small-angle neutron scattering and dynamic light scattering, *Indian Acad. Sci.*, **63(2)**: 291-295

Soppimath, K.S., Aminabhavi, T.M., Kulkarnia, A.R. and Rudzinski, W.E. (2001). Biodegradable polymeric nanoparticles as drug delivery devices, *J Controlled Release*, **70**: 1-20.

Talsania, S.K., Yongmei, W., Rajagopalan, R. and Mohanty, K.K. (1997). Monte Carlo Simulations for Micellar Encapsulation *J Colloid Interface Sci.*, **190**, 92-103.

Nave, S., Eastoe, J., and Penfold, J. (2000). What Is So Special about Aerosol-OT? 1. Aqueous Systems, *Langmuir*, 16(23): 8733-8740

Vauthier, C., Dubernet, C., Fattal, E., Pinto-Alphandary, H., Couvreur, P., (2003). Poly(alkylcyanoacrylates) as biodegradable materials for biomedical applications. Adv. Drug Deliv. Rev. 55, 519-548, 2003.

Wan, T., Zang, T.S., Wang, Y.C., Zhang, R. and Sun, X.C. (2010). Preparation of water soluble Am-AA-SSS copolymers by inverse microemulsion polymerization, *Polym. Bull.*, **65** : 565-576.

Watnasirichaikul, S., Davies, N.M., Rades, T., and Tucker, I.G. (2000). Preparation of biodegradable insulin nanocapsules from biocompatible microemulsions, *Pharm. Res.*, **17**: 684-689.

Watnasirichaikul, S., Rades, T., Tucker, I.G.  and Davies, N.M. (2002). In-vitro release and oral bioactivity of insulin in diabetic rats using nanocapsules dispersed in biocompatible microemulsion, *J Pharm Pharmacol.*, **54**: 473-480.

Yordanov, G. and Bedzhova, Z. (2011). Poly(ethylcyanoacrylate) colloidal particles tagged with Rhodamine 6G: preparation and physicochemical characterization, *Central Euro. J. Chem.*, **9**: 1062-1070.

# CHAPTER 5

## Synthesis and Characterization of Magnetic Iron Oxide Nanoparticles

### 5.1 Introduction

In Chapter 2, nanomaterials, nanoparticles, their different forms, synthesis and applications in drug delivery was introduced. In this chapter, the synthesis and characterisation of one type of nanoparticles namely magnetic iron oxide nanoparticles, IONs will be presented. Some of their properties and important parameters will also be described.

### 5.2 Objectives

The objective of this work, concerned with the preparation and characterization of IONs via chemical co-precipitation in order to gain further insight into the understanding of the structure and behaviour of iron oxide nanoparticles. Specifically, this work was designed to:

- Synthesize IONs by using a chemical co-precipitation method
- Determine the structure of the IONs
- Characterise the surface nature and magnetization of the IONs
- Investigate the effect of oleic acid content during the synthesis of IONs

This work was required to provide material for the magnetic hyperthermia studies (see Chapter 6) and to help with understanding the behaviour and properties of the materials during those studies.

## 5.3 Synthesis of IONs

The procedure for the synthesis of IONs via co-precipitaion followed a previously published method by Lopez and co-workers (2005). Two salt solutions containing 18.0 gm of iron (II) sulphate heptahydrate and 34.0 gm of iron (III) chloride hexahydrate, dissolved in 175 and 200 ml of water, respectively were prepared separately. The two salt solutions were thus mixed in a molar ratio of 1:2. After mixing, the mixtures were then titrated with 88 ml 30 % ammonium hydroxide under vigorous mechanical stirring at 333 rpm in a stirred reactor to achieve a pH value of 10 under inert conditions ($N_2$). Immediately, 8 ml of oleic acid was added to the alkaline solution and the mixture stirred for 1 h at $25^{o}$C. The resulting emulsion was heated up to 95 $^{o}$C. This is converted iron hydroxide to magnetite. As soon as the desired temperature was reached the suspension, now called ferrofluid was cooled down to room temperature.

1M of HCl was added to 10 ml of the ferrofluid to obtain a pH value of 2. A dark precipitate was obtained. The solution was decanted and the dark precipitate was resuspended, washed and centrifuged three times with water until the supernatant reached a pH value of 7. The precipitate was further resuspended and washed three times with ethanol. Finally, the precipitate was dried in a vacuum dessicator.

The whole procedure was repeated but adding different amount of oleic acid; 10, 6 and 4 ml. Figure 5.1a-c depicts the experimental setup and the final products in the synthesis of IONs.
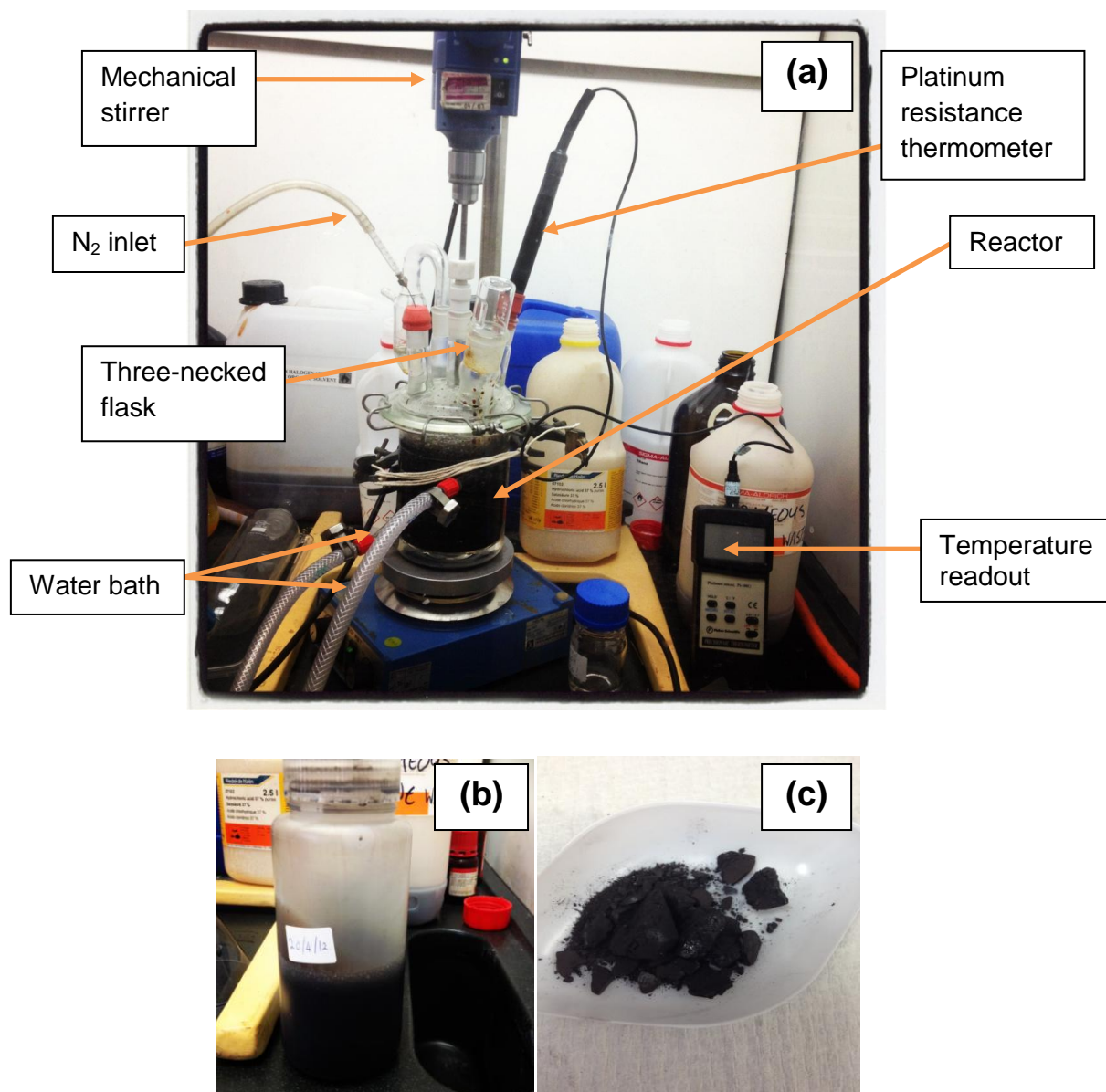
**Figure 5.1** The synthesis of IONs via co-precipitation method showing (a) the experimental setup, (b) IONs in solution form (ferrofluid) and (c) in dried and ground form.

## 5.4 Results and discussion

### 5.4.1 TEM of IONs

Figure 5.2 shows the TEM images of IONs synthesised using different amounts of oleic acid. It was observed that IONs prepared using this method showed slight nonuniformity in terms of shape and size and are therefore polydisperse.
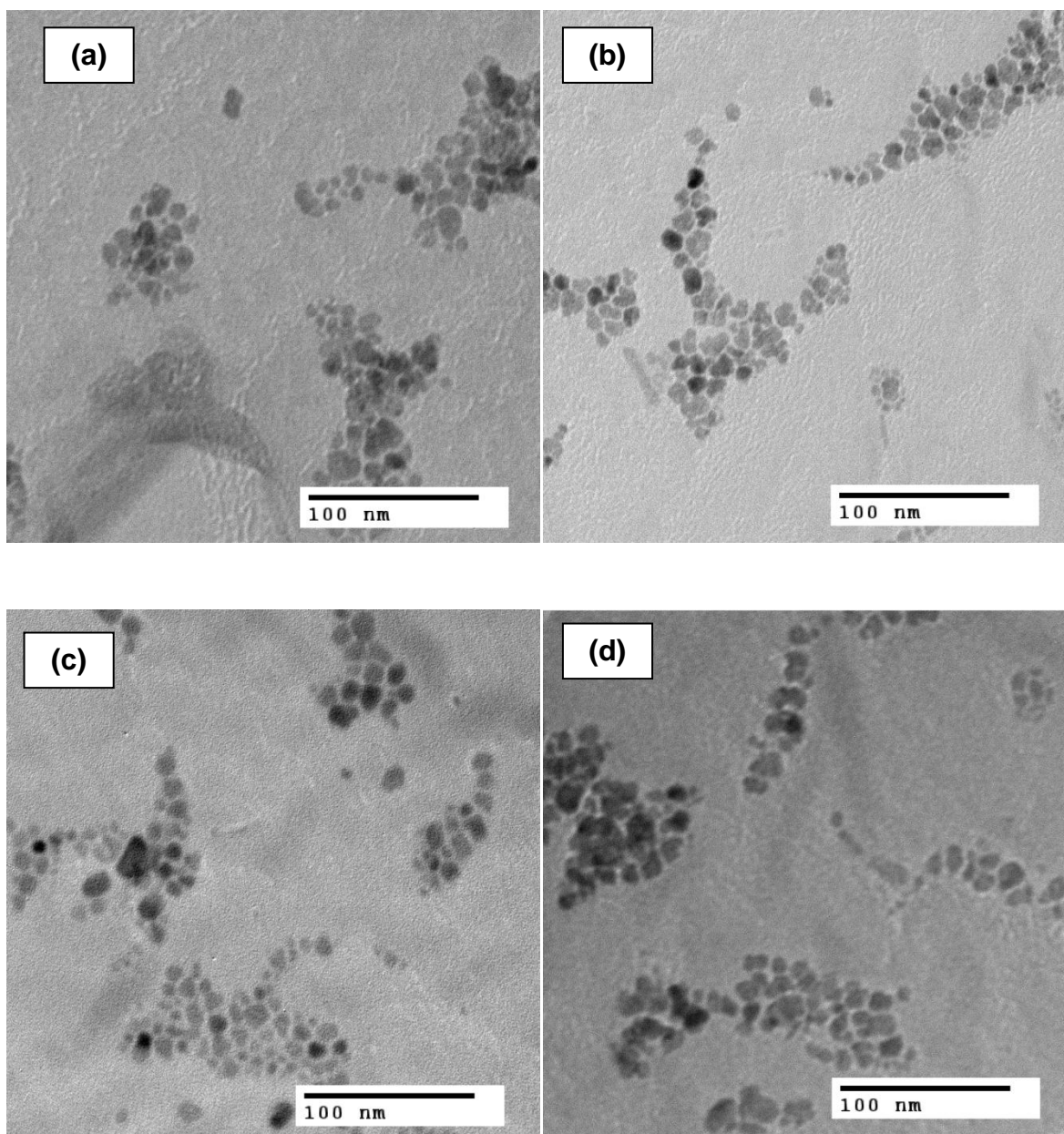
**Figure 5.2** TEM images showing the IONs prepared by co-precipitation method with (a) 4, (b) 6, (c) 8, and (d) 10 ml of oleic acid, respectively.

## 5.4.2 DLS of IONs

DLS was employed as an additional method to determine the particle size and distribution. Figure 5.3a-c showed the particle size distribution described as number, intensity and volume percent, respectively for IONs synthesised with different amount of oleic acid.
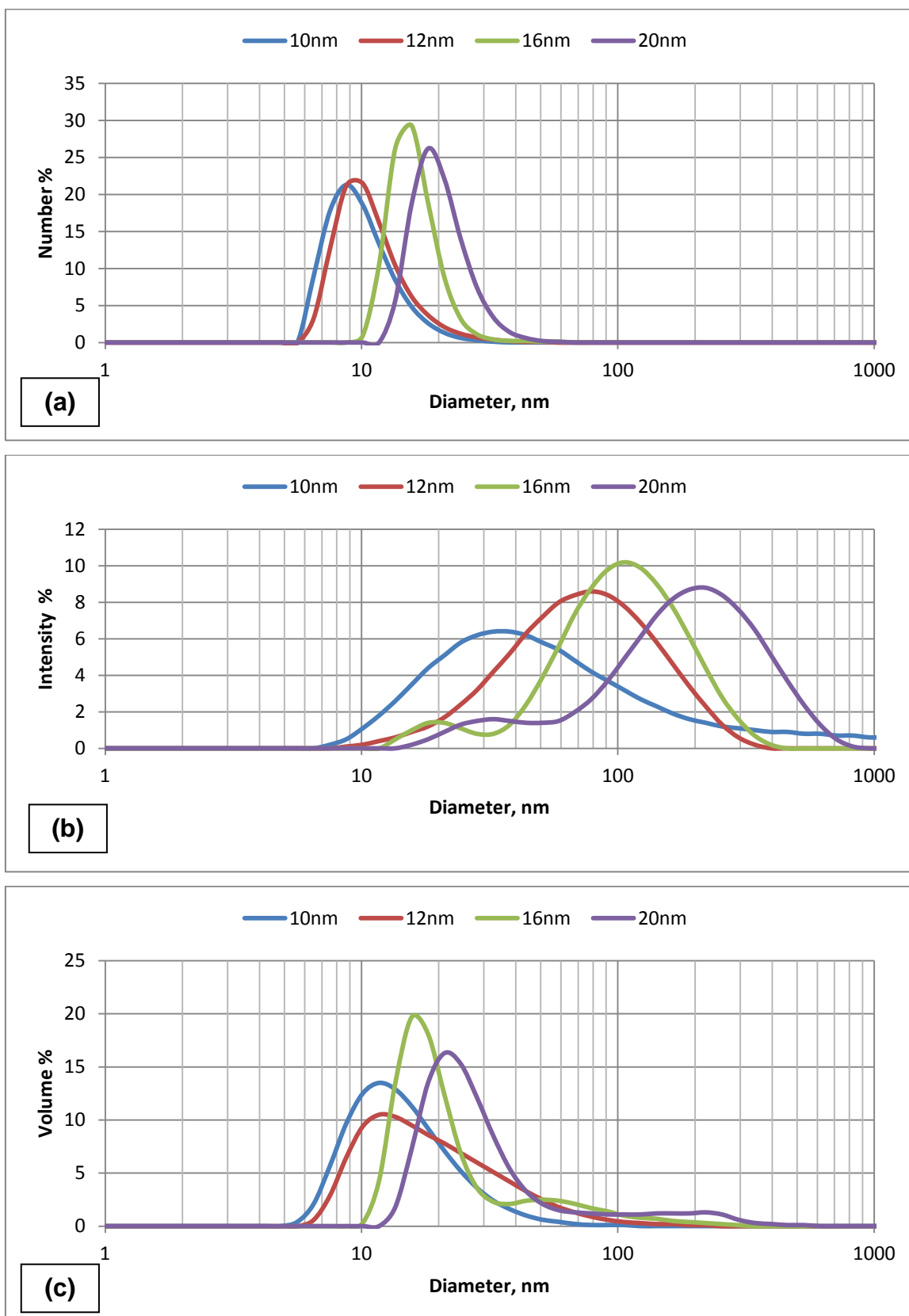
**Figure 5.3** The particle size distribution by DLS of IONs described as (a) number, (b) intensity and (c) volume %, respectively.

The figures showed that the range of size distributions varies when using the number, intensity and volume percent as the y-axis. The size range is however found to be wider for the intensity and volume percent compared to the number percent. The distribution by number percent also shows a higher percent values of 21 - 30 %. With that, in this work the size distribution represented by number percent is chosen to describe the mean size of the nanoparticle, since it is ultimately the number of particles undergoing magnetisation on RF field that will control hyperthermia heating.

As mentioned above, the sizes presented by the number percent are chosen to represent the mean sizes of the IONs. These sizes are then compared with that of equivalent data but from the TEM measurement as shown in Table 5.1. From the result, the hydrodynamic diameter measured by DLS was found to be larger than the size determined from TEM. This is expected since the hydrodynamic diameter includes the oleic acid stabilising ligand layer and the iron oxide nanoparticle core. For convenience, the mean diameter of IONs obtained for 4, 6, 8 and 8 ml of oleic acid by DLS in Table 5.1 is rounded to 20, 16, 12, and 10 nm from this point onward, when discussing the properties and behaviour of the particles.

**Table 5.1** The mean diameter of IONs from TEM and DLS measurement. For TEM, the particles were measured from the micrographs in order to elucidate mean and standard deviation (S.D.). PDI is the polydispersity index.

| Amount of Oleic Acid in the synthesis (ml) | Mean diameter ± S.D., nm | | |
|---|---|---|---|
| | TEM | DLS | PDI |
| 4 | 8.7 ± 3.8 | 20.4 ± 1.5 | 0.39 |
| 6 | 6.9 ± 3.1 | 16.3 ± 2.5 | 0.27 |
| 8 | 5.3 ± 2.7 | 11.5 ± 1.5 | 0.27 |
| 10 | 3.1 ± 1.5 | 10.2 ± 2.0 | 0.42 |

### 5.4.3 X-ray powder diffraction

Figure 5.4 shows X-ray diffraction, XRD patterns of the IONs with particle size 20 nm. It was observed that a series of peaks occurred at different 2θ values. The XRD

peaks observed were at 2θ = 30.03, 35.46, 43.04, 57.07, and 62.81°. These peaks correspond to (220), (311), (400), (422), and (440) Bragg reflections, respectively. Among these peaks, it was observed that three strong peaks stood out, the strongest one being the (311) Bragg reflection at 2θ = 35.46° followed by (440) and (220).
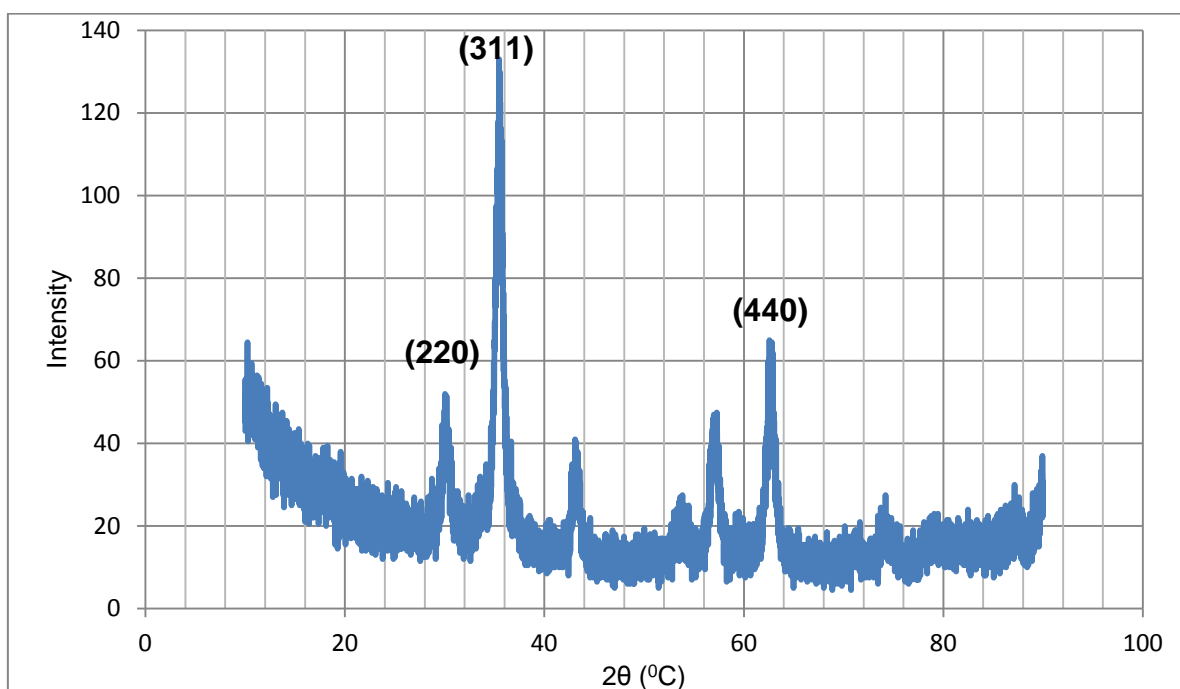


**Figure 5.4.** XRD pattern of IONs with particle size of 20 nm.

For the iron oxide nanoparticles with particle size of 16, 12 and 10 nm, similar XRD pattern at various 2θ were observed with the strongest peak at (311) Bragg reflection. The parameters for all of the three strong XRD peaks at (220), (311), and (440) were calculated for their d-spacing values and intensity ratio, $I/I_1$. These values were then tabulated and compared with those of standard iron oxide as presented in the JCPDS Card Number 19-629, 4-755, and 13-534 for standard magnetite, γ-maghemite and hematite, respectively as shown in Table 5.2.

From the table, the type of iron oxide nanoparticle can be inferred. This can be achieved by comparing each of the d-spacings for every particle size at different Bragg reflection angles with the standard data. For instance, for the particle size at 20 nm, the d-spacings at (220), (311), and (440) peaks give a value of 2.974, 2.529 and 1.478 Å, respectively. These values, when compared to the standard data,

closely matched that of the corresponding standard cubic phase of magnetite of 2.97, 2.53, and 1.49 Å (Table 5.3). This illustrated that the XRD pattern for the iron oxide nanoparticle with particle size 20 nm is that of magnetite. Similar comparison was performed for the rest of the particle sizes and it can be summarised that again in each case it matched that of the magnetite pattern. However, it is worth noting here that for the particle size of 10 nm, the pattern may resemble that of γ-maghemite. This might be reasonable since magnetite easily converts to γ-maghemite upon oxidation. However, since the values for the size of the particles are incredibly similar and that it is near impossible to state with conviction whether it is magnetite or γ-maghemite. It is clear that none of the samples resemble that of standard hematite, since the hematite XRD pattern has no peaks at (311) and (440) (see Table 5.3).

**Table 5.2** XRD experimental data at different particle sizes and comparing them with the standard iron oxide data from JCPDS Card

| | | | | | [*]JCPDS Card Number | | | | | |
| | | | | | 19-629 magnetite | | 4-755 γ-maghemite | | 13-534 hematite | |
| Lattice (hkl) | Particle Size (nm) | $2\theta$ | $I/I_{1, expt}$ | $d_{expt}$ (Å) | $I/I_1$ | d (Å) | $I/I_1$ | d (Å) | $I/I_1$ | d (Å) |
|---|---|---|---|---|---|---|---|---|---|---|
| (220) | 20 | 30.03° | 31.42 | 2.974 | 30 | 2.97 | 34 | 2.95 | 8 | 1.26 |
| | 16 | 30.14° | 31.31 | 2.963 | | | | | | |
| | 12 | 30.13° | 33.95 | 2.964 | | | | | | |
| | 10 | 30.13° | 34.61 | 2.964 | | | | | | |
| (311) | 20 | 35.46° | 100 | 2.529 | 100 | 2.53 | 100 | 2.52 | - | No peak |
| | 16 | 35.44° | 100 | 2.531 | | | | | | |
| | 12 | 35.41° | 100 | 2.533 | | | | | | |
| | 10 | 35.41° | 100 | 2.522 | | | | | | |
| (440) | 20 | 62.81° | 47.09 | 1.478 | 40 | 1.49 | 53 | 1.48 | - | No peak |
| | 16 | 62.83° | 49.70 | 1.478 | | | | | | |
| | 12 | 62.86° | 47.09 | 1.477 | | | | | | |
| | 10 | 62.86° | 52.66 | 1.479 | | | | | | |

[*]JCPDS Number Card for magnetite, γ-maghemite and hematite are shown in Appendix C.

**5.4.4 FTIR of IONs**

The Fourier transform infrared spectroscopy (FTIR) analysis was performed on dried powders to characterize the functional group and the surface characteristics of the iron oxide nanoparticles. Figure 5.5 showed FTIR spectra of iron oxide nanoparticles prepared by co-precipitation. The spectrum showed the presence of organic peaks. The peak at ~3284 to 3325 cm$^{-1}$ observed in the spectrum is attributed to the -OH group. The peaks at ~2900 and ~2800 cm$^{-1}$ are due to the stretching vibrations of -CH$_2$ and -CH$_3$ in oleic acid. The peak at ~1709 cm$^{-1}$ is due to the vibration of the carbonyl group, C=O of oleic acid. The peak at ~1500 and ~1600 cm$^{-1}$ is the vibration of C=C in oleic acid. The peaks at ~1500 and ~1400 cm$^{-1}$ are attributed to the vibration of -CH. Finally, the peak at ~ 540 cm$^{-1}$ relates to an Fe−O bond vibration of the iron oxide nanoparticles. Taken together, this provides strong evidence for the presence of a stabilising ligand of adsorbed oleic acid on the IONs surface.
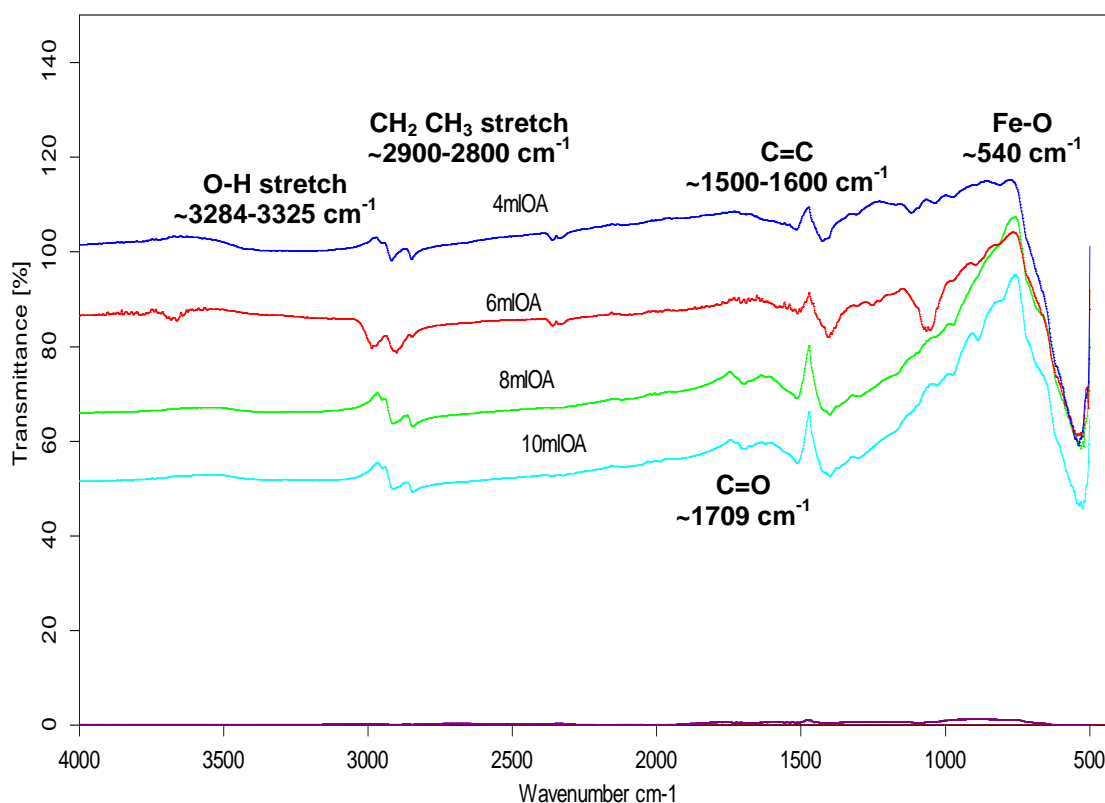


**Figure 5.5** The FTIR spectra of IONs with amount of oleic acid (OA) at 4, 6, 8 and 10 ml.

## 5.4.5 Magnetic behaviour

The behaviour of magnetic materials, M in the presence of an applied field, H is well described by the characteristic sigmoidal shape of the M-H curve known as a hysteresis loop. This loop is characterized by a parameter called coercivity which is related to the thickness of the curve. Dealing with fine particles, the coercivity is most important, and it is strongly size-dependent. It has been reported that as the particle size is reduced, the coercivity increases to a maximum and then decreases toward zero (Akbarzadeh *et al.*, 2012; Zhao *et al.*, 2009).

Figures 5.6a-d showed the hysteresis loops for different sizes of the synthesised magnetic nanoparticles. The hysteresis loops were measured with an applied field of 70000 Oersteds (Oe) which is equivalent to 7 T. Figure 5.6a shows the hysteresis loop for the magnetic nanoparticle with diameter of 20 nm. The curve increased sharply from the origin and then reduces its slope until it reaches a plateau representing the saturation magnetization. It is observed that the value for the saturation magnetization ($M_s$) is 77 emu/g when the applied field reaches 2000 (oe), and the coercitivity ($H_c$) approximately is zero Oersteds (oe). Figures 5.6b-d show similar pattern of the curves as in Figure 5.6a but at 16, 12, and 10 nm, respectively.
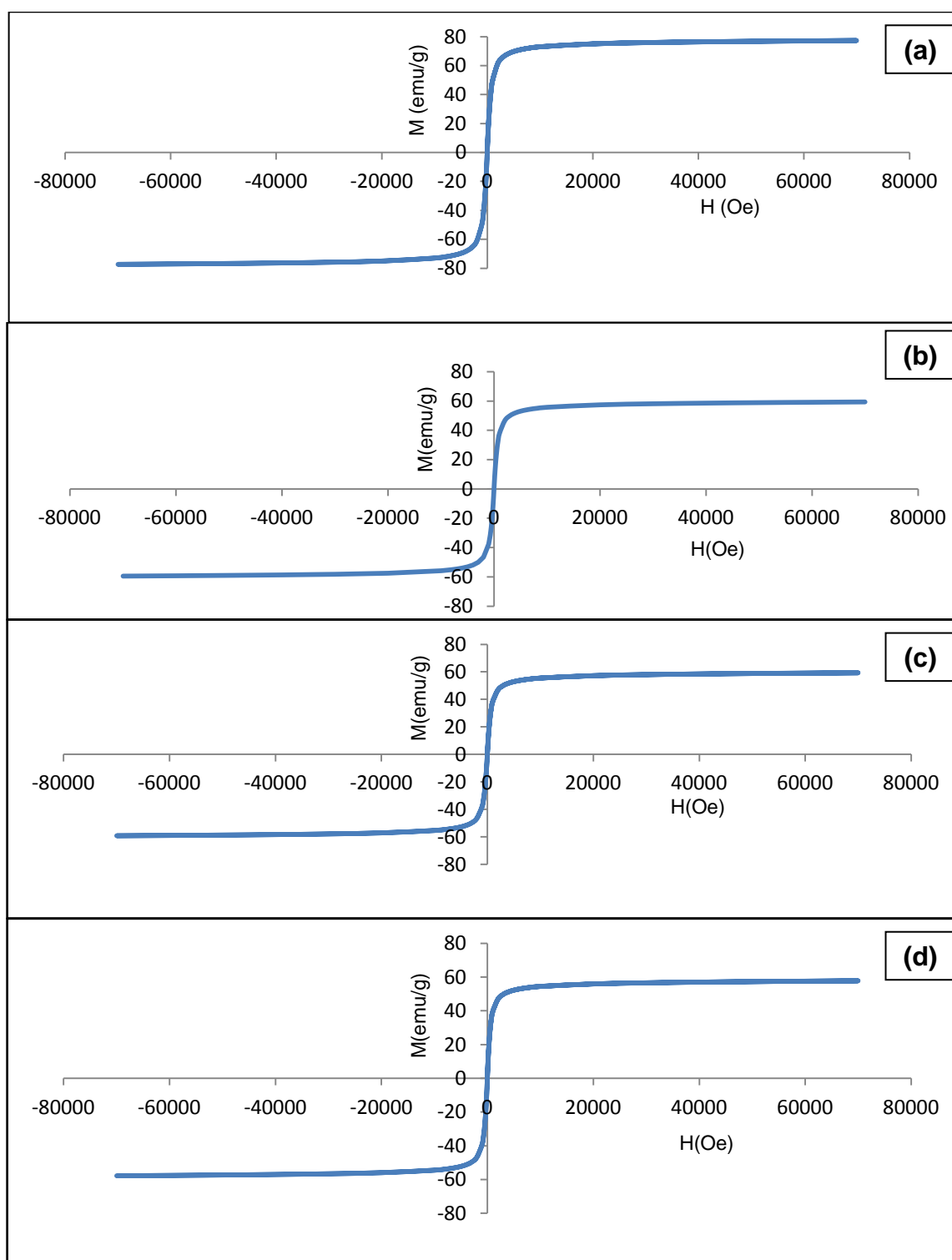
**Figure 5.6** Magnetic hysteresis of IONs with particle size of (a) 20 nm, (b) 16 nm, (c) 12 nm, and (d) 10 nm, measured using a Quantum Design MPMS SQUID VSM Magnetometer (San Diego, USA) at 300 K using a field range of ± 70000 Oe (± 7T).

In order to quantify further these observations, equivalent data but at different sizes was tabulated as shown in Table 5.3. From the table, it was observed that the value of Ms increases with the increment of the size of the particle. This is expected due to the surface disorder as explained in a previous report (Rao *et al.*, 2007). This result is very satisfying as it is known that larger particle should exhibit higher magnetisation. This observation is also in agreement with the observed behaviour previously reported by Khandar and co-workers (2011) by synthesising similar magnetic nanoparticle but in organic solvents. It is also worth noting here that the value for bulk magnetite nanoparticles is 100 emu/g and the Ms values depending on the particle size may reach up to 80 percent of the bulk saturation value as reported in the literature (Cornell and Schwertmann, 1996). The value of 77 emu/g for the 20 nm particles is very close to this. From the table it also indicated that the iron oxide nanoparticles synthesised by the co-precipitation method has zero coercivity but high saturation magnetization value. This indicates that the sample becomes superparamagnetic and exhibit superparamagnetism behaviour (Jiang *et al.*, 2004).

This means that the nanoparticles become magnetic in the presence of an external applied field, but will be spontaneously demagnetized once the applied field is removed. Therefore, these nanoparticles have zero coercivity and have no hysteresis. This spontaneous 'switching on' and switching off' ability gives them the unique advantage in working in biological environments i.e. applying magnetic field only when needed and at an appropriate time or interval.

**Table 5.3** The values of saturation magnetisation and coercivity at different particle size.

| Oleic Acid, ml | Size, nm | Saturation magnetisation, Ms (emu/g) | Coercivity, Hc |
|---|---|---|---|
| 4 | 20 | 77 | 0 |
| 6 | 16 | 59 | 0 |
| 8 | 12 | 59 | 0 |
| 10 | 10 | 58 | 0 |

## 5.4.6 TGA analysis

Figure 5.7 shows the TGA curve in air for 10 nm IONs. The weight loss curve shows three step inflections in the temperature range of 40-700 $^oC$. The first step of weight loss occurs at 40–200 °C. This due to the endothermic loss of surface OH groups in IONs (Chu *et al.* 2007). The maximum weight loss occurs in the second step. The combustion of oleic acid begins at a temperature higher than 200 °C, and is nearly completed around 400 °C. The final weight loss occurred when the temperature was higher than 500 °C. A previous work has shown that the $Fe_3O_4$ will transfer to $Fe_2O_3$ by surface oxidation when the temperature is higher than 500 $^oC$ (Xuan *et al.*, 2007). Therefore, from the TG analysis, the weight ratio of the $Fe_3O_4$ core is about 80.0 % by weight, the remainder (20.0 %) being the oleic acid surface ligands. These data were then used to calculate the density of oleic acid molecules on the nanoparticle surface by taking into account the density of magnetite (5.24 g/cm$^3$) and the nanoparticle diameter (3.1 nm) The formula by Chang and co-workers (2009) is adopted here to calculate the surface density. From the formula, the calculated density is 1.44 oleic acid molecules per nm$^2$ (refer to Appendix F for calculations).
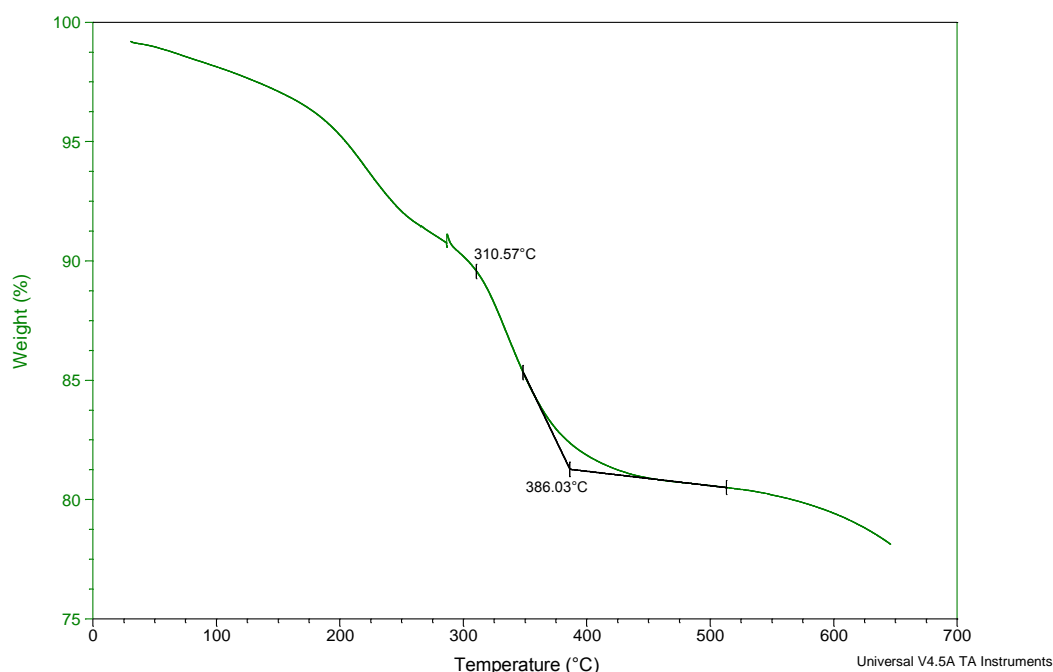


**Figure 5.7** TGA curve for IONs at particle size of 10 nm.

## 5.5 Conclusion

The use of magnetic nanoparticles such as IONs in the medical field has paved new ways into targeting and controlled drug delivery. Hence, it is imperative to prepare IONs with the proper properties such as the correct size, shape and magnetic capability in order to get the optimum output from them. In this work, IONs have been successfully prepared via co-precipitation of $Fe^{2+}$ and $Fe^{3+}$ with aqueous ammonium hydroxide solution. Their structure and composition are characterized by TEM, DLS, XRD and FTIR. The TEM image showed that the iron oxide nanoparticles are polydisperse while the XRD pattern showed that the iron oxide nanoparticles exhibit a cubic crystalline structure. The average particles sizes were also found to be decreasing with the increment of the content of oleic acid. The magnetism of the iron oxide nanoparticles was also dependent on the content of the oleic acid. The value of the maximum saturation magnetization, $M_S$ is 77 emu/g at the lowest oleic acid content and 58 emu/g at the highest oleic acid content. Finally the iron oxide nanoparticles prepared in this work, via co-precipitation method showed superparamagnetic behaviour at room temperature as shown by the hysteresis loop observed.

It should be emphasised that there are many alternative approaches to making higher quality new monodisperse IONs (Sun *et al.*, 2004), but that these are much more complex and yield low amounts (often only 10's of mg). In this work, a very simple approach was used requiring only low toxicity and pharmaceutically approved chemicals. The method is also scalable. Here it was used on a 10 to 20 g scale, but it could easily be done on an industrial scale. This is essential, bearing in mind the amount required for subsequent studies and the envisaged end use, which would require low cost mass production.

## 5.6 References

http://apps.webofknowledge.com

Akbarzadeh, A., Samiei, M., and Davaran, S. (2012). Magnetic nanoparticles: preparation, physical properties, and applications in biomedicine, *Nanoscale Research Letters*, **7**: 144-157.

Chang, Y., Bai, Y.P., Teng, B., and Li, Z.L. (2009). A new drug carrier: Magnetite nanoparticles coated with amphipilic block copolymer, *Chinese Sci. Bull.*, **54(7)**: 1190-1196.

Chu, W., Chernavskii, P. A., Gengembre, L., Pankina, G.A., Fongarland, P., and Khodakov, A.Y. (2007). Cobalt species in promoted cobalt alumina-supported Fischer–Tropsch catalysts, *J. Catal.* **252**: 215-230.

Cornell, R.M. and Schwertmann, U. (1996) in *The iron oxides: structure, properties, reactions, occurrence and uses*, Weinheim, New York.

Jiang, W., Yang, H.C., Yang, S.Y., Horng, H.E., Hung, J.C., Chen Y.C., and Hong, C.Y. (2004). Preparation and properties of superparamagnetic nanoparticles with narrow size distribution and biocompatible, *J Magn Magn. Mater.*, **283**: 210-214

Khandhar, A.P., Ferguson, R.M., and Krishnan, K.M. (2011). Monodispersed magnetite nanoparticles optimized for magnetic fluid hyperthermia: Implications in biological systems, *J. Applied Phys.* 109(7): 07B310-07B310-3

Lopez, M.T.L., Duran, J.D.G., Delgado, A.V. and Caballero, F.G. (2005). Stability and magnetic characterization of oleate-covered magnetite ferrofluids in different nonpolar carriers, *J Colloid Interface Sci.*, **291**: 144-151.

Rao, B.P., Caltun, O., Cho, W.S., Kim, C.O , and Kim, C. (2007). Synthesis and characterization of mixed ferrite nanoparticles, *J Magn. Magn. Mater.,* **310**: e812–e814

Sun, S. H., Zeng, H., Robinson, D. B., Raoux, S., Rice, P. M., Wang, S. X., and Li, G. X. (2004). Monodisperse $MFe_2O_4$ (M = Fe, Co, Mn) nanoparticles. *J. Am. Chem. Soc.*, **126 (1)**; 273-279.

Xuan, S., Hao, L., Jiang, W., Gong, X., Hu, Y., and Chen, Z. (2007). A facile method to fabricate carbon-encapsulated $Fe_3O_4$ core/shell composites, *Nanotechnology*, **18**: 035602-035608.

Zhao, D.L., Zenga, X.W., Xia, Q.S., and Tang, J.T. (2009). Preparation and coercivity and saturation magnetization dependence of inductive heating property of $Fe_3O_4$ nanoparticles in an alternating current magnetic field for localized hyperthermia, *J. Alloys Compounds*, **469**: 215–218.

# CHAPTER 6

## Developing Nanoparticle containing Capsule Coatings

## for Magnetic Hyperthermia

## 6.1 Introduction

In order to develop a capsule coating that can be melted by magnetic hyperthermia, it is necessary to investigate the nanoparticle loading required to achieve adequate heating and the thickness of the coating required to protect the capsule until release is required. In this work, combinations of coating materials, i.e. fatty acids, paraffins and IONs in various proportions were investigated in order to optimise the formulation for the targeted releases purposes. The optimisation was focused on the susceptibility of the coating formula upon exposure to a radiofrequency field. The power level for heating employing magnetic nanoparticle hyperthermia, MNH will also be described. This chapter ends by reporting the results from dissolution studies on the coated capsules.

## 6.2 Objectives

The aim of this study was to investigate the utility of hyperthermia treatment using magnetised IONs. To do this, the hard capsules were coated with various amounts of IONs in the coating layers. The addition of IONs allowed the capsules to be heated at an appropriate time, in order to release the drug, by exposure of the capsule to an external magnetic field.

In order to achieve the aim of this study, the specific objectives were:

- To assess the effectiveness of fatty acids and paraffins as coating materials.
- To formulate an optimum composition of the coating materials and IONS to be embedded in the coatings.

- To find the optimum radiofrequency and the power level for heating the IONs with MNH

## 6.3 Results and Discussion

In order to find the optimum coating materials, the materials must melt at a safe and accessible hyperthermia temperature but also withstand the heat of normal body temperature and the various pH gradients of the environment in the GI tract. These are crucial and become the determining factors for a good and robust coating. Therefore, a good coating should be resistant to body temperature, but melt at a temperature not too high to achieve by external excitation. It should also be pH insensitive due to the wide ranging pH variation through the GI tract. Results of the thermal properties of the investigated coating materials individually and as mixtures will be presented in the following sections.

### 6.3.1 Thermal analysis of individual coating materials and their mixtures

In this work, an investigation was carried out to find the optimum composition (mixtures) to coat the capsule. Two saturated fatty acids, namely lauric and myristic acids, were chosen and were subjected to heating, individually as well as their mixtures at different mole ratios. The two fatty acids differ only in the number of carbon in the hydrocarbon chain i.e. C14 and C12; an increase of 2 methylene ($CH_2$) groups. The other material investigated were paraffins, namely eicosane ($C_{20}H_{42}$) and docosane ($C_{22}H_{46}$).

### 6.3.1.1 Individual fatty acids

Both of the fatty acids i.e lauric and myristic acid are solid at room temperature. Solids will melt when subjected to continuous heating. They will change from the solid state to the liquid state when the heating temperature reaches the melting point or the fusion temperature.

Figures 6.1a and b showed the DSC curves for the individual fatty acids when subjected to continuous heating. Figure 6.1a showed the DSC curve for myristic acid.
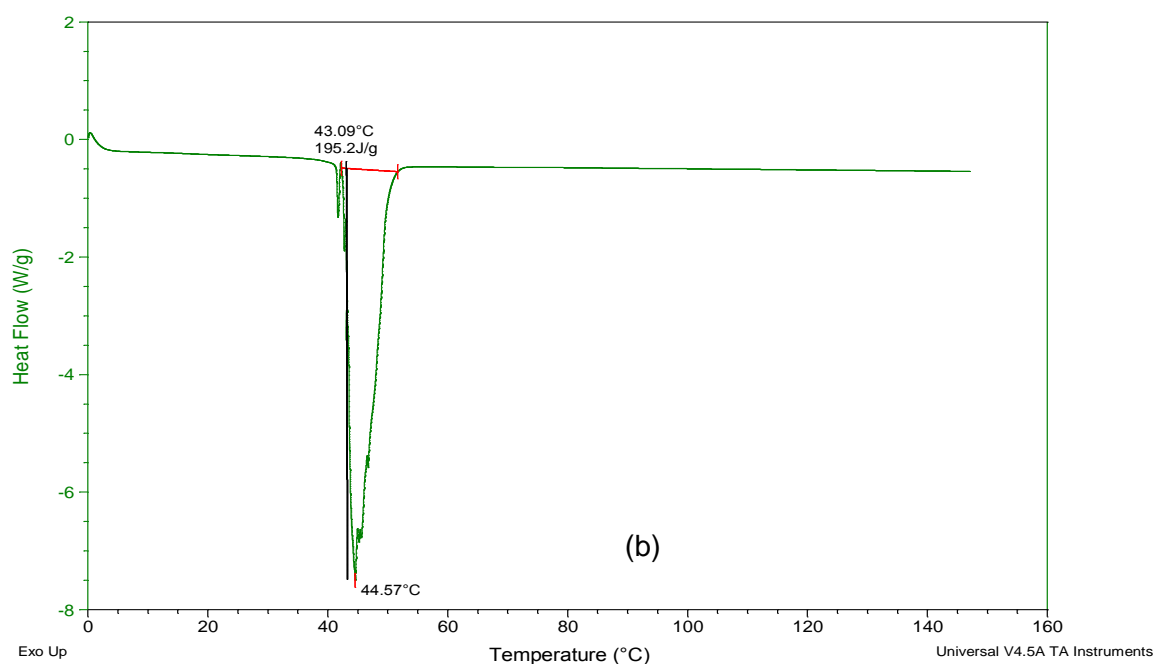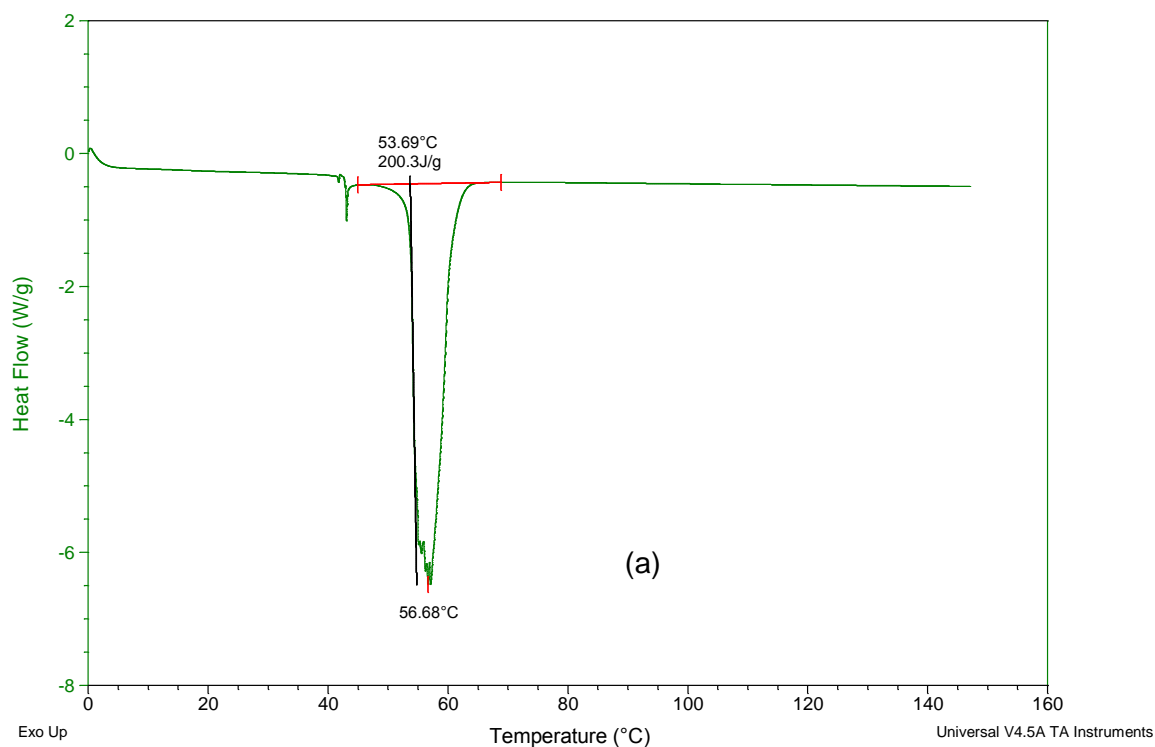


**Figure 6.1** DSC curve for (a) myristic acid and (b) lauric acid

From the curve, a sharp peak is observed at 56.7°C. The total area under the curve which corresponds to the latent heat of fusion for myristic acid was found to be 200.3 J/g with a melting point of 53.7°C. Part b of Figure 6.1 showed equivalent data, but for lauric acid. A similar trend in the curve was observed as for that depicted in Figure 6.1a. The peak occurred at 44.6°C and the latent heat of fusion was found to be 195.2 Jg$^{-1}$ with a melting point of 43.1°C. From the results, it showed that the melting point and the latent heat for myristic acid are higher compared to lauric acid. This difference in the melting point is due to myristic acid having a longer hydrocarbon chain length when compared to lauric acid: a difference of 2 CH$_2$ groups which translates to about 0.252 nm in length. It is known that when any solid materials are heated, their atoms move rapidly due to increase in the kinetic energy. At the phase transition temperatures, when the atoms have acquired enough energy, the materials change from their original solid state to liquid state. With that, myristic acid which is a longer fatty acid requires more latent heat compared to lauric acid in order for phase transition to take place. The difference is 5 J g$^{-1}$.

### 6.3.1.2 Individual paraffins

Similar procedures were repeated for the individual paraffins namely eicosane (C$_{20}$H$_{42}$) and docosane (C$_{22}$H$_{46}$). Figure 6.2a and b showed the DSC curves for docosane and eicosane, respectively. From the DSC curves, a sharp peak at 44.7°C was detected for docosane (Figure 6.2a) and 40.1°C was detected for eicosane (Figure 6.2b). The latent heat for docosane was calculated to be 251.2 Jg$^{-1}$ with a melting point of 43.7°C, while for the eicosane counterpart the melting point was observed at 37.8°C with a latent heat of 259.5J/g.
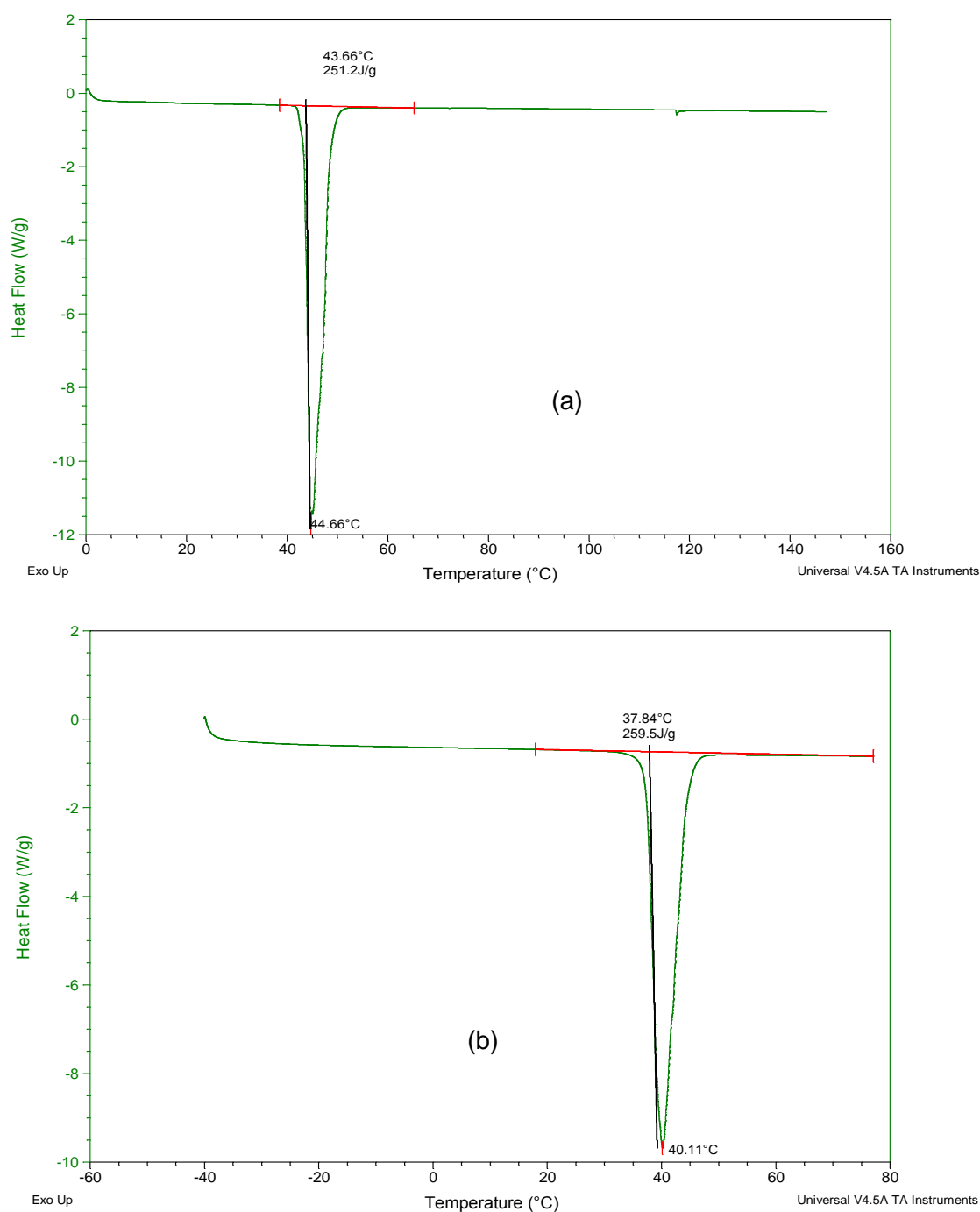
**Figure 6.2** DSC curve for (a) docosane and (b) eicosane

The values of the melting point and latent heat observed for both of the paraffin and fatty acids are in good agreement with the values reported in the literature (Domalski and Hearing, 1996; van Miltenburg *et al.*, 1999).

## 6.3.2 Thermal analysis of mixtures

It is known that mixtures do not only exhibit different properties compared to their single component but also can usually be produced at lower cost. The superiority in performance for mixtures is largely due the synergistic interaction amongst the mixtures molecules. Many contributions on mixtures have been reported in the literature such as in surfactant systems (Clint and Walker, 1975; Hamdan and Laili, 1995), triglycerides (Deman *et al.*, 1983), lipids (Mabrey and Sturtevant, 1976), and fatty acids (Cedeno *et al.*, 2001; Costa *et al.*, 2007; Inoue *et al.*, 2004))

### 6.3.2.1 Mixtures of fatty acids

Figure 6.3 showed the DSC curves for the mixture of lauric acid and myristic acid at different mole ratios. From these curves, the melting point of each ratio of myristic acid was elucidated and further plotted as shown in Figure 6.4. With that information becoming available (Figure 6.4), the behaviour of these mixtures becomes obvious. The result showed that the melting point in the mixture of the two fatty acids was always lower than the individual fatty acid. This agrees closely with the values reported in the literature (Cedeno *et al.*, 2001). In addition, the melting point values of the mixtures were also observed to be decreasing in a crescent manner with the increment of mole percent of myristic acid with three distinct regions. The first region commences from 0 and 30 mole percent of myristic acid. Followed by the second region within 30-50 and finally the third region continue onward from 50 to 100 mole percent of myristic acid. This result is in good agreement with previously reported work (Costa *et al.*, 2007).
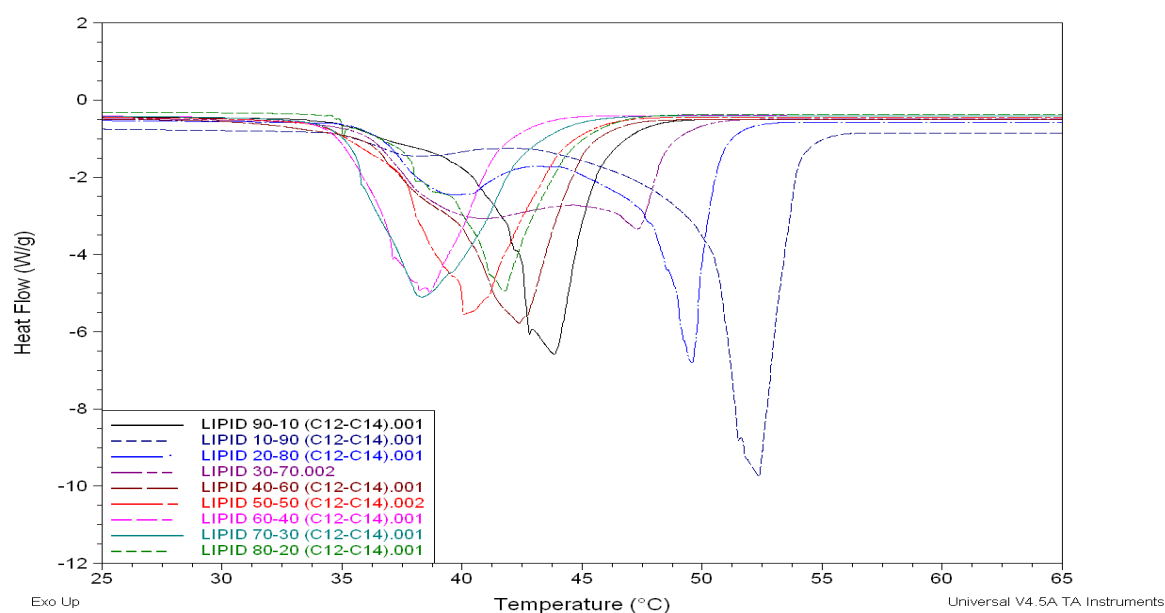
**Figure 6.3** DSC curves for the mixture of myristic acid and lauric acid at different mole percent
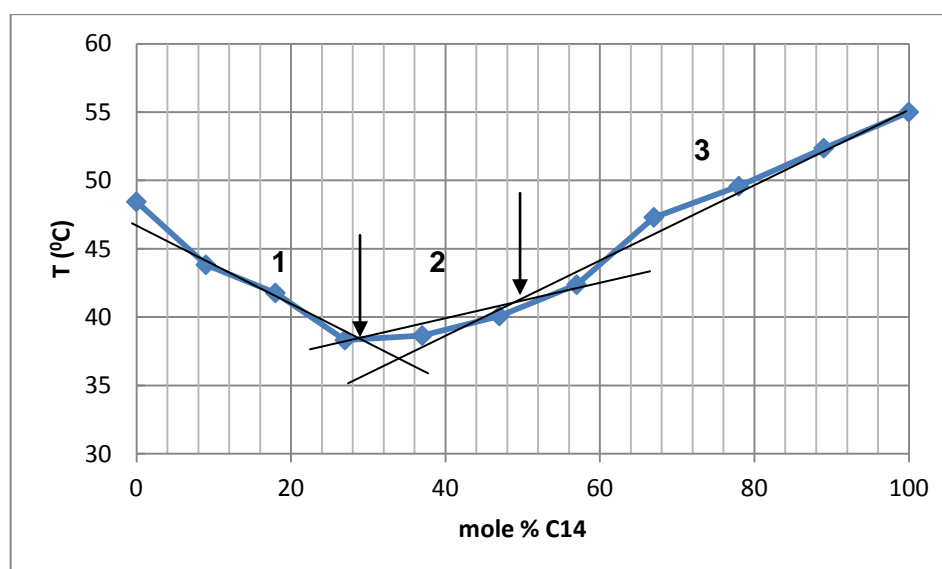


**Figure 6.4** The melting points for the mixture of lauric and myristic acid at different mole percent of myristic acid showing the 3 distinct regions.

In order to elucidate the effect of embedding oleic acid coated IONs in the fatty acids, two compositions of the fatty acid mixtures at percent weight ratios of 40:60 and

60:40 were chosen as shown in Figure 6.5. The results showed that in both of the systems, the melting points dropped slightly with the increment of ION content. This suggests that the effect of IONs on the melting points of the mixtures is small but quite significant, given the necessity to keep the melting point above, but not too far above, body temperature.
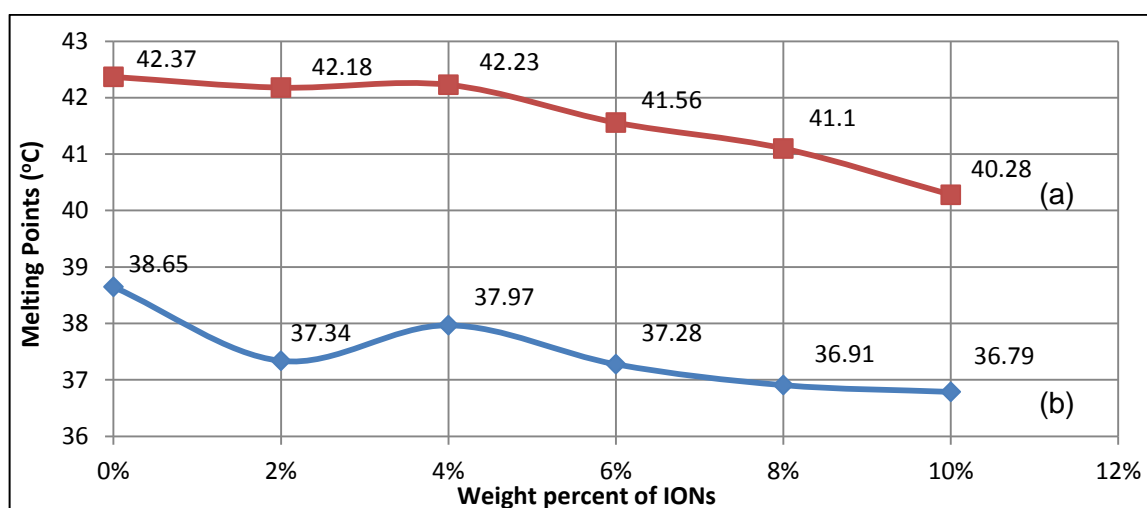


**Figure 6.5** The variation of melting point values for C12:C14 mixtures with the percent by weight of IONs at (a) C12:C14 (40:60) w/w (b) C12:C14 (60:40) w/w

## 6.3.2.2 Mixtures of paraffins

The mixing behaviour of paraffins with different hydrocarbon chain lengths are of great industrial importance and it was discussed in a number of publications (Bonsor and Bloor, 1977; Dorset, 1986; Gilbert, 1999) with the first publication by Mazee (1958). Based on this information, two paraffins, namely eicosane and docosane, which also differed by 2 $CH_2$ groups were chosen and mixed at various mole percent of docosane.

Figure 6.6 showed the variation of the melting points with the mole percent of docosane. The observations were similar to those observed for mixed fatty acids (Figure 6.5) but with a possibility of 5 regions.
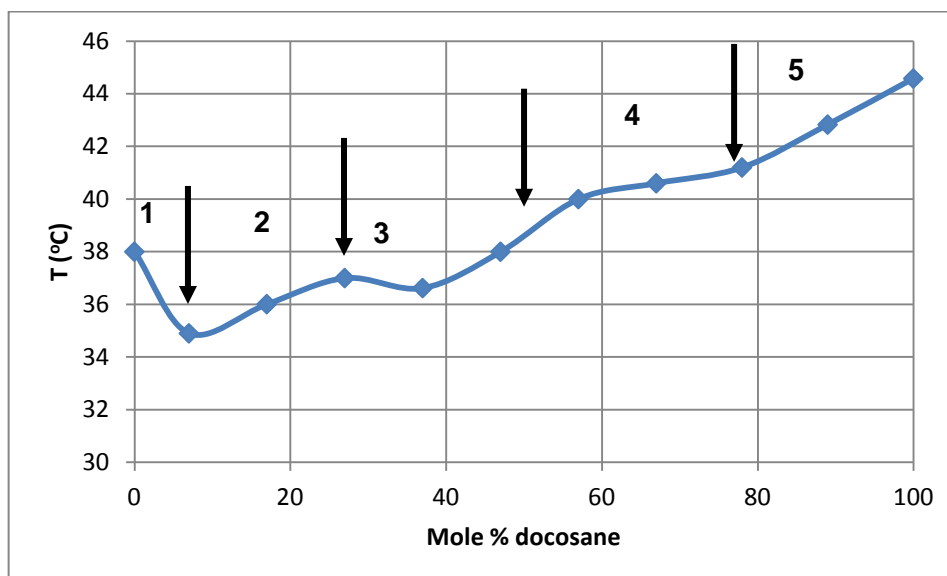
**Figure 6.6** The melting points for the mixture of eicosane and docosane at different mole percent of docosane showing 5 possible regions.

The first region ranged from 0 to 8 mole percent of docosane, followed by the next regions ranging from 8 to 20 (region 2), 20 to 50 (region 3), 50 to 80 (region 4) and finally the fifth region ranging from 80 to 100 percent weight of docosane. These results suggest that there are many transitions occurring when both of these paraffins are heated. This behaviour compares well with that reported previously using the same paraffins. Lüth and co-workers (1974) reported that when constructing the phase diagram of eicosane and docosane, they found that the phase diagram exhibited not less than 6 distinct solid phases. Here we found at least five regions and felt that for this work the findings are adequate and in good agreement with the previously reported data. No attempt was made to explain the missing region as it is beyond the scope of this work. The key requirement was simply to identify a mixture with an appropriate melting point.

Figure 6.7 showed equivalent data to that of Figure 6.5 but with IONS embedded in (a), eicosane, (b), docosane and (c), its mixture. A similar trend in the dependency of melting points with the increment of IONs content was observed illustrating little or no dependency of melting point in the presence of IONs for the eicosane system.

However, for docosane, there was a slightly larger decrease in the melting point effect as the amount of IONs was increased.
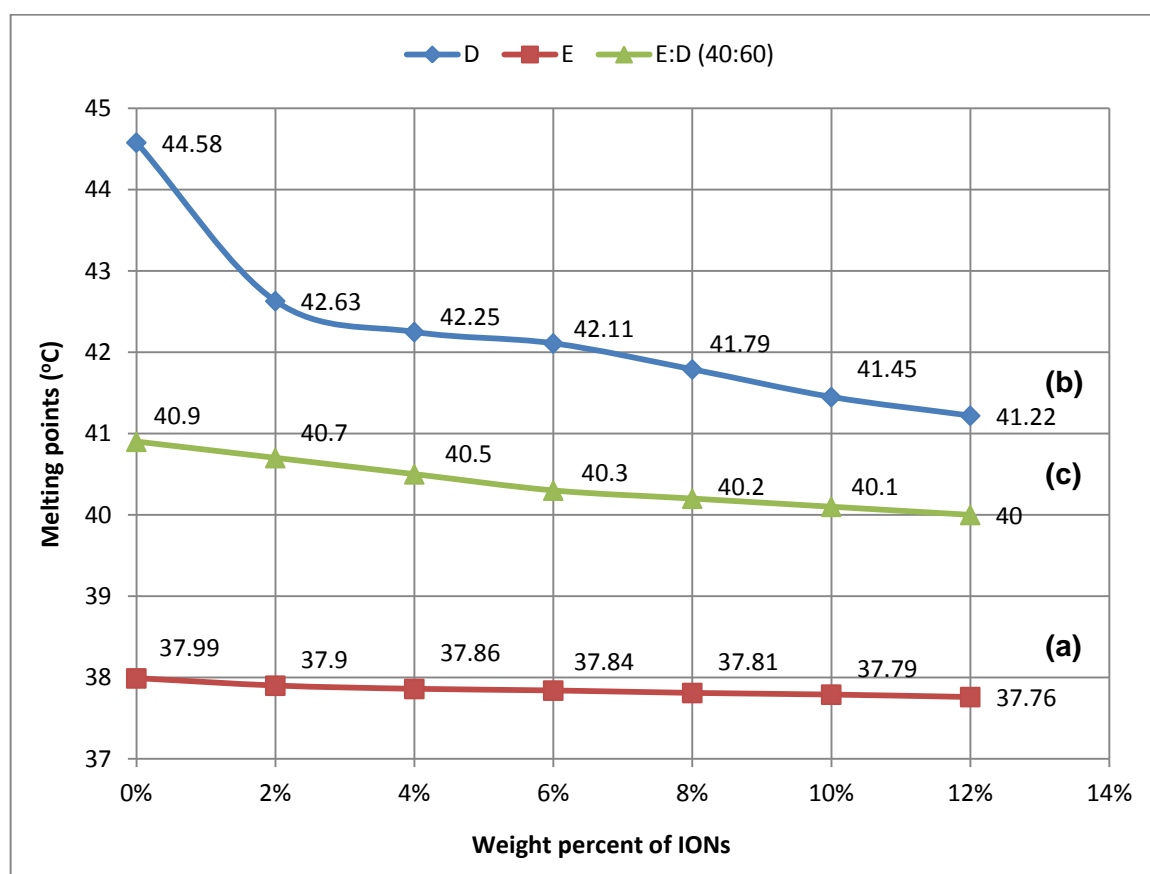


**Figure 6.7** The melting point values for (a) eicosane, (b) docosane and (c) its mixture at 40:60 (w:w) upon addition of variable amounts of IONs. E and D represent eicosane and docosane, respectively.

### 6.3.3 Hyperthermia studies

For the hyperthermia studies, four compositions of ferrofluid were selected. The compositions were those using 4, 6, 8, and 10 ml of oleic acid (OA) during synthesis which corresponds to particle sizes of 20, 16, 12, and 10 nm, respectively. Various frequencies of RF radiation produced by an external RF device (magneTherm) using two different coils turn were applied in order to observe the heating effect.

**6.3.3.1 Frequencies with 9 turn coil**

In this part of the work, only IONs were used in order to observe their heating ability. When a magnetic field at various frequencies is applied, the IONs, being superparamagnetic, will gain magnetism and start to oscillate. This oscillation will then generate heat during exposure to the magnetic field. The heating temperature was then measured and plotted. The values for the frequencies, voltage, current and magnetic field for the 9 turn coil are shown in Table 6.1.

**Table 6.1** Values of frequencies, voltage, current and magnetic field for the 9 turn coil (www.nanotherics.com)

| Nominal Frequency, (kHz) | DC power supply Voltage (V) | DC power supply Current (A) | Magnetic field (mT) |
|---|---|---|---|
| 173.9 | 14.6 | 12.2 | 23.0 |
| 521.3 | 22.5 | 11.0 | 24.0 |
| 737.5 | 17.3 | 7.3 | 17.0 |

Figures 6.8a-c showed the time-dependent temperature curves for each of the particle sizes at 173.9, 521.3, and 737.5 kHz with 9 turn coil. It was observed that all of the figures showed a nonlinear relationship for all four of the particle sizes at all three different frequencies. Heating rates are higher initially, but progressively slow down and eventually the temperature equilibrates. Presumably this is the temperature at which heat loss to the environment is equal to heat input from the hyperthermia heating effect

As shown in Figure 6.8a, after being exposed for 600 seconds, the maximum temperature ranged from 50.2 to 71.2°C. The maximum temperature reached 71.2 °C for the particle size at 10 nm. Figure 6.9 summarised the results obtained from both Figures 6.8b and c where the maximum temperatures are plotted against their corresponding sizes and frequencies after 600 seconds exposure time.
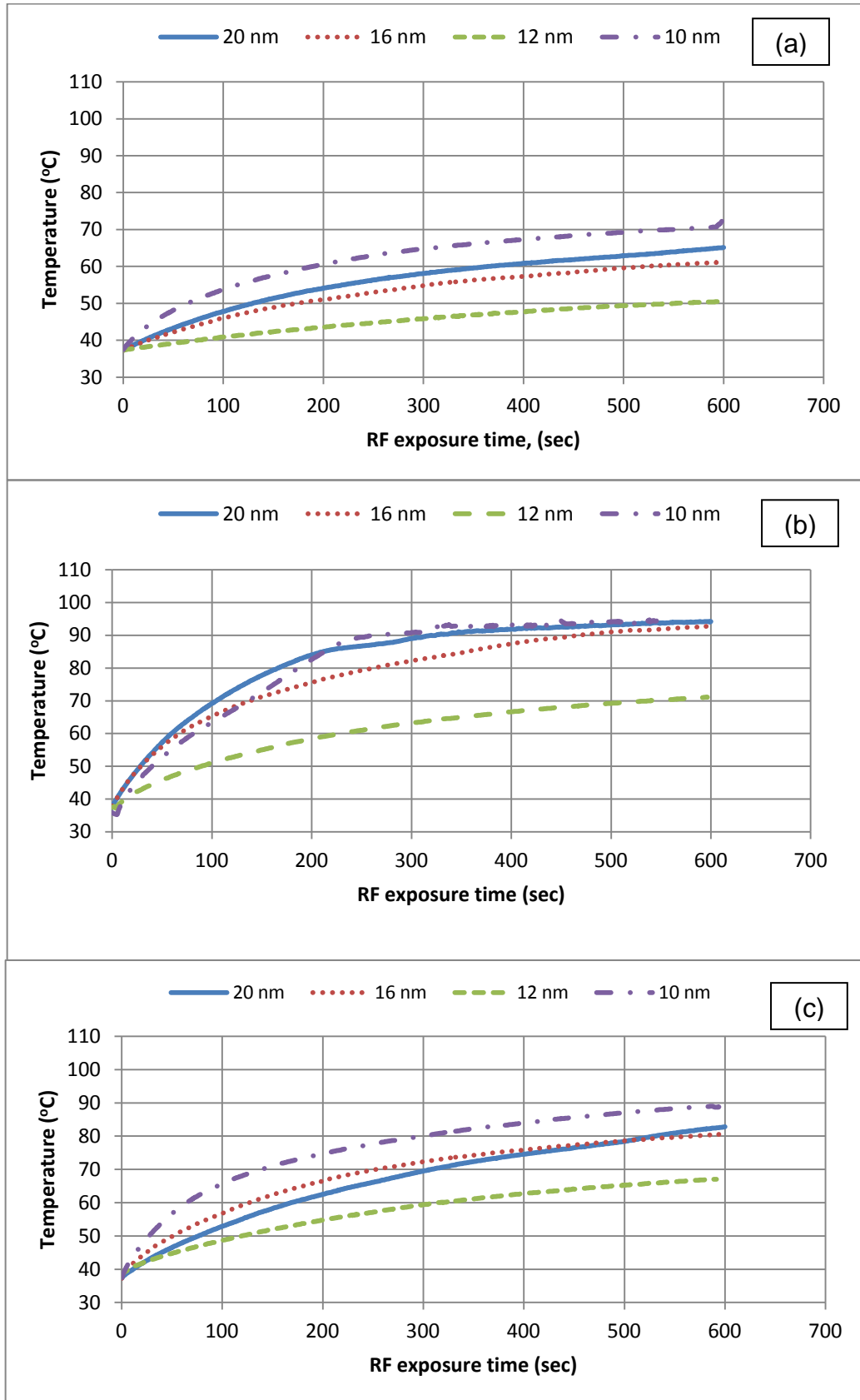
**Figure 6.8** The heating curves at (a) 173.9, (b) 521.3, and (c) 737.5 kHz
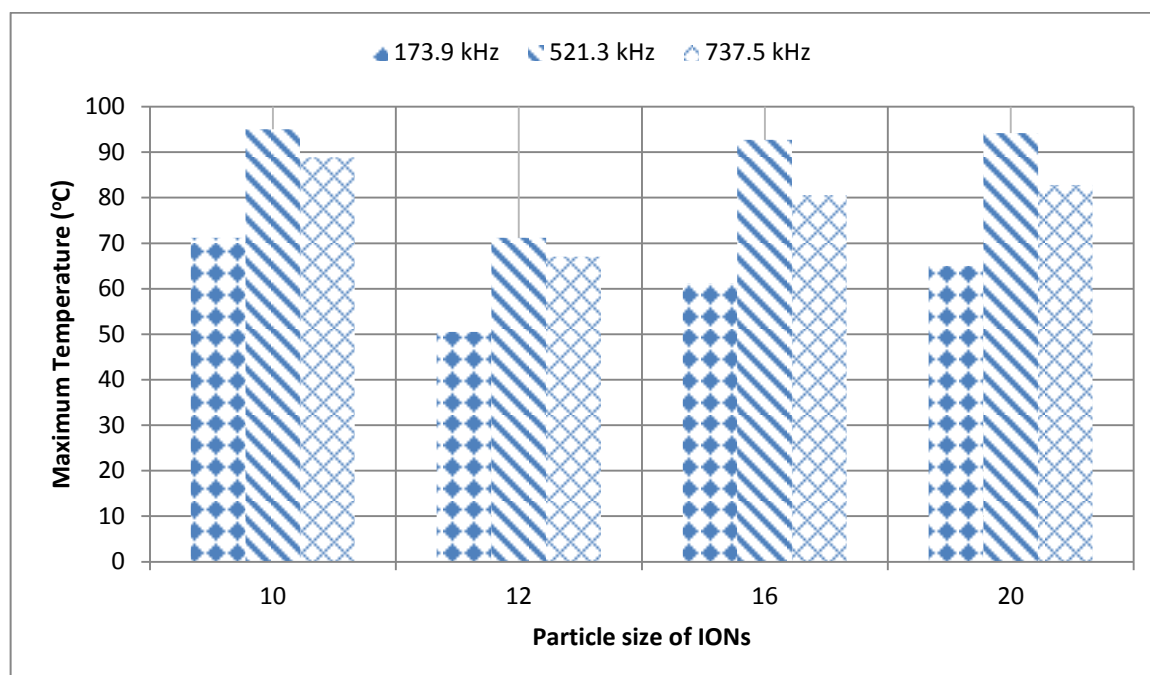
**Figure 6.9** The variation of maximum heating temperatures at different particles size and frequencies with 9 turn coil after 600 seconds exposure.

With the information available from the figure, the heating behaviour became more obvious. A direct relationship was observed for the maximum heating temperatures with the different particle sizes. Interestingly however, at 10 nm the heating temperature showed an opposite effect where instead of exhibiting a lower heating temperature, it showed a higher value. This behaviour was observed at all of the three frequencies (Figure 6.9). It was also observed from the figure that the particle size at 10 nm showed the highest heating temperature at all three frequencies. The highest heating temperatures for all of the particle sizes occurred at 521.3 kHz.

Finally, the rates of heating during the first 100 seconds for all three frequencies and the maximum temperature reached after 600 seconds of exposure are tabulated as shown in Table 6.2. From the table, the particle size at 10 nm at 521.3 kHz was chosen for further testing due to its highest rate of heating after 50 seconds.

**Table 6.2** The rate of heating for the first 100 seconds and the maximum temperature after 600 seconds of exposure. The highlighted box at 521.3 kHz indicates the highest rate after 50 seconds of exposure time.

| Frequency, kHz | Size, nm | Rate at | | | Maximum Temperature, °C after 600 sec |
|---|---|---|---|---|---|
| | | 0 sec | 50 sec | 100 sec | |
| 173 | 20 | 0.14 | 0.12 | 0.04 | 65.0 |
| | 16 | 0.16 | 0.08 | 0.08 | 61.2 |
| | 12 | 0.08 | 0 | 0 | 50.5 |
| | 10 | 0.40 | 0.10 | 0.04 | 71.2 |
| 521.3 | 20 | 0.80 | 0.28 | 0.18 | 94.2 |
| | 16 | 0.54 | 0.24 | 0.16 | 92.7 |
| | 12 | 0.14 | 0.12 | 0.12 | 71.2 |
| | 10 | 0.78 | 0.26 | 0.20 | 95.0 |
| 737.5 | 20 | 0.36 | 0.14 | 0.10 | 82.8 |
| | 16 | 0.58 | 0.14 | 0.10 | 80.5 |
| | 12 | 0.58 | 0.10 | 0.06 | 67.0 |
| | 10 | 0.76 | 0.22 | 0.18 | 88.8 |

### 6.3.3.2 Frequencies with 17 turn coil

The same procedure was applied for the corresponding 17 turn coil. For this coil, turn, the values for the frequencies, voltage, current and magnetic field are tabulated in Table 6.3. It should be noted here that the three frequencies used here were different from those with the 9 turn coil.

**Table 6.3** Values of frequencies, voltage, current and magnetic field for 17 turn coil (www.nanotherics.com)

| Nominal Frequency, (kHz) | DC power supply Voltage (V) | DC power supply Current (A) | Magnetic field (mT) |
|---|---|---|---|
| 109.9 | 26.5 | 12.4 | 25.0 |
| 165.1 | 21.5 | 8.2 | 17.0 |
| 330.3 | 31.1 | 7.9 | 17.0 |

Similar patterns from the hyperthermia curves were observed at these frequencies and the corresponding parameters either calculated or extracted from the hyperthermia curves are summarized and tabulated as shown in Table 6.4.

**Table 6.4** The rates of heating during the first 100 seconds for all the frequencies and the maximum temperature achieved after 600 seconds of exposure. The highlighted box at 330.3 kHz indicates the highest rate after 50 seconds of exposure time.

| Frequency, kHz | Size, nm | Rate at | | | Maximum Temperature, $^{o}$C after 600 sec |
|---|---|---|---|---|---|
| | | 0 sec | 50 sec | 100 sec | |
| 109.9 | 20 | 0.14 | 0.06 | 0.10 | 59.7 |
| | 16 | 0.02 | 0.04 | 0 | 50.8 |
| | 12 | 0.04 | 0 | 0 | 47.2 |
| | 10 | 0.04 | 0 | 0 | 50.7 |
| 165 | 20 | 0.30 | 0.10 | 0.04 | 55.3 |
| | 16 | 0 | 0.04 | 0.04 | 45.1 |
| | 12 | 0 | 0 | 0 | 41.6 |
| | 10 | 0.04 | 0.06 | 0 | 45.2 |
| 330.3 | 20 | 0.52 | 0.16 | 0.14 | 77.4 |
| | 16 | 0.18 | 0.02 | 0.04 | 50.5 |
| | 12 | 0.14 | 0.02 | 0 | 46.9 |
| | 10 | 0.14 | 0.04 | 0 | 54.2 |

From Table 6.4, much lower temperatures at the maximum exposure time were observed. The highest maximum heating temperature reached after 600 seconds of RF exposure was about 77.4 $^{o}$C for the particle size at 20 nm and at a frequency of 330.3 kHz. This is followed by 10 nm with a maximum temperature of 54.2 $^{o}$C at the same frequency but with a higher heating rate after 50 seconds of exposure.

Figure 6.10 showed the variation of temperature at different particle sizes and frequencies after 600 seconds of exposure time. This demonstrated the effect of the particle size on heating at all three frequencies. From the figure, it was observed that the highest temperature for all three compositions occurred at 330.3 kHz. Also at the frequencies with the 17 turn coil, the particle size of 20 nm showed the highest temperature at all of the frequencies. This pattern was repeated for the 9 turn coil. As the particle size decreased from 20 to 12 nm, the final temperature also decreased. The temperature however, increased again at 10 nm. Since it was observed that the rate of heating and the maximum temperature were highest for all of the particle sizes at 330.3 kHz, the particle size at 10 nm was chosen for further testing instead of 20 nm. The reason for the selection is due the heating rate after 50 seconds of exposure and size factor of the IONS. It has been shown (see Table 6.4) that the rate after 50 seconds exposure was highest for the particle size 10 nm. Also the larger

size may be hazardous and harmful to the body (Veiseh *et al.*, 2010). With these findings, the particle size of 10 nm at 330.3 kHz was chosen for further testing due to its highest rate of heating after 50 seconds of exposure.
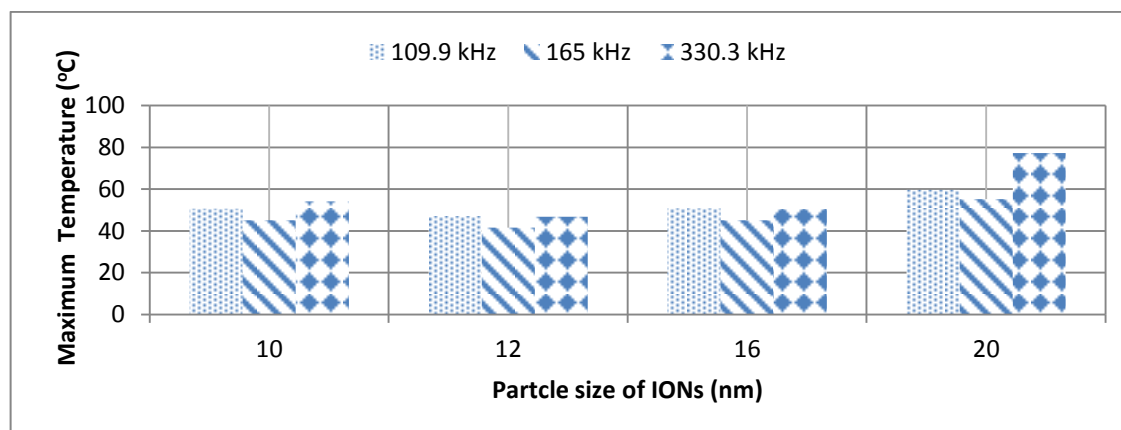


**Figure 6.10** The variation of maximum heating temperatures at different particles size and frequencies with 17 turn coil after 600 seconds of exposure.

The variation in the heating rate of temperature observed at different particle sizes (Figures 6.9 and 6.10) may be explained by their dependency on the spin relaxation processes. This phenomenon has been predicted by Rosensweig (2002) for IONs. In general, heating occurs due to hysteresis losses and spin relaxation. Since in this case the IONs used are superparamagnetic, heating cannot occur due to the hysteresis losses since they show negligible hysteresis, therefore the observed heating must be due to the spin relaxation processes namely Néel and/or Brown relaxation. Overall, the net heating depends on which relaxation dominates. For high heating effect, it has been demonstrated elsewhere that the Brown relaxation must dominate the Néel relaxation (Rosensweig, 2002). It also has been demonstrated that the Brown relaxation becomes more effective as the particle size is increased (Rosensweig, 2002). It is worth noting here that the cross over from Néel to Brown and vice versa does not only depend on the size but is also dependent on many other variables such as the saturation magnetization, Ms, magnetic anisotropy, applied magnetic field and frequency. In the context of size, theory shows that there exists a critical value where both relaxations contribute equally. Above that critical

size, Brown relaxation dominates (Pino and Pelaz, 2012). Therefore, at this juncture it is speculated that the increase of the heating temperature with the increment of IONs (Figures 6.9 and 6.10) from 12 to 20 nm is due to the dominance of the Brown relaxation. The opposite effect exhibited by the particle size at 10 nm is due to crossing over from Brown to Néel relaxation. More work needs to be done to investigate the effect of various other variables before any conclusive remark can be made. This is however, left as a subject for future work.

### 6.3.3.3 Effect of amount of IONS embedded in the coating on hyperthermia behaviour

Once the above size-dependency result was available it was necessary to investigate the optimum amount of IONS to be embedded in the coating materials in order to produce the required hyperthermia effect. In this part of the work, IONS with a particle size of 10 nm were chosen. The IONS were embedded in the coating at different weight % loadings in order to heat the coating when magnetic field was applied. The resulting mixtures were then subjected to hyperthermia studies and exposed for a maximum 600 seconds at 521.3 and 330.3 kHz.

### 6.3.3.3.1 Effect at 521.3 kHZ

### 6.3.3.3.1.1 Mixture of fatty acids

In this part of the work, a coating containing a mixture of fatty acids was subjected to hyperthermia and not the individual fatty acids. This was because from the DSC studies the melting points for lauric and myristic acid are higher than the hyperthermia temperature of $42^{\circ}C$ (Figure 6.1). A mixture of lauric and myristic acid at 40:60 (by weight ratio) with a melting point of $42.4^{0}C$ (Figure 6.5a) was used as the coating for the capsule as explained earlier. Figure 6.11 showed the time-dependent temperature curves when the mixed fatty acid/ION nanocomposite was exposed to RF treatment at 521.3 kHz.
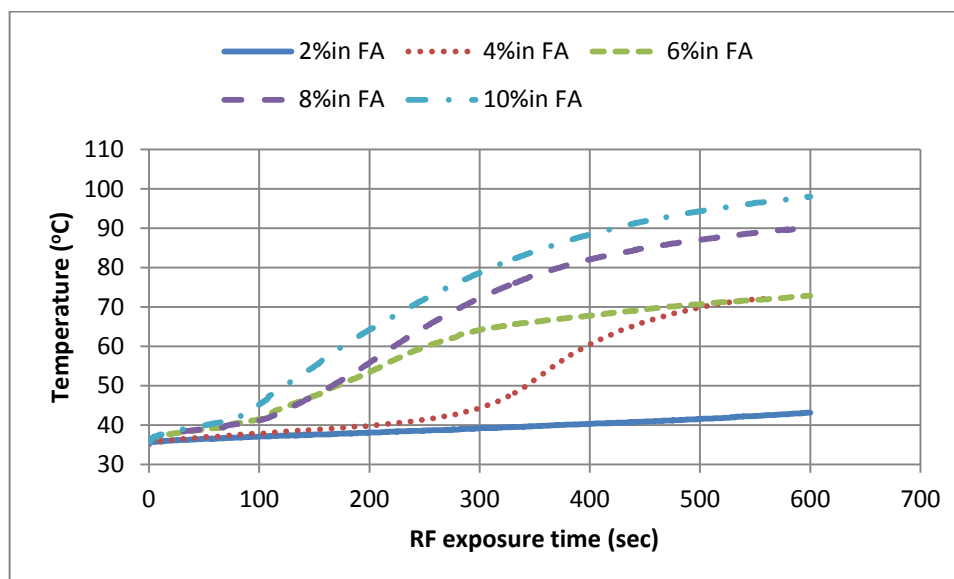
**Figure 6.11** The time-dependent temperature curves at different percentage by weight of IONs embedded in C12:C14 (40:60 / w:w) exposed to RF at 521.3 kHz

As illustrated in Figure 6.11, exposed in magnetic field for 600 seconds, the maximum temperatures reached are in the range between 43.1 to 97.6°C. The temperature reached 97.6°C in 600 seconds for mixtures with 10 % by weight of IONS. An interesting behaviour is observed whereby at the first 100 seconds of exposure, the temperature increases just slightly. After 100 seconds of exposure, it was observed that the temperatures increased sharply especially at 8 and 10 percent by weight of IONs (Figure 6.11). This phenomenon was due to the fact that during the first 100 seconds, the temperature was less than the melting point of the mixed fatty acids i.e. 42.4°C. At this stage, the IONs were still embedded in the fatty acid. However, once the melting point was reached, after about 100 seconds of exposure, the fatty acid melted and released the IONs molecules. Once the IONs are free to move and spin, new heating mechanisms become available due to the spin relaxation processes, hence the rate of heating increases rapidly. This is the reason for the sudden increase in the heating temperature observed after 100 seconds.

### 6.3.3.3.1.2 Eicosane

Figure 6.12 showed the time-dependent temperature curves exposed to RF treatment at 521.3 kHz for the eicosane system. Similar trends in the temperature curve behaviour were observed.



**Figure 6.12** The time-dependent temperature curves at different percentage by weight of IONS embedded in eicosane exposed to RF at 521.3 kHz. Inset is an enlargement of the curve from 0 to 100 seconds RF exposure time

All of the curves increased sharply up to 200 seconds of exposure and reduced their slope from 200 to 600 seconds. The maximum temperatures reached ranged between 57.5 and 146.7$^o$C. The temperature reached 146.7$^o$C in 600 seconds for mixtures with 10 percent by weight of IONS. Once again, the same phenomenon as that of fatty acids was observed whereby during the first 100 seconds, there was a sharp increase in the curves especially at 8 and 10 percent by weight of IONs. For this coating, it was observed that at less than 15 seconds of exposure, the increase in the slope of the curves was slow. However, after 15 seconds of exposure, the slopes of curves increased drastically and especially at 8 and 10 percent weight of IONs (see inset of Figure 6.12). This can be explained from the fact that at lower than 15 seconds, the temperatures have not reached the melting point of eicosane which is at 38$^o$C. After 15 seconds of exposure, the melting point is reached and the IONs start to absorb and transfer energy through multiple mechanisms and thus caused the sudden increase in the heating rate and final temperature.

### 6.3.3.3.1.3 Mixture of eicosane and docosane

Figure 6.13 shows the time dependent temperature curves for the mixture of paraffins. In this system, the maximum temperatures are in the range between 39.5 and 99.9 $^o$C.
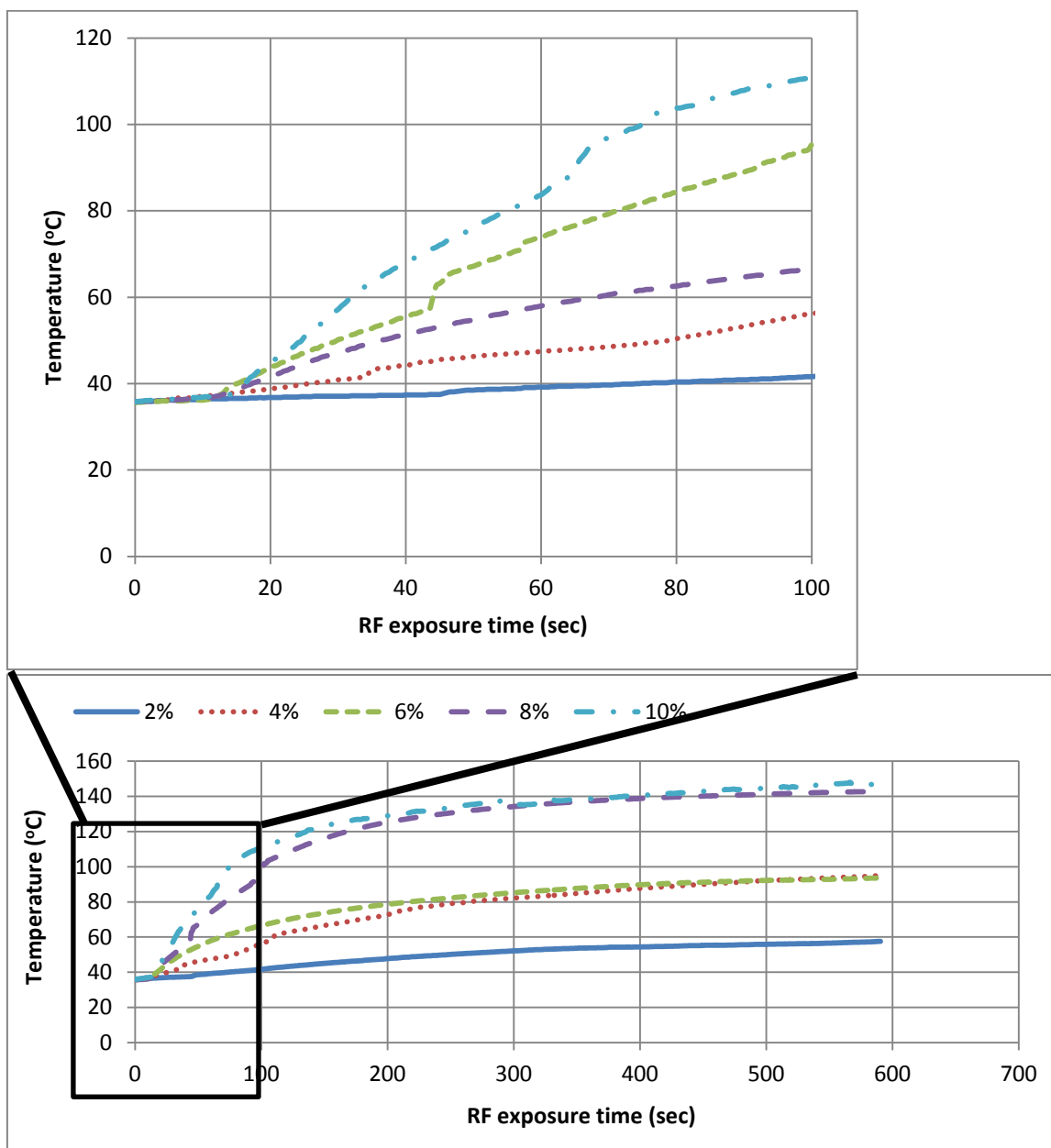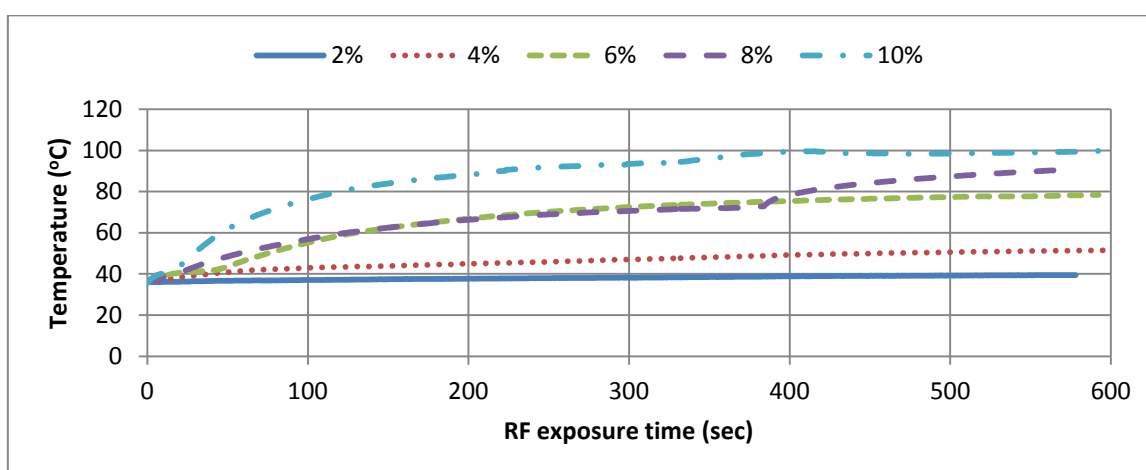


**Figure 6.13** The time-dependent temperature curves at different percentage by weight of IONS embedded in eicosane and docosane (40:60/w:w) exposed to RF at 521.3 kHz.

### 6.3.3.3.1.4 Comparison between coatings

The difference in the heating effect of the three coating materials, namely the mixture of lauric acid and myristic acid (40:60/ w:w), eicosane and mixture of eicosane and docosane (40:60/w:w) with the percent weight of IONs can be obtained from the comparison between Figures 6.11 – 6.13. Figure 6.14 summarised the variation of the amount of IONs with the maximum temperatures. It showed that the temperatures are increased with the increment of IONs for all of the systems (Figure 6.14). But one striking feature is that, overall, in the presence of IONs, the temperatures for the eicosane system were the highest. This phenomenon implied that eicosane required lesser energy compared to other coating materials in order to raise the same amount temperature. Literature however, showed that the values of specific heat capacity for eicosane, its mixture with docosane and fatty acids are almost the same which are in the range of 2.0-2.5 J/gK (Domalski and Hearing, 1996). This is perplexing and it is therefore speculated that the observed heating effect of the coating materials were not due to the specific heat capacity of the coating materials but rather on the spin relaxation process namely Néel and/or Brown relaxation of the magnetic IONs. In this case, eicosane having the lowest melting points among the coatings, melted earlier and thus more of IONs are free to oscillate. This causes the Brownian relaxation to dominate. For high heating effect, literature has shown that the Brown relaxation must dominate the Néel relaxation (Rosensweig, 2002).
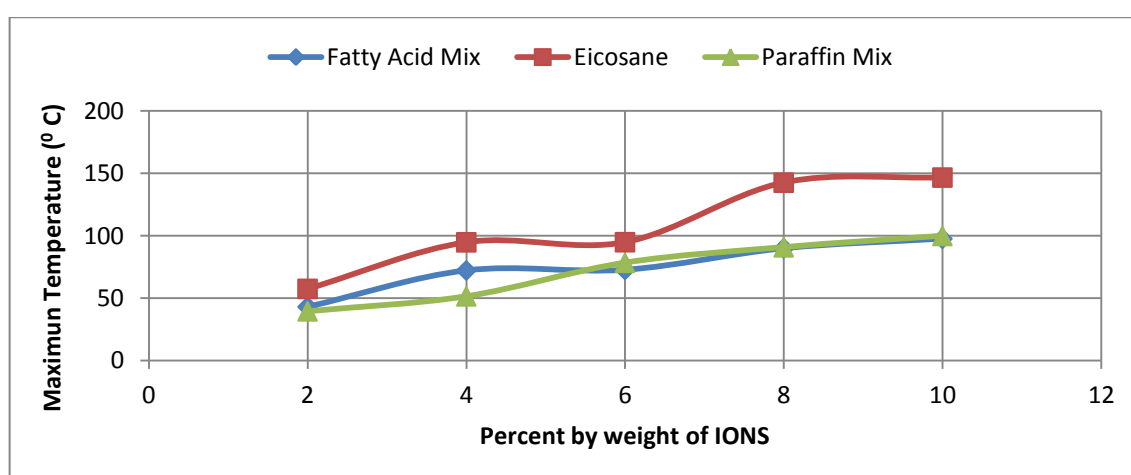


**Figure 6.14** The variation of maximum temperatures at different percentage by weight of IONS embedded in different coatings and coating exposed to RF at 521.3 kHz.

### 6.3.3.3.2 Effect at 330.3 kHz

### 6.3.3.3.2.1 Mixture of fatty acids

Figure 6.15 showed the time-dependent temperature curves for IONs embedded in fatty acid mix exposed to RF treatment at 330.3 kHz. The maximum temperatures are from 36.9 to 49.9$^{o}$C with 10 percent by weight of IONs exhibiting the highest value. The curves increase slightly up to about 300 seconds and then increase sharply after 300 seconds onwards. This was explained earlier, is due to the melting point of the fatty acids. Once the melting point is reached the, the fatty acids melt and IONS molecules are released, causing more rapid heating.
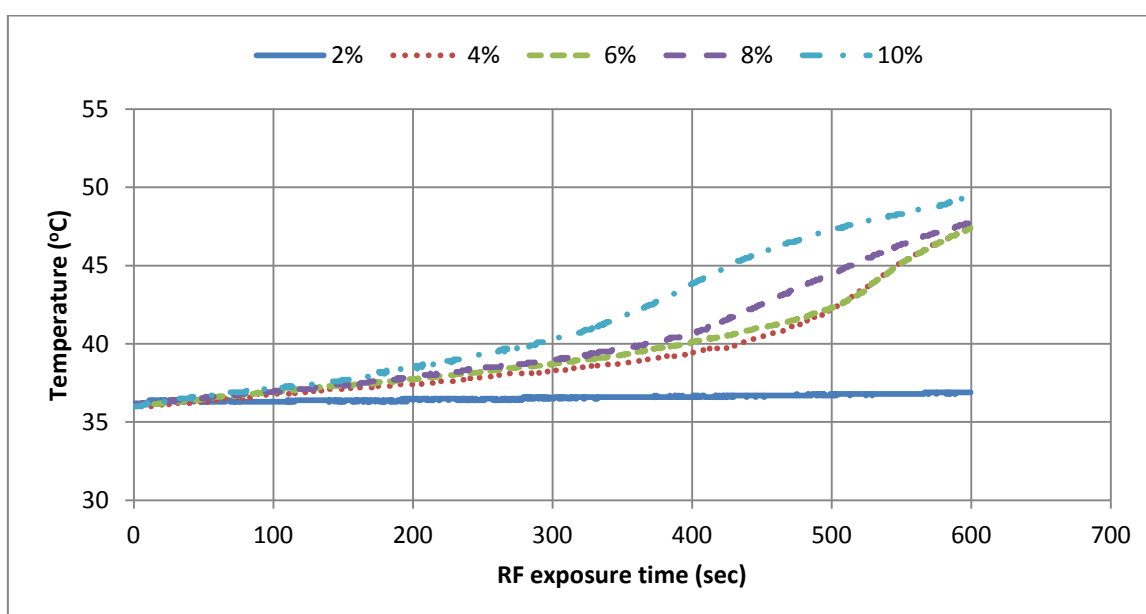


**Figure 6.15** The time-dependent temperature curves at different percentage by weight of IONS embedded in C12:C14 (40:60 / w:w) exposed to RF at 330.3 kHz

### 6.3.3.3.2.2 Eicosane

For the eicosane coating, the time-dependent temperature curves were shown in Figure 6.16. The curves show a clear distinction from each other and on an upward trend with the highest maximum temperature of 108$^{o}$C observed at 10 percent by weight of IONS. After 6 seconds of exposure time, once the melting point of eicosane is reached at 38$^{o}$C, it is obvious that for the 10 percent by weight of IONS, the curve increases sharply (see inset of Figure 6.16).
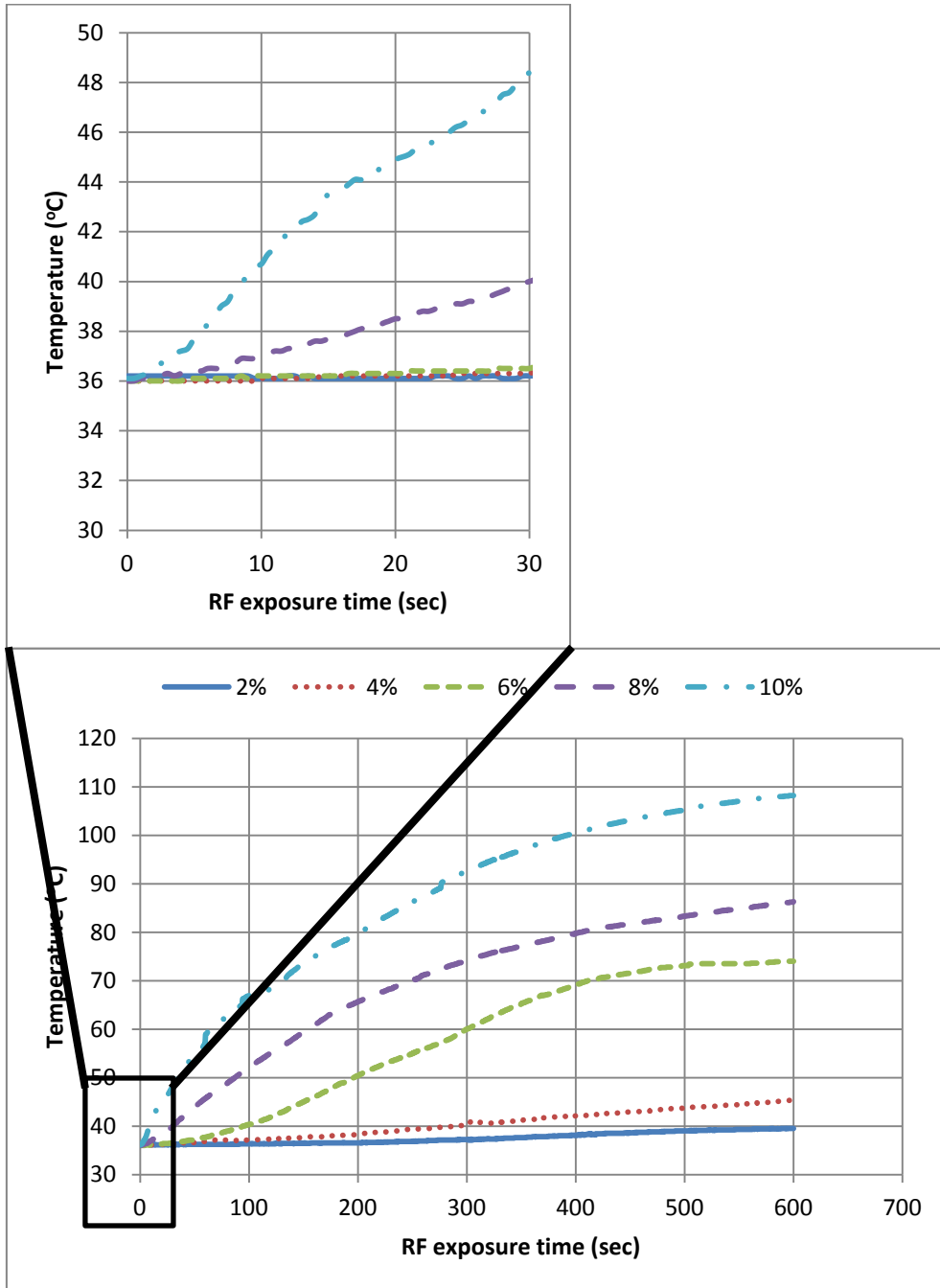
**Figure 6.16** The time-dependent temperature curves at different percentage by weight of IONS embedded in eicosane exposed to RF at 330.3 kHz. Inset is an expansion showing the equivalent data but up to 30 seconds of exposure time.

### 6.3.3.3.2.3 Mixture of eicosane and docosane

Figure 6.17 showed the time-dependent temperature curves for the mixture of paraffins exposed to RF at 330.3 kHz. The maximum temperatures are in the range between 45.4 to 84.4$^{o}$C. Again, the highest maximum temperature of 84.4$^{o}$C was observed at 10 percent by weight of IONs
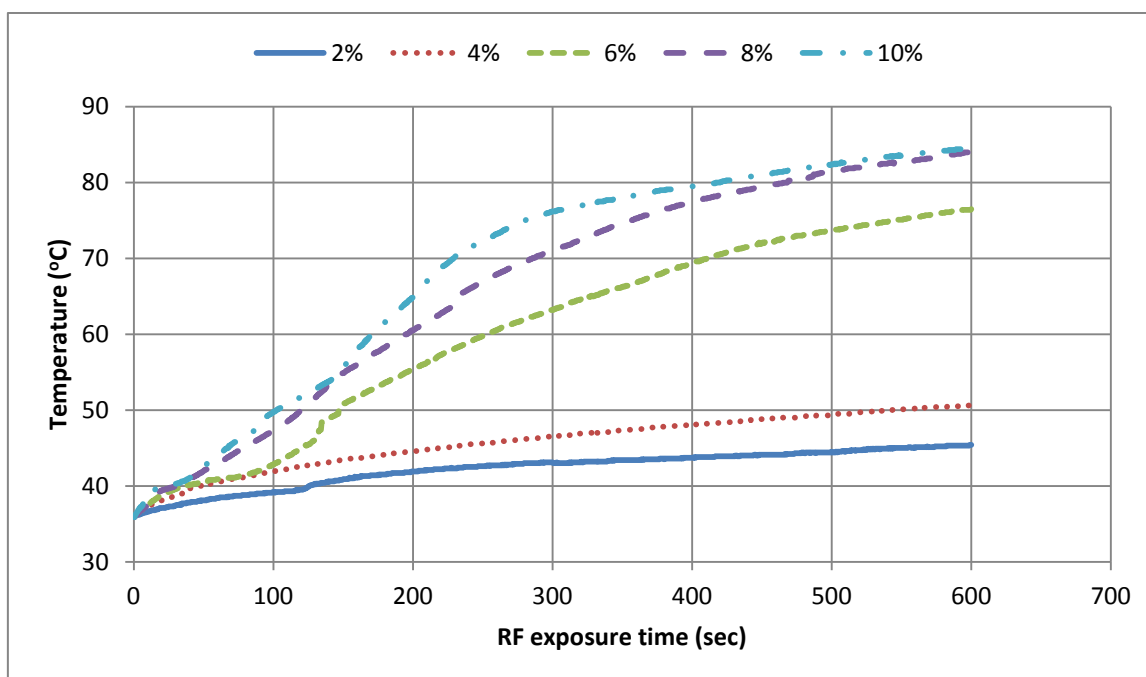


**Figure 6.17** The time-dependent temperature curves at different percentage by weight of IONs embedded in a mixture eicosane and docosane at 40:60 (w:w) exposed to RF at 330.3 kHz.

### 6.3.3.3.2.4 Comparison amongst coatings

By comparing the parameters obtained from Figures 6.15 – 6.17, the melting effect on the different types of coating can be inferred as depicted in Figure 6.18. The result showed that the maximum temperatures increased with the increment of IONs content for all the coatings. It is also observed that the eicosane coated capsules exhibit the highest maximum temperature values only at 10 percent by weight of IONs at this frequency. This difference of the fatty acids, maybe due to other factors such as a degree of ION aggregation leading to non-uniform mixing
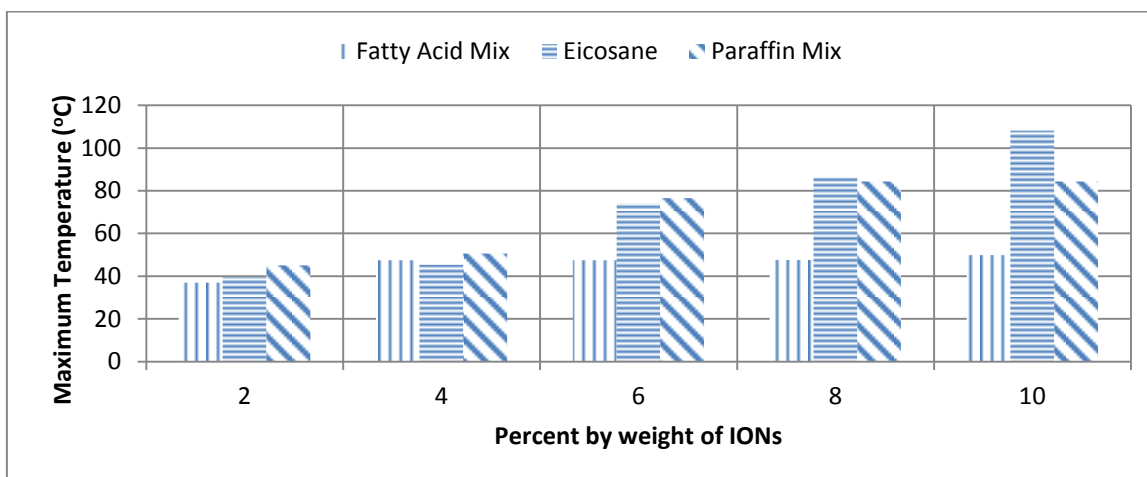
**Figure 6.18** The variation of maximum heating temperatures at different percentage by weight of IONs and coating exposed to RF at 330.3 kHz.

Finally, the coating materials consisting of eicosane, the mixture of fatty acids and mixtures of paraffins at 40:60 by weight, with 10 weight % IONs with a particle size of 10 nm were chosen for further dissolution testing to study drug release properties. The frequencies selected were 521.3 kHz and 330.5 kHz. These were the combinations that generated the highest temperatures and heating rates, and are thus expected to be the most efficient for RF-triggered drug release. This will be described next.

### 6.3.4 Dissolution studies

Figure 6.19 shows the coated capsule resulted from dip coating process. Various thickness for coated capsules shown in Appendix G.



**Figure 6.19** Optical images of coated capsules

The coating materials consist of eicosane, the mixture of fatty acids and mixtures of paraffins at 40:60 by weight, with 10 weight % IONs with a particle size of 10 nm. A drug dissolution studies were then carried out on the coated capsules to assess the dissolution performances and how well the coatings protected the drug from being released until triggered. Paracetamol was used as the drug model. The sensitivity and responsivity to pH and temperature of the capsule was tested, using buffer solutions and bile salts. Bile salt and buffer solutions were used here to mimic the microenvironment of the GI tract of the human body. This was to gain deeper *in-vitro* insight into the delivery and release of drug into the lower GI tract.

The following goals are important:

- Assessing the effect of the number of layers of coating
- Providing different environments that mimic the various compartments of the GI tract.
- Studying the drug release under these different environmental conditions

In this work, it should be mentioned that the main interest is primarily on prolonging and controlling the drug release time and not so much on the amount of drug released, which could be altered if required by adjusting the drug loading in the capsules.

### 6.3.4.1 Effect of number of dippings on drug release.

For the dissolution studies, the capsules containing the drug were coated using different materials that had been formulated with IONs at 10 percent by weight. It was thought that information on the number of layers of coating needed for dipping the capsules was essential in order to obtain the optimum number of dipping to provide adequate protection and also efficient release when triggered. The capsules were dipped three times and at each dip (or layer), a dissolution test was performed in various media, pH values and temperatures. This was because as mentioned earlier, the capsules will be administered orally and therefore they will undergo the harsh environment of the GI tract (see Table 2.6).

**6.3.4.1.1 Biphasic dissolution test 1 (in pH 1.2 and buffer pH 7.4 at 37 °C)**

*In vitro* drug release studies were conducted at pH 1.2 and 7.4 to simulate *in vivo* conditions in the stomach and small intestine. Figure 6.20a showed the percent drug release for the mixed fatty acids coated capsules at pH 1.2 and 7.4. At pH 1.2, the results showed that the curve increased sharply after 1 h, for coating with 1 layer of dipping. The 2 and 3 layers at this pH show no drug release. At pH 7.4, the 1 layer coating continues to increase and release more drug about 60 ± 14.8 percent after 6 h. For the 2 and 3 layers of dipping, the drug starts to be release slowly after 180 min in the dissolution medium at pH 7.4. The maximum drug release was observed to be 5.6 ± 3.3 %. The dissolution behaviour of the drug contained in the fatty acid coated capsules depended on the thickness of the fatty acids layer. It showed that 1 layer of coating was not adequate to protect the capsule from the surrounding. Thus, the 1 layer of dipping provides a poor barrier which allows medium to penetrate or erode the layer and cause capsule dissolution. It is not clear whether this leakage is due to general porosity/ erosion, or maybe due to individual particles or imperfections in the coating causing localised release. This is discussed further in section 6.3.4.1.2
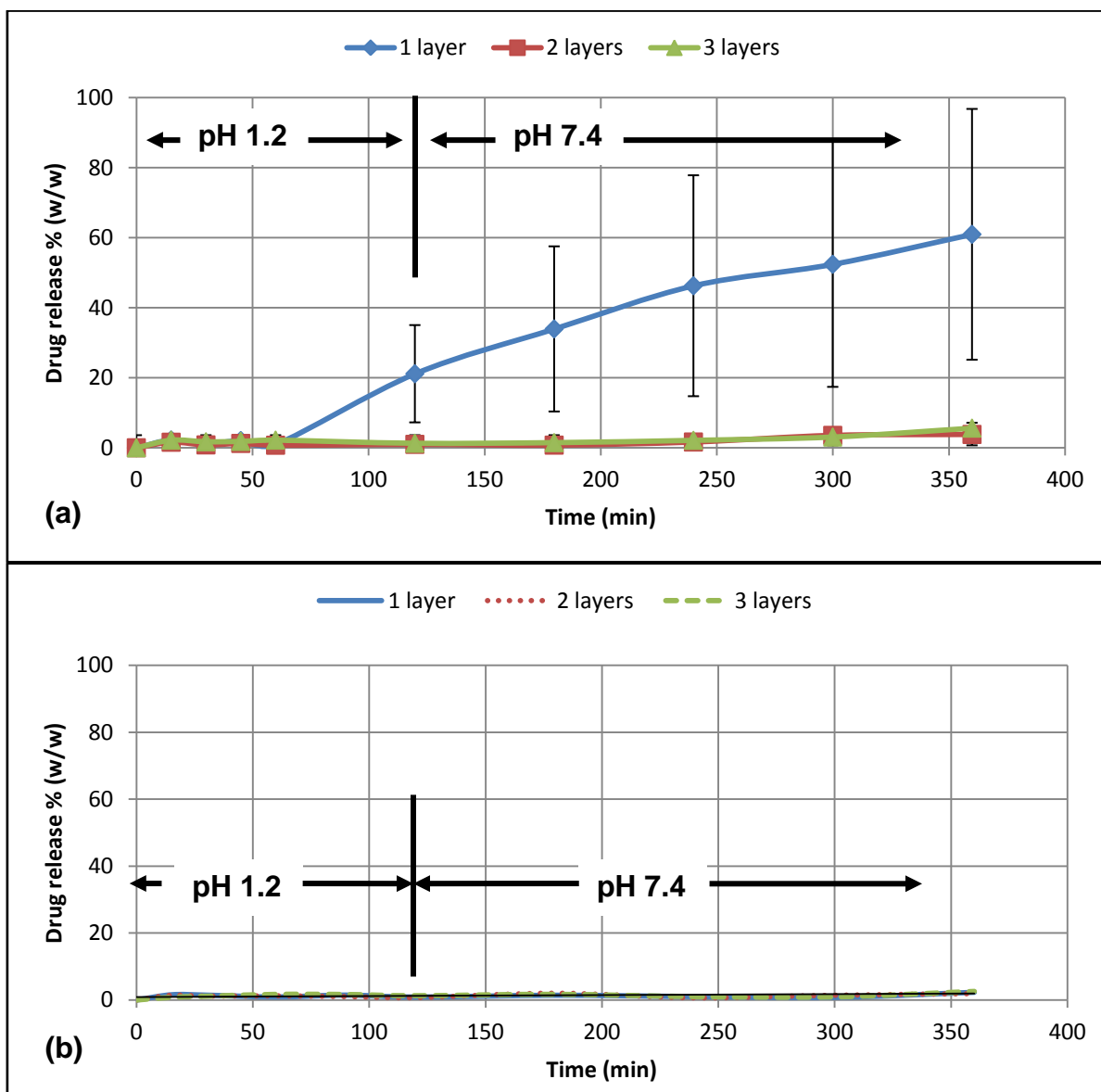
**Figure 6.20** The percent drug release curves for (a) C12:C14 (40:60) (w/w) and (b) eicosane coated capsules coated with 1, 2, and 3 layers embedded with 10% IONs in medium pH 1.2 and buffer at pH 7.4 at 37°C .

Figure 6.20b showed the percent drug release at pH 1.2 and 7.4 by using eicosane as a coating. The results showed that no drug was released with eicosane even with only one dipping layer. This suggests that the paraffin gave a higher quality layer with no defects. The same behaviour was observed for the coatings with docosane and mixture of eicosane and docosane at 40:60 by weight.

**6.3.4.1.2 Biphasic dissolution test 2 (in pH 1.2 and FaSSIF pH 6.5 at 37$^{o}$C)**

In these *in* vitro drug release studies, the dissolution profiles were conducted at pH 1.2 and 6.5. As mentioned earlier, the media at pH 1.2 represent stomach conditions and pH 6.5 is FaSSIF media that mimics the fasted state condition in the intestine. The temperature of the dissolution bath was set at 37$^{o}$C.

Figure 6.21a showed the percent drug release for the mixed fatty acids coated capsules at pH 1.2 and 6.5. At pH 1.2, the results showed the curve increased sharply after 1 h, for the coating with 1 layer of fatty acid. The 2 and 3 layer coatings at this pH show no drug release. At pH 6.5, the 1 layer coating curve continued to increase drastically showing release or more drugs; about 90 ± 14.4 percent after a period of 6 h. For the 2 and 3 layers of dipping, the drug started to be released slowly after 1 h in the dissolution medium at pH 6.5. The percent of drug release was observed to be at 9 ± 2.4 % after 6 h. It seemed that the dissolution behaviour of the drug contained in the fatty acid coated capsules depended on the thickness of the fatty acids layer, as discussed in the previous section.

The dissolution behaviour for different numbers of coating layers for the eicosane coated capsules is shown in Figure 6.21b. Similar procedures were performed under pH 1.2 and 6.5. The results showed that no drug entered the solution for any of the coatings at both pH values. The same behaviour was observed for the coatings with docosane and the mixture of eicosane and docosane.

**Figure 6.21** The percent drug release curves for (a) C12:C14 (40:60) (w/w) and (b) eicosane coated capsules coated with 1, 2, and 3 layers embedded with 10% IONs in medium pH 1.2 and FaSSIF at pH 6.5 at 37°C.
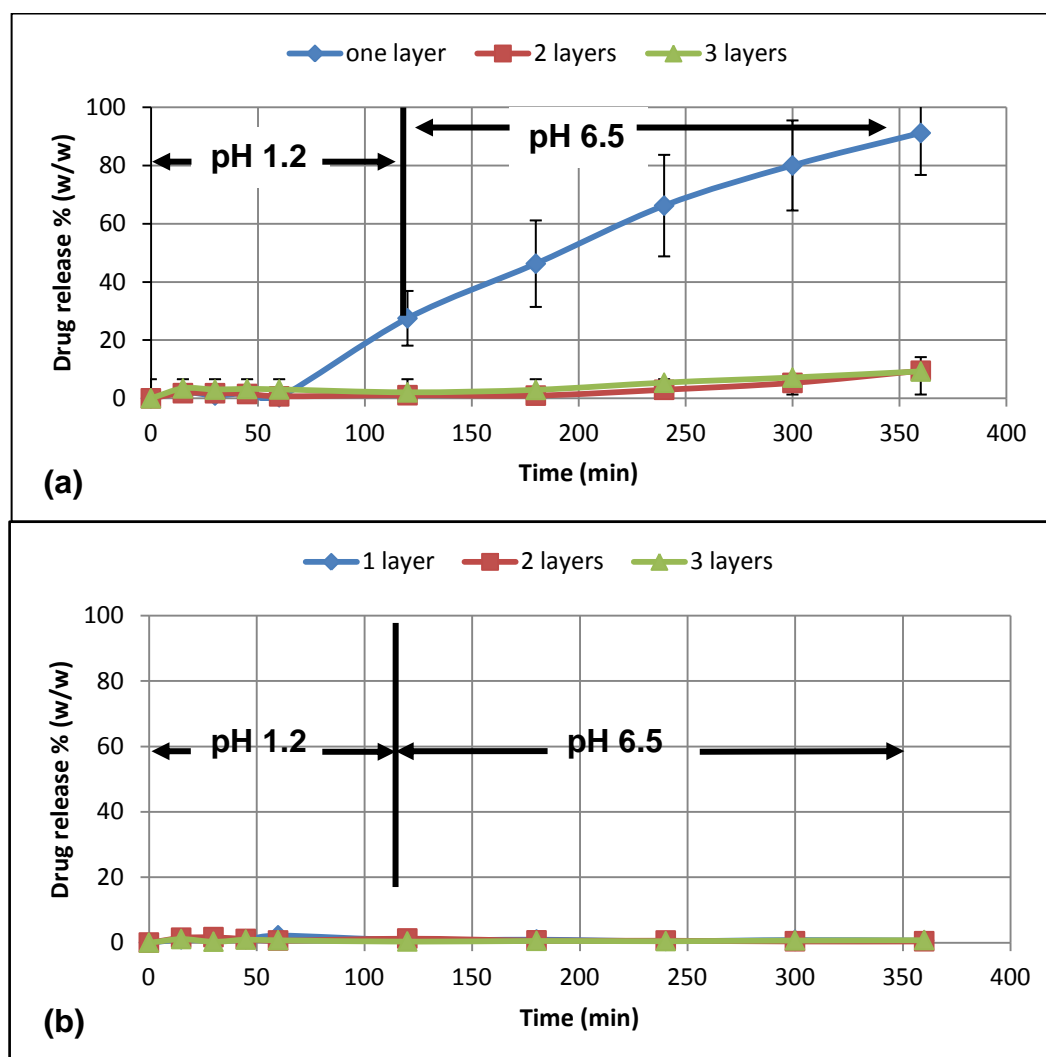
From the above results, it shows that 1 layer of coating is not adequate to protect the capsule from the acidic, phosphate buffer and FaSSIF conditions, and especially for the FaSSIF conditions for the mixture of fatty acids as the coating material. This behaviour can be explained by the pKa values of the fatty acids. Most short-chain fatty acids have a pKa value of about 4.8 (Kanicky *et al.*, 2000) as shown in Figure 6.22.
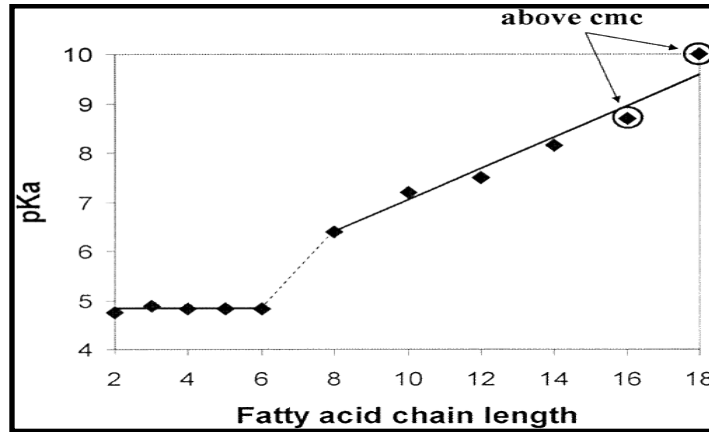
**Figure 6.22** The effect of chain length on the pKa values of fatty acid (adapted from Kanicky *et al.*, 2000).

It was reported that as the chain length is increased, the pKa value also increases. These pKa values for fatty acids are crucial to their behaviour in solutions with various pH values. Figure 6.23a-c shows the behaviour of fatty acids at different pH values (Kanicky *et al.*, 2000).
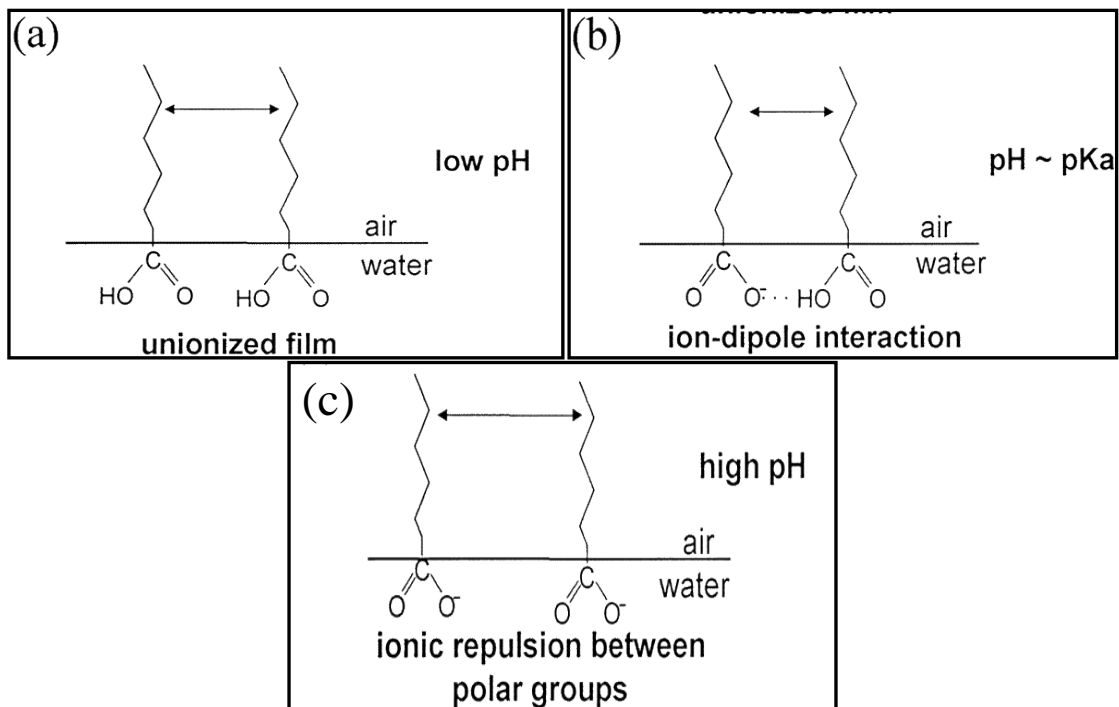


**Figure 6.23** The behaviour of fatty acid molecules at (a) low, (b) approximate value that of pKa and (c) high pH values (adapted from Kanicky *et al.*, 2000).

It shows that at low pH value (~1-2), the fatty acids molecules are un-ionised and the polar carboxyl group of the fatty acid is oriented at the air/water interface as shown in part a of Figure 6.23. At pH values close to that of pKa, 50 % of the fatty acid molecules are ionised and a strong ion-dipole interaction between the carboxyl groups occurs (part b, Figure 6.23). These interactions result in the molecules being packed closer to each other. However at higher pH values (~9-10), the fatty acids are completely ionised and this causes ionic repulsion between the polar groups (part c, Figure 6.23). This leads to greater solubility in water. The reported pKa value for lauric and myristic acid is 7.5 and 8.2, respectively (Figure 6.22) and the mixture of lauric and myristic acids used to coat the capsules are subjected to solutions at pH 6.5 and 7.4. Since the pH values of the solution are close to that of the pKa value for fatty acids, the fatty acid molecules are therefore partially ionised and some are readily soluble in the solutions. This explains the behaviour observed when 1 layer of fatty acids is coated on the capsules- significant dissolution can cause erosion and loss of layer integrity.

Another possible explanation is that under these conditions, a surfactant-like bile salts are present at 3 mM. This explanation is only directed for the FaSSIF conditions at pH 6.5. At this concentration, the bile salt spontaneously forms micelles in the aqueous environment (Norman, 1960; Small, 1971). The result for the 1 layer of coating under FaSSIF conditions maybe not only due to the pKa values of fatty acids but also due to the presence of bile salt. Bile salts could increase the dissolution rate by two possible mechanisms; i) decreasing the interfacial energy between the coating and the dissolution medium. This would result in the ability of the medium to wet the coating more effectively and increase the contact area available for dissolution and ii) the solubilisation effect of the bile salts micelles (Bates *et al.*, 1966). The second mechanism is a more likely explanation for the observation since the concentration of the bile salts used is at the critical micelle concentration where micelles are already formed and therefore could interact with the fatty acid molecules to form mixed micelles as shown in Figure 6.24.
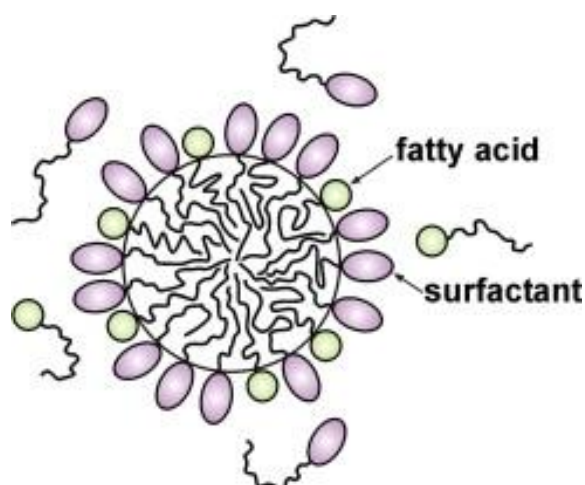
**Figure 6.24** A sketch adapted from Tzocheva and co-workers (2012) to illustrate the formation of a mixed micelle comprising of surfactant (bile salt) and fatty acid molecules (Tzocheva *et al.*, 2012).

On the other hand, the results from eicosane and its mixture with docosane at a ratio of 40:60 by weight indicate the high hydrophobicity of the paraffin surfaces. This reduces the ability of the dissolution media to wet the coating and there are no molecules to ionise at different pH values. The long hydrocarbon chain length of eicosane (C20) and docosane (C22) also prohibits it to be solubilised in the micellar solution of bile salts when it is in solid state, due to the high energy required to break all the Van der Waals bonds and extract a molecule from the surface. This indicates that the paraffin coatings prevent drug release better than the fatty acid ones.

## 6.4 Conclusion

In this work, values of the melting points are elucidated for coating materials: lauric acid, myristic acid, lauric + myristic, eicosane, docosane and eicosane + docosane. The melting point for each coating material was obtained through thermal analysis performed by DSC. In summary, the values of melting points for the mixtures were found to be lower than individual components. This also served as guidance to the selection of appropriate coating compositions to achieve the desired melting points. It was found that the presence of IONs had a small but significant effect on the melting

points, probably due to the stabilising ligands (oleic acid) interacting with the coating materials to reduce crystallinity and packing order

The hyperthermia study revealed the heating effect of IONs on the coatings to be dependent on its particle size. The hyperthermia study performed at 521.3 kHz showed that as the particle size of the IONs increases, the heating is also increased. However, no direct relationship was observed on the effect of heating between the coating materials. This is due to many variables that need to be taken into account such as voltage, current, and magnetic field. For future studies, it is recommended to investigate the effect of these variables on the heating effect of IONs, so that more conclusive comments can be made.

From the dissolution studies, it can be concluded that by manipulating the number of layers the drug release can be further controlled and also the release time can be prolonged. The result also shows that the type of coating plays a crucial role in prolonging the drug release. In this case, the paraffin coatings offer better protection than the fatty acids ones. For the subsequent studies, 3 layers of dipping was chosen. It was expected that the thicker layer and higher overall ION loading would generate more local heating for hyperthermic release.

## 6.5 References

http://www.nanotherics.com

Bates, T.R., Gibaldi, M., and Kanig, J.L. (1966). Rate of dissolution of griseofulvin and hexoestrol in bile salt solutions, *Nature*, **210**: 1331-1333.

Bonsor, D. H. and D. Bloor. 1977. Phase transitions of n-alkane systems. *J. Mater. Sci.* **12**: 1559-1564.

Cedeno, F.O., Prieto, M.M., Espina, A., and Garcia, J.R. (2001). Measurements of temperature and melting heat of some pure fatty acids and their binary and ternary mixtures by differential scanning calorimetry *Thermochimica Acta*, **369**: 39-50.

Chen, H., and Langer, R. (1998). Oral particulate delivery: status and future trends, *Adv. Drug Delivery Reviews*, **34**: 339-350.

Clint, J.H., and Walker, T. (1975). Thermodynamics of Micellization of Homologous Series of n-Alkyl Methyl Sulphoxides and n-Alkyl(dimethy1)phosphine Oxides. *J Chem. Faraday Trans. I*, **71(4)**: 946-954.

Costa, M.C., Rolemberg, M.P., Boros, L.A.D., Krähenbühl, M.A., de Oliveira, M.G., and Meirelles, A.J.A., (2007). Solid-liquid equilibrium of binary fatty acid mixtures, *J. Chem. Eng. Data*, **52**: 30-36.

Deman, J.M., Deman, L., and Blackman, B. (1983). Melting-point determination of fat products, *J. Am.Oil Chemists' Soc.*, **60(1)**: 91-94.

Dorset, D.L. (1986). Crystal Structure of Lamellar Paraffin Eutectics *Macromolecules*, **19**, 2965-2973.

Domalski, E.S., and Hearing, E.D. (1996). Heat capacities and entropies of organic compounds in the condensed phase. Volume III, *J. Phys. Chem. Ref. Data*, **2**: 1-525.

Gilbert, E.P. (1999). The stability of binary alkane blends, *Phys. Chem. Chem. Phys.*, **1**: 1517-1529

Hamdan, S., and Laili, C.R. (1995). Association Phenomenon of a Mixed Cationic Surfactant in Nonaqueous System, *J. Disp. Sci. Technol.*, **16(3&4)**: 233-247.

Inoue, T., Hisatsugu, Y., Ishikawa, R., and Suzuki, M. (2004). Solid–liquid phase behavior of binary fatty acid mixtures 2. Mixtures of oleic acid with lauric acid, myristic acid, and palmitic acid, *Chem Phys Lipids*, **127**: 161–173.

Jordan, A., Scholz, R., and Maier-Hauff, K., (2001). Presentation of a new magnetic field therapy system for the treatment of human solid tumors with magnetic fluid hyperthermia. *J. Magn. Magn. Mater.*, **225**: 118-126.

Kanicky, J. R., Poniatowski, A.F., Mehta, N.R., and Shah D.O. (2000). Cooperativity among Molecules at Interfaces in Relation to Various Technological Processes: Effect of Chain Length on the p$K$a of Fatty Acid Salt Solutions, *Langmuir*, **16**: 172-177.

Lüth, H., Nyburg, S.C., Robinson, P.M., and Scott, H.G. (1974). Crystallographic and calorimetric phase studies of the n-eicosane, $C_{20}H_{42}$: n-Docosane, $C_{22}H_{46}$ system, *Mol. Cryst. Liq. Cryst.,* **27(3&4)**: 337-357.

Mabrey, S., and Sturtevant, J.M. (1976). Investigation of phase transitions of lipids and lipid mixtures by high sensitivity differential scanning calorimetry, *Proc. Natl. Acad. Sci. USA*, **73(11)**: 3862-3866.

Mazee, W.M (1958). The phase behavior of n-alkanes and some of their binary mixtures American Chemical Society, Division of Petroleum Chemistry,**3(4)**: 35-47.

Norman, A. (1960). The conductance of conjugated and unconjugated bile acid salts in aqueous solution, *Acta Chem. Scand.*, **14**: 1300-1309.

Pino, P.D and Pelaz, B. (2012). *"Hyperthermia Using Inorganic Nanoparticles"*, in Nanobiotechnology: Inorganic nanoparticles vs organic nanoparticles, Vol 4, Ch 13, pp 309-319, de la Fuente, J.M. and V. Grazu, V. (Editors), Elsevier, Amsterdam.

Rogers, J.B., Dieffenbacher, A., and Holm, J.V. (2001) Lexicon of lipid nutrition (IUPAC Technical Report), *Pure Appl. Chem.*, **73(4)**: 685-744.

Rosensweig, R. E. (2002). Heating magnetic fluid with alternating magnetic field. *J. Magn. Magn. Mater.*, **252**: 370-374.

Small, D.M. (1971) in *The Bile Acids* (Nair, P.P. & Kritchevsky, D. eds.) Vol 1, Ch 8, pp 249-356, Plenum Press, New York,.

Tzocheva, S.S., Kralchevsky, P.A., Danova, K.D., Georgieva, G.S., Post, A.J., and Ananthapadmanabhan, K.P. (2012). Solubility limits and phase diagrams for fatty acids in anionic (SLES) and zwitterionic (CAPB) micellar surfactant solutions, *J.Colloid Interface Sci.*, **369**: 274-286.

van Miltenburg, J.C., Oonk, H.A.J., and Metivaud, V. (1999). Heat Capacities and Derived Thermodynamic Functions of *n*-Nonadecane and *n*-Eicosane between 10 K and 390 K, *J. Chem. Eng. Data*, **44**: 715-720.

Veiseh, O., Gunn, J.W., and Zhang, M. (2010) Design and fabrication of magnetic nanoparticles for targeted drug delivery and imaging, *Adv. Drug Delivery Rev.*, **62**: 284-304.

Wilding, I.R., 2000. Site-Specific drug delivery in the gastrointestinal tract. *Crit. Rev. Ther. Drug Carr. Syst.*, **17**: 557–620.

# CHAPTER 7

## Demonstrating *in vitro* "Release on Demand" using Magnetic Hyperthermia

## 7.1 Introduction

From the studies performed in chapter 6, it was observed that the coated materials either melted at a certain temperatures or were solubilised by the bile salts in the dissolution media. The melting or solubilisation of the coating thus exposed the capsule to the dissolution media. This caused the capsule to dissolve and allowed media ingress, which subsequently resulted in the release of the solubilised drug. Information from visual observation of coated capsules during RF exposure should shed more light on the heating, melting and solubilising behaviour of the coated capsule. This chapter will begin by describing the work done to visually observe the behaviour of coated capsules during RF heating. The coated capsules in this part of the work were subjected to different environments in order to visually observe their behaviour under an applied magnetic field. The visual observation was done by using a thermal imaging camera, video camera and fibre-optic thermosensors. This chapter ends by proposing a simple experimental set up for a drug release system and discusses the experimental results that support feasibility of the proposed set up.

## 7.2 Objectives

The aim of the work was to observe visually the behaviour of the coated capsule when a magnetic field is applied. These observations were done on coated capsules which were subjected to three different environments.

Using these observations, a new experimental setup for a drug release delivery system was proposed. It was hoped that from this new setup, one will be able to;

- Compare various materials to obtain the best materials or compositions to be used to coat the capsule.

- Observe the heating effect of embedded IONs in the coating and the surrounding dissolution media.

- Simultaneously study the behavioural pattern of drug release such as the time taken for the release process.

- Elucidate the effect of different frequencies and a magnetic field strengths on heating.

## 7.3 Results and Discussion

### 7.3.1 Visual and thermal imaging of the hyperthermia effect

The heating, melting, and solubilisation behaviour were observed previously with the entire coated capsule is fully immersed in the dissolution media. Equivalent information on dry or half-immersed coated capsules was not available. This is another impediment to better understanding of the heating, melting and solubilisation of the coated capsule. In this part of the work, the coated capsule was subjected to three different environments namely in open air, partially and fully immersed in dissolution media.

In order to obtain this visual information, it was thought that a similar experiment using a hyperthermia system that could be monitored visually using an ordinary camera or a thermal imaging video camera should be carried out. Fortunately, such a system was readily available within the research group of Prof Q. Pankhurst at University College, London, UCL. The experimental setup using the UCL hyperthermia system is shown in Figure 7.1. The UCL hyperthermia system consists of a Magnetic Alternating Current Hyperthermia, MACH, designed by Resonant Circuit Limited, RCL (www.resonantcircuits.com). RCL is a medical technology based spin-out company from UCL. The frequency is 1MHz and an AC current of 120 A is used. The diameter of the coil is 44 mm and consists of 3 turns with a pitch of 6 mm. An IR video camera is connected to the setup to capture thermal images during hyperthermia studies.
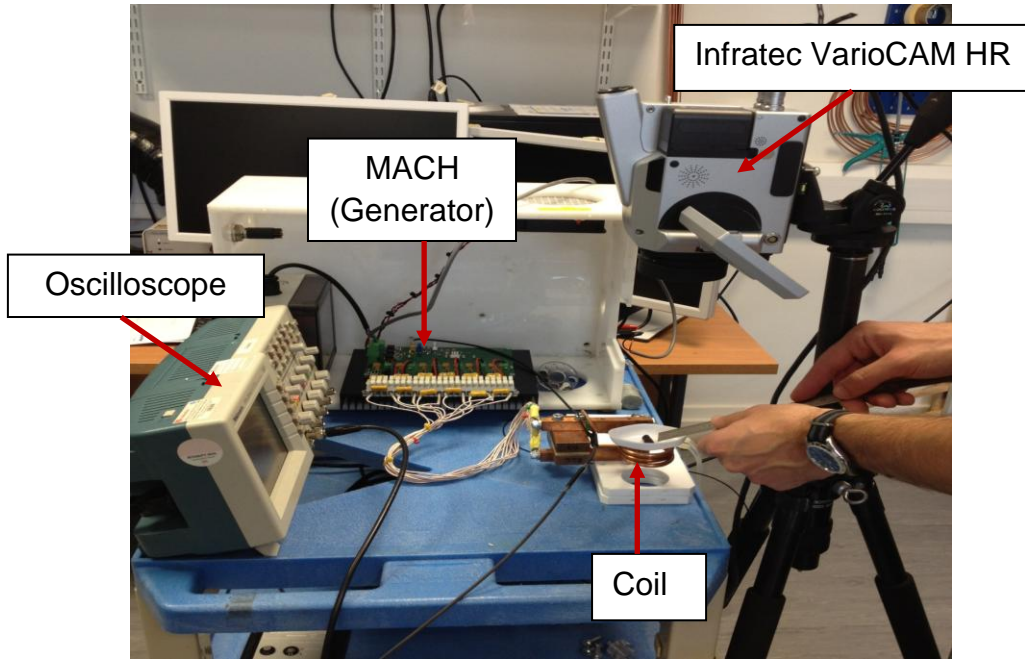
**Figure 7.1** The experimental setup using the UCL hyperthermia system.

The strength of the magnetic field depends on the distance from the central axis as shown in Figure 7.2a. For instance if the distance of the sample is placed 10 mm above the center of the coil, the field strength is 6000 A/m (7.5 mT). The maximum field strength at the centre of the coil is 7300 A/m (9.2 mT). Both of these values are shown by the red line of Figure 7.2a.
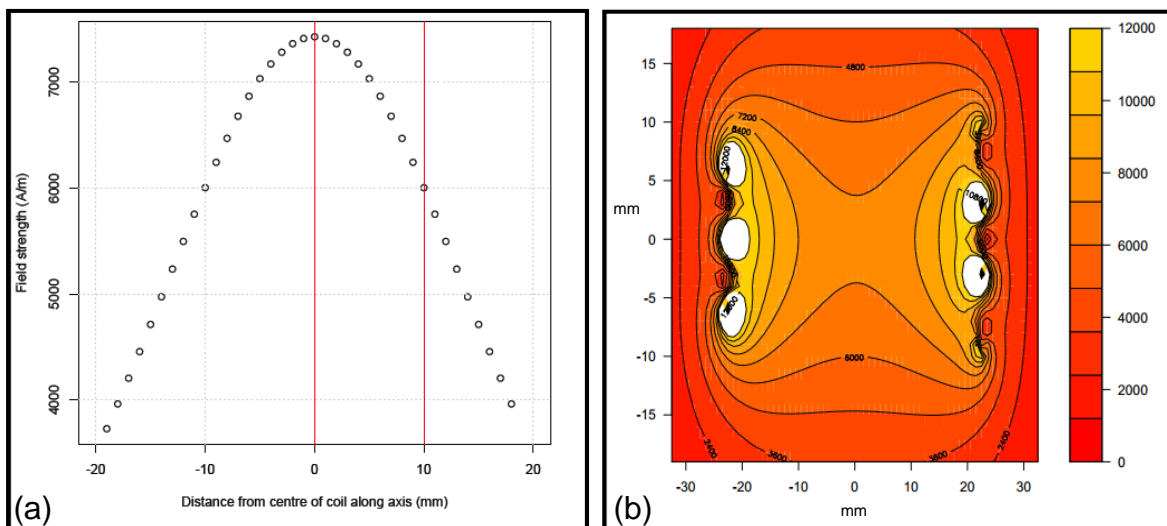


**Figure 7.2** (a) The variation of magnetic fields with the distance from the centre of the coil and (b) The field map for the 3 turn coils with a diameter of 44mm, at frequency of 1 MHz and an AC current of 120A (data from P. Southern, UCL) .

Figure 7.2b shows the field map at a frequency of 1 MHz and an AC current of 120A. The field map illustrates the field observed at a cross section through the central plane in the coils. The figure shows the 'hot spots' the location of highest field which is at the centre of the coil.

### 7.3.1.1 Coated capsule in open air

The information on the visual and thermal imaging of the heating behaviour of the coated capsule in open air can be obtained using the UCL hyperthermia system by placing the coated capsule in a weighing boat on top of the coil as shown in Figure 7.3.
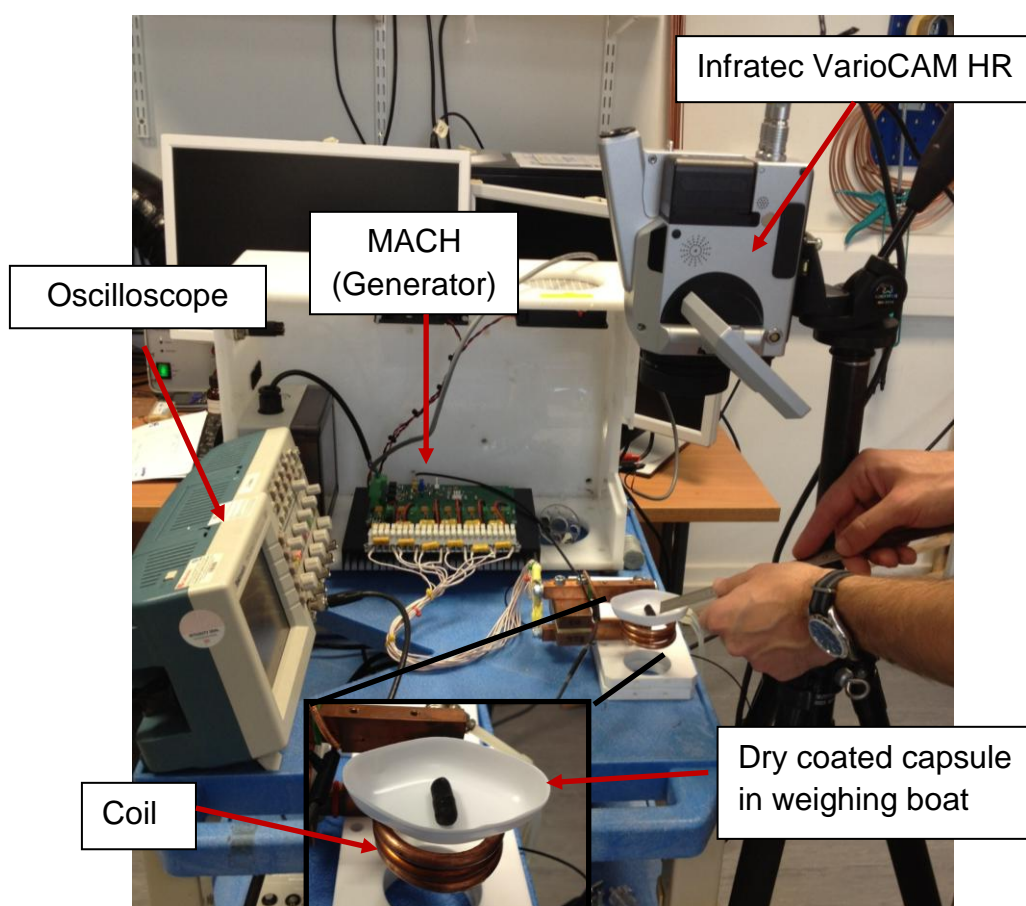


**Figure 7.3** The experimental setup to observe the heating behaviour of dry coated capsule. Insert shows the enlarged image of the coated capsule in a weighing boat.

The weighing boat was placed approximately 10 mm above the coil. At this distance, the strength of the magnetic field is about 6000 A/m (see Figure 7.2a). The frequency

was 1 MHz and an AC current of 120 A. The image was captured using an Infratec VarioCAM HR with a frame capture rate of 5 Hz.

Figures 7.4-7.6 depicted the IR image, photographs and temperature plot of a coated capsule in open air at the beginning, the initial melting and the continuous melting at higher temperature, respectively for a mixture of fatty acids C12:C14 (40:60/w:w) as the coating material. Figure 7.4 showed the data for the coated capsule when the maximum temperature reached 36.33$^{o}$C as recorded by the imaging camera. It was observed that the coated capsule was still intact at this temperature.
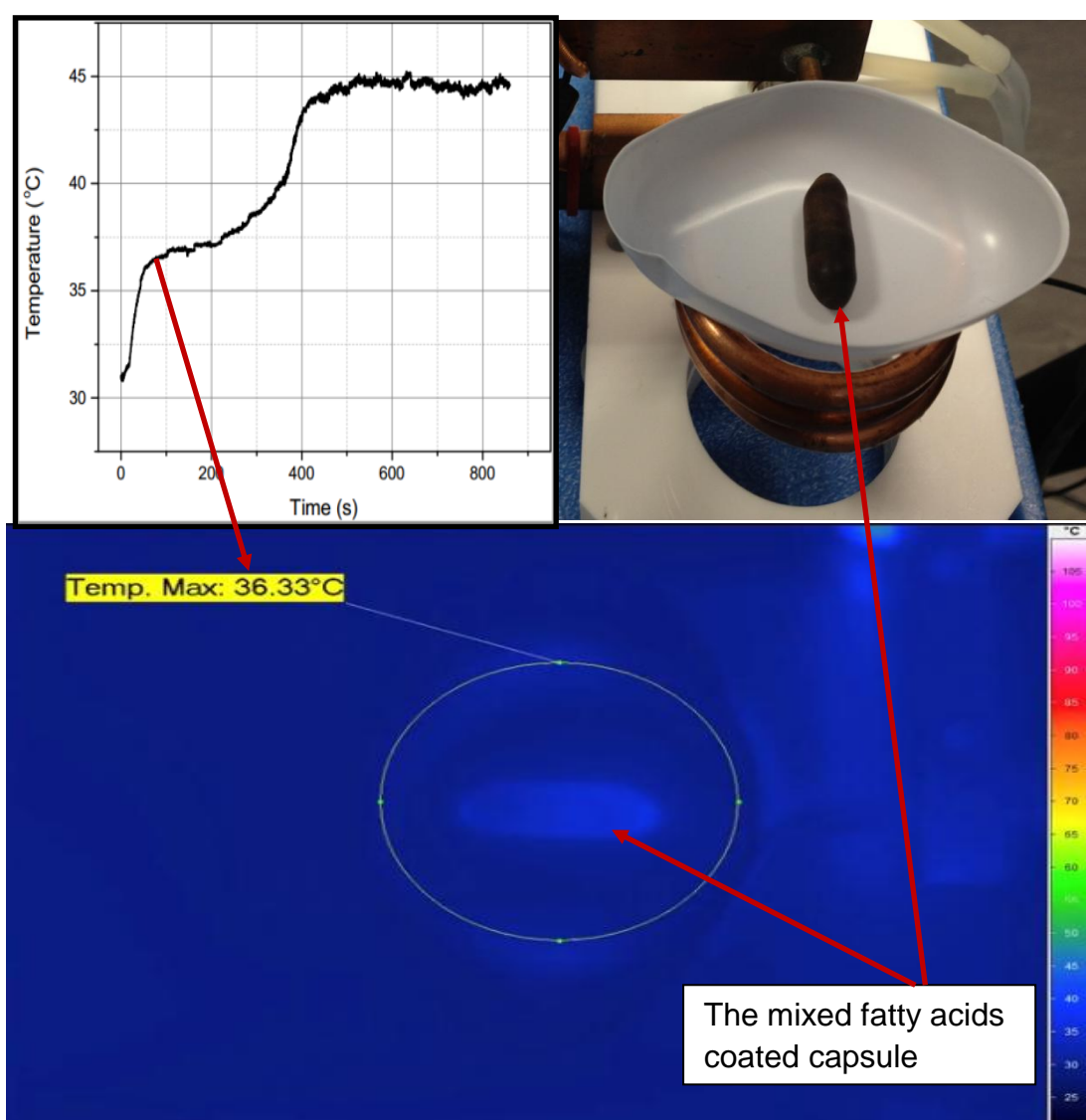


**Figure 7.4** The IR image, photograph and temperature plot at the maximum temperature of 36.33$^{o}$C for the mixture of fatty acids, C12:C14 (40:60/w:w).

Figure 7.5 showed the data for the coated capsule when the maximum temperature reached 42.92$^{o}$C. It was observed that the coating started to melt at the bottom of the capsule which was in contact with the weighing boat. As mentioned earlier the melting point for the mixture was measured using a DSC instrument was 40.28$^{o}$C (please refer to Figure 6.5a).
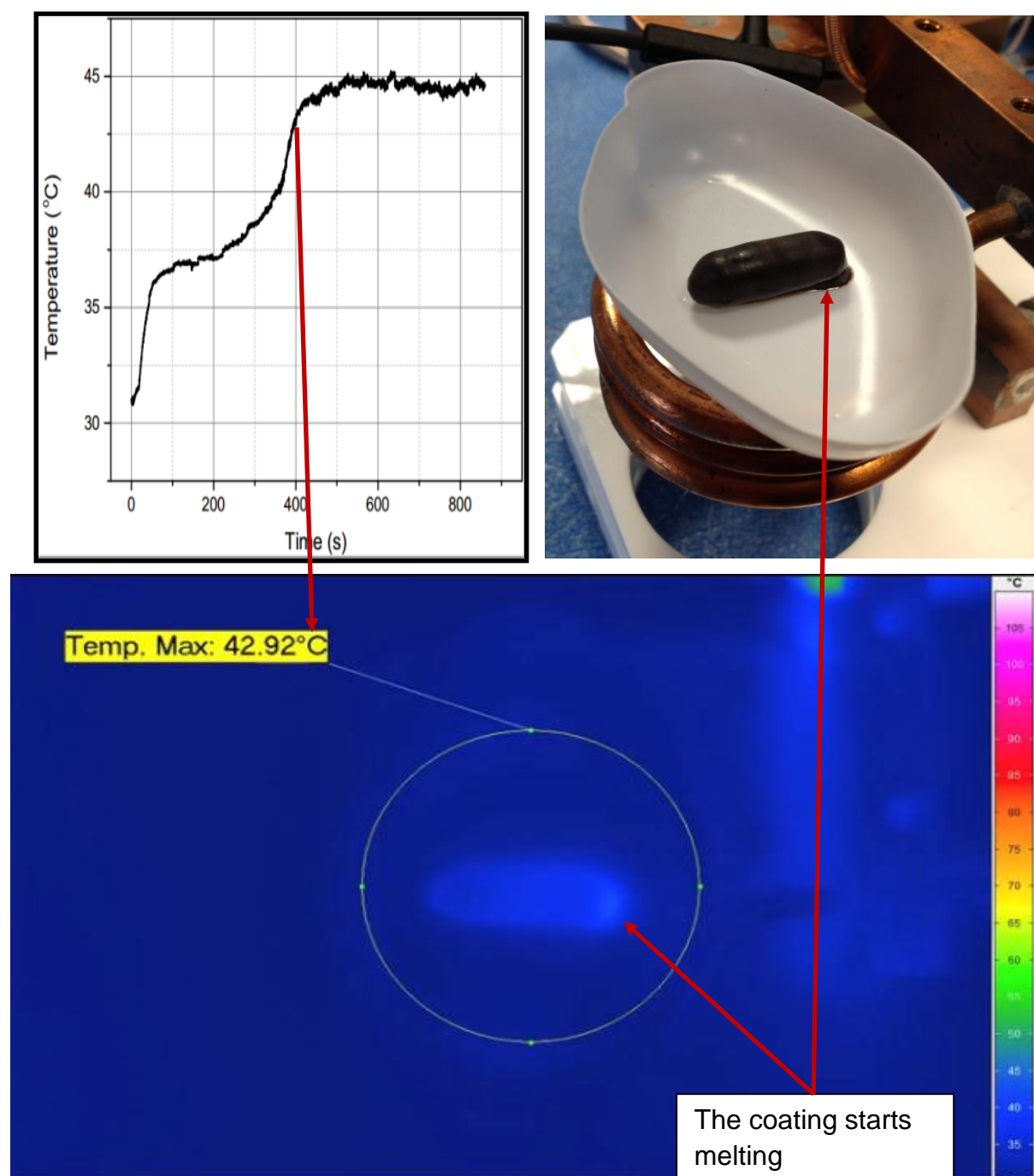


**Figure 7.5** The IR image and photographs at the maximum tempermature of 42.92 $^{o}$C for the mixture of fatty acids, C12:C14 (40:60/w:w).

In this experiment, the coating started to melt at 42.92 $^o$C, which was about 2 $^o$C higher than the melting point.

Figure 7.6 shows the data for the coated capsule when the maximum temperature reached 44.79$^o$C. It was observed that the coating did not melt any further at this temperature.
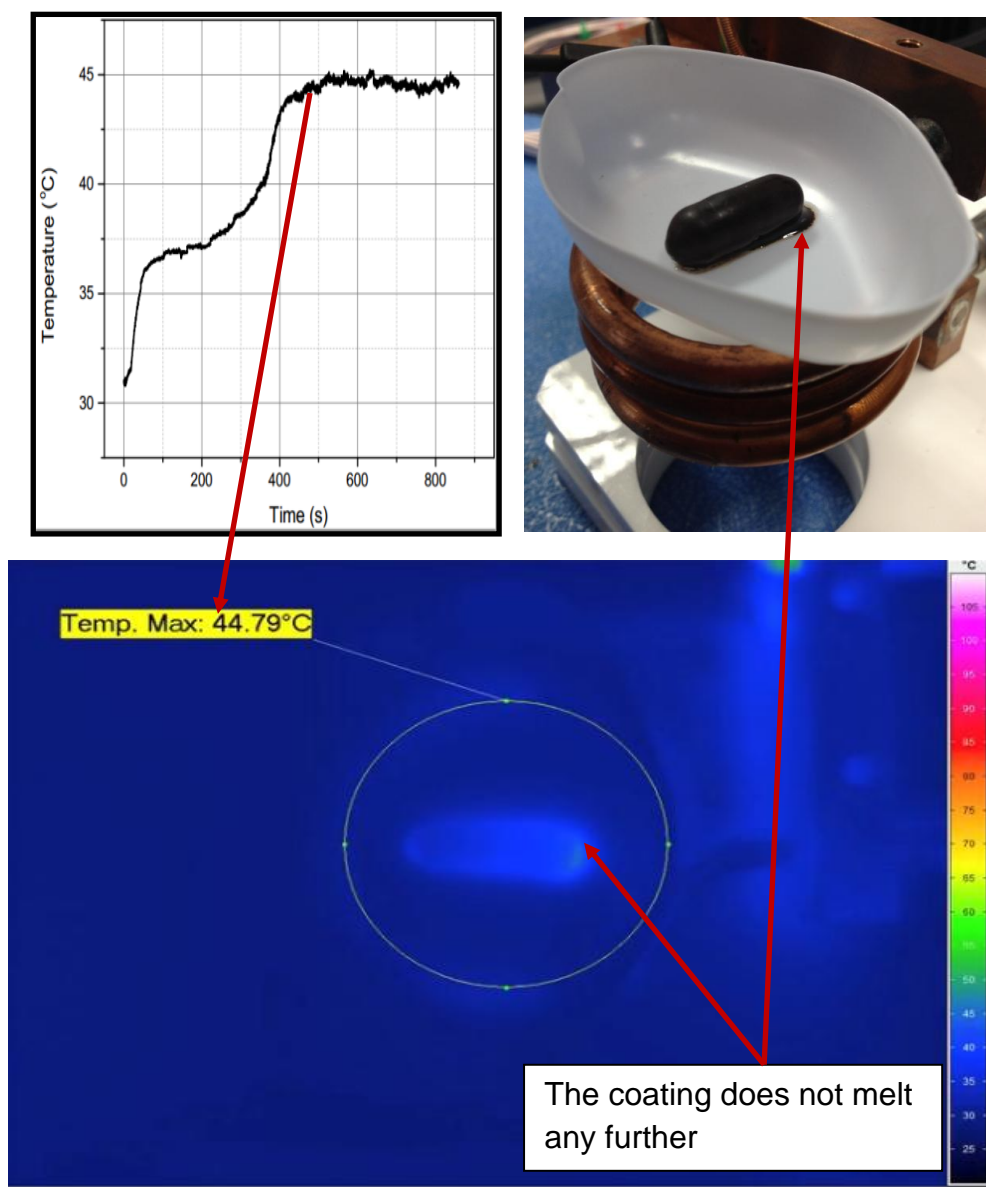


**Figure 7.6** The IR image and photographs at the maximum temperature of 44.79 $^o$C for the mixture of fatty acids, C12:C14 (40:60/w:w).

Figures 7.7-7.9 depict the IR image and photographs of the coated capsule at the beginning, the initial melting and the continuous melting at a higher temperature, respectively using eicosane as the coating material. Figure 7.7 shows the images for the coated capsule in open air when the maximum temperature reached 37.12$^{\circ}$C. The coated capsule was still intact at this temperature.
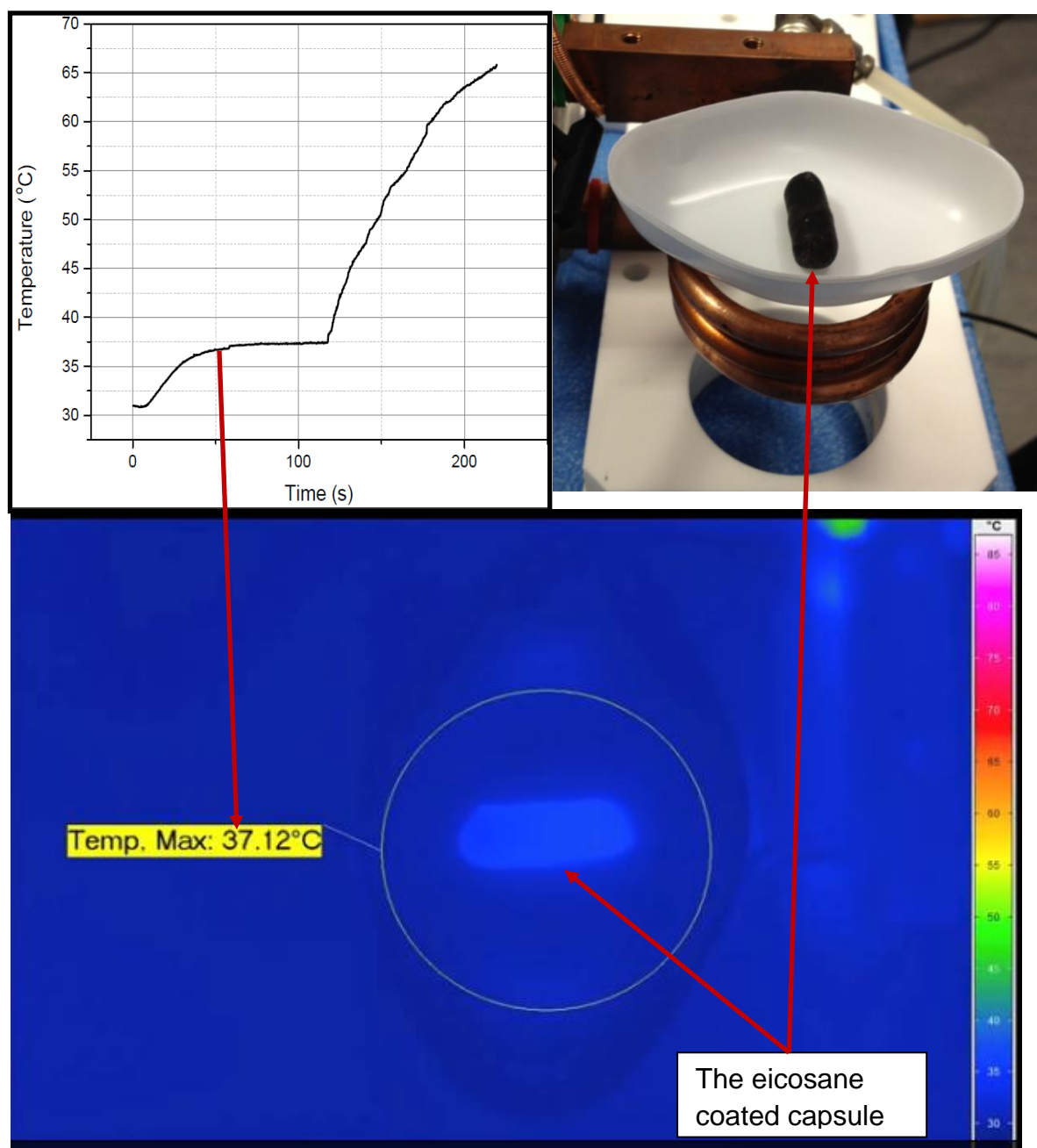


**Figure 7.7** The IR image and photographs at the maximum temperature of 37.12$^{\circ}$C for eicosane.

Figure 7.8 shows the images for the coated capsule when the maximum temperature reached 40.73$^o$C. It was observed that the coating started to melt at the bottom of the capsule which was in contact with the weighing boat. Again the melting of the coating occurred at 2$^o$C higher than the melting point of eicosane which was 37.79$^o$C as determined by the DSC instrument (please see Figure 6.7a).
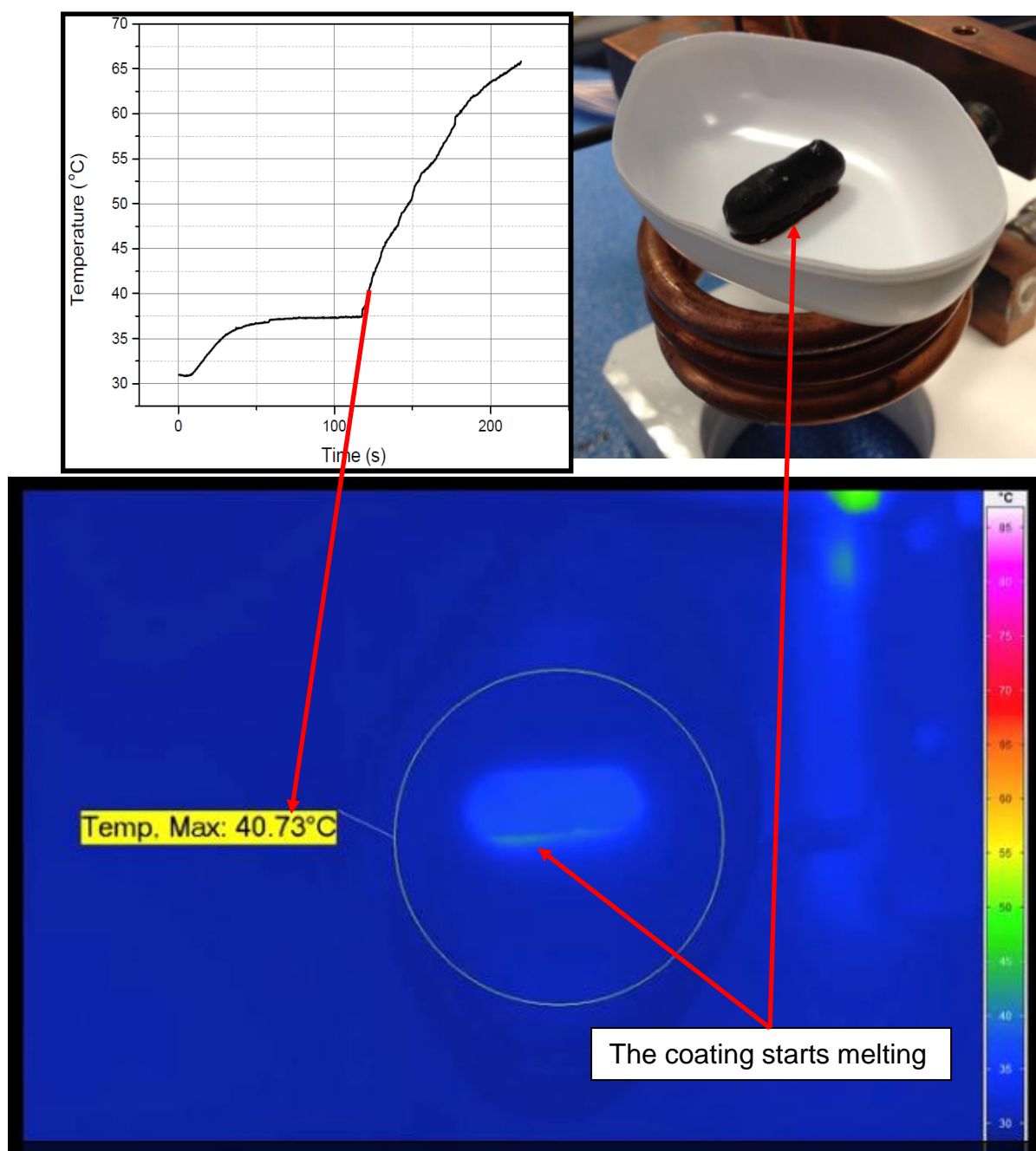


**Figure 7.8** The IR image and photographs at the maximum temperature of 40.73 $^o$C for eicosane.

Figure 7.9 shows the images for the coated capsule when the maximum temperature reached 64.58°C. It was observed that the coating melted completely starting from the part that was in contact with the weighing boat and the liquidised coating all run off the capsule surface under gravity.



**Figure 7.9** The IR image and photographs at the maximum temperature of 64.58°C for eicosane.

Figures 7.10-7.12 depict the IR image and photographs of a coated capsule at the beginning, the initial melting and the continuous melting at higher temperature, respectively using the mixture of eicosane and docosane (40:60/w:w) as the coating material. Figure 7.10 shows the images for the coated capsule in open air when the maximum temperature reached 35.53$^{o}$C. The coated capsule was still intact at this temperature.
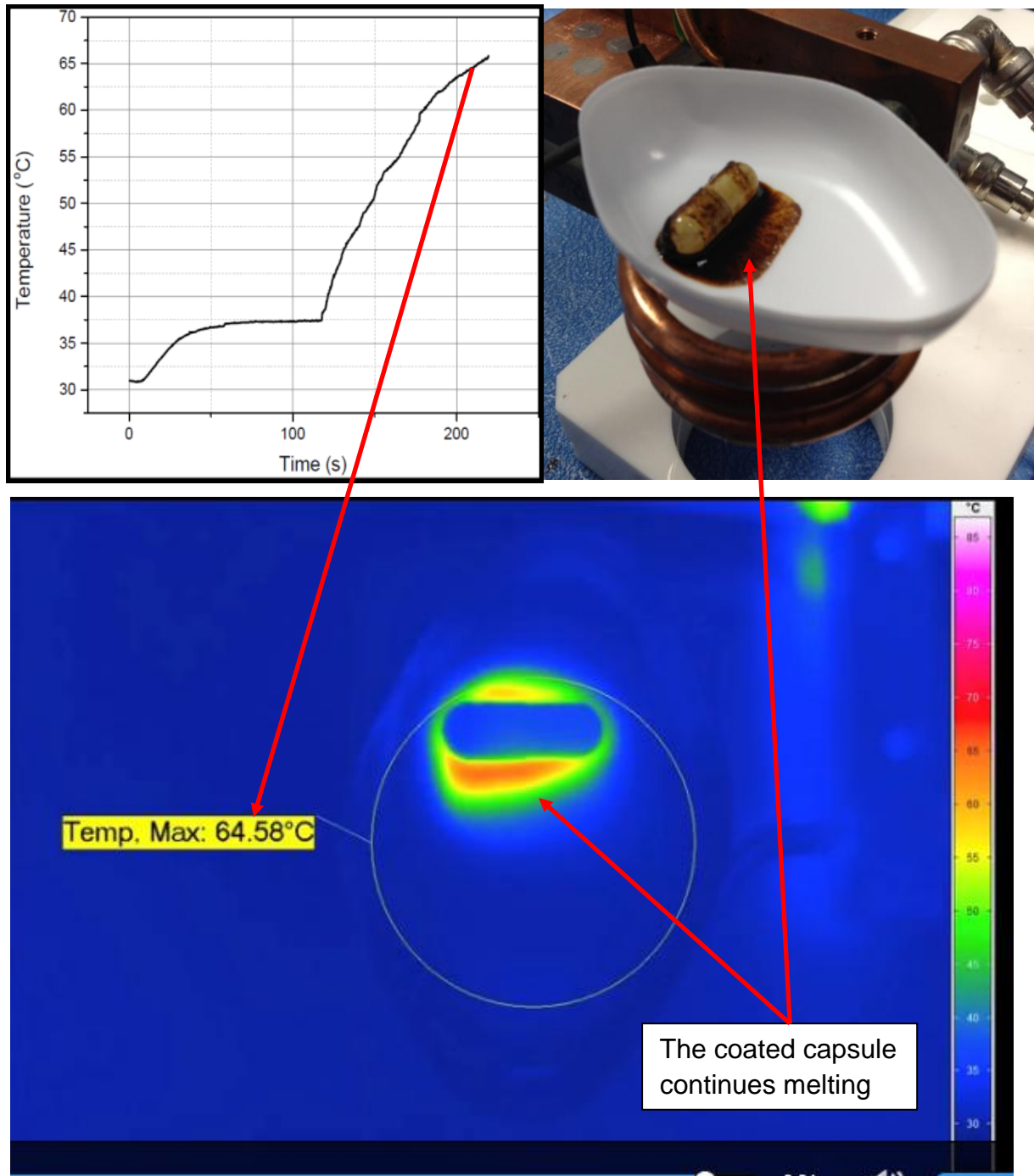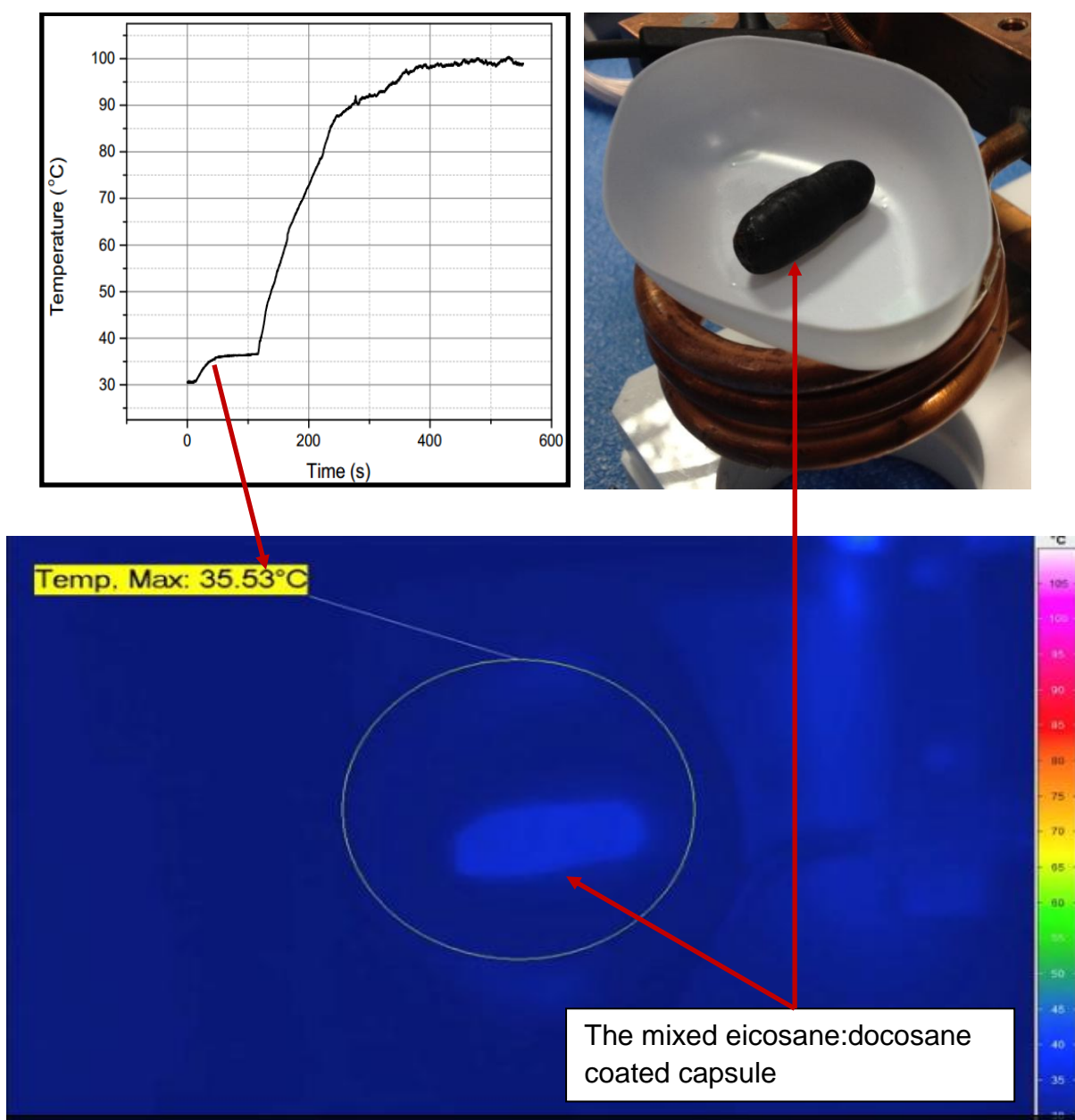


**Figure 7.10** The IR image and photographs at the maximum temperature of 35.53 $^{o}$C for mixture of eicosane and docosane (40:60/w:w).

Figure 7.11 shows the images for the coated capsule when the maximum temperature reached 41.80°C. It was observed that the coating started to melt at the bottom of the capsule which was in contact with the weighing boat. Again the melting of the coating occurred at approximately 2°C higher than the melting point of the mixture of eicosane and docosane which occurred at 40.10°C (please refer to Figure 6.7c).
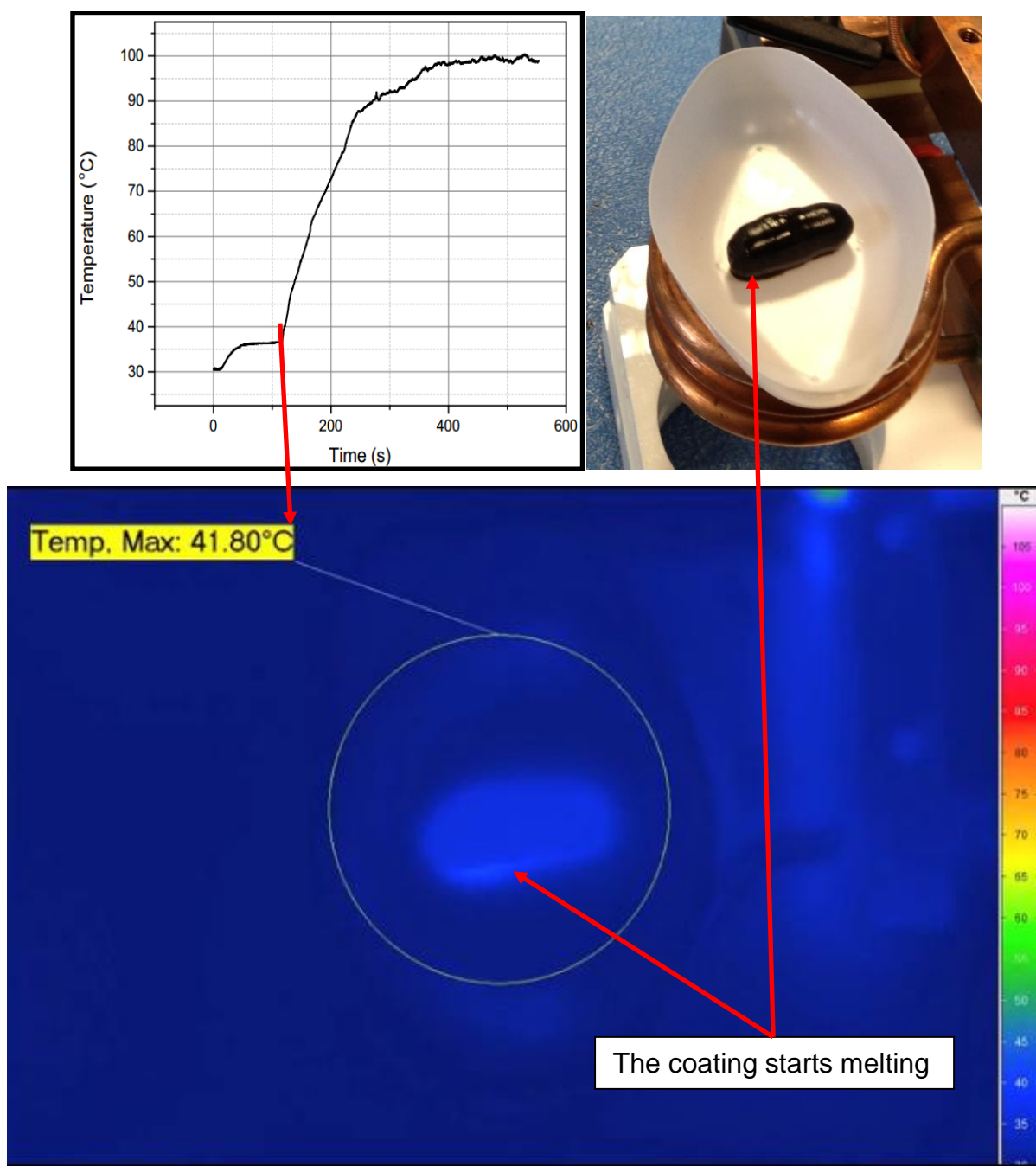


**Figure 7.11** The IR image and photographs at the maximum temperature of 41.80°C for mixture of eicosane and docosane (40:60/w:w).

Figure 7.12 shows the images for the coated capsule when the maximum temperature reached 86.90°C. It was observed that most of the coating had melted and run off the capsule.
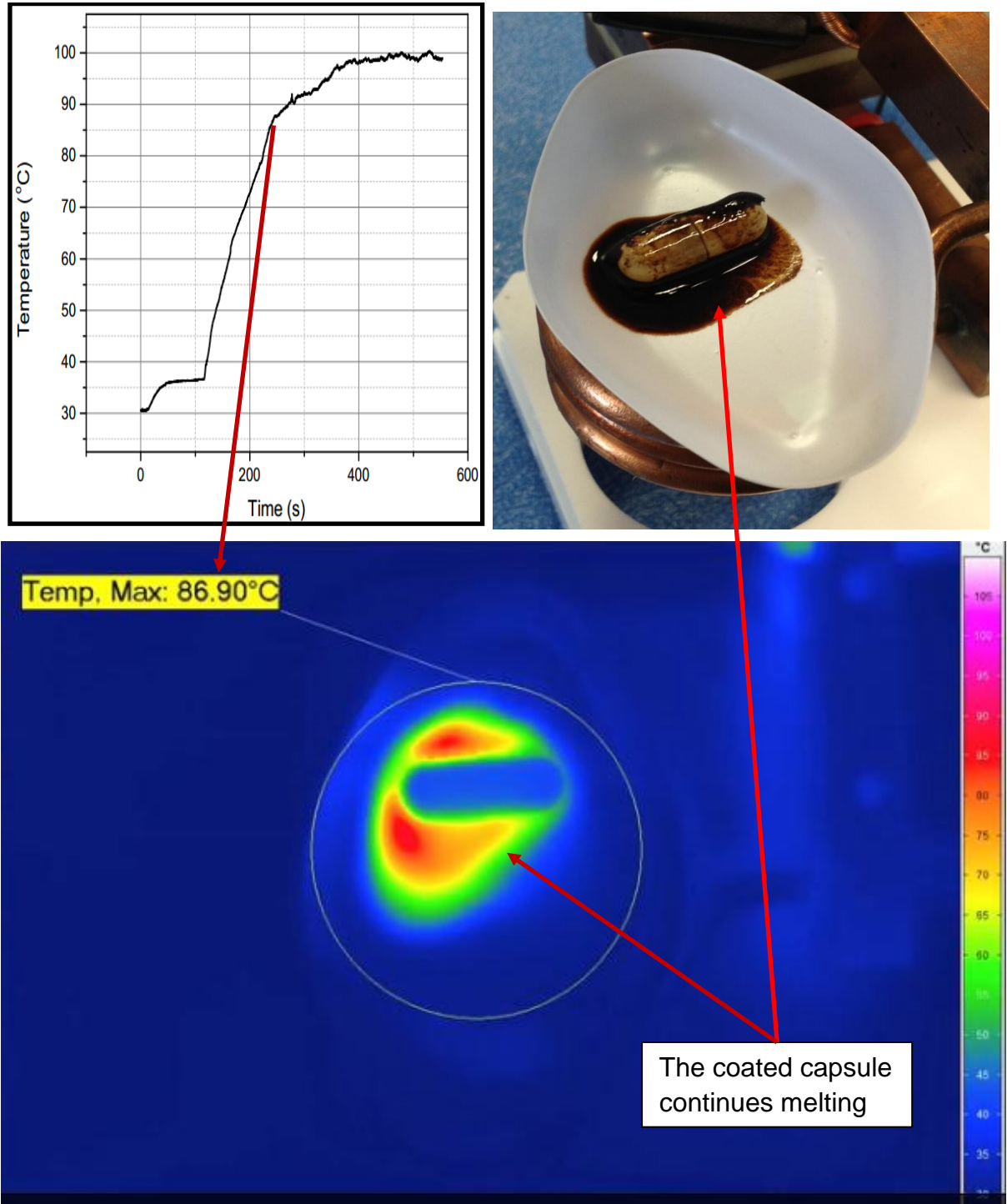


**Figure 7.12** The IR image and photographs at the maximum temperature of 86.90°C for mixture of eicosane and docosane (40:60/w:w).

From all of the visual observations obtained when the coated capsule was placed in open air, it can be summarised that heating by RF hyperthermia to above the melting point of the coating materials was able to melt the coatings. The delayed melting of the capsules (about 2$^o$C higher) may be due to difference in the DSC instrument which is running under controlled adiabatic conditions, where heat loss is negligible, whereas, here in this experiment; it is carried out in open air where heat loss from the surface may keep the layer "solid" even though the internal layer temperature is slightly higher, as shown by the IR camera. Both of these setups are therefore subject to possible experimental inaccuracy. Secondly, the thermal imaging camera used in these setups only measures the surface temperature of the sample. The main sample then experiences a different heating temperature than the surface temperature. Hence, the thermal imaging camera may report the melting temperature a few degrees above what was previously determined from DSC measurements. Another observation is that the melting starts from the middle of the capsule body which is in direct contact with the weighing boat and spreads outwards towards one end of the capsule. This could be due to several factors such as the unevenness of the capsule coating or the distribution of IONs embedded in the capsule. While the coatings with eicosane and the mixture with docosane melted completely, the capsule coated with the mixture of fatty acids hardly melted and stayed intact even until completion of the experiment. This is illustrated in Figure 7.13a-c.
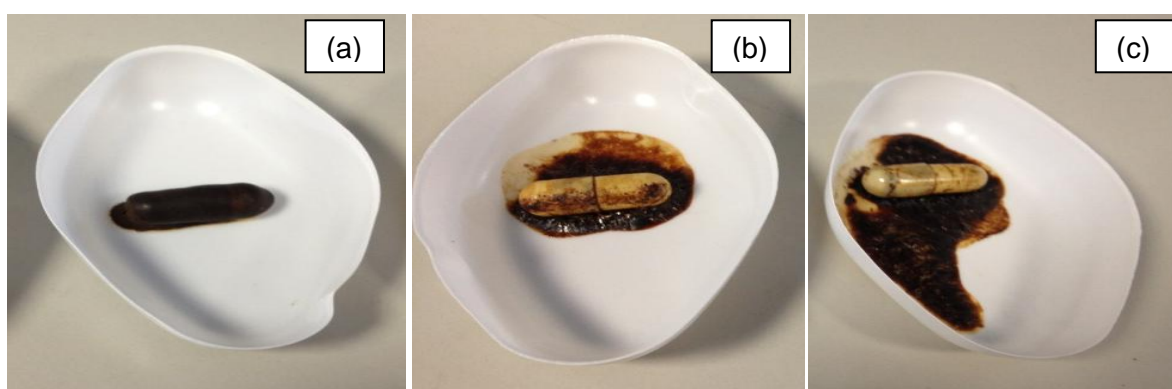


**Figure 7.13** The melting of the coating by the end of experiment for (a) mixture of fatty acids, (b) eicosane and (c) mixture of eicosane and docosane as the coating materials.

**7.3.1.2 Coated capsule partially immersed in dissolution media**

Figure 7.14 shows the equivalent setup but with the coated capsule being half-immersed in the dissolution medium. The dissolution medium used was the simulating fasting state (FaSSIF) with a pH at 6.5. In this experiment, a water soluble dye bromo-cresol green purchased from BDH replaced the drug. This made it easier to visualise the moment of "drug" release. The dye was filled into a capsule. The capsule was then coated with coating materials and floated in a container containing the dissolution medium. The container was then placed in the middle of the coil. This gave an exposure to a higher magnetic strength of about 7300 A/m compared to the setup with the coated capsule in the weighing boat. The image was captured using the Infratec VarioCAM HR with a frame capture rate of 5 Hz.



Coated capsule half-immersed in medium
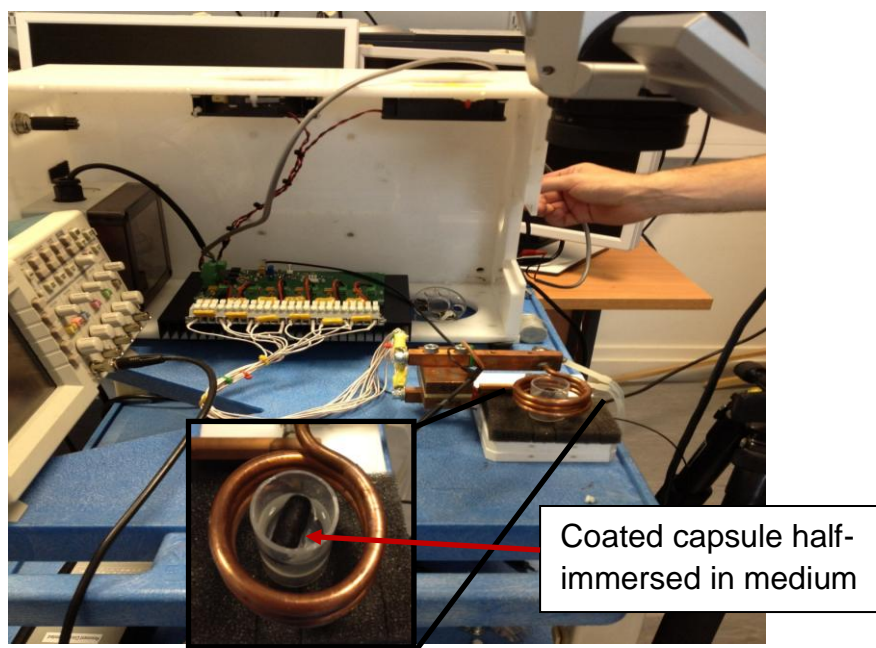
**Figure 7.14** The experimental setup to observe the heating behaviour of coated capsules half-immersed in medium. The insert shows an enlarged image of the coated capsule half-immersed in the medium.

When compared to the capsules exposed to open air, similiar results were obtained when the coated capsule was half-immersed in the dissolution medium. Among the three coating materials tested, the eicosane coated capsule was chosen to illustrate the behaviour of the half-immersed capsule.

Figure 7.15 illustrates the IR image, photograph and temperature plot for a coated capsule half-immersed in the dissolution medium using eicosane as the coating material. The image shows that coated capsule was still intact when the maximum temperature reached 36.03$^o$C.
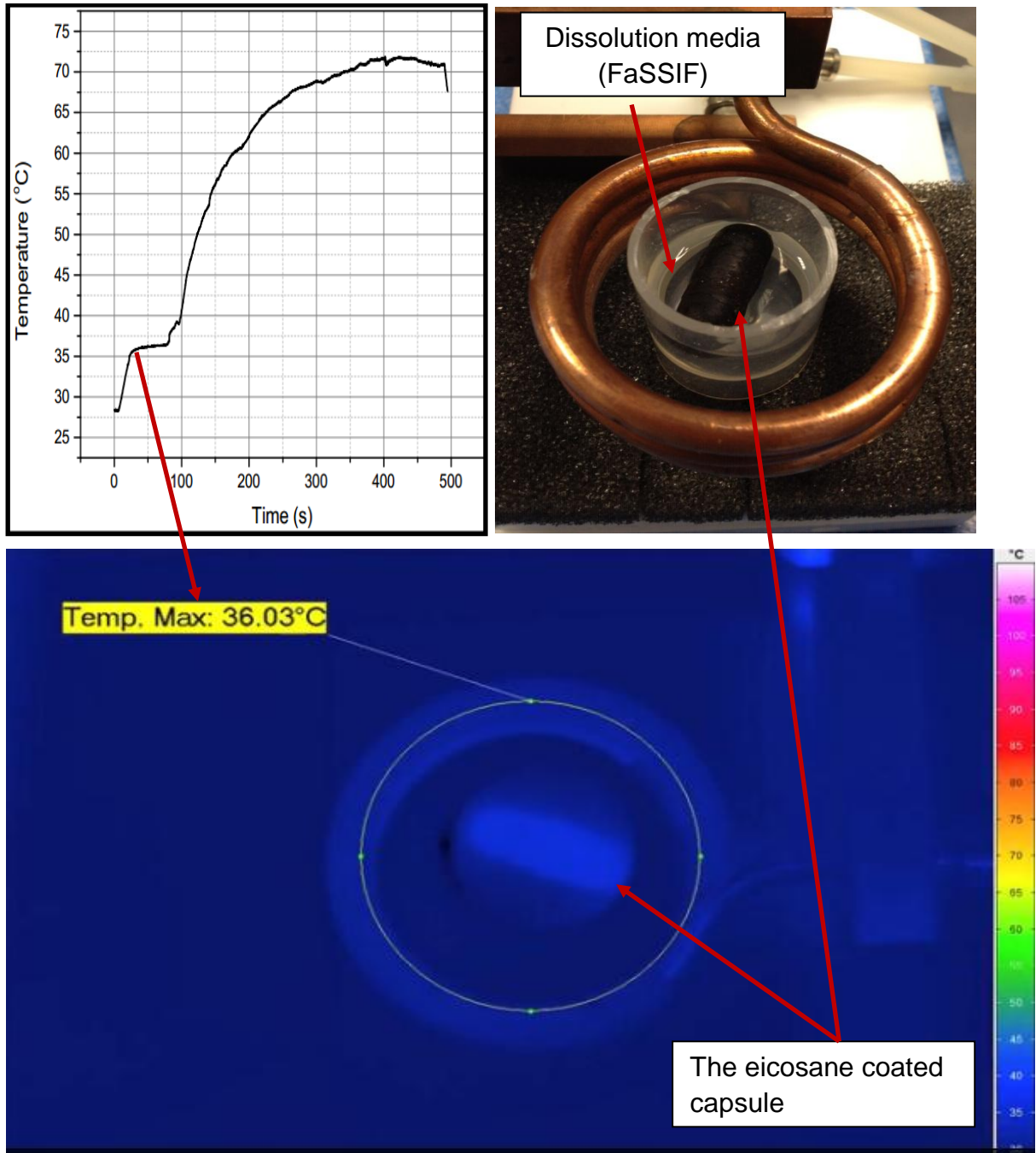


**Figure 7.15** The IR image and photographs at the maximum temperature of 36.03$^o$C for the eicosane as the coating material.

Figure 7.16 shows the images for the coated capsule when the maximum temperature reached 39.04$^{\circ}$C. It was observed that the coating started to melt but this time it was from the upper part of the capsule and it flowed the coating down to the medium. The upper part of the capsule melted earlier compared to the bottom part of the capsule because the bottom part was immersed in the media., which has a much higher thermal conductivity and specific heat capacity than air, hence it cools the capsule much more effectively, delaying the onset of the melting.
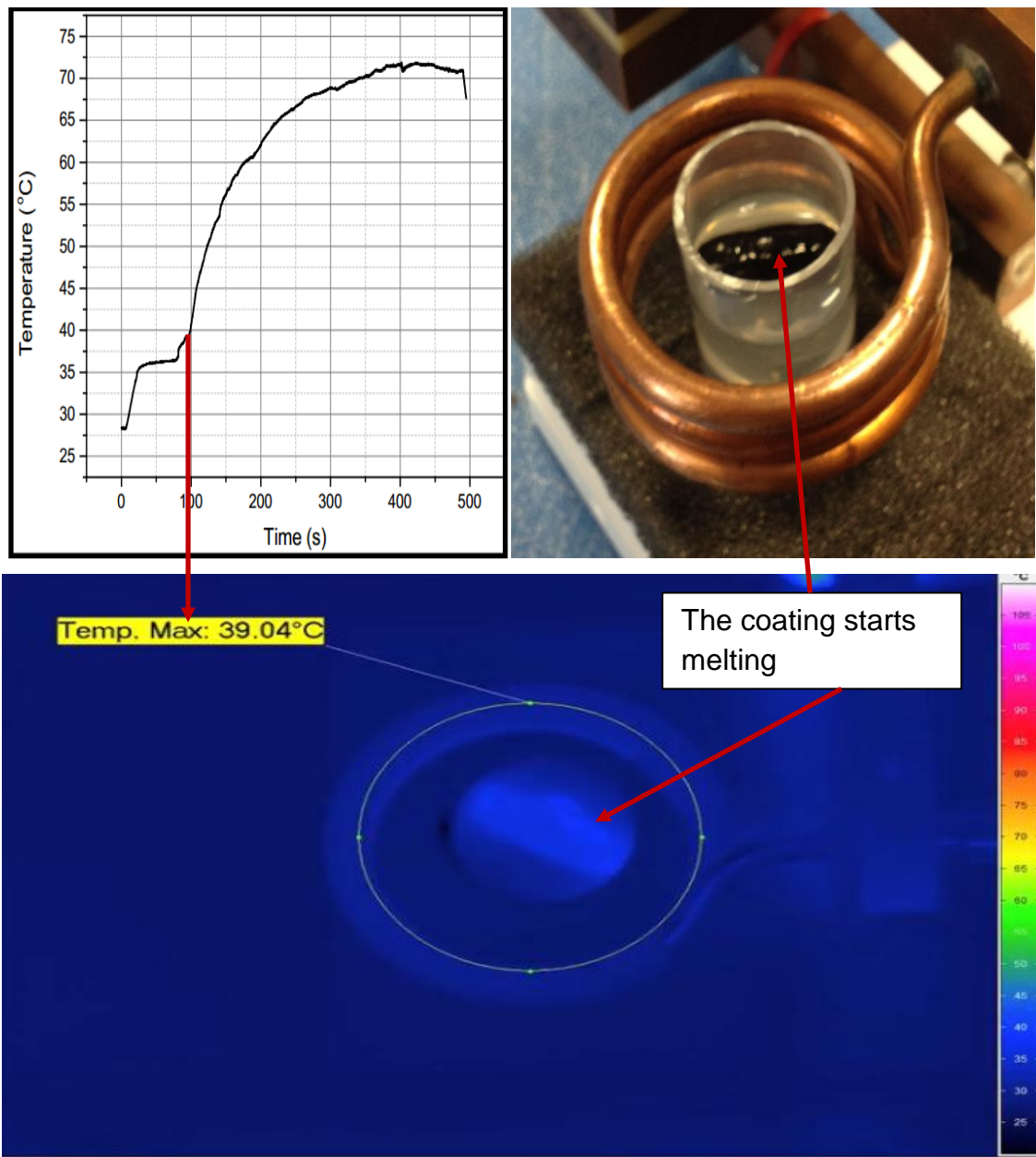


**Figure 7.16** The IR image and photographs at the maximum temperature of 39.04$^{\circ}$C for the eicosane as the coating material.

Figure 7.17 shows the images for the coated capsule when the maximum temperature reached 69.76°C. It was observed that the upper coating of the capsule melted completely and flowed down to the medium. Upon further heating, it was observed that the dye diffused out into the dissolution medium as shown in Figure 7.18.



**Figure 7.17** The IR image and photographs at the maximum temperature of 69.76°C for the eicosane as the coating material.
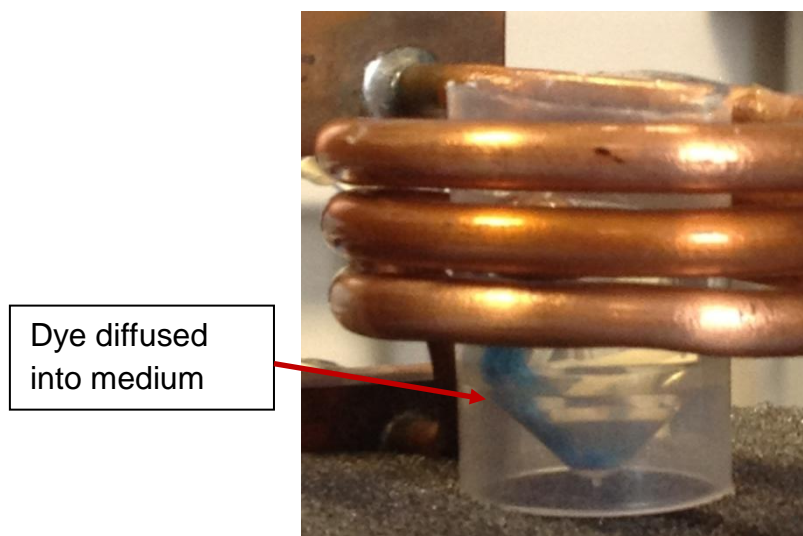
**Figure 7.18** The diffusion of dye upon further heating of the capsule as indicated by the blue colour (bromo-cresol green at pH 6.5) for system in eicosane.
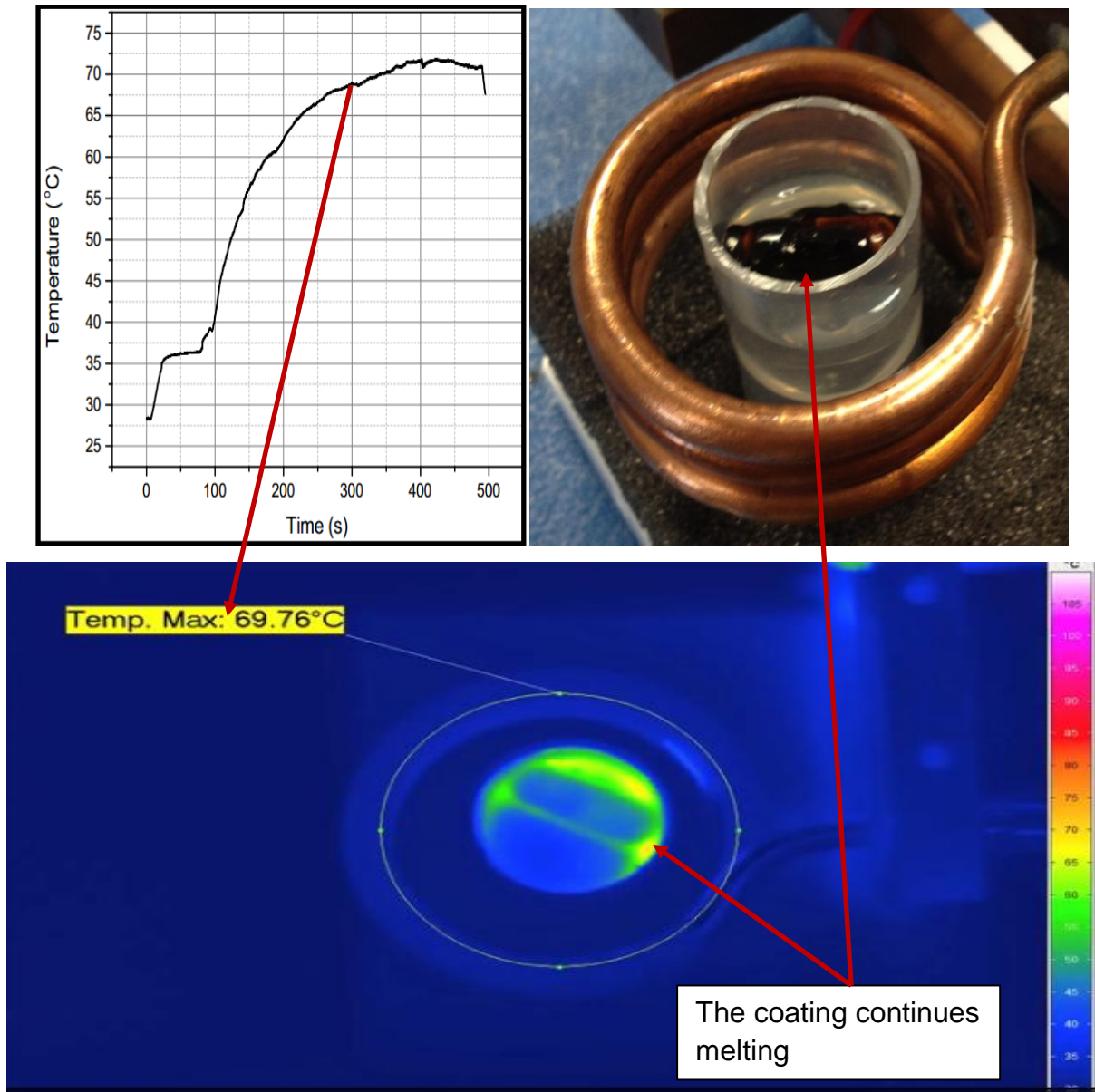
Finally, Figure 7.19a-c shows all three of the coated capsules after completion of the experiment. Note that the coating was still intact in some parts of the capsule with the capsule coated with the mixture of fatty acids being the least affected by the heating.
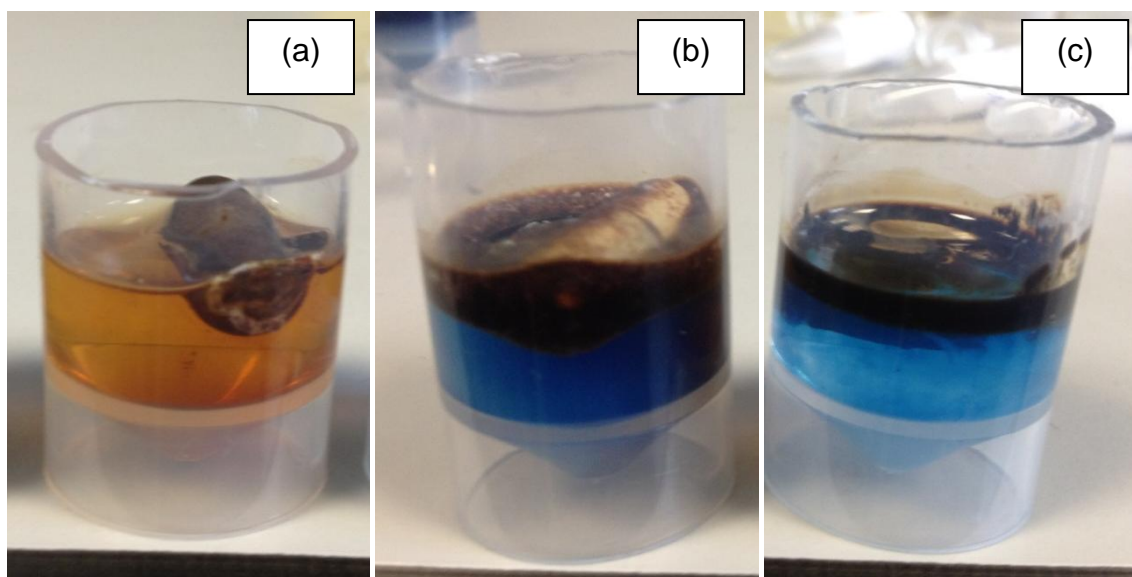


**Figure 7.19** The melting of the coating and the diffusion of dye into the medium at the completion of the experiment for (a) mixture of fatty acids, (b) eicosane and (c) mixture of eicosane and docosane as the coating materials.

For the setup with the coated capsules half-immersed in the dissolution medium, the results yielded were similar to those of coated capsules monitored in open air. One

important observation was the visual observation of the release of dye, which represented the release of drug. One interesting difference was that the melting of the coating began from the upper part of the coated capsule in contrast to that for the coated capsule in open air, but this is easily understood in terms of thermal mass and the coating effect. The video for both open air and half-immersed systems showing temperature as a function of time for the IR video recording, are burned into a CD and attached in this thesis.

Overall, the findings from both of the setups have successfully provided visual information on the heating behaviour of the coated capsules.

### 7.3.1.3 Coated capsules fully immersed in dissolution media

In order to witness the behaviour of fully immersed coated capsules, visually as well as graphically, the experimental setup of the hyperthermia system shown Figure 7.20 was used.
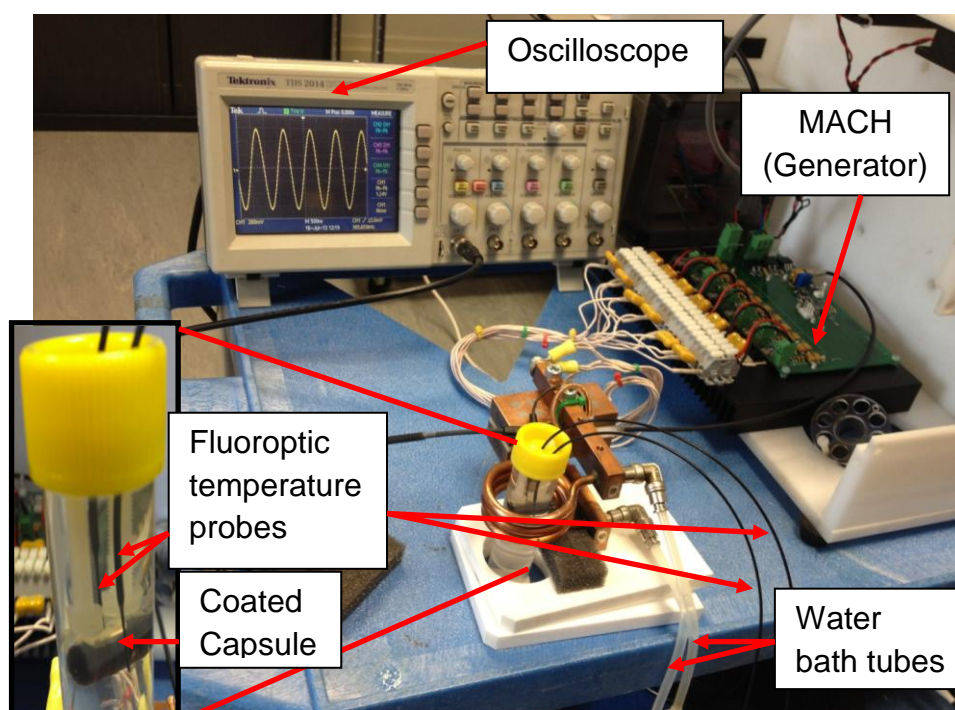


**Figure 7.20** The experimental setup to observe the release of drug by visual inspection. Inset is the enlarged sample tube showing the position of the coated capsule and the two fluoroptic temperature probes.

In this experiment the drug was again substituted with bromo-cresol green. Two fluoroptic temperature probes (Luxtron FOT Lab Kit) were inserted into the sample tubes containing the dissolution medium in order to monitor the temperature (see inset of Figure 7.20). The temperatures close to the capsule and in the dissolution medium were recorded with these probes at a capture rate of 1 Hz. The coated capsule in the sample tube was centrally located in the coil. The frequency was 1MHz and an AC current of 120 A. The magnetic field was about 7200 A/m (9.1 mT).

The results obtained from this experimental setup are illustrated in Figures 7.21-7.23 for the three different coatings. Figure 7.21 shows the graphical and visual illustration of the variation of temperature with the exposure time for the mixture of fatty acids as the coating material.
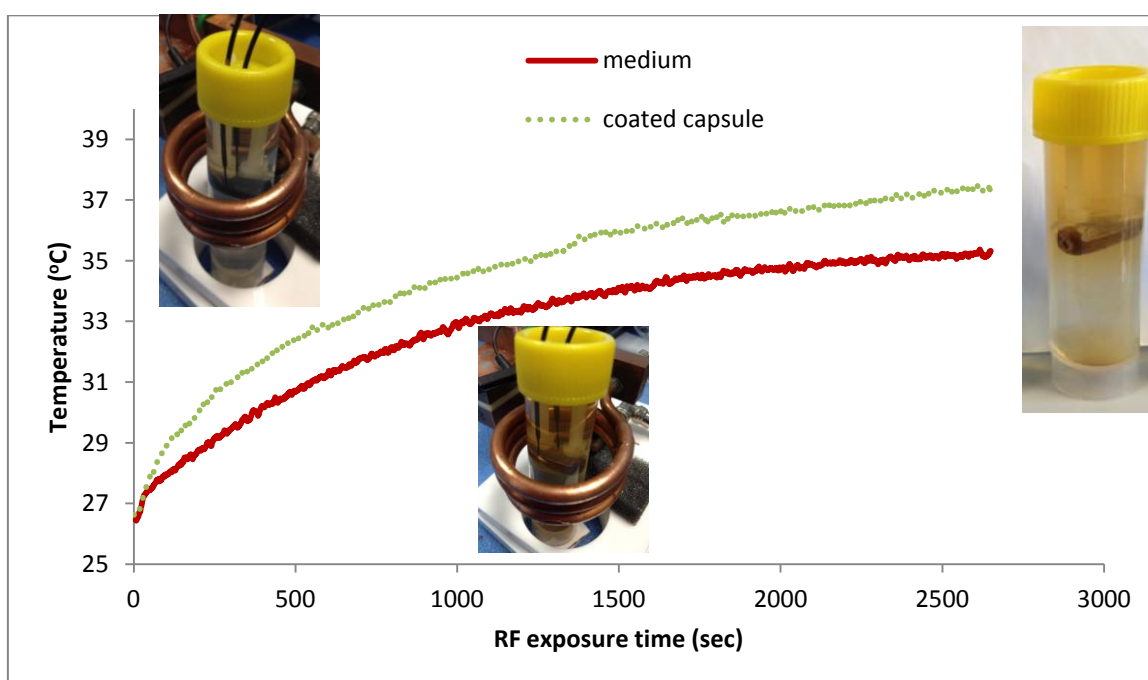


**Figure 7.21** The variation of temperature of a capsule coated with a mixture of fatty acids (40:60/w:w) with RF exposure time at a frequency of 1MHz.

It was observed that the melting point of the mixture of 40.3°C was not reached in this experiment. Even though the melting point was not reached, the dye readily diffused into the medium. This was verified by visual observation, captured in the photographs shown in Figure 7.21 at three different time intervals. It was also seen that some of the coating was still intact on the body of the capsule.

Figure 7.22 shows the graphical and visual illustration of the variation of temperature with the exposure time for eicosane as the coating material. From the graph, the melting point of eicosane of 37.79$^o$C was reached after about 800 seconds of exposure.
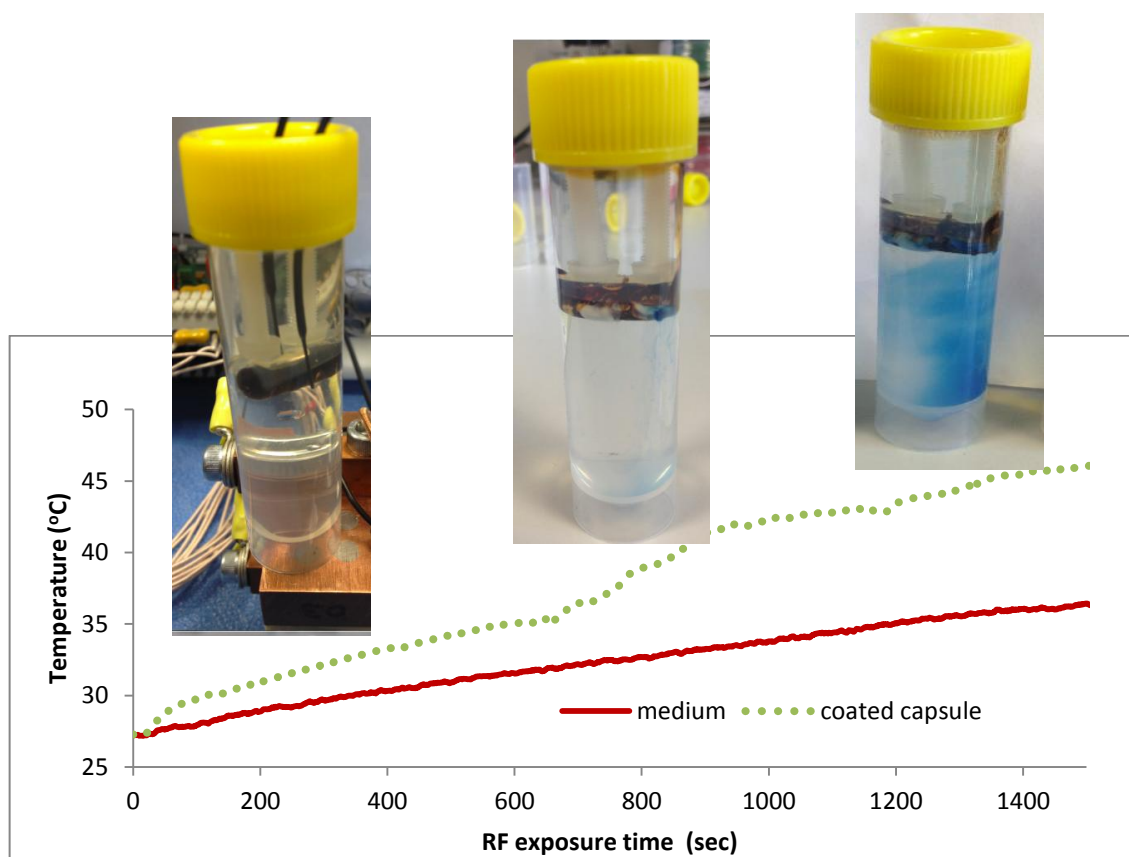


**Figure 7.22** The variation of temperature of a capsule coated with eicosane with RF exposure time at a frequency of 1MHz.

Visually it was seen that at this temperature, the coating started to melt and then slowly released the dye (blue colour in the dissolution medium). It was also observed that the first point of exit for the dye was observed at one of the terminal ends of the capsule. As the exposure time increased, more dye was released into the medium since more of the capsule was dissolved in the dissolution medium. This was indicated by the intensity of the blue colour of the medium increasing with time.

For the mixture of eicosane and docosane as the coating material, similar behaviour to that of eicosane was observed, both in term of the curves and visual inspections.

Finally, Figure 7.23a-c showed all three of the coated capsules after completion of the experiment. Note that the coating was still intact in some parts of the capsule.
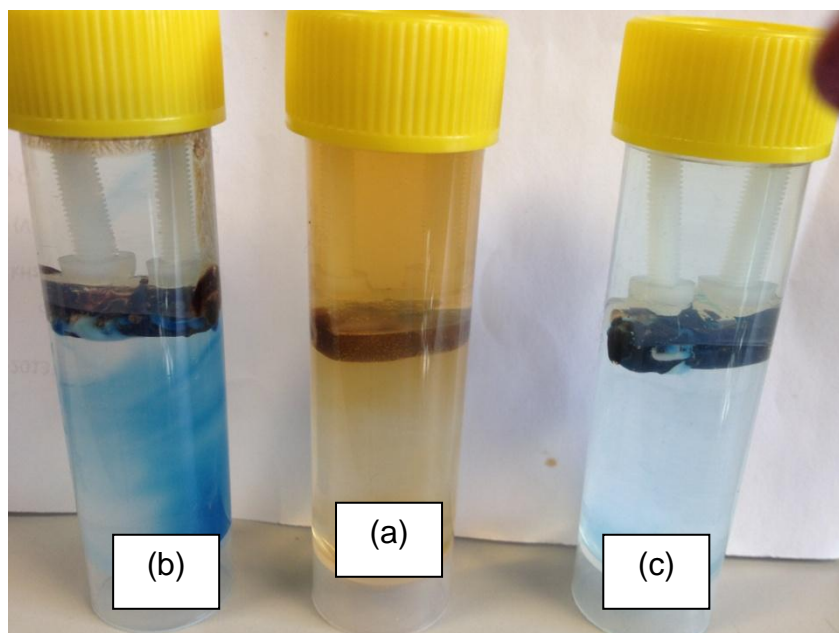


**Figure 7.23** The melting of the coating and the diffusion of dye into the media until completion of experiment for (a) mixture of fatty acids, (b) eicosane and (c) mixture of eicosane and docosane as the coating materials.

The above visual observation when the coated capsule was fully immersed shows that the drug (in this case dye) would be released once it came into contact with the dissolution media. This is indicated by the dissolution of the dye and the colouring of the media. Another observation is that under this condition, the coating began to melt once the melting point is reached. This was not observed in the previous two setups (i.e. in open air and half-immersed) where the melting of the coatings occurred above the melting points of the coatings. Finally, the observation where the first point of exit for the dye is at one of the terminal ends of the capsule is an interesting one. It is postulated that it related to the 'hot spots' mentioned in Figure 7.2b whereby the melting of the coating occurred more quickly at certain parts of the capsule and thus exposed the capsule to the dissolution medium or open air. This may relate to variations in the coating thickness, due to the rather crude manual coating procedure. .

## 7.4 Monitoring *in vitro* "Release on Demand" under Hyperthermia Conditions

Finally with the findings from the formulation, hyperthermia, dissolution studies and visual observation at UCL, a new experimental setup was proposed to study the *in vitro* released drug delivery system. The materials chosen to coat the capsules consisted of eicosane, and mixtures of fatty acids and paraffins both at a weight ratio of 40:60. The dissolution medium was the simulating fasting state at pH 6.5 and 37 $^{o}$C, mimicking the intestine condition in the GI tract. The whole system was designed as a non-invasive physical release mechanism that works with an orally-delivered capsule having a universal and relatively simple encapsulating coat that can be mass produced.

The basic setup follows that of the magnetherm setup (please see Figure 3.15) but with an additional UV spectrometer and a My PCLab A/D interface to convert the voltage output of the spectrometer into a digital signal that could be filed along with the output of 2 thermocouples. Two separate my PClab interface boxes were used, since each has only one thermocouple input.

Figure 7.24 shows the overall schematic representation of the proposed experimental setup. A UV spectrometer was attached to the sample holder to measure the drug released. A peristaltic pump was used to recirculate the medium through the flow cell in the spectrophotometer and back to the sample holder.
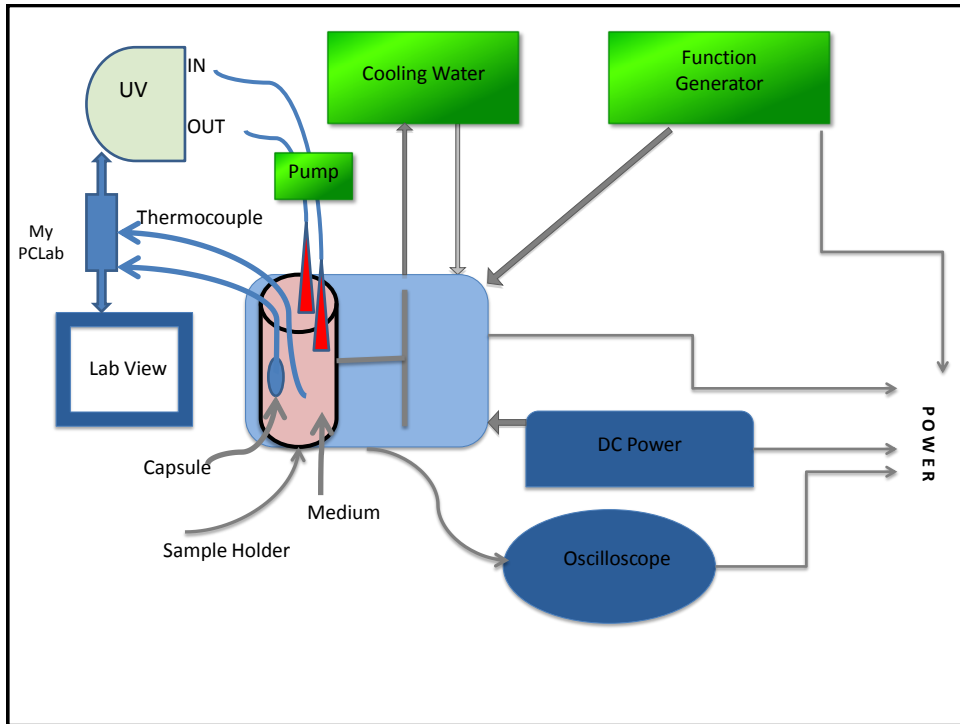
**Figure 7.24** Schematic representation of the experimental setup

The novelty of this setup was also in the use of two separate thermocouples attached through the lid of the sample container. One thermocouple was attached directly to the coated capsule (it was embedded during the coating process) and the other was immersed directly in the medium as shown in Figure 7.25.
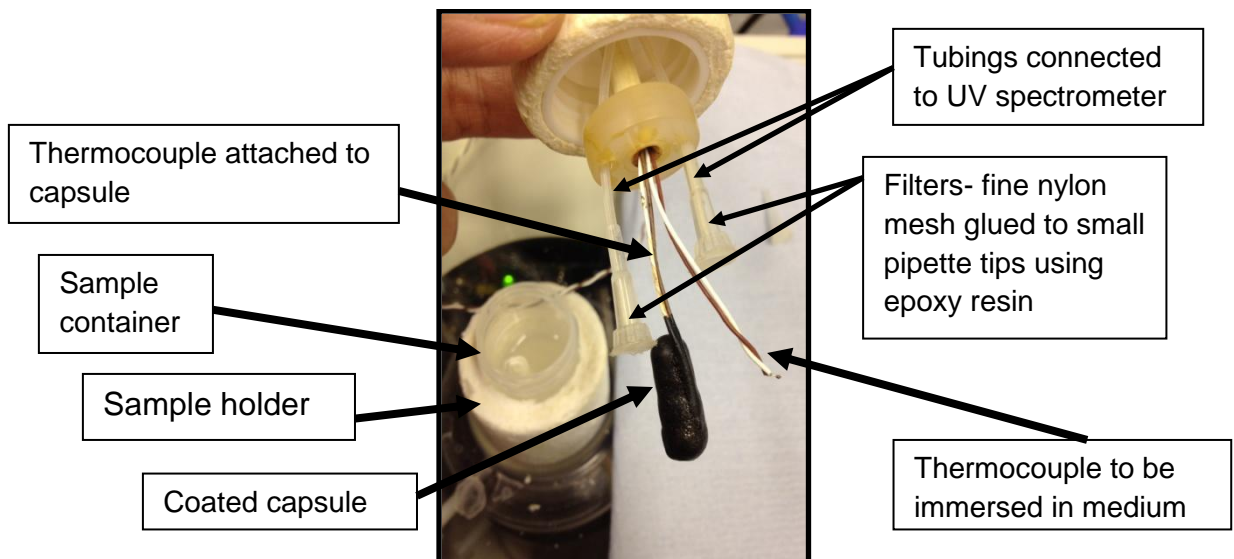


**Figure 7.25** The sample container consisting of two thermocouples connected to the coated capsule and the medium solution.

The other novelty was the two tubings which were immersed in the dissolution medium and connected to a micro cuvette (Figure 7.26). A micro pump was used to recirculate medium through the tubing into the cuvette in the UV spectrometer to measure the presence of drug release with time. The RF frequencies used were 521.5 and 330.3 kHz with a magnetic field of 24 and 17 mT, respectively. The sample container was then placed into the sample holder as shown in Figure 7.27.
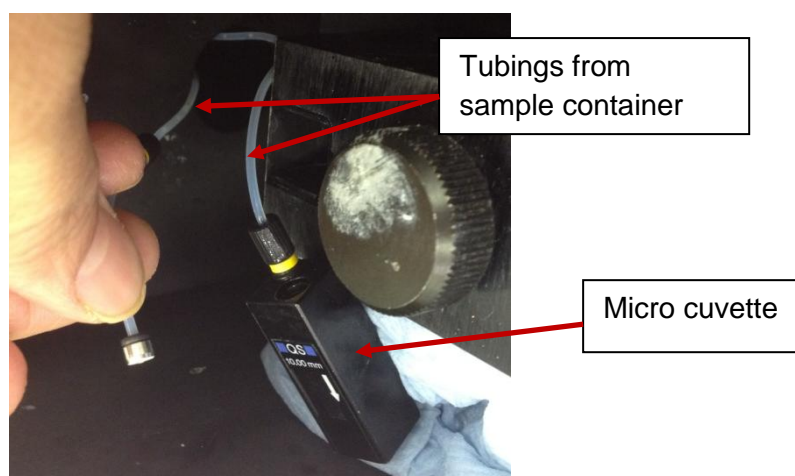


**Figure 7.26** The two tubings from the sample container are connected to a micro cuvette.
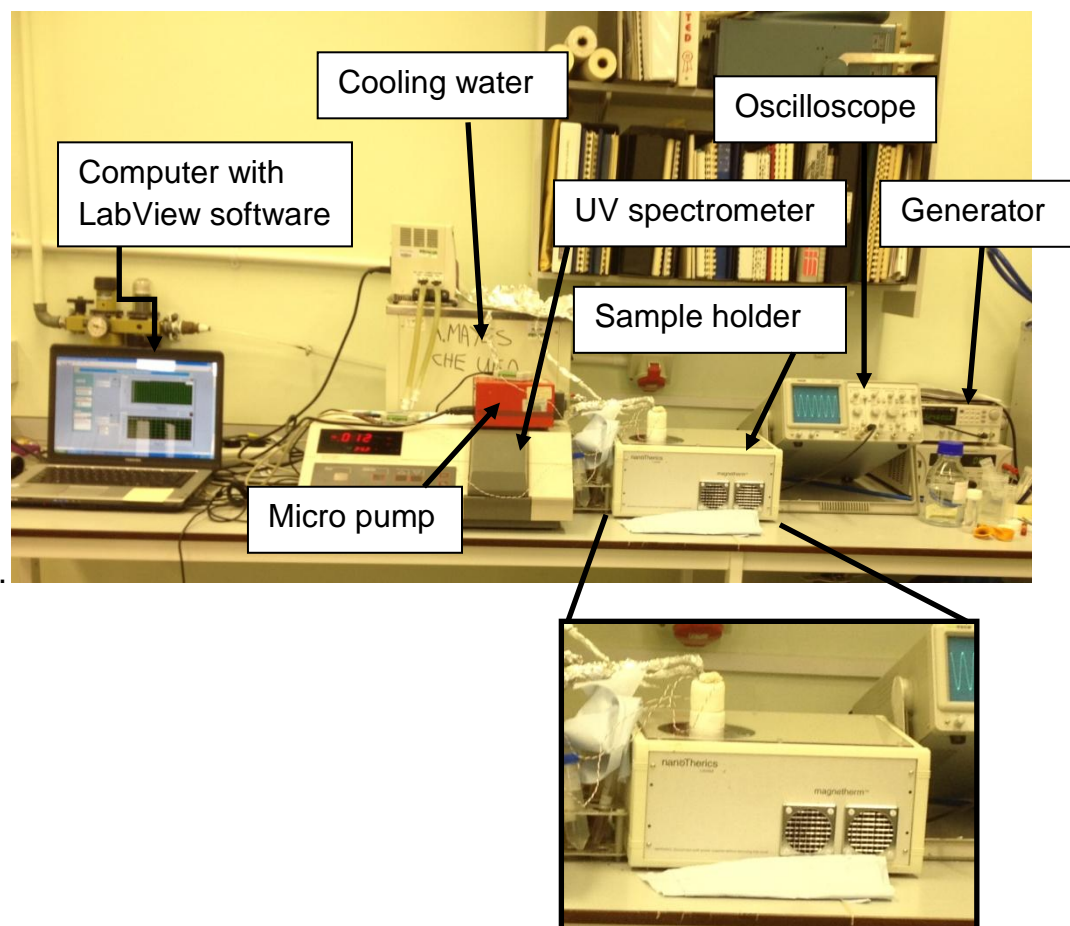
**Figure 7.27** The experimental setup showing the arrangement of instruments and location of the sample holder of the MagneTherm hyperthermia instrument.

Figure 7.28a shows the variation of temperatures with the exposure time for a capsule coated with a mixture of fatty acids exposed to RF at 521.3 kHz. It also showed the variation of UV absorbance with the exposure time. The dotted (green) curve of Figure 7.28a which corresponds to the temperature in the capsule coating layer showed a rapid increase up to 39$^{o}$C during the first 100 seconds and then plateaus off at that temperature until 800 seconds.
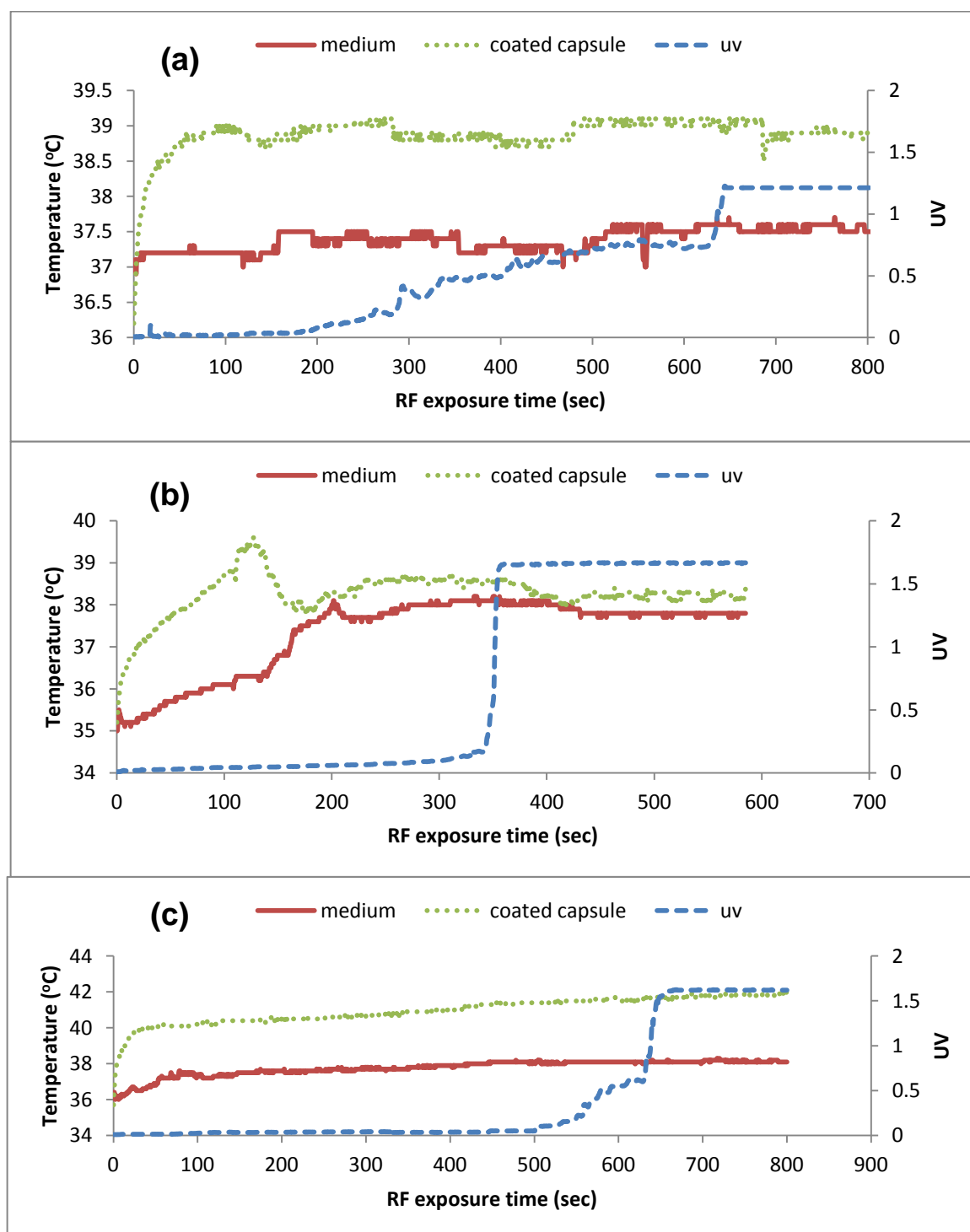
**Figure 7.28** The curves of temperatures with exposure time resulting from hyperthermia heating by IONs at 10 % by weight in (a) mixture of fatty acid C12 :C14 (40:60/w:w), (b) eicosane and (c) mixture of eicosane and docosane (40:60/w:w) exposed to RF at 521.3 kHz (24 mT). The dotted (green) and solid (red) curves are the heating temperatures at the capsule surface and in the dissolution medium, respectively. The broken (blue) curve is the variation of the UV absorbance, showing the release of drug with exposure time.

The solid (red) curve of Figure 7.28a, corresponds to the temperature of the dissolution medium, however this shows negligible changes in temperature eventhough after the heating of the coated capsule had started. It remained at 37$^{o}$C i.e. the temperature set for the dissolution medium throughout the exposure time.

The melting of the mixture of fatty acids observed at 39$^{o}$C was not expected since previous result from the visual observation at UCL showed that the melting of this mixture did not occur. The explanation for this observation is the presence of bile salts in the dissolution medium. It is known that bile salts exhibit surfactant properties and are capable of forming micelles. Therefore, the solubilisation effect of bile salts micelles (Bates *et al.*, 1966) towards the mixture of fatty acids is responsible for the observed phenomena. In other words, the coating material is solubilised by the bile salts instead of being melted by the heat generated. This exposes the capsules to the dissolution media and dissolves the capsule to release the drug.  This was supported by the observation of the UV absorbance of the released drug as shown by the broken (blue) curve of Figure 7.28a. This curve showed the drug was slowly being released after it was being exposed for about 200 seconds. After 650 seconds, the entire drug was released even though the capsule temperature had not reached the melting point. This observation confirms that the mixture of fatty acids as a coating material is inappropriate for this application.

Figure 7.28b showed similar curves as in Figure 7.28a but with eicosane as the coating material. The dotted line (green) of Figure 7.28b showed a sudden increase in temperature and plateau off at 38 $^{o}$C after 150 seconds. This observation is satisfying since the melting point for eicosane as determined previously by DSC was 37.79 $^{o}$C (please refer to Figure 6.7a). It is at 38 $^{o}$C that the coating starts to melt and exposed  the capsule to the dissolution medium, leading to the subsequent release of the drug into the medium. It took about 350 seconds for the entire drug to be released as shown by the broken (blue) curve of Figure 7.28b. The solid (red) curves showed slight variation in temperature of the dissolution medium but this was maintained at about 37$^{o}$C throughout the experiment.

Figure 7.28c showed the curves obtained using the mixture of eicosane and docosane (40:60/w;w) as the coating material. Once again, the dotted (green) curve showed a sudden increase in the temperature up to $40^{\circ}$C in less than 50 seconds. The curve then stabilised at temperatures between 40 and $42^{\circ}$C. The melting point for this mixture has been previously determined to be $40.1^{\circ}$C (please refer to 6.7c). The result showed that the melting point was reached after 50 seconds of exposure time. Once it reached the melting point, it began to slowly melt the coating over 500 seconds. This then led to the exposure of the capsule to the dissolution medium which then dissolved the capsule and released the drug. The entire drug was released after 650 seconds (see broken (blue) curve of Figure 7.28c). Finally, the solid (red) curve of Figure 7.28c shows that the temperature of the medium stayed constant at 37 $^{\circ}$C throughout the exposure.

Of the three coating materials tested at a frequency of 521.3 kHz, it may be concluded that, eicosane is the most suitable coating material, followed by the mixture of eicosane and docosane. This is supported by the results obtained from Figure 7.28a-c. Eicosane is the better coating material due to the rapid release of the drug. The mixture of fatty acids is not suitable as a coating material because of the presence of bile salts in the dissolution medium. Another interesting behaviour observed from these figures is the temperatures difference between that observed at the capsule (dotted (green) curves) and in the dissolution medium (solid (red) curves). In all of the figures, the temperature of the dissolution media is maintained at about $37^{\circ}$C throughout the experiment even though the heating of the capsules has started. It is exciting since this indicates that the heating of the capsules does not affect the surroundings material. This is a relief because when applied in the body, the heat generated from heating of the capsules at an affected area will not disturb the unaffected area or healthy cells of the body.

The same experiments were repeated but at an RF frequency of 330.3 kHz with a magnetic field of 17 mT. Figure 7.29a-c showed the curves resulted from exposing the different coatings at 330.3 kHz.
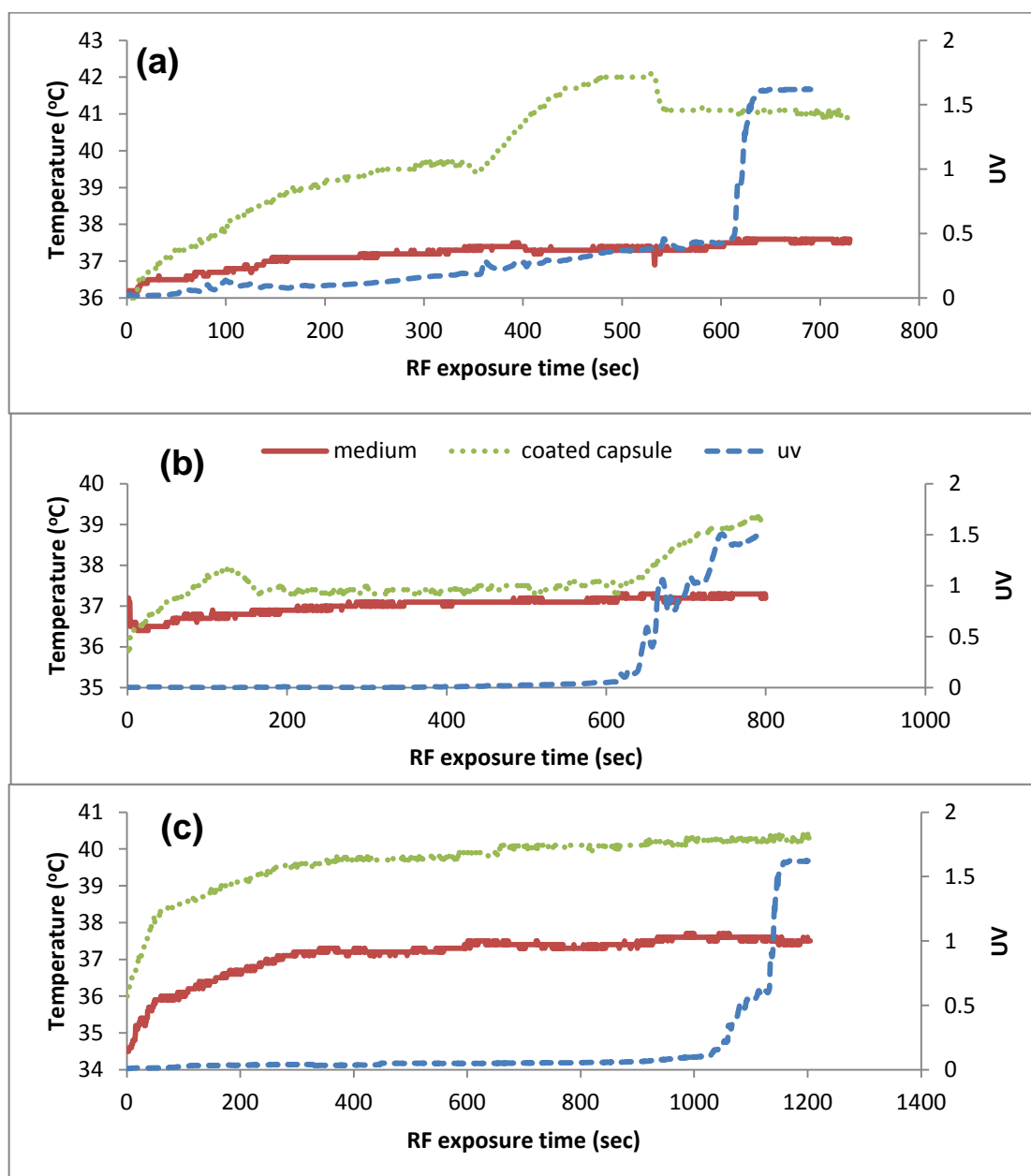
**Figure 7.29** The curves of heating temperatures with exposure time resulting from hyperthermia heating by IONs at 10 % by weight in (a) mixture of fatty acid C12 :C14 (40:60/w:w), (b) eicosane, and (c) mixture of eicosane and docosane (40:60/w:w) exposed to RF at 330.3 kHz. The dotted (green) and solid (red) curves are temperature at the capsule and of the dissolution medium, respectively. The broken (blue) curve is the variation of the UV absorbance of the released drug with exposure time.

Similar behaviours were observed as those obtained at 521.3 kHz. However, the release of drug at this frequency was observed to be slower than that at higher frequency. Again, it is concluded that even at a frequency of 330.3 kHz, eicosane is

the better coating material followed by the mixture of eicosane and docosane. The mixture of fatty acid is again not suitable as coating material because of the problems discussed previously. The same behaviour of the temperature at the capsule and the dissolution medium was observed which again indicated the heating of the capsules did not affect the surroundings much.

## 7.8 Conclusion

The visual observation at UCL was carried out for three different conditions and using three different coating materials. This was to see the effect of heating on the coated capsules. It can be summarised from the visual observations that the behaviour of coated capsules towards heating is dependent on the type of coating materials used, the condition of the environment and the location of the sample in the coil. Another important observation was the heating of the coated capsule only melted the coating and did not rupture the capsule. Therefore, it can be concluded that release of the drug was not due to the rupture of the capsule by heat but rather by solubilisation of the capsule by dissolution medium, as expected.

Taking into account all the results, an experimental setup for drug monitoring release was proposed. It was easy to setup and can be used to study the suitability of materials for coating the capsule, the drug release and the heating effects at various frequencies, magnetic field etc. The results presented using this proposed setup give strong support to its success in achieving the targeted objectives and could be applied to many other situations where delivery on demand is required. The magnetic nanoparticles embedded in the coating used in this experiment are IONs which are easy to prepare and can be mass produced. In addition, the heat generated by IONs does not affect the surrounding. This suggests that the heating of the capsule at a targeted area in the body will not affect the unaffected area of the body. Finally, a capsule is used in this setup to transport the drug. This could be administered orally and thus is the preferred form of drug delivery.

## 7.9 References

http://www.resonantcircuits.com

Atsumi, T., Jeyadevan, B., Sato, Y. & Tohji, K. (2007).Heating efficiency of magnetite particles exposed to AC magnetic field. *J. Magnetism and Magnetic Materials* **310**: 2841-2843.

Bates, T.R., Gibaldi, M., and Kanig, J.L. (1966). Rate of dissolution of griseofulvin and hexoestrol in bile salt solutions, *Nature*, **210**: 1331-1333.

# CHAPTER 8

## Conclusions and Future Work

## 8.1 Conclusions

Overall, this work describes the developments of novel drug delivery system exploiting special opportunities afforded by synthesis of nanoscale materials leading to a new drug delivery concept. The work started with the preparation of nanomaterials via two different methods. Nanocapsules and iron oxide nanoparticles, IONs, were prepared via microemulsion polymerisation and co-precipitation methods, respectively. The results of this work have been elaborated in Chapters 4 and 5.

Chapter 4 presented the work on preparation of nanocapsule through interfacial microemulsion polymerisation in a water-in-oil system. The association behaviour of the microemulsion components was presented using typical phase diagrams. The particle size and surface morphology of the nanocapsules were investigated using DLS and SEM. From the results obtained, the size of nanocapsules was found to be large (>140 nm) but they were produced only in very low yield. Most of the material formed a kind of porous honeycomb material, as indicated by SEM studies. These results did not meet the targeted objectives of this work whereby smaller particle sizes and high yield of clearly defined capsules were required. With that, this part of the work was halted in favour of a different drug delivery approach using magnetic hyperthermia. This required the synthesis of IONs via a co-precipitation method.

In Chapter 5, IONs were successfully synthesised through a co-precipitation method. Several techniques were employed to characterise their properties such as TEM, DLS, XRD, SQUID, FTIR and TGA. Various particle sizes of IONs were also synthesised using different amounts of stabilising ligand (oleic acid) during synthesis. The synthesised IONs demonstrated superparamagnetic properties as shown by the absence of a hysteresis loop in the SQUID data and zero coercitivity values. The IONs were then used for further studies in this work. This approach to IONs was

chosen because it uses only low toxicity compounds which are already pharmaceutically approved in the synthesis and, crucially, the methodology can be easily scaled up to produce large amounts of particles if required. This is not true, for example, for hot injection methods, which use more toxic materials and cannot be easily scaled, although they can produce more homogeneous particles.

Chapter 6 exploited two of the IONs properties, their particle size and magnetic behaviour, in formulating good coating materials for capsules. The IONs with various sizes were embedded in different coating materials. These materials were used to coat standard gelatine-based capsules. In order to investigate their thermal properties, thermal analysis of the non-embedded coating materials was carried out using DSC techniques. After that, IONs of various sizes were embedded in the coatings and hyperthermia studies were undertaken. IONs, with their magnetic properties were able to generate heat when an RF magnetic field was applied. Hyperthermia studies were therefore performed to investigate the heating effects of IONs towards the coating materials. Once the information from the hyperthermia studies was obtained, capsules containing a model drug were coated with the coating materials. The coated capsules underwent dissolution testing at various pH values using solutions prepared using acid, phosphate buffer and bile salts. These environments mimic that of the GI tract and the dissolution studies were done to investigate the ability of the coatings to withstand the environment in the GI tract for a certain period of time and their ability to prevent drug release until it is triggered, on demand, in the lower intestine via RF hyperthermia.

In Chapter 7, the focus of the work was to monitor the effect of heating and melting on the coated capsules through the lenses of a thermal imaging camera and video camera. Visual images or photographs were captured using three different experimental setups. The setups differed in the location of the coated capsules relative to the RF coil and their exposure to open air, half-immersed and fully immersed in dissolution medium.

Finally, taking into account all of the above observations, the grand design of a colonic-targeted drug delivery system, together with an experimental setup for testing the "release in demand" was proposed. The overall design of the delivery concept and the experimental setup is schematically shown in Figure 8.1 The approach is generic and could also be applied to many other situations where delivery on demand is required. The results presented using this experimental design strongly supported its success in achieving drug release under different environmental conditions that mimics the GI tract and also allowed the optimum radiofrequency to be established. It is easy to set up and IONs embedded in the coating used were favourable due to their ease in preparation, cost effectiveness, presumed safety in use and mass production potential. Finally, the capsules would be used in this setup to transport the drug to the lower intestine. The capsule can be delivered orally which is the favoured form of drug delivery wherever possible.
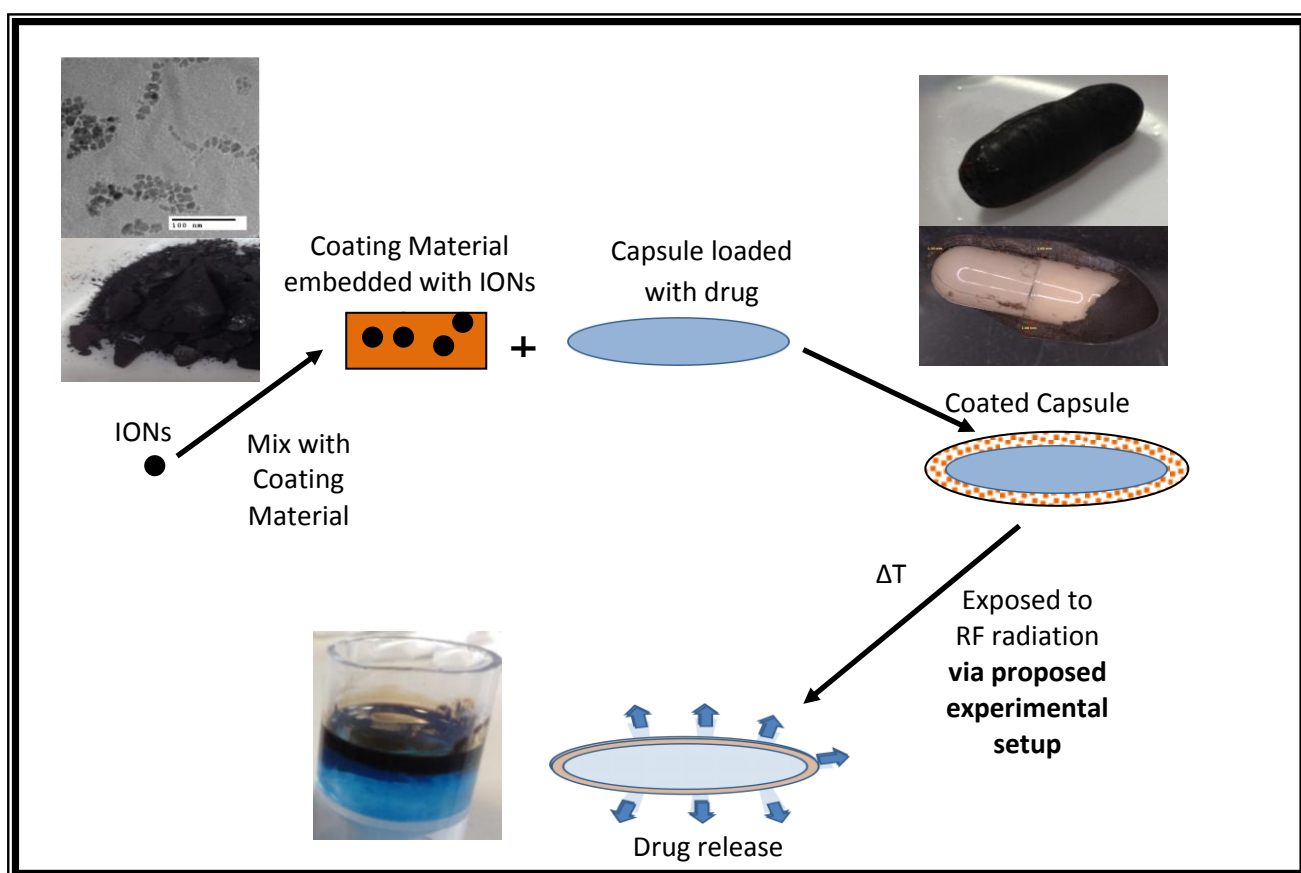


**Figure 8.1** Schematic summarising the results from the new and simple colonic targeted drug delivery system.

## 8.2 Future Work

Initial findings from the proposed experimental setup in this work have shown promising results and appear to be robust under various conditions. The setup can now be readily utilised to study the suitability of materials for coating a capsule, to qualitatively determine the drug release together with the time taken and to investigate the heating effects at various frequencies. The setup also gives significant insight into the biological implications of hyperthermia, whereby it has been shown the heat generated by IONs in this configuration does not affect the surroundings much. This suggests that the heating of the capsule at a targeted area in the body will not affect the unaffected area of the body through non-specific hyperthermia effects.

There is still much additional work required to map out completely the optimum experimental setup. In order to study the heating effect, many parameters need to be taken into account. For instance, various methods to synthesise IONs need to be carried out to produce highly monodispersed IONs with different shapes and sizes and assess whether this produces larger heating effects. The effect of the magnitude of voltage, current, and magnetic field applied should also be looked into. Further functionalisation of IONs should also be studied in order for it to be better dispersed in the coating materials. For future studies, it is highly recommended to investigate the effect of these variables on the heating effect of IONs in order to understand the system in more detail. The study of drug release can be further improved and extended to calibrating the spectrophotometer and measuring the volume of the recirculating system so that the exact amount of drug released could be quantitated.

The tracking and location of the capsules through the gut so that release can be triggered at the correct point should also be looked into. The location of the diseased part of the colon or GI tract can be determined by conventional methods such as MRI. It is then important to know when the coated capsule reaches the location site taking into account the amount of time for the capsule to reach the target after swallowing. Since IONs are magnetically active, the capsule can be readily tracked

by MRI imaging. It will also be too time consuming, expensive and likely uncomfortable for patients to be applied for routine clinical administration. A simple and low cost way of detecting the capsule is therefore suggested as another future study. This could be achieved using passive UHF RFID (Ultrahigh frequency Radiofrequency Identification) tags. By inserting small passive RFID tags inside the capsule, it might be possible to locate the capsule with sufficient accuracy using a simple hand-held scanner. Alternatively, some kind of frame with multiple detectors might be required to provide more accurate spatial positioning via triangulations of signals from several detectors. The capsules arrival in the diseased area should be readily detected by the back-scattered RF from the tags. This part of the work, however, would be an engineering project rather than a chemical one.

The toxicity of the nanoparticles must also be tested for their safe use in human body for clinical trial studies. Finally, work should be carried out including model animal studies. To date, all of our studies have been *in vitro*. In order to truly demonstrate the potential of this approach, appropriate *in vivo* studies would be required, starting with small rodent studies. Both the magnatherm instrument and the open coil geometry at UCL would suitable for this. The capsules would need to be scaled down to suitable dimensions and appropriate ethical approval sought, but in principle there are no major obstacles to such a study taking place.
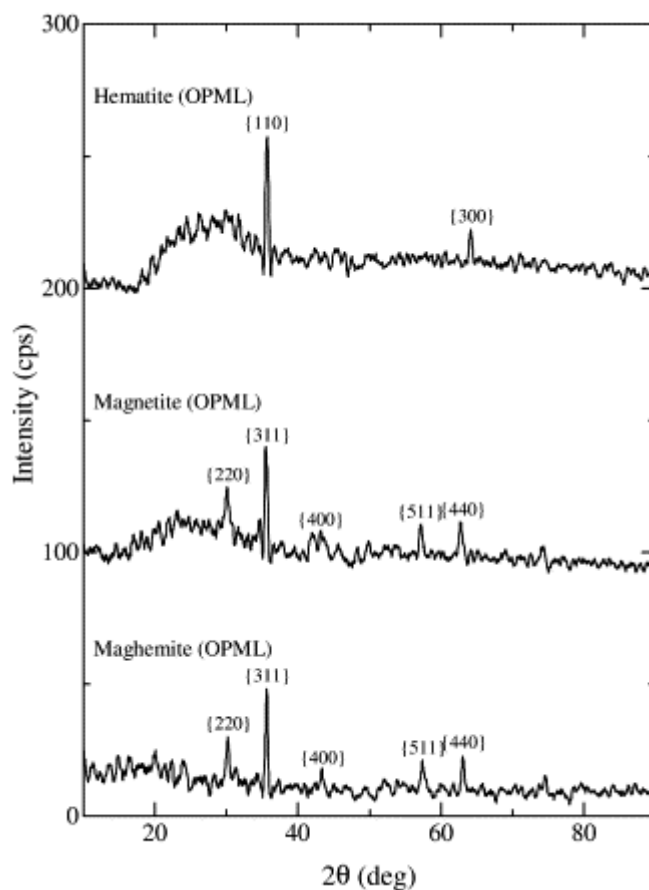
# Appendix

## Appendix A: Nanocarriers for drug delivery
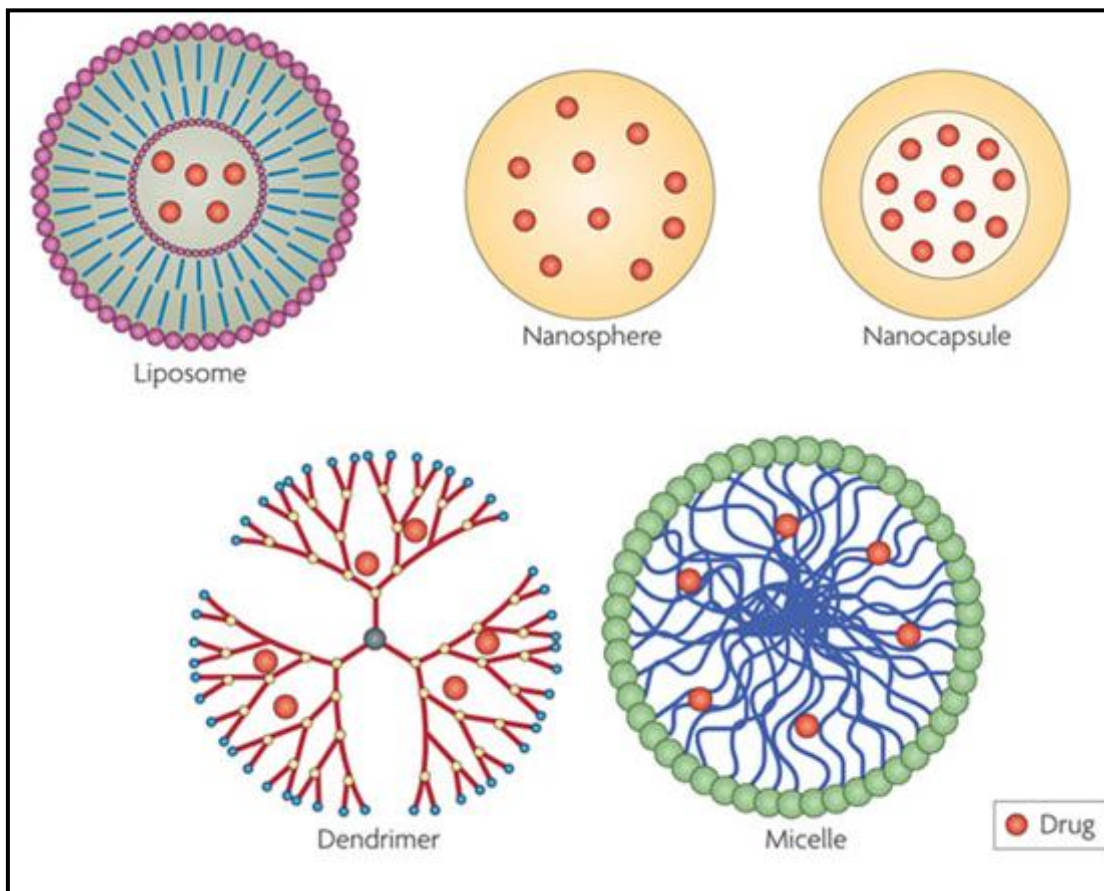


**Figure A.1** Schematic structure of different nanocarriers for drug delivery

Orive, G., Anitua, E., Pedraz, J.L., and Emerich, D.F. (2009). Biomaterials for promoting brain protection, repair and regeneration, *Nature Reviews Neuroscience*, **10**: 682-692.

## Appendix B:  XRD pattern for magnetite, maghemite and hematite



**Figure B.1** XRD pattern for magnetite, maghemite and hematite (Itoh and Sugimoto, 2003)

Itoh, H and Sugimoto, T. (2003). Systematic control of size, shape, structure, and magnetic properties of uniform magnetite and maghemite particles, *Jf Colloid Interface Sci.* **265**: 283-295.

## Appendix C:  JCPDS Card Number

**19-629**

| d | 2.53 | 1.49 | 2.97 | 4.85 | Fe$_3$O$_4$ | | ★ |
|---|---|---|---|---|---|---|---|
| I/I$_1$ | 100 | 40 | 30 | 8 | Iron Oxide | | (Magnetite) |

Rad. CuKα$_1$ λ 1.5405   Filter Ni   Dia.
Cut off       I/I$_1$ Diffractometer
Ref. National Bureau of Standards, Monograph 25, Sec. 5
31 (1967)

Sys. Cubic       S.G. Fd3m (227)
a$_0$ 8.396 b$_0$    c$_0$   A   C
α   β   γ   Z 8   Dx 5.197
Ref. Ibid.

2V   D   mp   Color Black
Ref. Ibid.

Sample obtained from the Columbian Carbon Co., New York 17, New York.
Spectrographic analysis showed the following major impurities: 0.01 to 0.1% Co, 0.001 to 0.01% Ag, Al, Mg, Mn, Mo, Ni, Si, Ti and Zn.
Pattern taken at 25°C.

| d A | I/I$_1$ | hkl | d A | I/I$_1$ | hkl |
|---|---|---|---|---|---|
| 4.85 | 8 | 111 | .8952 | 2 | 664 |
| 2.967 | 30 | 220 | .8802 | 6 | 931 |
| 2.532 | 100 | 311 | .8569 | 8 | 844 |
| 2.424 | 8 | 222 | .8233 | 4 | 1020 |
| 2.099 | 20 | 400 | .8117 | 6 | 951 |
| 1.715 | 10 | 422 | .8080 | 4 | 1022 |
| 1.616 | 30 | 511 | | | |
| 1.485 | 40 | 440 | | | |
| 1.419 | 2 | 531 | | | |
| 1.328 | 4 | 620 | | | |
| 1.281 | 10 | 533 | | | |
| 1.266 | 4 | 622 | | | |
| 1.212 | 2 | 444 | | | |
| 1.122 | 4 | 642 | | | |
| 1.093 | 12 | 731 | | | |
| 1.050 | 6 | 800 | | | |
| 0.9896 | 2 | 822 | | | |
| .9695 | 6 | 751 | | | |
| .9632 | 4 | 662 | | | |

**4-755**

| d | 2.52 | 1.48 | 2.95 | 5.90 | γ-Fe$_2$O$_3$ | | |
|---|---|---|---|---|---|---|---|
| I/I$_1$ | 100 | 53 | 34 | 2 | gamma Iron Oxide | | (Maghemite) |

Rad. FeKα λ 1.9373   Filter None   Dia.
Cut off       I/I$_1$ Photometric   I/I cor.
Ref. Haul and Shoon, Z. Phys. Chemie, 44 216-226 (1939)

Sys. Cubic       S.G. *
a$_0$ 8.350 b$_0$    c$_0$   A   C
α   β   γ   Z   Dx
Ref. Ibid.

εα   nωβ   εγ   Sign
2V   D   mp   Color
Ref.

*T$^4$ – P2$_1$3 or O$^2$ – P4$_2$3.
†Davies and Evans, J. Chem. Soc., 4373 (1956)
Low angle lines calculated from cell dimensions.

| d A | I/I$_1$ | hkl | d A | I/I$_1$ | hkl |
|---|---|---|---|---|---|
| 5.90 | 2 | 110 | 1.32 | 7 | 620 |
| 4.82 | 5 | 111 | 1.27 | 11 | 533 |
| 4.18 | 1 | 200 | 1.26 | 3 | 622 |
| 3.73 | 5 | 210 | 1.21 | 5 | 444 |
| 3.41 | 2 | 211 | 1.12 | 7 | 642 |
| 2.95 | 34 | 220 | 1.09 | 19 | 553,731 |
| 2.78 | 19 | 221 | 1.07 | 1 | 650 |
| 2.64+ | -- | 310 | 1.04 | 8 | 800 |
| 2.52 | 100 | 311 | 1.04 | 1 | 652,740+ |
| 2.41 | 1 | 222 | 1.03 | 1 | 554,741+ |
| 2.32 | 6 | 320 | | | |
| 2.23 | <1 | 321 | | | |
| 2.08 | 24 | 400 | | | |
| 1.87 | <1 | 420 | | | |
| 1.70 | 12 | 422 | | | |
| 1.61 | 33 | 511,333 | | | |
| 1.55 | <1 | 432,520 | | | |
| 1.53 | 1 | 521 | | | |
| 1.48 | 53 | 440 | | | |
| 1.43 | 1 | 433,530 | | | |

**13-534   MAJOR CORRECTION**

| d | 2.69 | 1.69 | 2.51 | 3.66 | α-Fe$_2$O$_3$ | | ★ |
|---|---|---|---|---|---|---|---|
| I/I$_1$ | 100 | 60 | 50 | 25 | IRON OXIDE | | (HEMATITE) |

Rad. CoKα   λ 1.7902   Filter –   Dia. 114.6MM
Cut off       I/I$_1$ MOLL RECORDING MICROPHOTOMETER
Ref. ARAVINDAKSHAN AND ALI, COUNCIL OF SCI. AND INDUST. RES., CENTRAL FUEL RESEARCH INSTITUTE, BIHAT, INDIA.

Sys. RHOMBOHEDRAL       S.G. R3c (167)
a$_0$ 5.0340 b$_0$    c$_0$ 13.752 A   C
α   β   γ   Z 6   Dx 5.271
Ref. KASTALSKY ET AL., AUST. J. CHEM., 21 1061 (1968)

εα 2.94   nωβ 3.22   εγ   Sign –
2V   D 5.26   mp 1350-1360 Color DEEP-BROWN
Ref. IBID., DANA'S SYSTEM OF MINERALOGY, 7TH ED.

| d Å | I/I$_1$ | hkl | d Å | I/I$_1$ | hkl |
|---|---|---|---|---|---|
| 3.66 | 25 | 012 | 1.102 | 14 | 226 |
| 2.69 | 100 | 104 | 1.076 | 2 | 042 |
| 2.51 | 50 | 110 | 1.055 | 18 | 2110 |
| 2.285 | 2 | 006 | 1.042 | 2 | 1112 |
| 2.201 | 30 | 113 | 1.038 | 2 | 404 |
| 2.070 | 2 | 202 | 0.9890 | 10 | 232,318 |
| 1.838 | 40 | 024 | .9715 | 2 | 229 |
| 1.690 | 60 | 116 | .9601 | 18 | 324 |
| 1.634 | 4 | 211 | .9578 | 6 | 0114 |
| 1.596 | 16 | 018 | .9512 | 12 | 140,0213 |
| 1.484 | 35 | 214 | .9314 | 6 | 413 |
| 1.452 | 35 | 300 | .9204 | 6 | 048 |
| 1.349 | 4 | 208 | .9080 | 25 | 1310 |
| 1.310 | 20 | 1010,119 | | | |
| 1.258 | 8 | 220 | | | |
| 1.226 | 2 | 036 | | | |
| 1.213 | 4 | 223 | | | |
| 1.189 | 8 | 128 | | | |
| 1.162 | 10 | 0210 | | | |
| 1.141 | 12 | 134 | | | |

**Figure C.1** JCPDS Card Number for magnetite (19-629), maghemite (4-755) and hematite (13-534).

## Appendix D: Calibration curves for dissolution studies at various pH.
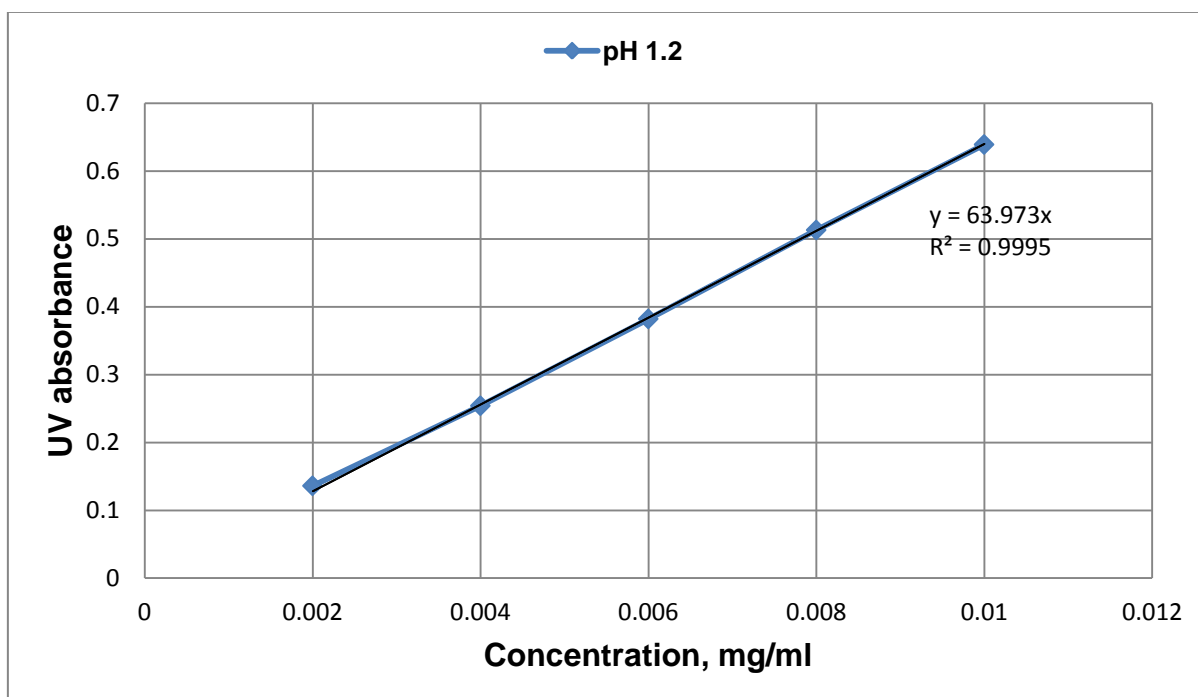


**Figure D.1** Calibration curve for paracetamol at pH 1.2 at 243 nm
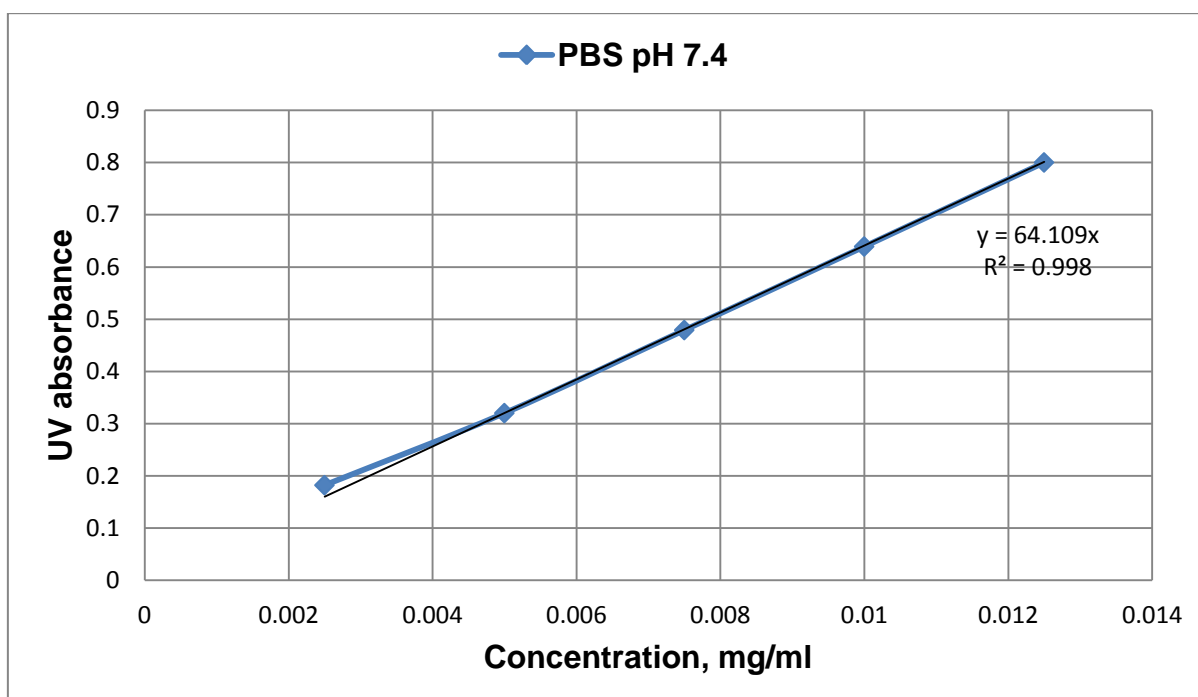


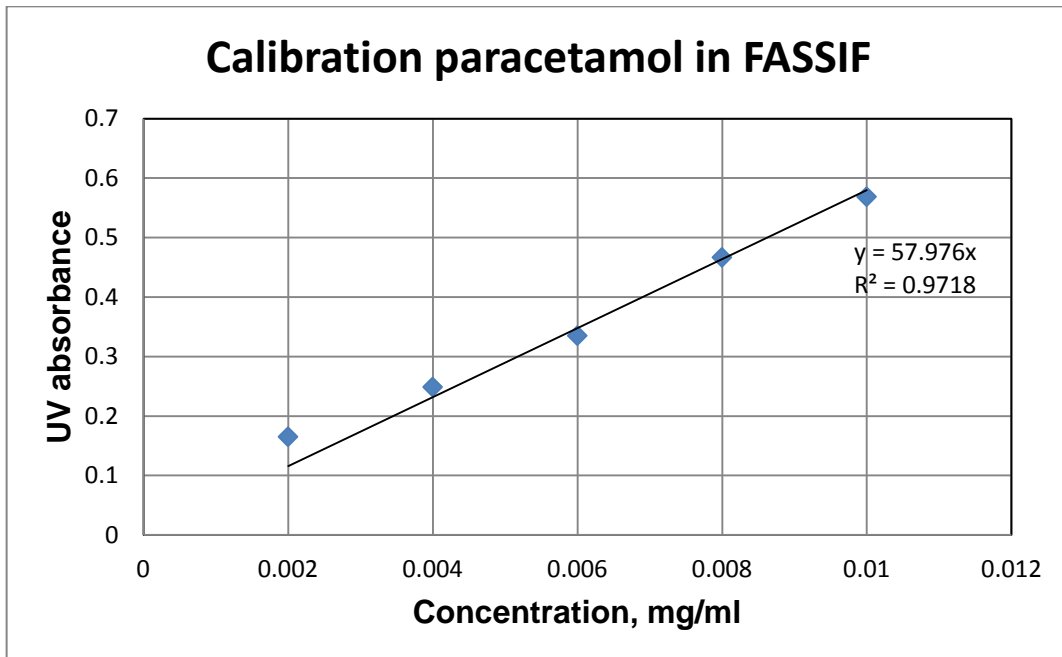**Figure D.2** Calibration curve for paracetamol at pH 7.4 at 243 nm

**Figure D.3** Calibration curve for paracetamol in FaSSIF at pH 6.5 at 243 nm

## Appendix E: Calculation of density of oleic acid on the surface of IONs

The surface density of oleic acid was calculated using the formula below (Chang *et al.* 2009).

Surface density = N/Φ = ρRωA/3Mr(1−ω)

where,

N is the total molecular number of the surface oleic molecules in the sample

ω is the weight loss ratio,

A is Avogadro constant,

Mr is the molecular weight of the surface oleic acid molecules

Φ is the total surface area of the nanoparticles in the sample

ρ is the density of the nanoparticles  and

R is radius of the nanoparticles

$$\text{Surface density} = \frac{\rho R \omega A}{3Mr(1-\omega)}$$

$$= \frac{5.24 \times 10^{21} \frac{g}{nm^3} (1.55nm)(0.2)(6.02 \times 10^{23} \frac{molecules}{mole})}{3 (282.46 \frac{g}{mole})(0.8)}$$

$$= 1.44 \frac{molecules}{nm^2}$$

Chang, Y., Bai, Y.P., Teng, B., and Li, Z.L. (2009). A new drug carrier: Magnetite nanoparticles coated with amphipilic block copolymer, *Chinese Sci. Bull.*, **54(7)**: 1190-1196.

## Appendix F:  Images of coated capsules
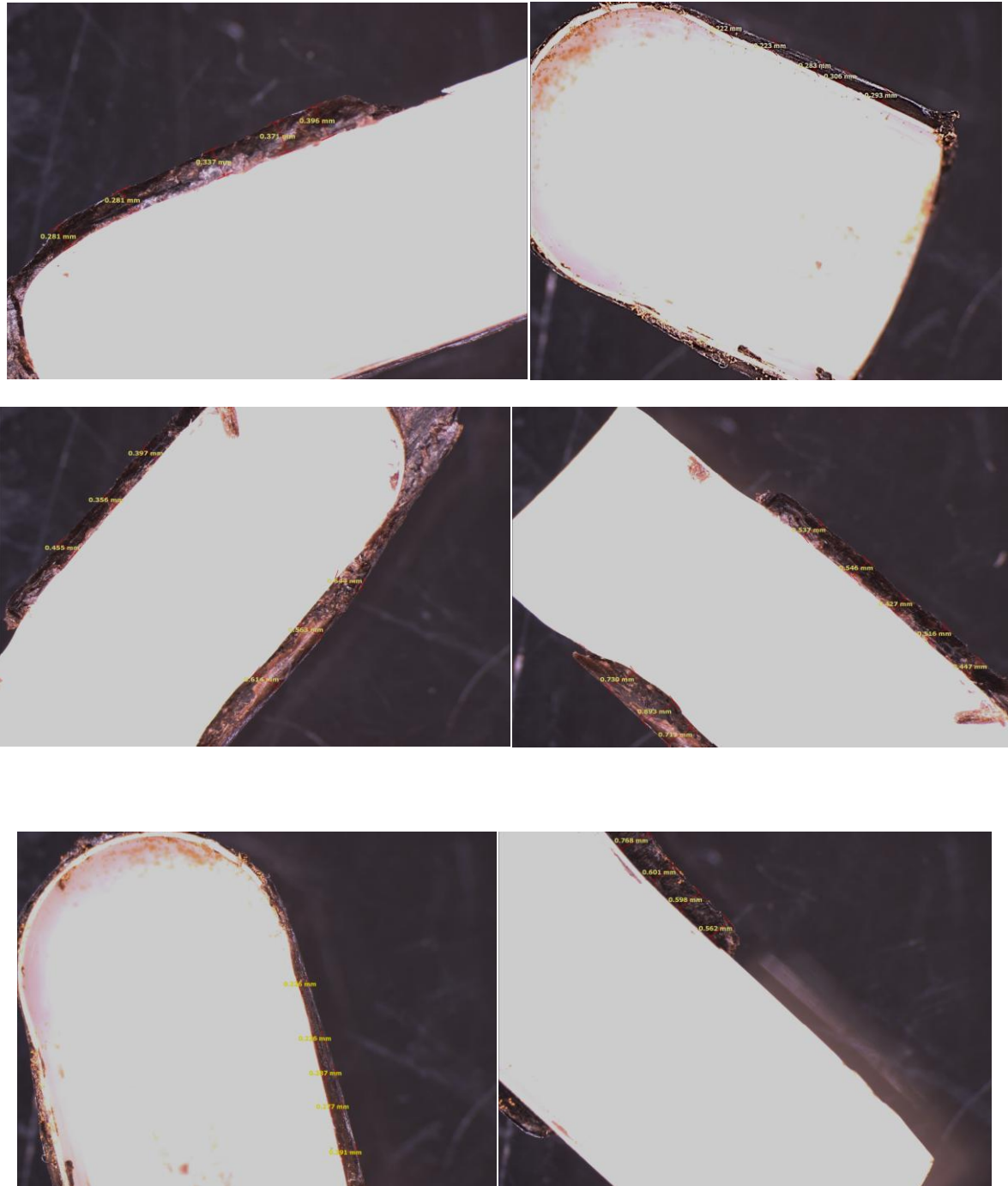


**Figure F.1** Optical images of fatty acid-coated capsules

**Figure F.2** Optical images of paraffin-coated capsules